



UNIVERSITY OF  
BIRMINGHAM

# Synthesis and Structural Characterisation of Solid Oxide Fuel Cell Materials

By

Benjamin Corrie

Supervisor: Professor Peter Slater

A thesis submitted to The University of Birmingham

For the degree of Doctor of Philosophy

The School of Chemistry

College of Engineering and Physical Sciences

The University of Birmingham

Sep 2014

UNIVERSITY OF  
BIRMINGHAM

**University of Birmingham Research Archive**

**e-theses repository**

This unpublished thesis/dissertation is copyright of the author and/or third parties. The intellectual property rights of the author or third parties in respect of this work are as defined by The Copyright Designs and Patents Act 1988 or as modified by any successor legislation.

Any use made of information contained in this thesis/dissertation must be in accordance with that legislation and must be properly acknowledged. Further distribution or reproduction in any format is prohibited without the permission of the copyright holder.

## Abstract

In this thesis three general systems were studied. These were tetrahedrally coordinated  $A_2MO_4$  oxides, apatite oxides such as  $La_8Sr_2Ge_6O_{26}$  and brownmillerite type  $Ba_2Sc_2O_5$  systems.

Powder X-ray diffraction indicated the successful incorporation of aluminium and gallium into both  $Ba_2GeO_4$  and  $Sr_2GeO_4$ . This led to the creation of oxide ion vacancies and an increase in ionic conductivity. A further increase in conductivity by an order of magnitude was observed in wet atmospheres due to additional proton conductivity.

Incorporation of strontium into  $LaBaGaO_4$  was also successful with phase pure sample observed up to a total of 50% barium replacement with strontium. The addition of strontium had a negative effect on the conductivity which reduced by almost two orders of magnitude for  $LaSrGaO_4$  when compared with  $LaBaGaO_4$ .

Neutron diffraction and TGA studies indicated the successful incorporation of water and fluorine into both the  $La_8Sr_2Ge_6O_{26}$  and  $La_8Sr_2Si_6O_{26}$  samples. The interstitial positions for fluorine and water ions were different from each other and between the germanium and silicon apatites. This suggested the interstitial site in the structure was composition dependant rather than universal for all apatite samples.

A stabilisation of an oxygen deficient perovskite structure was achieved by doping  $Ba_2Sc_2O_5$  with titanium to form  $BaSc_{0.7}Ti_{0.3}O_{2.65}$ . A reduction in the cost of this material was achieved by doping with yttrium or ytterbium for scandium. This was

found to have a negligible effect on the ionic conductivity in dry conditions and a slight increase in wet conditions.

Proton positions in hydrated  $\text{BaSc}_{0.25}\text{Y}_{0.45}\text{Ti}_{0.3}\text{O}_{2.65}$  were located using neutron diffraction of hydrated and deuterated samples at 4 K. the positions were found to be located in a 48k position slightly displaced from the proton positions reported in the literature for the related  $\text{Ba}_2\text{In}_2\text{O}_5$  systems.

## Acknowledgements

Without help and support from a lot of people this thesis wouldn't be complete and it is at this point I have an opportunity to say thanks.

Firstly thanks go to my supervisor professor Peter Slater for all of his help and guidance over the last four years and for the increased knowledge I now have of all things pie. I would also like to thank the past and present members of Pete's research group including Cathryn, Felix, Alaric, Jose, Matt, Bastian, Olli, Phil and Laura.

I would also like to thank the rest of the 5<sup>th</sup> chemistry group who offered help or assistance whenever it was needed and made my time in Birmingham enjoyable

Thanks must also go to Kevin, Steve, Ron and Richie at ISIS and Vladimir at SINQ for their help and support collecting neutron data, in particular the pesky in situ cells.

Thanks also go to all my friends and family who gave me a much needed place to step away from the thesis from time to time.

Last but by no means least I'd like to thank Katie as without her support I'd have given in long ago.

# Contents

---

Abstract .....	ii
Acknowledgements.....	iv
List of Abbreviations.....	viii
1 Introduction .....	1
1.1 Why do we need a change to energy production.....	1
1.2 Fuel Cell history .....	5
1.3 How fuel cells work .....	6
1.4 Types of fuel cell.....	8
1.4.1 Proton Exchange Membrane Fuel Cell (PEMFC) .....	9
1.4.2 Alkaline Fuel Cell (AFC).....	9
1.4.3 Phosphoric Acid Fuel Cell (PAFC).....	10
1.4.4 Molten Carbonate Fuel Cell (MCFC).....	10
1.5 Solid Oxide Fuel Cell (SOFC) .....	11
1.5.1 SOFC Design.....	12
1.5.2 Electrolyte materials .....	14
1.6 Project Aims .....	23
1.7 References.....	24
2 General Experimental.....	29
2.1 Synthesis Methods .....	29
2.1.1 Experimental .....	29
2.1.2 Hydration.....	30
2.1.3 Fluorination .....	30
2.2 Structural characterisation.....	31
2.2.1 Crystal Symmetry .....	31
2.2.2 Bragg's Law.....	34
2.2.3 X-Ray generation .....	36
2.2.4 X-Ray Diffraction .....	37
2.2.5 Neutron Diffraction .....	44
2.3 Thermogravimetric Analysis (TGA).....	47
2.4 Impedance Spectroscopy .....	48

2.4.1	Data Analysis .....	52
2.5	Raman Spectroscopy .....	57
2.6	References.....	58
3	Electrolyte materials with tetrahedral moieties .....	60
3.1	Introduction .....	60
3.2	Ba <sub>2</sub> GeO <sub>4</sub> /Sr <sub>2</sub> GeO <sub>4</sub> .....	61
3.2.1	Experimental .....	61
3.2.2	Ba <sub>2</sub> GeO <sub>4</sub> .....	61
3.2.3	Sr <sub>2</sub> GeO <sub>4</sub> .....	70
3.3	LaBaGaO <sub>4</sub> / LaSrGaO <sub>4</sub> .....	75
3.3.1	Experimental .....	75
3.3.2	LaBaGaO <sub>4</sub> .....	76
3.4	LaBaAlO <sub>4</sub> .....	82
3.5	Conclusions .....	86
3.6	References.....	88
4	Water incorporation and Fluorination in Apatite Systems .....	89
4.1	Introduction .....	89
4.2	Germanate apatites .....	90
4.2.1	Experimental .....	90
4.3	La <sub>8</sub> Sr <sub>2</sub> Ge <sub>6</sub> O <sub>26</sub> .....	90
4.3.1	Structure.....	91
4.3.2	Hydration.....	92
4.3.3	Fluorination .....	102
4.3.4	In-Situ dehydration / defluorination examined by XRD .....	109
4.4	Hydration studies of La <sub>9.75</sub> Ge <sub>6</sub> O <sub>26.625</sub> .....	110
4.4.1	Experimental .....	111
4.4.2	Structure.....	111
2.1.1.1.	Hydration.....	116
4.5	Silicate apatites .....	119
4.5.1	Experimental .....	119
4.5.2	La <sub>8</sub> Sr <sub>2</sub> Si <sub>6</sub> O <sub>26</sub> .....	119
4.6	Conclusions .....	132
4.7	References.....	134

5	Yttrium and ytterbium doping in titanium doped barium scandate systems.....	136
5.1	Introduction .....	136
5.2	Experimental .....	137
5.3	Ti doping in BaScO <sub>2.5</sub> .....	137
5.4	Yttrium doping in BaSc <sub>0.65</sub> Ti <sub>0.3</sub> B <sub>0.05</sub> O <sub>2.65</sub> .....	141
5.4.1	Conductivity .....	143
5.4.2	Hydration of yttrium doped samples .....	146
5.1.1	Neutron diffraction studies.....	147
5.1.1	CO <sub>2</sub> Stability.....	154
5.5	Ytterbium doping in BaSc <sub>0.65</sub> Ti <sub>0.3</sub> B <sub>0.05</sub> O <sub>2.65</sub> .....	156
5.5.1	Conductivity data .....	157
5.6	Conclusions .....	159
5.7	References.....	161
6	Conclusions and Further Work.....	163
6.1	A <sub>2</sub> MO <sub>4</sub> electrolyte materials .....	163
6.2	Water and fluorine incorporation in apatite systems.....	165
6.3	Yttrium and ytterbium doping in barium scandate systems.....	167
6.4	Further work.....	169

## List of Abbreviations

AFC	- Alkaline Fuel Cell
BCC	- Body Centred Cubic
CCS	- Carbon Capture and Storage
CGO	- Gadolinia stabilised Ceria
CIF	- Crystallographic Information File
DMFC	- Direct Methanol Fuel Cell
DTA	- Differential Thermal Analysis
FCC	- Face Centred Cubic
FCEV	- Fuel Cell Electric Vehicle
GSAS	- General Structure Analysis Software
HRPD	- High Resolution Powder Diffractometer
HRPT	- High Resolution Powder Diffractometer for Thermal Neutrons
LSGM	- Lanthanum Strontium Gallium Magnesium Oxide
MCFC	- Molten Carbonate Fuel Cell
MS	- Mass Spectrometry
PAFC	- Phosphoric Acid Fuel Cell
PEMFC	- Proton Exchange Membrane Fuel Cell
PSI	- Paul Scherrer Institut
PTFE	- Polytetrafluoroethylene
PVDF	- Polyvinylidene fluoride
PXRD	- Powder X-ray Diffraction
SOFC	- Solid Oxide Fuel Cell
TGA	- Thermogravimetric Analysis
TOF	- Time of Flight
XRD	- X-ray Diffraction
YSZ	- Yttria Stabilised Zirconia

# 1 Introduction

---

## 1.1 Why do we need a change to energy production

The green energy debate has been a frequently reoccurring topic in science and politics for decades. Most scientists are in agreement with the need for a “greener” future and to prevent the environmental impacts the production of CO<sub>2</sub> is having on the world. The science and engineering research into green energy is somewhat challenging and has only become significant within the last few decades. Several factors have to be taken into consideration when researching and designing methods of energy production. Before mass production and a widespread roll out can begin an assessment into whether the energy devices are feasible and have potential in changing the world’s energy production for the better must be researched. This can involve assessing whether the devices are robust, durable, efficient, easy to manufacture, have a good life span, low cost, practical size and low maintenance. All these factors are thought-provoking, however they all play an important role in shifting the way the world embraces green energy scientific discovery and puts inventions into practice and mass production.

Green energy devices are designed to service the energy demand of the human population in order to reduce the production of CO<sub>2</sub>. This is important due to the environmental impact CO<sub>2</sub> has on the world, which is commonly known as “the greenhouse effect”. Currently the global energy consumption is increasing every year with an increase of 2.3% during 2013. A total 87% of the world’s energy is currently

obtained from burning fossil fuels. However the increase in consumption of fossil fuels will create a higher demand for the limited resources.<sup>1</sup> (Figure 1.1)

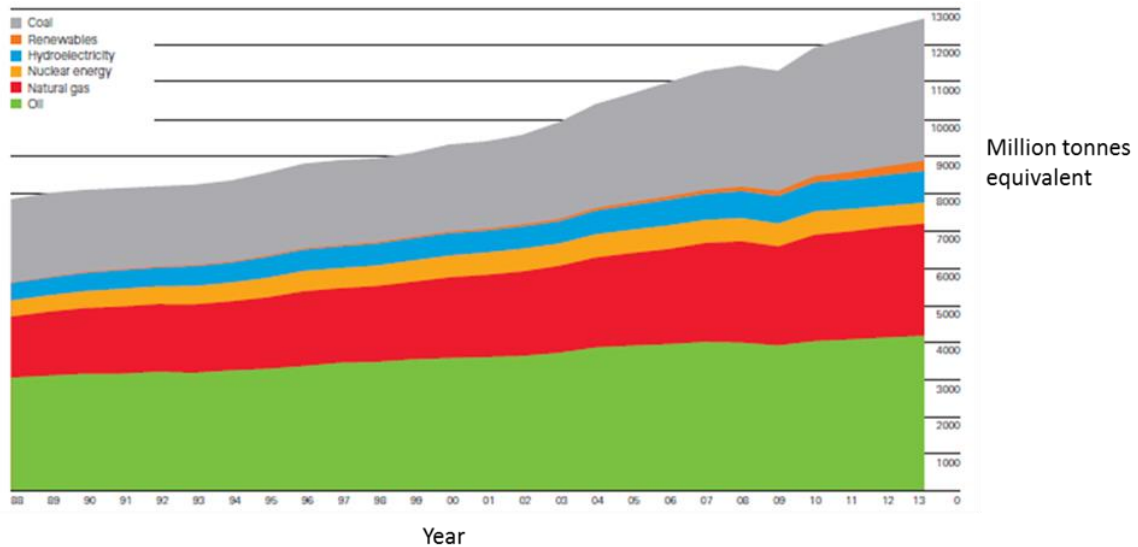


Figure 1.1 - World energy usage by source material from 1988 - 2013 converted to an equivalent amount of oil.<sup>1</sup>

The fossil fuel reserves are of a substantial size; however the length of time they will last depends on the demand for fossil fuels for the consumption in energy. At current rates oil and gas reserves will be depleted within 50 years,(Table 1.1) which may drop below 40 years once increases in consumption are factored in, this is unless greener energy methods are created to replace the use of fossil fuels.

Another factor behind the extensive research into alternate energy sources is the introduction of legislation on greenhouse gas emissions which are given off during the burning of fossil fuels, for example the UK's Climate Change Act 2008. The Climate Change Act 2008 set a target of an 80% reduction in the emission of greenhouse gases in the UK by 2050 compared with a baseline set in 1990.<sup>3</sup>

**Table 1.1 - Share of energy production by source in 2013. \* Resources remaining is the length of time the reserves of a resource will last if current production rates continue<sup>1,2</sup>.**

<b>Source</b>	<b>Primary Energy (%)</b>	<b>Resources remaining*</b>
Oil	32.9	53.3
Natural Gas	23.7	55.1
Coal	30.1	113
Hydroelectric	6.7	N/A
Nuclear	4.4	90
Renewables	2.2	N/A

There have been several approaches towards a solution for these two problems; the first approach involves increasing the efficiency of current devices, so that the current fuel resources last for longer allowing more time for a complete sustainable solution. This will result in a lower amount of the fossil fuels being used per year which will in turn increase the amount of time the reserves will last and decrease the amount of greenhouse gases released on an annual basis.

Current projects such as the Shell Peterhead carbon capture and storage (CCS) project and the White Rose CCS project assessing and developing ways of capturing CO<sub>2</sub> from power plants. The aim is to then store the gas under the North Sea in old depleted gas wells, which will reduce the amount of CO<sub>2</sub> released into the atmosphere.<sup>4,5</sup>

The main area of research to meet the two challenges is in renewable energy, this looks for alternative sources of energy such as wind, solar, hydroelectric and biofuel. Wind farms are currently being constructed both on land and out at sea alongside an increase in solar panels on buildings and houses. However in both cases they are heavily affected by the weather as neither method can store energy; e.g. no energy is available when there is no wind etc. The same is true of solar panels overnight and

on winter days (which are much shorter and have a greater cloud cover than summer days) where a lower amount of energy is produced. This is an issue as most household energy is used in the evenings and more energy is used in winter for lighting and heating. These issues are not present for biofuels as biofuels are burnt in the same way as fossil fuels and therefore more or less can be burnt depending on the energy requirements at a given time. However, for biofuels to meet the current energy requirements, more available land for the planting of fuel crops is required. The burning of biofuels also releases greenhouse gases in the same way as the burning of fossil fuels. Hydroelectric dams are a clean efficient power supply but require a very specific terrain on a large river which is often a long way from where power is required causing issues in transport and storage although these also exist in conventional power plants. Therefore a combination of methods will be required to meet the supply demands and requirements for emissions.

Batteries have potential to meet some of the needs for storage and transport of energy for portable devices and vehicles. Batteries can be used for storing excess generated electrical energy when it is not required as chemical energy, which can be released when demand is higher. Research into batteries includes the investigation of improvements to charging speed and capacity to weight and volume ratios.

Related to these energy areas are hydrogen fuel cells. Hydrogen fuel cells are electrochemical cells which react a fuel (e.g. hydrogen, syngas, and natural gas) with an oxidant (oxygen or air) to create electrical energy and heat. There are many different types of fuel cell, which each have different potential applications.

## 1.2 Fuel Cell history

Despite the large amounts of current research into fuel cells and the potential for fuel cells to have a major role in energy production, the technology of basic fuel cells has been around for around 200 years. The discovery of fuel cells began approximately 200 years ago with the discovery of electrolysis in 1800 by Sir Anthony Carlisle and William Nicholson. They discovered that water could be separated into its fundamental parts, hydrogen and oxygen by applying electricity using a Volta battery. This is the reverse electrolytic reaction to what is observed in a fuel cell.<sup>6,7</sup>

In 1838 William Grove was able to reverse this process by immersing a platinum cathode in sulphuric acid and a zinc anode in zinc sulphate, with the non-submersed ends of the electrodes in contact with hydrogen and oxygen. He observed the production of water and a constant current flowing between the electrodes. By using multiple pairs of electrodes in series it was possible to obtain both a higher current and voltage.<sup>6,8</sup>

In 1933, Francis Thomas Bacon created the first practical alkaline fuel cell using pure oxygen and hydrogen as oxidant and fuel respectively. During World War 2 he developed fuel cells for use by the Royal Navy. These cells were expensive but reliable; the patent was later licenced to Pratt and Whitney who developed cells which were used in the Apollo and space shuttle space programs. NASA spent tens of millions of dollars on the program which used alkaline fuel cells to power electrical equipment and provide drinking water.<sup>6</sup>

Since the 1950s, work on fuel cells has expanded with the discovery of new electrolyte materials, such as polymer electrolyte membranes. This has led to the

development of proton exchange membrane fuel cells, direct methanol fuel cells, phosphoric acid fuel cells, molten carbonate fuel cells and solid oxide fuel cells.

Since 2000, public awareness of fuel cells has increased with fuel cell prototypes and tests on larger scales. Fuel cell cars became available as test fleets including the Honda FCX Clarity (2007)<sup>9</sup> and the Hyundai I-Blue (2007)<sup>10</sup>. The Hyundai ix35 FCEV is due to be released in 2015 and will be the first production model fuel cell electric vehicle with plans for 1,000 to be made by 2015 and an increase to 10,000 soon after.<sup>10</sup> The Toyota Mirai was also announced as a commercially available fuel cell electric vehicle at the Los Angeles Auto Show and sales began in Japan in December 2014 with plans for release to the USA mid-2015 and the UK for September 2015.<sup>11</sup>

### **1.3 How fuel cells work**

A fuel cell consists of three main parts, the anode, cathode and electrolyte. The electrolyte is a dense non porous material which is capable of allowing ions to pass through it but has no electrical conductivity. The electrodes are porous materials which conduct electricity and ions and catalyse the reactions that happen at them.

In a basic high temperature fuel cell, which has an oxide ion conductor as the electrolyte (Figure 1.3 a), the fuel is pumped to the anode where electrons are removed from the hydrogen to leave protons. The electrons travel by the external electrical circuit to the cathode as they cannot pass through the electrolyte. The flow of electrons through a wire creates a current which can be used in electrical devices. At the cathode the electrons are added to oxygen molecules to form  $O^{2-}$  ions; these

$O^{2-}$  ions are capable of passing through the electrolyte to the anode where they bond with the protons to form water. This reaction is exothermic and heat is also generated.

Where a proton conducting electrolyte is used (Figure 1.3 b) in low temperature devices it is the protons which pass through the electrolyte and water is formed at the cathode rather than the anode. An advantage of a proton conducting fuel cell is that the fuel and water remain separate and therefore the fuel is not diluted.

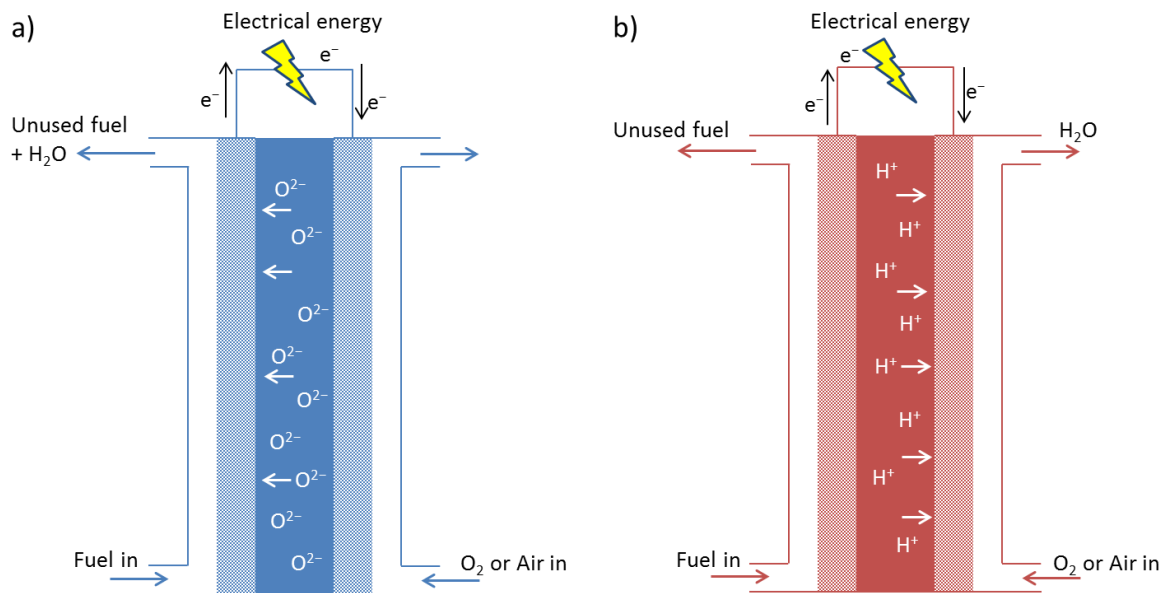


**Figure 1.2 - a) A fuel cell involving oxide ion conducting electrolytes, b) A fuel cell involving proton conducting electrolytes.**

This operation is similar to that seen in batteries; however a battery uses internally stored energy and must be recharged after a period of time, whereas a fuel cell will operate continually as long as the fuel and oxidant are provided. Fuel cells are usually used in stacks containing multiple cells to increase the power output so the energy can be used for more demanding applications.

Hydrogen fuel cells operating on pure hydrogen gas as a fuel are a clean source of electrical energy as the only waste gas from the cell is water vapour. If other fuels such as natural gas or syngas are used then CO<sub>2</sub> is also locally released from the cell as the carbon / carbon monoxide component reacts with the oxide ions. Almost all of the hydrogen gas used in industry is generated from the reformation of hydrocarbons (~95%) with electrolysis providing a smaller amount of hydrogen. It must also be considered that most of the electricity in the UK is from fossil fuel power plants therefore a large portion of the current hydrogen supply is derived from fossil fuels. High temperature fuel cells such as MCFCs and SOFCs can internally reform light hydrocarbons providing a link to the currently available networks for natural gas as a fuel source.

A fuel cell isn't a power source in the same way as solar or wind, but an energy conversion device capable of converting the chemical energy stored in fuel into electricity and heat without the need for direct combustion. This results in much higher conversion efficiencies than conventional combustion methods.

## **1.4 Types of fuel cell**

There are several types of fuel cell which have different operating temperatures and conditions which lead to uses in different applications. Fuel cells are generally classified by their electrolyte material and although there are many types, there are five that are more common than the others.

### 1.4.1 Proton Exchange Membrane Fuel Cell (PEMFC)

A proton exchange membrane fuel cell (PEMFC) has a polymer membrane electrolyte which conducts protons. Nafion®, a perfluorosulfonic acid polymer, is the best performing electrolyte and was developed by DuPont (USA) in the 1970s. It can have an operational lifetime of  $10^4 - 10^5$  hours in PEMFCs with an operating temperature 50-80°C. PEMFCs often have an efficiency of 40-50%.<sup>6</sup>

There is a wide range of applications for PEMFCs because of their high power densities and low start up times due to the low temperature operation. Disadvantages of PEMFCs include the use of expensive platinum catalysts at the electrodes and a high sensitivity to CO and H<sub>2</sub>S which could be present in the gas feeds.<sup>13</sup>

### 1.4.2 Alkaline Fuel Cell (AFC)

An alkaline fuel cell uses a solution of potassium hydroxide (KOH) as the electrolyte and was the first type of fuel cell used in practical applications. AFCs were used in the space shuttles and the Apollo missions because they had high power densities and long lifetimes using pure H<sub>2</sub> and O<sub>2</sub>. Where air is used as the oxidant rather than O<sub>2</sub> the efficiency can be reduced as AFCs are readily poisoned by CO<sub>2</sub>.<sup>14</sup> The operating temperature of an AFC is typically 50-200°C with an efficiency of 50-55%.<sup>6</sup>

### 1.4.3 Phosphoric Acid Fuel Cell (PAFC)

A phosphoric acid fuel cell (PAFC) uses liquid phosphoric acid ( $\text{H}_3\text{PO}_4$ ) as the electrolyte. Early issues with PAFCs were due to reactions between the acid electrolyte and the electrode materials which initially prevented the use of 100%  $\text{H}_3\text{PO}_4$ . Advances in electrode material have since increased resistance to dissolution by the acid and 100%  $\text{H}_3\text{PO}_4$  is now used. The operating temperature of the cell is between 180-210°C.  $\text{H}_3\text{PO}_4$  solidifies at 42°C reducing the transport of ions at low temperatures. Uses of PAFCs include a power plant in Japan which used an 11 MW PAFC that operated for 6 years between 1991 and 1997.<sup>15,16</sup> PAFCs yield typical efficiencies in the 40% region although combined heat and power systems can increase this to around 70%.<sup>6</sup>

### 1.4.4 Molten Carbonate Fuel Cell (MCFC)

Molten carbonate fuel cells (MCFCs) have a mixture of alkali metal carbonates as the electrolyte. When the cell is operated the temperature (630-650°C) is above the melting point of the electrolyte and the  $\text{CO}_3^{2-}$  ion in the molten electrolyte acts as a charge carrier.  $\text{CO}_2$  must also be provided to the cathode to replace the  $\text{CO}_3^{2-}$  in the electrolyte although this is recovered at the anode. Although the materials in the cell are of low cost there are problems with breakdown of the electrolyte resulting in a short lifetime.<sup>17</sup>

The efficiencies of MCFCs are around 40% although this could rise to ~80% with heat recovery systems. The high operating temperature of MCFCs allows for the use of multiple hydrocarbon fuels such as  $\text{CH}_4$  and syngas.<sup>6</sup>

## 1.5 Solid Oxide Fuel Cell (SOFC)

Solid oxide fuel cells (SOFCs) are high temperature fuel cells that use a solid ceramic electrolyte. Conventionally the electrolyte was an oxide ion conductor such as yttria stabilised zirconia (YSZ) and which required operating temperatures between 800-1000°C for operation. More recently proton conducting materials are under investigation and it is hoped that they could lower the operating temperature to 500-600°C. The high temperature operation eliminates the need for the use of platinum in the electrodes and the heat can be recycled in combined heat and power systems. This was demonstrated by Siemens Westinghouse on a 220kW system where a total of 70% electrical efficiency was achieved running on natural gas.<sup>6</sup>

The high temperature operation also allows for the use of a wide range of fuels such as hydrocarbons, syngas and hydrogen gas. There are disadvantages related to the high temperature operation which include poor sealing of the cells at operating temperature for prolonged times and chemical reactions between the electrolyte and electrode materials.

SOFCs typically have an operating temperature between 600-1000°C with an efficiency of 50-70% although heat recovery or combined heat and power systems can increase this value.<sup>6</sup>

### 1.5.1 SOFC Design

Fuel cells are usually combined in an array or stack so that the power output is large enough for use in devices. Fuel cells are either supported or un-supported where in a supported system there is an additional substrate added in between cells to add mechanical strength. In an un-supported SOFC the anode or cathode is used to support the remainder of the cell and add mechanical strength. There are two main designs of solid oxide fuel cell which are tubular cells and flat cell stacks. These are designed for efficient gas flow and stacking capabilities.

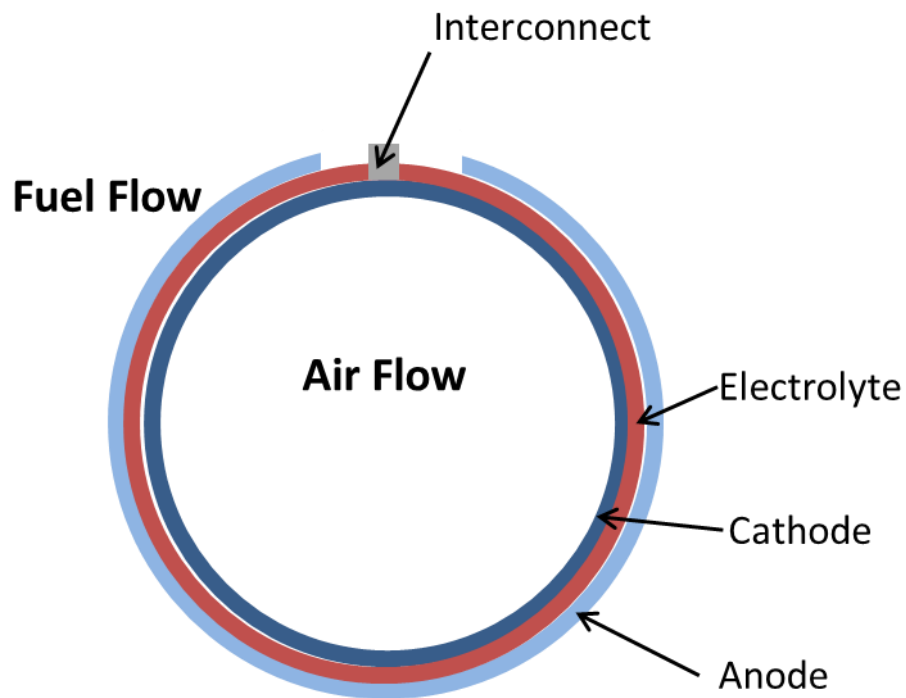


Figure 1.3 - Cross sectional diagram of a tubular fuel cell, where fuel is supplied to the outside of the cell and air the inside.

The tubular design (Figure 1.3) is more efficient for sealing as the electrolyte seals most of the cell whereas in a planar cell each layer requires sealing individually. An interconnect material then links the cathode to the outer of the cell this can also link several cells together in series. In a planar fuel cell stack the interconnect material also acts as a gas flow guide to both the cathode of one cell and the anode of another with the gases applied perpendicular to each other in order to reduce the number of parts required. The planar design of cell is more efficient and cheaper than the tubular design however finding suitable sealants for high temperature use is problematic. (Figure 1.4)

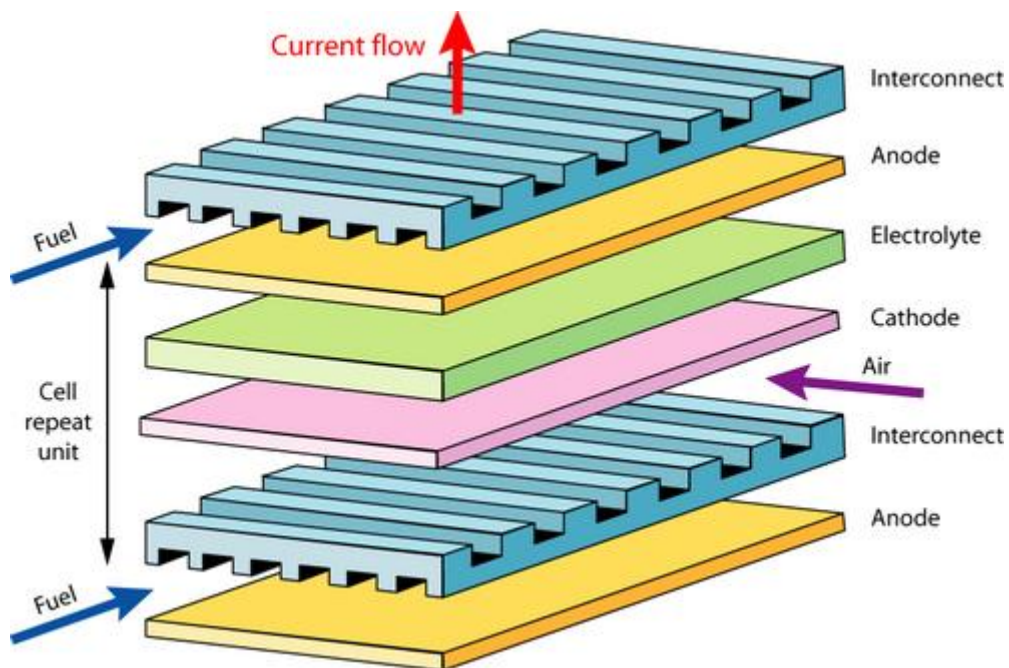


Figure 1.4 - Planar fuel cell stack design.<sup>18</sup>

## 1.5.2 Electrolyte materials

The requirements for an electrolyte in a SOFC cover a wide range of characteristics that include high ionic conductivity, low electronic conductivity, chemical stability in oxidising or reducing environments at high temperatures and good sinterability so strong gas tight membranes can be formed. Traditionally electrolytes have been made from materials with either fluorite or perovskite type structures although more recently other materials have been investigated.

### 1.5.2.1 Fluorite electrolytes

Most of the oxide ion conducting SOFC electrolytes have a fluorite structure including; yttria stabilised zirconia (YSZ), gadolinia stabilised ceria (CGO) and bismuth oxide. Materials with the fluorite structure have the chemical formula  $AO_2$  where A is a  $M^{4+}$  ion (Figure 1.5). The  $M^{4+}$  cations occupy the face centres and vertices with the anions in the eight tetrahedral sites around them.

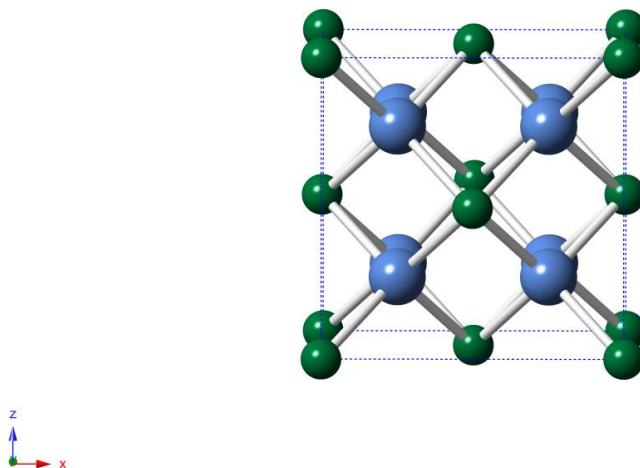


Figure 1.5 - Fluorite structure, large blue atoms are  $O^{2-}$  ions and small green atoms are  $M^{4+}$  ions.

Electrolytes based on zirconia ( $ZrO_2$ ) are the most researched SOFC electrolyte material and were first used in a fuel cell by Baur and Preis in 1937.<sup>19</sup> Zirconia at room temperature does not have a cubic fluorite structure and is a poor ionic conductor and the cubic fluorite structure is only present above  $2300^\circ C$ .<sup>20</sup> The fluorite structure can be stabilised at room temperature by doping with trivalent rare earth metals or divalent alkaline earth metals this also introduces oxygen vacancies which improves oxide ion conductivity. The most common electrolyte material is yttria stabilised zirconia (YSZ) which exhibits good oxide ion conductivity at high temperatures when doped with 8 mol%  $Y_2O_3$ . The other commonly used dopant in zirconia is scandium which yields a material with a higher ionic conductivity than YSZ (when doped with 11 mol%  $Sc_2O_3$ ). Due to the high cost of scandium YSZ is the industry preferred material.<sup>20,21</sup>

YSZ requires an operating temperature of  $800 - 1000^\circ C$  for the ionic conductivity to be sufficient for use as an electrolyte. This adds a lot of strain to the other components of the fuel cell as thermal expansion properties need to be closely matched to prevent cracking during operation. The high temperature of operation also reduces the viability of YSZ-based fuel cells being used in small portable applications.

Another material with the fluorite type structure used in solid oxide fuel cells is doped cerium oxide ( $CeO_2$ ). The most common dopants are gadolinium oxide ( $Gd_2O_3$ ) to produce cerium gadolinia oxide, CGO, and samarium oxide ( $Sm_2O_3$ ) to produce samaria doped ceria, SDC. Both of these materials have ionic conductivities that are higher than the YSZ electrolytes which allows for a lower operating temperature of  $500 - 650^\circ C$ . A disadvantage of CGO and other doped ceria electrolytes is the

levels of n-type electrical conductivity in reducing atmospheres above 600°C is too high to be considered negligible and this reduces the performance of the cell. This is caused by the partial reduction of  $\text{Ce}^{4+}$  to  $\text{Ce}^{3+}$  which although it introduces oxygen vacancies, it also creates carriers for electrical conductivity; this results in increases in both the ionic and electrical conductivity.<sup>23</sup> A number of different routes have been attempted to improve the properties of ceria electrolytes especially in the areas of high temperature stability in reducing atmospheres and mechanical strength using the introduction of sintering aids.  $\text{Ce}_{0.8}\text{Gd}_{0.2-x}\text{Y}_x\text{O}_{1.9}$  was shown to exhibit an increase in ionic conductivity and a decrease in electrical conductivity when compared with  $\text{Ce}_{0.8}\text{Gd}_{0.2}\text{O}_{1.9}$ .<sup>24</sup> The sintering temperature of CGO was found to be reduced by 200°C on addition of 1% cobalt oxide.<sup>25</sup>

Other attempts to improve the conductivity of YSZ and the chemical stability of CGO have been to dope one material into the other. This was found to increase both the mechanical strength and ionic conductivity when doping 6 mol% CGO into 3 mol% YSZ compared with the widely used 8 mol% YSZ.<sup>26</sup>

Bismuth oxide-based fluorite materials have the highest recorded oxide ion conductivities; however it is only the  $\delta$ -phase which exhibits the high conductivity. The structural change to the  $\delta$ -phase occurs at 730°C but bismuth oxide has a melting point of 804°C which limits the window of device operating temperatures.<sup>26,27</sup> Research into stabilising this  $\delta$ -phase at lower temperatures has been successful by doping with rare earth materials such as yttrium and erbium.<sup>28-30</sup> Further doping in yttrium or erbium doped bismuth oxide with niobium or tungsten also stabilises the  $\delta$ -phase and improves the long term stability of the material.<sup>31-34</sup> Disadvantages of bismuth oxide based electrolyte materials include poor stability under reducing

conditions (similar to those at the anode of a cell), a high thermal expansion and bismuth volatility. This significantly limits the use of bismuth-based solid oxide electrolytes until a solution to these problems is found.<sup>21,35,36</sup>

### 1.5.2.2 Perovskite electrolytes

The perovskite structure is frequently adopted by materials with the general formula  $ABX_3$ , where A and B are cations and X is an anion which can bond to both (often O). The A cation is larger than the B cation; an ideal cubic perovskite is shown in Figure 1.6.

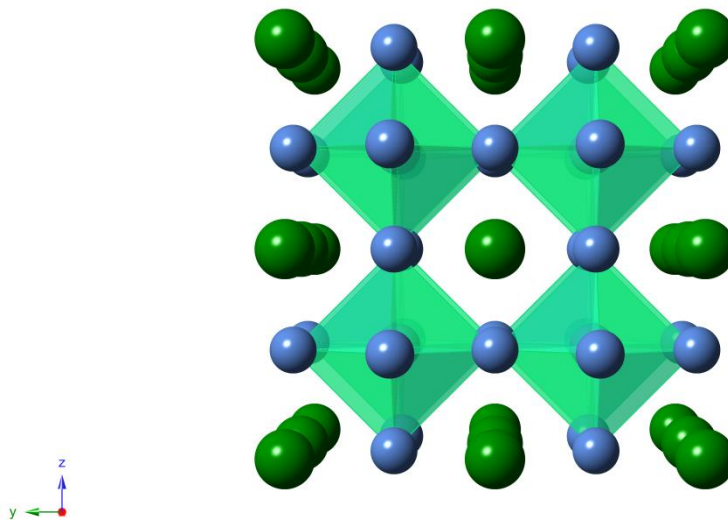


Figure 1.6 - Perovskite structure, A atoms in dark green, O atoms in blue and B octahedra in green

The perovskite structure can be hexagonal, cubic or orthorhombic / rhombohedral; to determine which will be formed, and whether a perovskite is possible, a Goldschmidt tolerance factor is used. The Goldschmidt tolerance factor ( $t$ ) is calculated from the

ionic radii of the atoms A, B and O by Equation 1.1, where  $r_A$ ,  $r_B$  and  $r_O$  are the ionic radii of A, B and O respectively.

Equation 1.1

$$t = \frac{r_A + r_O}{\sqrt{2}(r_B + r_O)}$$

An ideal cubic perovskite has a tolerance factor between 0.9 - 1, above 1 the structure is hexagonal, between 0.71 – 0.9 the structure is either orthorhombic or rhombohedral and below 0.71 non-perovskite structures are formed.

High oxide ion conductivity was reported in 1994 for oxygen deficient lanthanum gallate perovskite systems co-doped with strontium and magnesium to form  $\text{La}_{1-x}\text{Sr}_x\text{Ga}_{1-y}\text{Mg}_y\text{O}_{3-\delta}$  (LSGM).<sup>37,38</sup> The ionic conductivity of LSGM is higher than YSZ and similar to CGO at low temperatures.<sup>39-42</sup> Unlike CGO, LSGM does not contain an easily reducible  $\text{M}^{4+}$  ion and is therefore more stable in reducing atmospheres and superior to CGO in these conditions. Other dopants used in lanthanum gallate include cobalt and iron, which both increased the ionic conductivity (with slightly higher conductivities observed for cobalt), at higher dopant levels both increase electronic conductivity which lowers fuel cell performance.<sup>43-45</sup>

$\text{BaCeO}_3$  is another perovskite material with potential applications as a SOFC electrolyte. The most investigated dopants in  $\text{BaCeO}_3$  perovskites are  $\text{M}^{2+}/\text{M}^{3+}$  oxides on the  $\text{Ce}^{4+}$  site creating oxide ion vacancies. Attempted dopants include neodymium, gadolinium, erbium and ytterbium to form  $\text{BaCe}_{1-x}\text{M}_x\text{O}_{3-\delta}$ .<sup>45-49</sup> Gadolinium substituted  $\text{BaCe}_{0.9}\text{Ga}_{0.1}\text{O}_{5.9}$  has the highest ionic conductivity when compared with the other lanthanides tested.

A slight increase in proton conductivity was observed by Zhang and Zhao for co-doping strontium for barium in  $\text{Ba}_{1-x}\text{Sr}_x\text{Ce}_{0.9}\text{Nd}_{0.1}\text{O}_{3-\delta}$  although the oxide ion conductivity decreases with increasing strontium content.<sup>50</sup>

The main disadvantage of  $\text{BaCeO}_3$  perovskites for use as fuel cell electrolytes is the poor stability to increased partial pressures of  $\text{CO}_2$  or  $\text{H}_2\text{O}$  resulting in  $\text{BaCO}_3$ ,  $\text{Ba(OH)}_2$  and  $\text{CeO}_2$ . Stability to  $\text{CO}_2$  was increased by co doping with yttrium and niobium, ( $\text{BaCe}_{0.9-x}\text{Nb}_x\text{Y}_{0.1}\text{O}_{3-\delta}$  for  $x = 0 - 0.05$ ) and for  $\text{BaCe}_{0.7}\text{Gd}_{0.2}\text{Nb}_{0.1}\text{O}_{3-\delta}$  but in both cases ionic conductivity was reduced.<sup>51</sup>

The related system  $\text{BaZrO}_3$  has poor ionic conductivity but good stability to  $\text{H}_2\text{O}$  and  $\text{CO}_2$  atmospheres. Attempts to create a mixed  $\text{BaCeO}_3 - \text{BaZrO}_3$  system have successfully increased the stability to  $\text{H}_2\text{O}$  and  $\text{CO}_2$  at a cost of a reduction in ionic conductivity mainly due to an increase in grain boundary resistance.<sup>49,52,53</sup>

Related to the perovskite systems are brownmillerite structures such as  $\text{Ba}_2\text{In}_2\text{O}_5$  and  $\text{Sr}_2\text{Fe}_2\text{O}_5$ . These can be considered oxygen deficient perovskites and undergo an order-disorder transition at high temperatures after which they exhibit high oxide ion conductivity.<sup>54-56</sup> Doping on the Indium site with tungsten, titanium or gallium or on the barium site with lanthanum or strontium has been shown to stabilise the transition and increase ionic conductivity.<sup>57-61</sup> The presence of oxygen vacancies in the structure allows for proton conductivity with a conductivity of  $1.1 \times 10^{-3} \text{ S cm}^{-1}$  (reported for  $\text{Ba}_2\text{In}_{0.8}\text{Ti}_{0.2}\text{O}_{2.6}$  at  $450^\circ\text{C}$  at low hydration).<sup>62</sup> Ionic conductivity has also been improved on anion doping with phosphate and sulphate groups.<sup>63,64</sup>

As with many perovskite systems,  $\text{Ba}_2\text{In}_2\text{O}_5$  suffers from instability to  $\text{CO}_2$  although stability to  $\text{CO}_2$  can be improved by doping with lanthanum and zirconium but at a slight cost in ionic conductivity.<sup>65</sup>

### 1.5.2.3 Newer materials

Research into SOFC electrolytes has been dominated by work on oxide ion conducting fluorite and perovskite systems. The search for lower operating temperatures and improved chemical stability to electrode materials has however prompted a shift in focus towards other structure types which have shown high levels of ionic conductivity.

#### $\text{La}_2\text{Mo}_2\text{O}_9$ (LAMOX)

$\text{La}_2\text{Mo}_2\text{O}_9$  (LAMOX) was first reported in as an oxygen ion conductor in 2000 by Lacorre et al. and has higher ionic conductivity than YSZ.<sup>66</sup> The ionic conductivity of LAMOX increase by around two orders of magnitude due to a phase transition from the monoclinic  $\alpha$  form to the cubic- $\beta$  form at  $\sim 580^\circ\text{C}$ . Substitution on both the molybdenum and lanthanum sites has been attempted to improve the stability to reducing atmospheres and to stabilise the highly conducting  $\beta$ -phase at room temperature. Substitutions on the La site include rare earth, alkaline earth and alkali metals and on the Mo site include tungsten, vanadium, sulphur and chromium (to name a few). These have all stabilised the  $\beta$  phase at room temperature.<sup>67-72</sup> Tungsten doping on the molybdenum site has shown to vastly increase the stability towards highly reducing atmospheres although high levels of W doping lead to a large decrease in ionic conductivity.<sup>69</sup> The disadvantages to LAMOX electrolyte materials are related to the volatility of Mo at sintering temperatures and reactivity with cathode materials. There have been numerous attempts to synthesise dense

membranes using other lower temperature methods, such as a freeze-dried method and they have successfully lowered the temperatures by up to 300°C whilst still maintaining 95% density.<sup>73,74</sup>

### Apatite materials

Oxide ion conductivity was discovered in in apatite silicate systems in the 1990s where  $(\text{La/Nd})_{9.33}\text{Si}_6\text{O}_{26}$  based systems had the highest ionic conductivities observed (although other lanthanides were substituted on the La/Nd site with lower conductivity).<sup>75</sup>

The general formula for an apatite oxide material is  $\text{A}_{10}(\text{MO}_4)_6\text{O}_2$  where A is a rare earth or alkaline earth metal and M is either silicon, germanium or phosphorus. These materials are isostructural with hydroxyapatite bone materials. The structure can be described with a hexagonal unit cell and as containing isolated  $\text{MO}_4$  tetrahedra ordered to form A cation and oxide ion channels along the c axis. (Figure 1.7)

The highest oxide ion conductivities that have been reported are based on materials with either germanium or silicon tetrahedra, much poorer ionic conductivities have been reported for phosphorus containing samples.<sup>76-78</sup> It has been shown that unlike the fluorite and perovskite type electrolytes, which use oxide ion vacancies as a conduction mechanism, for the apatite systems it is the interstitial ions which are important for the ionic conductivity. The fully stoichiometric materials for both cations and anions such as  $\text{La}_8\text{Ba}_2\text{Si}_6\text{O}_{26}$  and  $\text{La}_8\text{Ca}_2\text{Si}_6\text{O}_{26}$  have much lower ionic conductivities when compared with oxygen excess samples e.g.  $\text{La}_9\text{BaSi}_6\text{O}_{26.5}$ .<sup>79,80</sup>

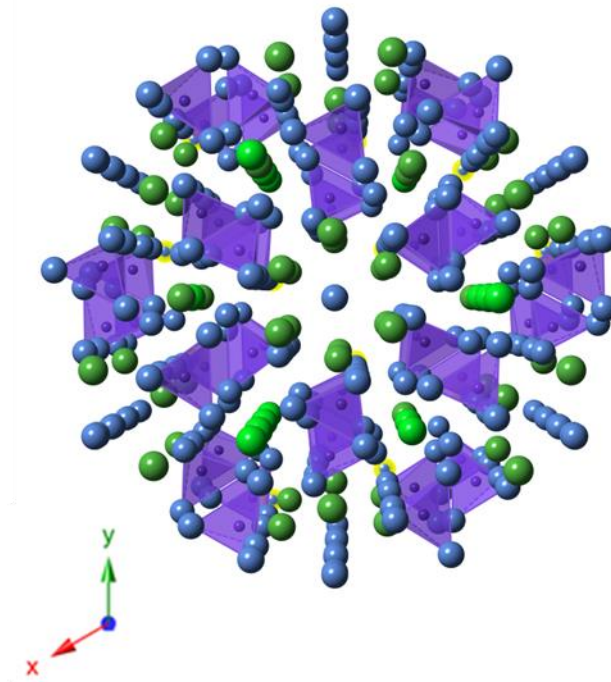


Figure 1.7 - Apatite structure looking down the c axis channel. A atoms are in green, MO<sub>4</sub> tetrahedra in purple and O in blue

The interstitial oxide ion position in the germanate system has been indicated by both modelling studies and neutron diffraction to be incorporated by the formation of a GeO<sub>5</sub> unit from the GeO<sub>4</sub> tetrahedra.<sup>81,82</sup> The location of the interstitial site in the silicon systems is less certain with reports for two possible sites. There have been computer modelling and neutron diffraction studies that suggest a site at the edge of the channel near to the SiO<sub>4</sub> tetrahedra and other reports which suggest a position much closer to the channel centre which could indicate a variation depending on the composition of the sample.<sup>83,84</sup>

Both the silicon and germanium systems have been widely investigated over a range of oxygen contents and phase pure samples can only be obtained for oxygen contents lower than 26.5 and 27 for the silicon and germanium systems

respectively.<sup>79</sup> High levels of oxide ion interstitials in the germanate systems result in a change in the room temperature structure from hexagonal to triclinic although this structure becomes hexagonal again at higher temperatures. This results in a reduction in ionic conductivity at temperatures below the phase change to hexagonal due to the higher strength oxygen bonds in the triclinic samples.<sup>85</sup> The hexagonal structure of the high oxygen excess apatites can be maintained with yttrium doping to form  $\text{La}_8\text{Y}_2\text{Ge}_6\text{O}_{27}$  that improves the conductivity at lower temperatures. The triclinic systems can also be returned to a hexagonal structure with treatment in ammonia to form  $\text{La}_{10}\text{Ge}_6\text{O}_{24}\text{N}_2$ .<sup>86</sup>

Cation doping with Mg, Al, Ga, Ba, Co on both the La and Si sites in both the germanate and silicate systems has been examined with mixed results.<sup>87-94</sup> Doping with Mg on the silicon site and aluminium on the germanium site has been shown to result in higher ionic conductivities.<sup>95,96</sup>

## 1.6 Project Aims

The aim of this project was to investigate materials for potential suitability as solid oxide fuel cell electrolytes.

Initially  $\text{A}_2\text{MO}_4$  (where A = La or Alkaline earth and M = transition metal) systems related to the known  $\text{LaBaGaO}_4$  protonic conductors will be investigated for their suitability as ionic conductors. To try and improve these materials oxide ion vacancies will be introduced by substituting  $\text{M}^{4+}$  ions for  $\text{M}^{3+}$  and changing the ratio of La to Ba. As hydrated forms of oxygen deficient materials have previously shown protonic conductivity which could potentially exist in other  $\text{A}_2\text{MO}_4$  samples.

Apatite materials related to the oxide ion conducting  $\text{La}_{9.33}\text{Si}_6\text{O}_{26}$  material with a hexagonal structure will be investigated for their ability to hydrate. Fluorination will also be used to see if a larger number of interstitial anions can be incorporated. There have been conflicting views on the location of interstitial anion positions for different apatite materials so neutron diffraction will be used to determine the location of the interstitial O or F atoms within the structure.

$\text{Ba}_2\text{Sc}_2\text{O}_5$  which is related to known proton conducting  $\text{Ba}_2\text{In}_2\text{O}_5$  based materials will also be investigated to discover if the oxygen deficient perovskite structure can be stabilised using titanium. Following this further substitution will be attempted in an effort to lower the cost of the material by lowering the total scandium content using other trivalent metals. If a successful material is found which exhibits protonic conductivity in humid atmospheres studies will be continued using neutron diffraction at 4 K to locate proton positions within the structure.

## 1.7 References

1. BP statistical review of World energy 2014, <http://www.bp.com/content/dam/bp/pdf/Energy-economics/statistical-review-2014/BP-statistical-review-of-world-energy-2014-full-report.pdf>, (accessed August 2014)
2. World Nuclear Association – Supply of Uranium, <http://www.world-nuclear.org/info/Nuclear-Fuel-Cycle/Uranium-Resources/Supply-of-Uranium/>, (accessed February 2015)
3. Climate Change Act 2008, <http://www.legislation.gov.uk/ukpga/2008/27/contents>, (accessed August 2014)
4. Peterhead CCS project, <http://www.shell.co.uk/gbr/environment-society/environment-tpkg/peterhead-ccs-project.html>, (accessed August 2014)
5. White Rose Carbon capture and storage project, <http://www.whiteroseccs.co.uk/>, (accessed August 2014)

6. A. B. Stambouli and E. Traversa, *Renewable & Sustainable Energy Reviews* 2002, **6**, 433.
7. E.I. Ortiz-Rivera, A.L. Reyes-Hernandez, and R. A-Febo, *Conference on the History of Electrical Power*, 2007, 91
8. J.M. Anujar, and F. Segura, *Renewable and Sustainable Energy Reviews*, 2009, **6**, 433.
9. Honda FCX Clarity Overview, <http://automobiles.honda.com/fcx-clarity/>, (accessed august 2014)
10. Hyundai Fuel cells, <http://www.hyundai.co.uk/about-us/environment/hydrogen-fuel-cell>, (accessed august 2014)
11. Mirai – Toyota’s FCV, <http://www.toyota.com/fuelcell/fcv.html>, (accessed February 2015).
12. L. Zhang, S.R. Chae, Z. Hendren, J.S. Park and M.R. Wiesner, *Chem Eng J*, 2012, **204**, 87
13. G.F. McLean, T. Niet, S. Prince-Richard, N. Djilali, *Int. J. Hydrogen Energy* , 2002, **27**, 507
14. G.J.K. Acres, *J. Power Sources*, 2001, **100**, 60.
15. N.R. Sammes, R. Bove, and K. Stahl, *Current Opinion in Solid State & Materials Science*, 2004, **8**, 372.
16. A.L. Dicks, *Curr. Opin. Solid State Mater. Sci.*, 2004, **8**, 379.
17. Tubular fuel cells, <http://americanhistory.si.edu/fuelcells/images/sofc2.jpg> (accessed september 2014)
18. Planar fuel cell Stacks, [http://www.doitpoms.ac.uk/tlplib/fuel-cells/figures/flat\\_plate\\_sofc\\_sml.png](http://www.doitpoms.ac.uk/tlplib/fuel-cells/figures/flat_plate_sofc_sml.png) (accessed September 2014)
19. E. Baur, and H. Preis, *Z. Electrochem*, 1937, **43**, 727
20. H.G. Scott, *J mater Sci*, 1975, **10**, 1527
21. A. Orera and P.R. Slater, *Chem. Mater.*, 2010, **22**, 675
22. S.P.S Badwal, F.T.Ciacchi and D. Milisevic, *Solid state Ionics*, 2000, **136**, 9
23. S. Wang, H. Inaba, H. Tagawa, M. Dokiya and T. Hashimoto, *Solid State Ionics*, 1998, **107**, 73
24. E. Jud, Z. Zhang, W. Sigle, and L.J. Gauckler, *J. Electroceram*, 2006, **16**, 191
25. T.H. Yeh, and C.C. Chou, *Solid State Ionics*, 2009, **180**, 1529
26. A.J. Jacobson, *Chem. Mater.*, 2010, **22**, 660
27. L. Malavasi, C.A.J. Fisher, and M.S. Islam, *J. Chem. Soc. Rev*, 2010, **39**, 4370
28. H.A. Harwig, and A.G. Gerards. *Thermochim Acta*, 1979, **28**, 121
29. T. Takahashi, and H. Iwahara, *Mater. Res. Bull*, 1978, **13**, 1447
30. H. Iwahara, T. Esaka, T. Sato, and T. Takahashi, *J. Solid State Chem.*, 1981, **39**, 173
31. A. Watanabe, *Solid State Ionics*, 2005, **176**, 2423
32. A. Watanabe and M. Sekita *Solid State Ionics*, 2005, **176**, 2429
33. Y.J. Lee, C.O. Park H.D. Baek, and J.S. Huang, *Solid State Ionics*, 1995, **76**, 1

34. A.A. Yaremchenko, V.V. Kharton, E.N. Naumovich, and A.A. Tonoyan, *Mater. Res. Bull.*, 2000, **35**, 515
35. A.M. Azad, S. Larosse, and S.A. Akbar, *J. Mater. Sci.*, 1994, **29**, 4135
36. P. Shuk, H.D. Wiemhofer, U. Guth, W. Gopel, and M. Greenblatt, *Solid State Ionics*, 1996, **89**, 179
37. M. Feng, and J.B. Goodenough, *J. Solid State Chem.*, 1994, **31**, 663
38. T. Ishihara, H. Matsuda, and Y. Takita, *J. Am. Chem. Soc.*, 1994, **116**, 3801
39. B.C.H. Steele and A. Heinzl, *Nature*, 2001, **414**, 345
40. D.J.L. Brett, A. Atkinson, N.P. Brandon, and S.J. Skinner, *Chem. Soc. Rev.*, 2008, **37**, 1568
41. N. Jiang, E.D. Wachsman, and S. Jung, *Solid State Ionics*, 2002, **150**, 347
42. J.W. Fergus, *J. Power Sources*, 2006, **162**, 30
43. J.W. Stevenson, K. Hasinska, N.L. Canfield, T.R. Armstrong, *J. Electrochem. Soc.*, 2000, **147**, 3213
44. T. Ishihara, M. Ando, M. Enoki, Y. Takita, *J. Alloys Compd.*, 2006, **408**, 507
45. S. Yamaguchi, N. Yamada, *Solid State Ionics*, 2003, **162**, 23
46. N.V. Sharova, V.P. Gorelov, *Rus. J. Electrochem.*, 2005, **41**, 1001
47. C. Chen, G. Ma, *J. Alloys Compd.*, 2009, **485**, 69
48. J. Yin, X. Wang, J. Xu, H. Wang, F. Zhang, G. Ma, *Solid State Ionics*, 2011, **185**, 6
49. D. Medvedev, A. Murashkina, E. Pikalova, A. Demin, A. Podias and P. Tsiakaras, *Progress in Materials Science*, 2014, **60**, 72
50. C. Zhang, H. Zhao, *Solid State Ionics*, 2010, **181**, 1478
51. A. Radojković, M. Žunić, S.M. Savić, G. Branković, Z. Branković, *Ceram. Int.*, 2013, **39**, 307
52. S. Ricote, N. Bonanos, A. Manerbino, W.G. Coors, *Int. J. Hydrogen Energy*, 2012, **27**, 7954
53. P. Sawant, S. Varma, B.N. Wani, S.R. Bharadwaj, *Int. J. Hydrogen Energy*, 2012, **37**, 3848
54. J.B. Goodenough, J.E. Ruiz-Diaz, and Y.S. Zhen, *Solid State Ionics*, 1990, **44**, 21
55. T.R.S. Prassanna, and A.J. Navrotsky *J. Mater. Res.*, 1993, **8**, 1484
56. J. Cheng, A. Navrotsky, X.D. Zhou, and H.U. Anderson, *Chem. Mater.*, 2005, **17**, 2197
57. T. Shimura, and T. Yogo, *Solid State Ionics*, 2004, **175**, 345.
58. V. Jayaraman, A. Magrez, M. Caldes, O. Joubert, M. Ganne, Y. Piffard, and L. Brohan, *Solid State Ionics*, 2004, **170**, 17.
59. T. Yao, Y. Uchimoto, M. Kinuhata, T. Inagaki, and H. Yoshida, *Solid State Ionics*, 2000, **132**, 189.
60. K. Kakinuma, H. Yamamura, H. Haneda, and J. Atake, *Therm. Anal. Calorim.*, 1999, **57**, 737.

61. T. Hashimoto, M. Yoshinaga, Y. Ueda, K. Komazaki, K. Asaoka, and S.J. Wang, *Therm. Anal. Calorim.*, 2002, **69**, 909.
62. E. Quarez, S. Noirault, M. T. Caldes and O. Joubert, *J. Power Sources*, 2010, **195**, 1136
63. J.F. Shin, L. Hussey, A. Orera, and P.R. Slater, *Chem. Commun.*, 2010, **46**, 4613
64. J.F. Shin, A. Orera, D.C. Apperley and P.R. Slater, *J. Mater Chem.*, 2011, **21**, 874
65. J.F. Shin and P.R. Slater, *J. Power Sources*, 2011, **196**, 8539
66. P. Lacorre, F. Goutenoire, O. Bohnke, R. Retoux and Y. Laligant, *Nature*, 2000, **404**, 856
67. D. Marrero-Lopez, J. Pena-Martinez, D. Perez-Coll, and P. Nunez, *J. Alloy Comp*, 2006, **422**, 249.
68. D. Marrero-Lopez, J. Canales-Vazquez, W.Z. Zhou, J.T.S. Irving, and P. Nunez, *J. Solid State Chem.*, 2006, **179**, 278
69. S. Georges, O. Bohnke, F. Goutenoire, Y. Laligant, J. Fouletier, and P. Lacorre, *Solid State Ionics*, 2006, **177**, 1715
70. D.S. Tsai, M.J. Hseih, J.C. Tseng, and H.Y. Lee, *J. Eur. Ceram. Soc.*, 2005, **25**, 481.
71. X.P. Wang, Z.J. Cheng, and Q.F. Fang, *Solid State Ionics*, 2005, **176**, 761.
72. C. Tealdi, G. Chiodelli, L. Malavasi, and G.J. Flor, *Mater. Chem.*, 2004, **14**, 3553
73. D. Marrero-Lopez, J.C. Ruiz-Morales, P. Nunez, J.C.C. Abrantes, and J.R. Frade, *J. Solid State Chem.*, 2004, **177**, 2378.
74. S. Georges, R.A. Rocha, and E.J. Djurado, *J. Phys. Chem. C.*, 2008, **112**, 3194.
75. S. Nakayama, T. Kageyama, H. Aono and Y. Sadaoka, *J. Mater. Chem*, 1995, **5**, 1801
76. H. Iwahara, *Solid State Ionics* **1996**, 86-8, 9.
77. N. Ito, M. Iijima, K. Kimura and S. Iguchi, *Journal of Power Sources* **2005**, 152, 200
78. S. Nakayama, Y. Higuchi, Y. Kondo, and M. Sakamoto, *Solid State Ionics*, 2004, **170**, 219
79. E. Kendrick, M.S. Islam, and P.R. Slater, *J. Mater. Chem.*, 2007, **17**, 3104
80. J.E.H. Sansom, D. Richings, P.R. Slater, *Solid State Ionics*, 2001, **139**, 205
81. L. Leon-Reina, J. M. Porras-Vasquez, E. R. Losilla and M. A. G.Aranda, *J. Solid State Chem.*, 2007, **180**, 1250
82. E. Kendrick, M. S. Islam and P. R. Slater, *Chem. Commun.*, 2008, **6**, 715
83. E. Bechade, O. Masson, T. Iwata, I. Julien, K. Fukuda, P. Thomas and E. Champion, *Chem. Mater.*, 2009, **21**, 2508
84. R. Tolchard and P. R. Slater, *J. of Phys. Chem. Solids*, 2008, **69**, 2433.

85. S. S. Pramana, W. T. Klooster and T. J. White, *Acta Crystallogr., B: Struct. Sci.*, 2007, **63**, 597.
86. A. Orera, D. Headspith, D. C. Apperley, M. G. Francesconi and P. R. Slater, *J. Solid State Chem.*, 2009, **182**, 3294
87. H. Yoshioka, *J. Am. Ceram. Soc.* 2007, **90**, 3099.
88. A. Najib, J.E.H. Sansom, J.R. Tolchard, M.S. Islam, and P.R. Slater, *Dalton Trans.* 2004, **19**, 3106.
89. E.J. Abram, D.C. Sinclair, and A.R. West, *J. Mater. Chem.*, 2001, **11**, 1978
90. A.L. Shaula, V.V. Kharton, and F.M.B. Marques, *J. Solid State Chem.*, 2005, **178**, 2050
91. E. Kendrick, M.S. Islam, P.R. Slater, *Solid State Ionics*, 2007, **177**, 3411.
92. J.R. Tolchard, P.R. Slater, and M.S. Islam, *Adv. Funct. Mater.*, 2007, **17**, 2564
93. E. Kendrick, M. S. Islam and P. R. Slater, *J. Mater. Chem.*, 2007, **17**, 3104.
94. S. Nakayama, Y. Higuchi, Y. Kondo and M. Sakamoto, *Solid State Ionics*, 2004, **170**, 219
95. H. Yoshioka, Y. Nojiri, and S. Tanase, *Solid State Ionics*, 2008, **179**, 2165
96. L. Leon-Reina, E.R. Losilla, M. Martinez-Lara, M.C. Martin-Sedeno, S. Bruque, P. Nunez, D.V. Sheptyakov, and M.A.G. Aranda, *Chem. Mater.*, 2005, **17**, 596

# 2 General Experimental

---

## 2.1 Synthesis Methods

### 2.1.1 Experimental

High temperature solid state synthesis is the most widely used synthesis method in solid state chemistry<sup>1,2</sup> and it usually involves using a stoichiometric mixture of metal oxides and/or carbonates. The mixture is then ground together either manually with a pestle and mortar or mechanically in a ball mill. The well ground mixture is then heated to high temperatures in a crucible for extended amounts of time. The temperature and length of time that a sample is in a furnace is dependent on the materials and planned product, however this is usually in excess of 800°C for more than 12 h. Most reactions require regrinding and reheating to reach completion with a single end product.<sup>1,2</sup>

The advantages of this method are that it is simple to perform and requires little specialist equipment. A successful experiment results in a 100% yield as there are no purification steps or recrystallisations. The disadvantages to this method are the high reaction temperatures and long reaction times which limit crystallite sizes. It is also always the most thermodynamically stable product which is formed, and so the method cannot be employed to form metastable products.

### 2.1.2 Hydration

In this work, two methods were used to hydrate samples. The first of these was to pass a gas flow through a H<sub>2</sub>O filled bubbler, which would then lead into a furnace containing the sample. The furnace would then be heated to 600°C and cooled slowly (0.5 – 1°C min<sup>-1</sup>) to allow water to be incorporated into the sample. The other method employed in this work used hydrothermal vessels, which allows the exposure of the samples to a much higher steam pressure. This method involved using a small amount of sample with approximately 8 ml H<sub>2</sub>O which was sealed in the hydrothermal vessel with a maximum capacity of 23 ml. The vessel was then heated to 220°C for 48 h. The sample was then filtered and surface water was removed in a low temperature drying oven at 80°C.

### 2.1.3 Fluorination

In this work, fluorination was used to replace an oxygen atom with two fluorine atoms where the extra fluorine atom would be forced into an interstitial site which meant that one interstitial atom was added per oxygen atom removed. There are several ways fluorination reactions can be carried out. The fluorination in this work was completed using polyvinylidene fluoride (PVDF, CH<sub>2</sub>-CF<sub>2</sub>) and polytetrafluoroethylene (PTFE, CF<sub>2</sub>-CF<sub>2</sub>). The sample to be fluorinated was ground together with the fluorine containing polymer and heated slowly in a furnace (the degree of fluorination can be controlled by varying the amount of polymer used). When PVDF was used it was heated to 360°C with a heating rate of 1°C min<sup>-1</sup> and when PTFE was used the

heating temperature was 400°C with a 1°C min<sup>-1</sup> heating rate. With the use of both polymers the reaction times were between 12 and 72h.

## 2.2 Structural characterisation

Within this work, diffraction techniques were used as the main analysis techniques to determine purity and to identify changes in the atomic structure of samples after various treatments or changes to reaction conditions. Both laboratory X-ray and large facility neutron diffraction (ND) have been used for structural analysis. To understand diffraction by crystals we must first consider the symmetry of the material and the basic concepts of crystallography.

### 2.2.1 Crystal Symmetry

A crystalline solid has a regular three dimensional lattice of atoms and/or ions. Its smallest repeat section is a unit cell which can be translated to create the rest of the lattice whilst maintaining all the symmetry. A unit cell can be defined by six parameters; these are the three cell lengths in the x, y and z directions (a, b, c) and the angles between the lengths ( $\alpha$ ,  $\beta$ ,  $\gamma$ ) and are known as the unit cell or lattice parameters. The level of symmetry in a lattice can be linked to one of seven crystal classes which have different shapes based on the lengths and angles that define them (Table 2.1). When these are combined with the four types of lattice, primitive (P), body centred (I) and face centred (F and C), the result is a possible fourteen bravais lattice types. (Figure 2.1)<sup>6</sup>

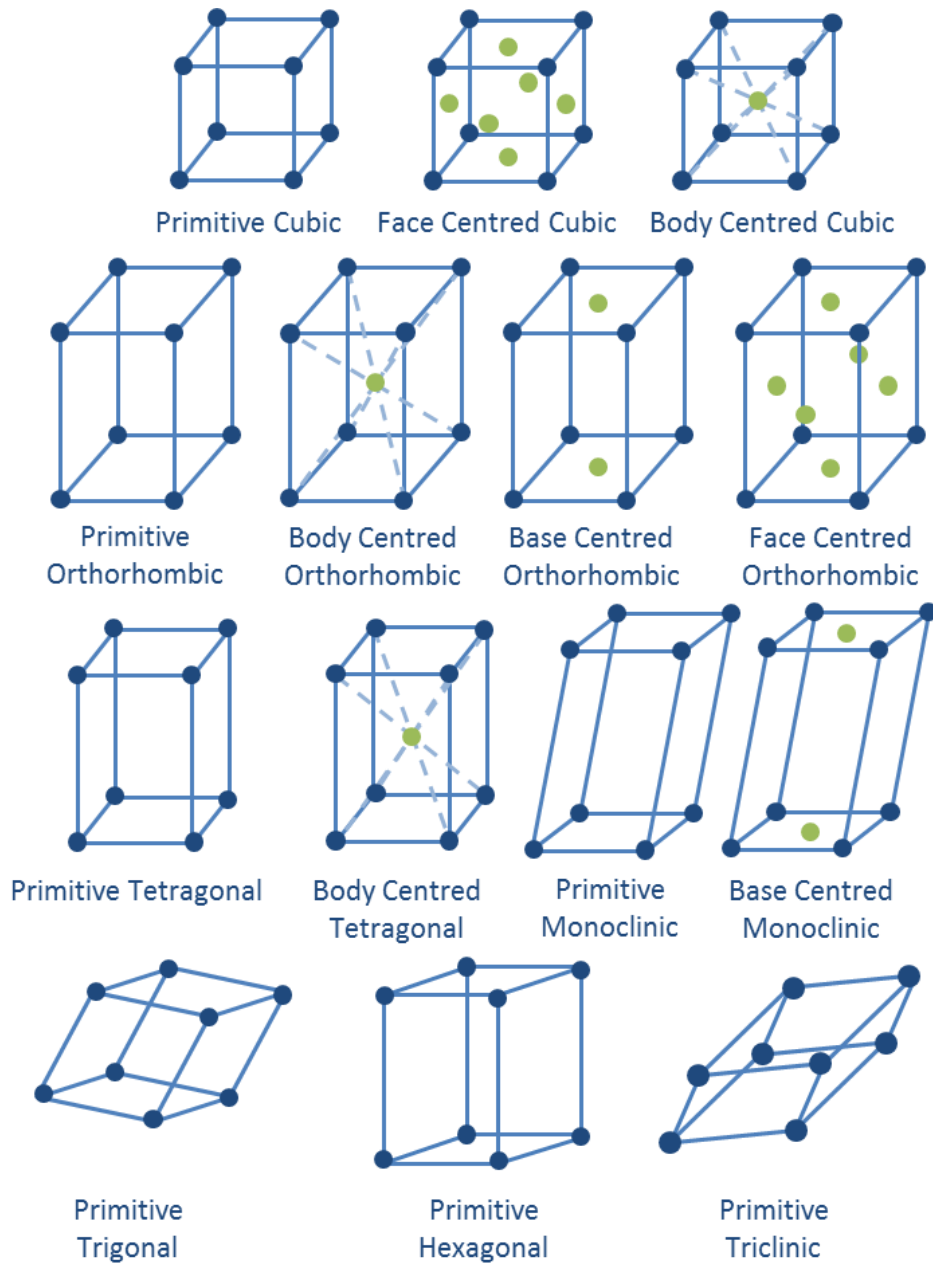


Figure 2.1 - The 14 Bravais lattice types.

Table 2.1 - The rules defining lengths and angles of the seven crystal classes.

Crystal Shape	Cell Lengths	Cell Angles
Cubic	$a = b = c$	$\alpha = \beta = \gamma = 90^\circ$
Tetragonal	$a = b \neq c$	$\alpha = \beta = \gamma = 90^\circ$
Orthorhombic	$a \neq b \neq c$	$\alpha = \beta = \gamma = 90^\circ$
Monoclinic	$a \neq b \neq c$	$\alpha = \gamma = 90^\circ \neq \beta$
Hexagonal	$a = b \neq c$	$\alpha = \beta = 90^\circ, \gamma = 120^\circ$
Trigonal	$a = b = c$	$\alpha = \beta = \gamma \neq 90^\circ$
Triclinic	$a \neq b \neq c$	$\alpha \neq \beta \neq \gamma \neq 90^\circ$

The atom positions within the unit cell are defined by direction vectors from the origin of the cell. A position on the vector is expressed by fractions of the unit cell lengths as coordinates. The vector is written as whole numbers representing the fractions. For example an atom at (0.5, 0.5, 0.5) is positioned at the centre of the cell as this is half way along the x axis (a side), half way along the y axis (b side) and half way along the z axis (c side) and sits on the directional vector [111]. (Figure 2.2)

The positions of the atoms within the cell complete the symmetry observed and the unit cell will fall into one of 230 possible space groups which describe the symmetry observed.

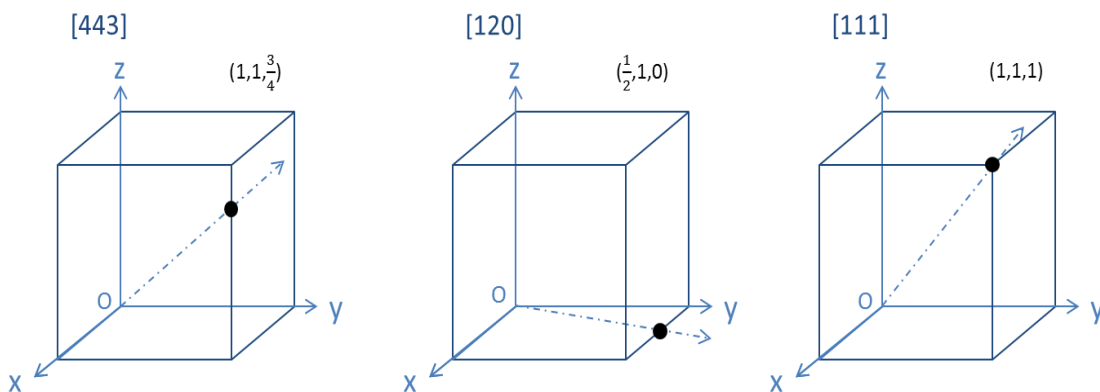


Figure 2.2 - Atom positions and lattice vectors in a cubic unit cell, [ ] are lattice vectors and () atomic positions.

Miller indices (hkl) are used to describe lattice planes, and these are defined by the inverse of the fractional intercepts along the lattice vectors (a, b and c). Examples of miller indices and lattice planes are shown in Figure 2.3. It is possible for more than one plane to be equivalent, for example in a cubic system the (100), (010) and (001) are equivalent. The number of equivalent planes is the multiplicity.<sup>5, 6</sup>

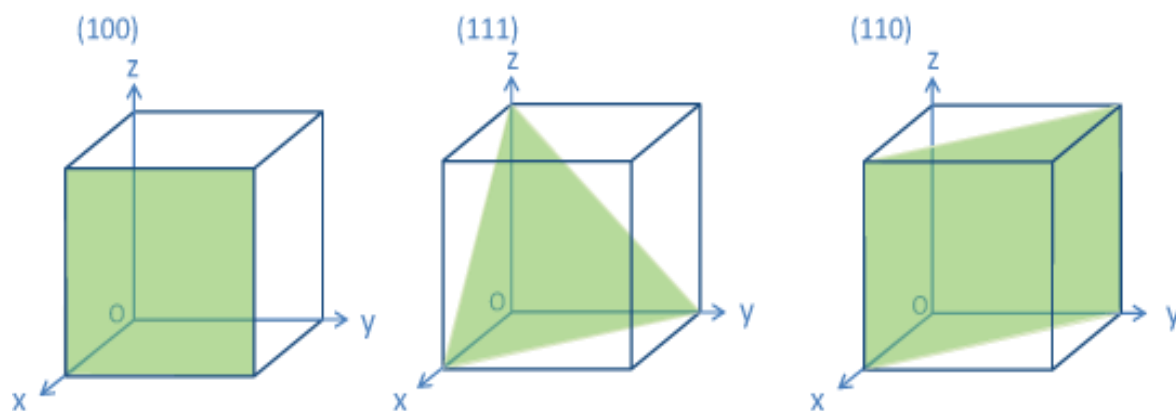


Figure 2.3 - Examples of lattice planes in a cubic unit cell.

The diffraction of X-rays by crystals was first observed by Max von Laue in 1912 and a technique for relating the diffraction observed to the crystal structure of the sample was first proposed in 1913 by W.H. Bragg and W.L. Bragg.<sup>4, 5</sup>

### 2.2.2 Bragg's Law

W.H. Bragg and W.L. Bragg proposed that diffraction in crystals occurred from sets of parallel planes separated by a constant distance.<sup>5</sup> A beam of X-rays is reflected as a complete beam of X-rays from each plane. The X-rays that have to travel to the further plane have to travel an extra distance. In Figure 2.4, this extra distance is C to D via B. If the total of the extra distance is an exact multiple of the wavelength, then the reflected waves will arrive at the detector in-phase. With in-phase waves the amplitude of the resulting radiation is far greater than a single reflected beam creating a peak intensity at the detector. These peaks are known as Bragg reflections. If the angle of the incident X-ray beam is changed the same two planes

will reflect the beam of X-rays in the same manner, however the distance travelled by the two beams will no longer in this instance equal an integer number of wavelengths causing disruptive interference and no peak is observed at the detector. For Bragg's law to be true a monochromatic X-ray beam is required as white radiation contains multiple wavelengths and no distinct peaks would be observed.<sup>5</sup>

The requirements for a Bragg peak to occur are set out by Bragg's Law (Equation 2.1) where  $n$  is an integer multiplier,  $\lambda$  is the wavelength,  $d$  is the spacing between the planes and  $\theta$  is the angle of incidence which is equal to the angle of reflection.

Equation 2.1 - Bragg's Law<sup>5</sup>

$$n\lambda = 2d\sin\theta$$

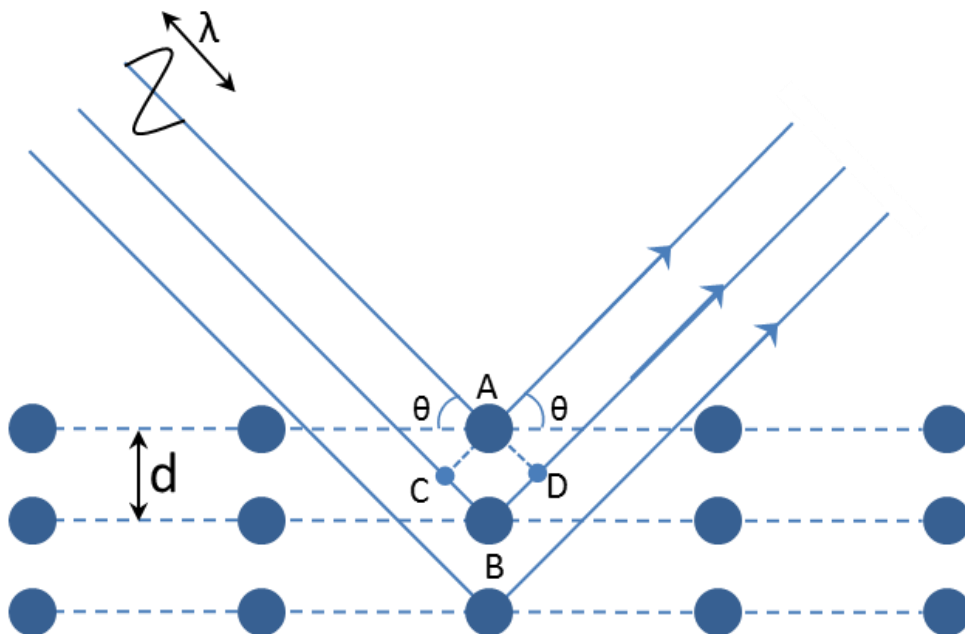


Figure 2.4 - Simplified geometry of Bragg's Law

### 2.2.3 X-Ray generation

The generation of X-rays occurs when an electron beam hits a metal target (in this work copper was used), and the electron beam ejects a core electron from the atom it strikes creating a hole. This hole is then filled by a higher energy electron from one of the outer orbitals, which drops in to fill the hole releasing an amount of energy as X-rays that is equal to the difference in energy between the higher energy and lower energy orbitals. This released X-ray is characteristic of the target material and in the case of copper, X-ray wavelengths for  $\text{CuK}_{\alpha 1}$ ,  $\text{CuK}_{\alpha 2}$ ,  $\text{CuK}_{\beta 1}$  and  $\text{CuK}_{\beta 2}$  are observed;  $\alpha$  and  $\beta$  represent energies from a drop from 2p and 3p orbitals to the 1s orbital and the 1 and 2 are because of the two different spin states. A broad humped background of X-rays is also observed due to the rapid deceleration of the high energy electrons as they contact the metal target. (Figure 2.5)<sup>6</sup>

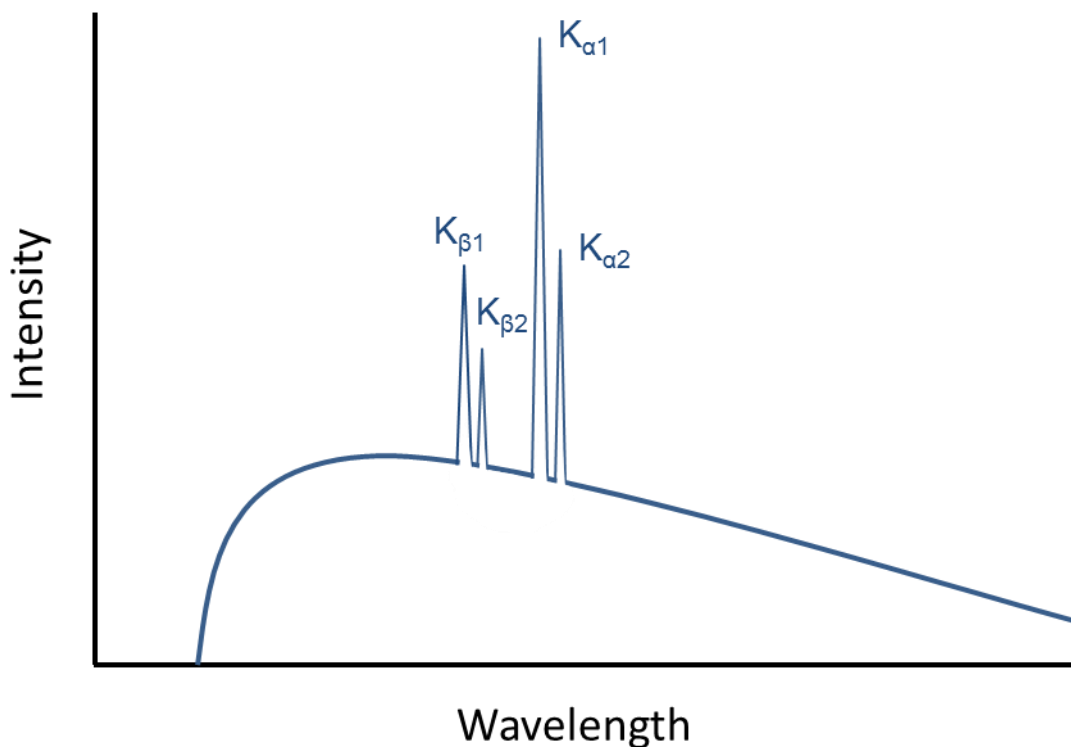


Figure 2.5 - X-ray spectrum for copper showing the two doublets for  $K_{\alpha}$  and  $K_{\beta}$ .

As mentioned previously, X-ray diffraction requires a single wavelength of X-rays, and this is achieved in this work by the use of a metal filter, Göbel mirror or crystal monochromator. A metal filter requires an adsorption edge between the  $K_{\alpha}$  and  $K_{\beta}$  lines (Nickel foil for copper radiation), which is sufficient to remove the peaks due to  $K_{\beta}$  radiation but cannot split the  $K_{\alpha 1}$  and  $K_{\alpha 2}$ . Fully monochromatic radiation can be achieved using a crystal monochromator (Ge in this work) which has a known plane spacing. This is then orientated so that only the  $K_{\alpha 1}$  radiation is diffracted towards the sample. Using metal foils and crystal monochromators reduces the flux of the X-ray beam as some of the intensity is lost. The use of either a foil or crystal monochromator is a compromise between resolution and intensity as an increase in resolution with a crystal monochromator results in a loss in intensity. New detectors claim to be able to have enough energy resolution to remove  $K_{\beta}$  without the need for metal filters or secondary monochromators.<sup>7</sup> With modern refinement programs the peaks due to  $K_{\alpha 2}$  radiation can be removed after collection at the data analysis step so that a structure can still be refined from data which contains  $K_{\alpha 1}$  and  $K_{\alpha 2}$  peaks.

#### 2.2.4 X-Ray Diffraction

In single crystal X-ray diffraction the crystal is moved through half rotations in all three dimensions, which orients the crystal so all atomic planes have been in diffraction positions. Each reflection is seen as a spot on a 3-D map of the crystal.<sup>8</sup> In powder X-ray diffraction (PXRD) the sample contains randomly orientated crystallites which are assumed to evenly represent every possible orientation, and this means

data is collected on a 1-D  $2\theta$  axis. A drawback of this is that a large amount of the data collected by single crystal X-ray diffraction is lost due to the overlap of Bragg peaks caused by the compression of 3-D data onto a 1-D axis. Rather than spots on the pattern, the data is seen as lines / peaks at the representative  $2\theta$  angle from the origin. A typical PXRD pattern of  $\alpha\text{-Al}_2\text{O}_3$  is shown in Figure 2.6.

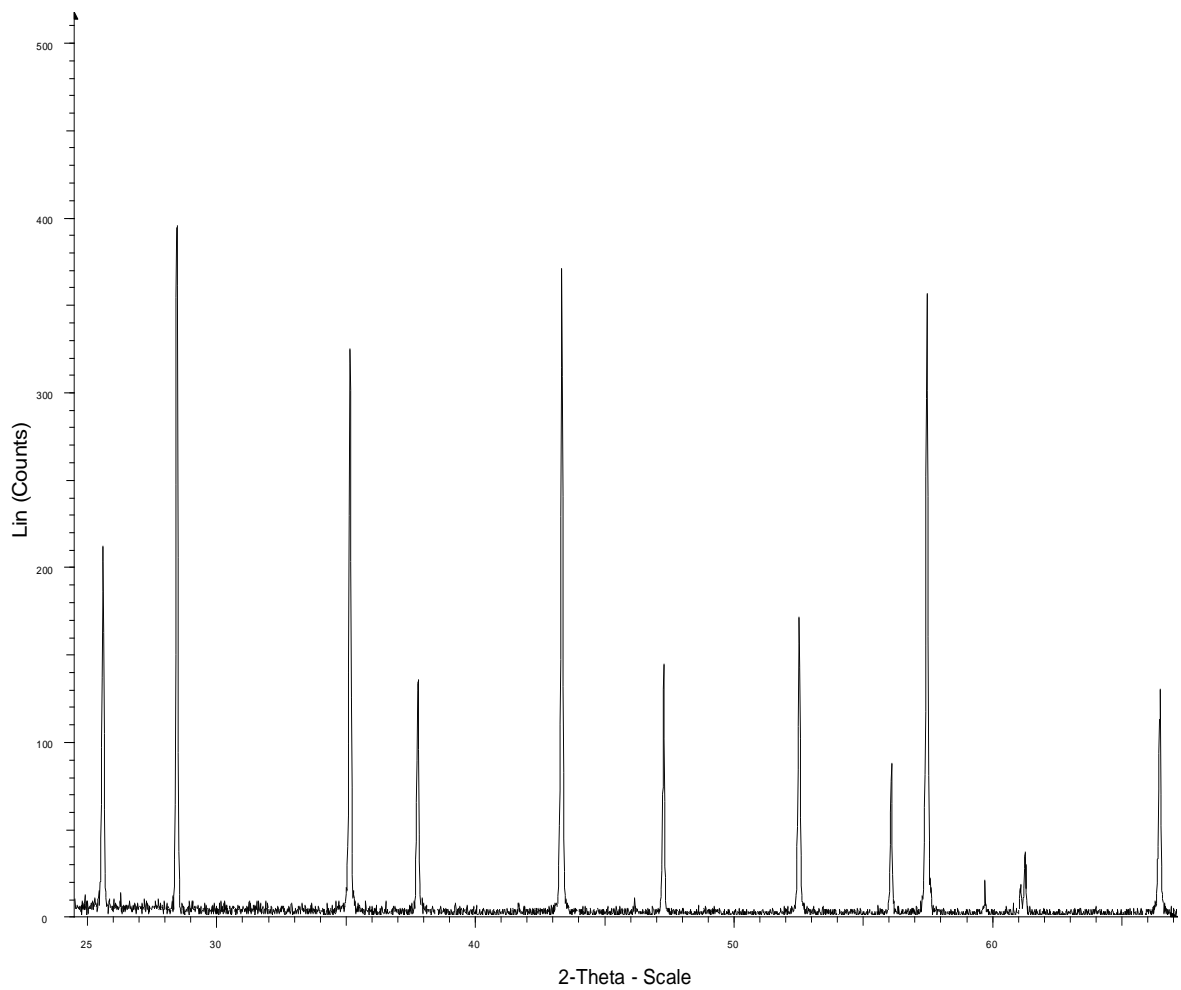
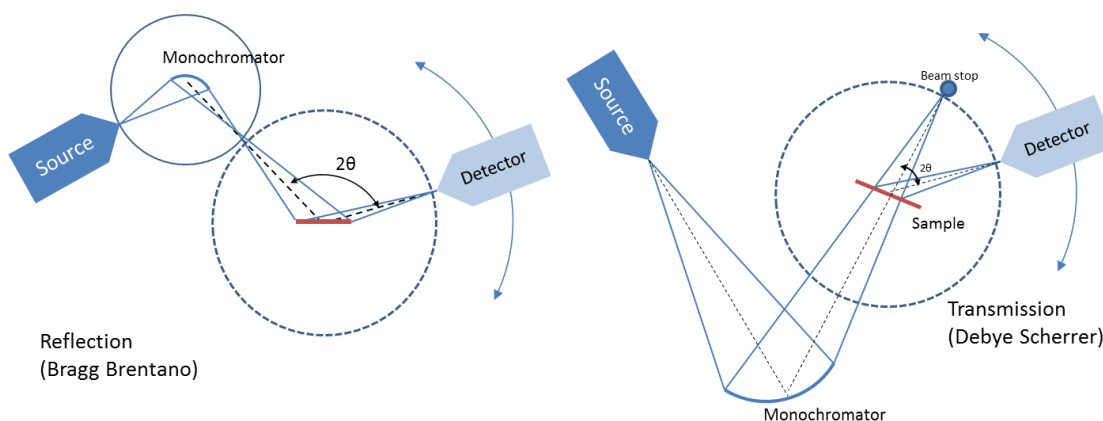


Figure 2.6 - PXRD pattern for  $\alpha\text{-Al}_2\text{O}_3$ .



**Figure 2.7 - Bragg Brentano and Debye Scherrer instrument set ups for XRD.**

There are two main types of set up for PXRD which are Bragg-Brentano (reflection) and Debye-Scherrer (transmission) (Figure 2.7). The transmission arrangement uses a thinner sample on an X-ray transparent film where diffracted X-rays are detected at a  $2\theta$  angle at a detector. The reflection arrangement uses a thicker sample which is not completely penetrated by the X-rays and diffracted X-rays are detected at a  $2\theta$  angle at the detector.

In this work the diffractometers used were Bruker D8 Advance diffractometers with copper X-ray tubes. Both Bragg-Brentano and Debye-Scherrer arrangements were used and data were collected using either a Ge monochromator or nickel foil. For non-ambient conditions, an Anton Parr HTK1200 heating stage was used.

#### **2.2.4.1 Rietveld Refinement**

Conventionally single crystal X-ray diffraction was the preferred method for solving crystal structures, but for some ceramic materials creating single crystals large

enough to perform single crystal XRD is not easy and can be an expensive process.<sup>6</sup> Initially only high symmetry structures could be solved with powder diffraction using the 'integrated intensity method', This was because the method could only work without peak overlap which is seen in more complex structures such as monoclinic and triclinic space groups.

In the late 1960s a Dutch crystallographer, Hugo Rietveld, used computers to analyse all the points of the powder pattern rather than just peak intensities to refine the observed pattern to a calculated pattern using least squares to find a best fit. This technique is now known as Rietveld refinement.<sup>9, 10</sup>

A Rietveld refinement of PXRD data first involves the creation of a calculated pattern based on the symmetry information and an approximate atomic structure. The observed and calculated patterns are then compared during the refinement. Rietveld refinement uses a least squares minimisation to compare every observed point for the data with the calculated plot and refines chosen structural parameters in the calculated plot to minimise the difference between the two plots.<sup>10</sup>

Several computer programs exist for the refinement process, the most commonly used three are General Structure Analysis System (GSAS),<sup>11,12</sup> Topas, and FullProf. In this work, GSAS and Topas were used. Both programs are capable of multiple phase refinements for X-ray and neutron data, Fourier mapping to locate atom positions and much more.

A Rietveld refinement requires some initial structural and instrumental information to be added before a calculated pattern can be generated. Data for an X-ray standard material is collected to calculate instrument parameters: this is a material which has a

well-known structure, which can be fixed to allow the refinement of instrument parameters (which may change over time). The most commonly used standards are  $\alpha$ -alumina ( $\text{Al}_2\text{O}_3$ , corundum), silicon, and lanthanum hexaboride ( $\text{LaB}_6$ ). Instrument parameters include zero point error, tube tails, soller slit sizes and the emission profile, and all of these can affect the observed pattern and need to be modified in the calculated pattern.

Structural information for the space group, unit cell parameters and approximate atomic positions need to be entered as a starting point for the calculated pattern. Many materials have a crystallographic information file (CIF) available from the International Crystallographic Structure Database (ICSD) which can be used in a lot of cases as a starting point for atomic positions especially for cation/anion doped materials which are related to a parent sample. Both GSAS and Topas allow for multiple atoms to be added on the same site which is useful for doped samples which have partially replaced one atom with another. As the scattering intensity varies for different atoms, doping can significantly change the intensities of peaks in the XRD pattern.<sup>10</sup>

The quality of the refinement fit can be assessed either visually or mathematically where a visual fit plots the calculated, observed and difference profiles on the same plot so it can be seen where mismatches occur. A perfect fit would have a straight line for the difference profile. Tick marks are usually also included to indicate the calculated positions of Bragg reflections. (Figure 2.8)

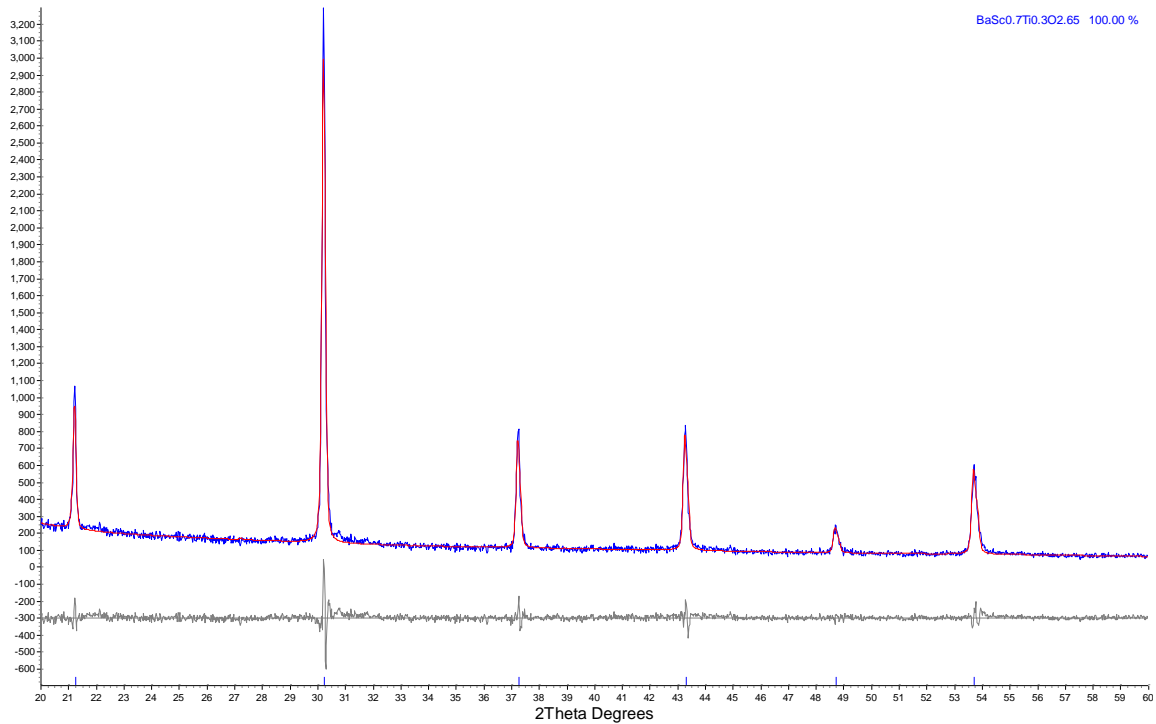


**Figure 2.8 - Rietveld refinement plot for BaSc<sub>0.7</sub>Ti<sub>0.3</sub>O<sub>2.65</sub> with observed (blue), calculated (red) and difference (grey) profiles. Tick marks (top of x axis) indicating Bragg peak positions are shown in blue.**

The quality of the fit obtained can also be calculated using residual factors or 'R factors' and a parameter,  $\chi^2$ . The R factors include R-profile,  $R_p$  (Equation 2.2), weighted R-profile,  $R_{wp}$  (Equation 2.3), R-expected,  $R_{exp}$  (Equation 2.4) and R-Bragg,  $R_{Bragg}$  (Equation 2.5) which are defined below. <sup>6</sup>

**Equation 2.2 - Calculation of R-profile**

$$R_p = \frac{\sum_i |y_i(obs) - y_i(calc)|}{\sum_i y_i(obs)}$$

$R_p$  compares the calculated and observed data at each observed data point. The current data point under comparison at any time is  $i$ ,  $y_i(obs)$  is the observed intensity at  $i$  and  $y_i(calc)$  is the calculated intensity at point  $i$ .

**Equation 2.3 - Calculation of the weighted R-profile.**

$$R_{wp} = \left[ \frac{\sum_i w_i (y_i(obs) - y_i(calc))^2}{\sum_i w_i (y_i(obs))^2} \right]^{\frac{1}{2}}$$

where  $w_i$  is a weighting factor and  $y_i(obs)$  and  $y_i(calc)$  are as above.

**Equation 2.4 - Calculation of the expected profile factor.**

$$R_{exp} = \left[ \frac{(N - P - C)}{\sum_i^N w_i (y_i(obs))^2} \right]^{\frac{1}{2}}$$

where  $N$  is the number of observations,  $P$  is the number of refined parameters and  $C$  is the number of constraints used.  $R_{exp}$  is the best possible R-value for the data although this is heavily influenced by the quality of the data. Data which has been collected for a long time and has a large number of observations will have a very small  $R_{exp}$ .

**Equation 2.5 - Calculation of the Bragg factor.**

$$R_{Bragg} = \left[ \frac{\sum |I_{hkl}(obs) - y_{hkl}(calc)|}{\sum |I_{hkl}(obs)|} \right]$$

where  $I_{hkl}$  is the intensity at a Bragg reflection (hkl). As  $R_{Bragg}$  uses the intensity difference at the Bragg reflection positions only, it requires a good starting model with peaks in correct positions for the unit cell.

Combination of the weighted profile factor and the expected profile factor can describe another term to describe the quality of the fit:  $\chi^2$  (Chi<sup>2</sup>) the square of the ratio between the two terms (Equation 2.6).

### Equation 2.6 - Calculation of Chi<sup>2</sup> ( $\chi^2$ )

$$\chi^2 = \left[ \frac{R_{wp}}{R_{exp}} \right]^2$$

When refining a pattern, a  $\chi^2$  value as close to 1 as possible is wanted. A value less than 1 indicates a  $R_{wp}$  value that is smaller than the  $R_{exp}$  value and should not be possible. With high quality data the  $R_{exp}$  value is very low which makes it much more difficult to obtain a low  $\chi^2$  value and the  $R_p$ ,  $R_{wp}$  and graphical fit should also be taken into consideration when describing the quality of the fit. When other sample environments are used which involve a change in atmosphere or temperature of the sample there is often interference which can add peaks to the pattern or have unusual effects on the background. These external factors can have an adverse effect on the fit and the R-factors that describe the quality of the fit.

### 2.2.5 Neutron Diffraction

Neutron diffraction (ND) differs from X-ray diffraction as the neutrons are scattered and diffracted by the nucleus of the atoms rather than the electron cloud. This means that the scattering intensity is not systematically dependant on atom size, which is the case with X-rays, making lighter elements easier to locate in ND. Scattering by X-rays is dominated by heavier atoms as they have larger electron clouds, whereas for neutrons deuterium has a larger scattering factor than vanadium for example.<sup>13</sup> (Figure 2.9) There is no trend in the scattering lengths of neutrons and the difference in scattering between neutrons and X-rays gives complimentary data.<sup>14</sup>

Neutrons can also differentiate between isotopes of elements for example  $^1\text{H}$  has a negative scattering length of  $-3.7$  fm and  $^2\text{H}$  has a positive scattering length of  $6.7$  fm.<sup>13</sup> This difference allows for protons to be found in structures by looking for a negative intensity difference in a Fourier map of the  $^1\text{H}$  data and a positive intensity difference in the  $^2\text{H}$  data. In X-ray diffraction, protons are invisible and cannot be seen or located. X-ray diffraction also suffers from a reduction in intensity at higher angles because the large size of the electron cloud. The incident X-rays at one part of the cloud can diffract slightly different to X-rays incident at another part of the cloud. At low angles the difference in phase caused by this is small but at higher angles, the phase separation is larger, this results in a portion of destructive interference reducing the intensity of the observed peaks. The nucleus of the atom is a lot smaller than the electron cloud so this effect is greatly reduced in neutron diffraction. This means that neutron diffraction can measure to a much lower d-spacing than X-rays.<sup>14</sup>

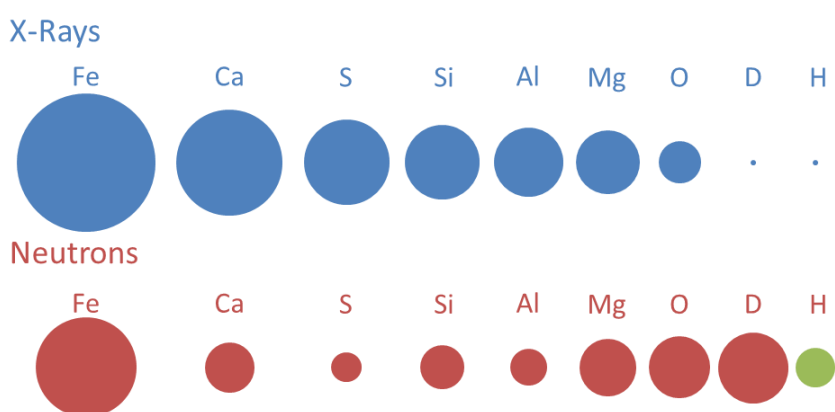


Figure 2.9 - Scale diagram of X-ray and neutron scattering lengths of selected atoms, Neutron scattering length for H is shown in green as it is a negative value. (values from 13)

Neutron diffraction experiments can only be performed at various large scale facilities around the world. These sites either use a nuclear reactor or a spallation reaction to produce the neutrons. In this work the two sources used were ISIS at the Rutherford Appleton Laboratory in Oxfordshire, England and SINQ at the Paul Scherrer Instiut in Villigen, Switzerland. Both of these sources are spallation, ISIS is a time of flight pulsed source and SINQ is a continuous constant wavelength source.

Spallation is where a proton beam is fired at a heavy metal target (e.g. Tungsten at ISIS) releasing high energy neutrons. These neutrons are then slowed down with collisions in a moderator (liquid D<sub>2</sub>O moderators were used on all of the beam lines used in this work).

Constant wavelength neutron diffraction has an experimental set up similar to X-ray diffraction as the wavelength is fixed and the angle of incidence is moved through a  $2\theta$  range. The data is then plotted in the same intensity versus  $2\theta$  angle format seen for most X-ray data.

Time of flight neutron diffraction differs as rather than all the neutrons having the same wavelength they have different wavelengths which can be calculated from the time it takes to cover a known path length using the de Broglie relationship (Equation 2.7) where  $\lambda$  is the wavelength,  $h$  is Planck's constant,  $m_n$  is the mass of a neutron and  $v$  is the velocity. In these experiments the incidence angle is fixed as effectively the wavelength is varied. The data can then be plotted as intensity versus time of flight; however this is often converted to intensity versus d-spacing using Bragg's law.

#### Equation 2.7 - Equation for calculating the wavelength of neutrons

$$\lambda = \frac{h}{m_n v}$$

### 2.3 Thermogravimetric Analysis (TGA)

In TGA, the mass of a sample is measured precisely whilst the sample is heated to a known temperature with a known heating rate in a controlled atmosphere. Depending on the sample the mass could be affected by decomposition, oxidation, reduction etc. The atmosphere at the sample can be controlled as an inert environment (N<sub>2</sub>/Ar/He) or could be a reactive gas to promote a reaction. The gases used in this work are N<sub>2</sub>, O<sub>2</sub>, H<sub>2</sub> and CO<sub>2</sub>. The sample is placed in an alumina crucible with an identical empty crucible alongside for differential thermal analysis (DTA) measurements. The crucible is then subject to a predetermined program for which an empty (blank) crucible has been run on so that changes in weight and heating rate due to the crucible can be subtracted and removed from the final data. An example plot can be seen in Figure 2.10, where the x axis is time (min) although it is possible to plot the x axis as temperature (°C). If more than one drop (or gain) in mass of the sample is observed it is possible to calculate the molecular mass of the sample at each step provided the molecular mass is known for at least one of the plateaus, the beginning, or the end of the analysis.

It is possible to also connect the TGA to a mass spectrometer (MS) to analyse the exhaust gases from the TGA to see what is given off from the sample.

In this work a Netzsch STA 449 F1 Jupiter Thermal Analyser was used.

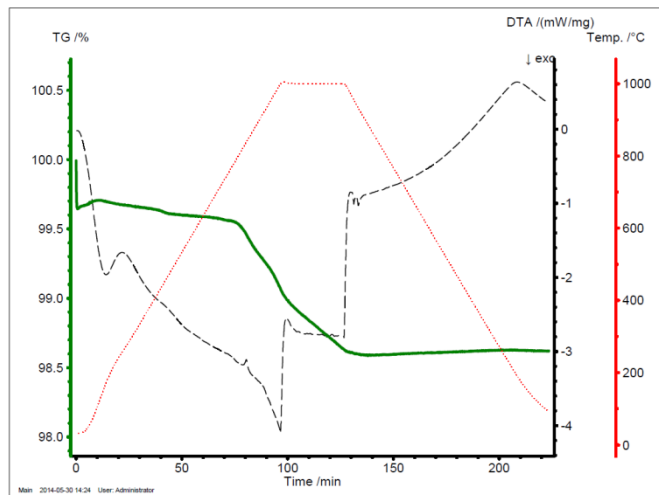


**Figure 2.10 - Example TGA plot showing temperature trace (red), mass trace (green) and DTA trace (black).**

## 2.4 Impedance Spectroscopy

Impedance spectroscopy is a technique used for characterising electrical properties of materials and the interfaces between materials and electrodes. It can be used for either solid or liquid materials which are ionic, semiconducting, mixed ionic/electronic conducting and insulators. In this work the technique was used for solid polycrystalline materials to calculate ionic conductivity.<sup>15</sup> The general approach is to apply a single-frequency voltage to the material and measure the phase shift and amplitude of the resulting current at that frequency then change the voltage frequency and measure the new current response. Analysers can measure the impedance of a sample at frequencies below 1 mHz and up to 40 Mhz; in this work a frequency range of 100 Hz to 13 Mhz was used.

Impedance is determined by measuring the response in the current when an ac voltage is applied across the sample. When the applied voltage is sinusoidal the recorded current will also be sinusoidal although it is highly likely that it will be out of

phase to the voltage as a phase shift will have occurred if capacitance behaviour exists.

Alternating current can be seen as voltage with a sine wave. Sinusoidal voltage can be expressed as having an amplitude  $V_0$  and a frequency of rotation  $\omega$  (Equation 2.8) where  $\omega = 2\pi f$  ( $f$  = frequency in Hz) and the observed voltage is then  $V_{(t)}$ .<sup>16</sup>

**Equation 2.8**

$$V_{(t)} = V_0 \sin \omega t$$

The resulting current is also sinusoidal and can be described by Equation 2.9 where  $\theta$  is a phase angle indicating the phase shift between the current and the voltage sine waves,  $I_{(t)}$  is the observed current at time  $t$ , and  $I_0$  is the amplitude of the current. The phase angle is either positive or negative depending on whether the current is either ahead or lagging behind the voltage. In a pure resistor the phase shift and therefore the  $\theta$  is 0.

**Equation 2.9**

$$I_{(t)} = I_0 \sin(\omega t + \theta)$$

When the phase angle is 0 (pure resistance) the current can be seen which is based on Ohm's law where  $R$  is the resistance.

**Equation 2.10**

$$I_{(t)} = (v_0/R) \sin \omega t$$

Impedance,  $Z$ , is a circuit's ability to resist alternating current and can be derived from Ohm's law which states the relationship between impedance,  $Z$ , voltage,  $V$  and current,  $I$  (Equation 2.11.)

**Equation 2.11**

$$I = \frac{V}{Z}$$

When AC voltage is used impedance at a given time,  $Z(t)$  becomes Equation 2.12.

Where  $Z_0$  is the amplitude of the impedance.

**Equation 2.12**

$$Z(t) = \frac{v(t)}{I(t)} = \frac{V_o \sin(\omega t)}{I_o \sin(\omega t + \theta)} = Z_0 \frac{\sin(\omega t)}{\sin(\omega t + \theta)}$$

Mathematical treatment of the data allows for it to be plotted in a complex plane and can be expressed by a vector sum of the components a and b where  $Z = a + jb$  where j is the imaginary number  $\sqrt{-1}$ , (Equation 2.13.) j indicates an anticlockwise rotation of the axes meaning that a the real part is on the x axis and the imaginary part jb is along the y axis.

**Equation 2.13**

$$j = \sqrt{-1} = \exp(j\pi/2)$$

Using the Euler relationship this can be plotted in a complex plane or Argand diagram (Figure 2.11) where the coordinates for  $Z'$  and  $Z''$  are defined in Equation 2.14 and Equation 2.15 .

**Equation 2.14**

$$Z' = |Z| \cos(\theta) \text{ and } Z'' = |Z| \sin(\theta)$$

Equation 2.15

$$Z(\omega) = |Z| \exp(j\theta) = |Z|(\cos\theta + j\sin\theta)$$

The phase angle,  $\theta$ , is defined by Equation 2.16 and  $|Z|$  is the magnitude of the sum of the vectors  $z'$  and  $z''$ .

Equation 2.16

$$\theta = \tan^{-1}(Z''/Z')$$

The resistance of the sample is determined from the real component,  $Z'$ . whereas imaginary component of  $Z$ ,  $Z''$ , is the reactance of the sample, also written as  $X$ . The reactance is the sum of the capacitive reactance,  $X_C$ , and the inductive reactance,  $X_L$ .<sup>15</sup>

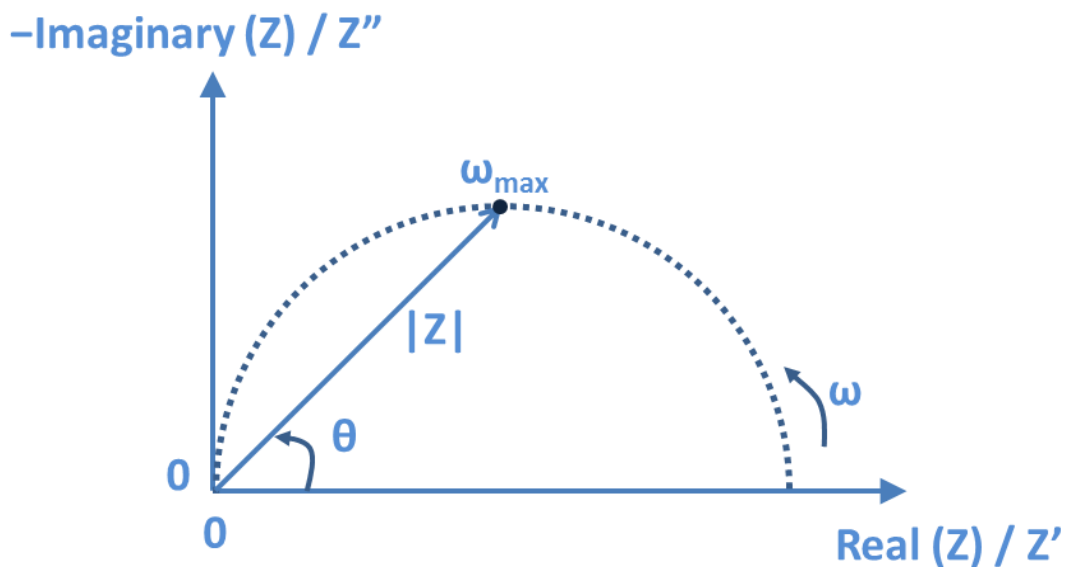


Figure 2.11 - The impedance plotted as a vector in a complex plane plot showing each quantity involved.

### 2.4.1 Data Analysis

Analysis of impedance data often consists of comparing the impedance of the sample  $Z$  to a calculated impedance of an equivalent circuit which is made up from ideal electronic resistors, capacitors and inductances. The electrochemical behaviour of an ionic conductor is often described as a resistor and a capacitor connected in parallel. The sum of the resistance,  $R$ , and capacitance,  $C$ , values is the relaxation time of the circuit,  $\tau$ .

#### Equation 2.17

$$\tau = RC = \frac{1}{\omega_{max}}$$

Where  $\omega_{max}$  is the maximum of the semi circle. Using Equation 2.17 both the resistance and capacitance can be obtained from the complex plane. The resistance of a semi circle can be taken from the difference in the two intercept points on the  $Z'$  axis and capacitance values can be calculated by applying Equation 2.17 to the angular frequency at the maximum of the semi circle. Capacitance values help to assign a physical feature of a sample to a semi circle in the data. For example capacitance values in the region of  $10^{-12}$  F indicate the bulk phase,  $10^{-11}$  F indicate a minor second phase and  $10^{-11} - 10^{-8}$  F indicate the grain boundary.<sup>17</sup>

A polycrystalline sample which has been pressed or sintered consists of multiple grains packed together with a boundary between the grain interiors. The current can either pass through the bulk and grain boundary phases or if there is less resistance could take a grain boundary pathway between the electrodes. (Figure 2.12)

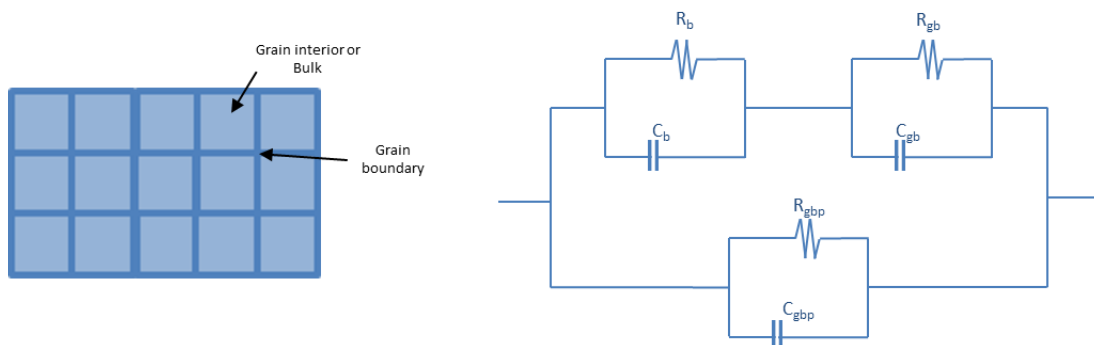


Figure 2.12 - Illustration of bulk and grain boundary components of a polycrystalline sample and an equivalent circuit for the possible routes. (b = bulk, gb = grain boundary and gbp = grain boundary pathway)

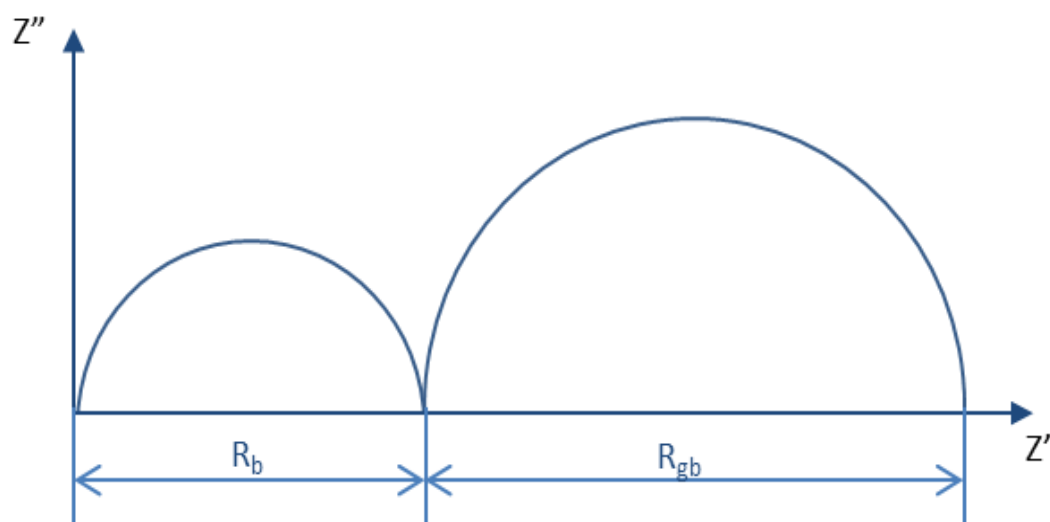
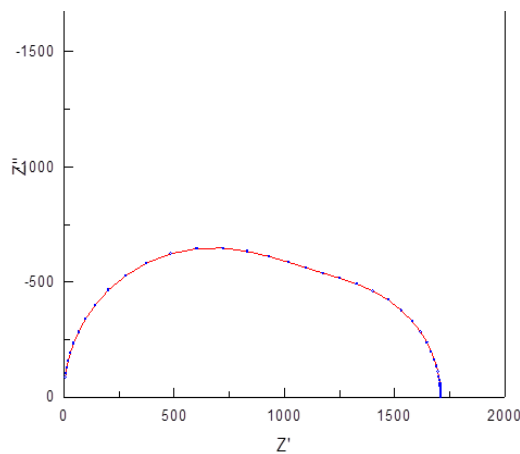


Figure 2.13 - Ideal impedance spectra with distinct regions for bulk and grain boundary components.

In the ideal result the semi circles relating to the bulk and grain boundary phases of the material have time constants which are different so that the resulting Nyquist plot semi circles are well defined and can be separated from each other giving a distinct result for both the bulk and grain boundary (Figure 2.13).<sup>17</sup> However this is not often

the case and the data more often consists of overlapping semi circles or a single distorted semi circle (Figure 2.14). Computer programs can calculate the influence of each component using equivalent circuit modelling and approximate start values for resistance and capacitance for each component. In this work Zview v3.3 (Scribner Associates) was used to analyse the impedance spectra.



**Figure 2.14 - Impedance data with overlap between the bulk and grain boundary components.**

In this work impedance spectroscopy is used for calculating ion mobility within ceramic samples for use as electrolyte materials. Ion mobility is usually described as the ionic conductivity of the sample which can be calculated from the resistance by Equation 2.18.

**Equation 2.18**

$$\sigma = \frac{1}{R} \times G_f$$

Where  $G_f$  is a geometric factor calculated from Equation 2.19. where  $l$  is sample thickness and  $A$  is the area of the sample.

**Equation 2.19**

$$G_f = \frac{l}{A}$$

Impedance spectra are recorded over a range of temperatures and atmospheres. The resultant conductivity values determined from a range of temperatures can be plotted in such a way that the activation energy of the sample in that atmosphere can be calculated using an Arrhenius type function. When the values are plotted  $\text{Log}_{10}(\sigma T / \text{S cm}^{-1} \text{K})$  against  $T^{-1} (\text{K}^{-1})$  the gradient of the plot becomes  $-E_a / 2.303 * R$  (where  $R$  is the universal gas constant): multiplying the gradient by  $-2.303 * R$  then results in the activation energy.

#### **1.1.1.1 - Instrumentation**

In this work two impedance analysers were used, the first was a Hewlett Packard LF 4192A impedance analyser and the second was a N4L NumetriQ phase sensitive multimeter with an Impedance Analysis Interface. Data were collected between 100 Hz and 13 MHz on a log scale with 20 steps per decade and an applied voltage magnitude of 100 mV was used.

Samples were pressed into pellets between 8 – 20 mm in diameter at pressures between  $300 \text{ kg cm}^{-2}$  and  $10,000 \text{ kg cm}^{-2}$  and sintered at temperatures in excess of  $1300^\circ\text{C}$ . Platinum ink was painted onto the faces of the pellets so that platinum foil electrodes could be attached, and this was bonded to the surface in a furnace at

800°C for an hour. Figure 2.15 shows the experimental set up used for impedance analysis and platinum wire was used to limit responses between different electrode materials. In this work, the gases used were  $N_2$ ,  $O_2$  and air; these were passed through a bubbler filled with concentrated sulphuric acid to yield dry gas flow and either  $D_2O$  or  $H_2O$  for wetgas flow. A second thermocouple was used as the thermocouple in the furnace is set away from the sample and would not be an accurate measure of the temperature at the sample.

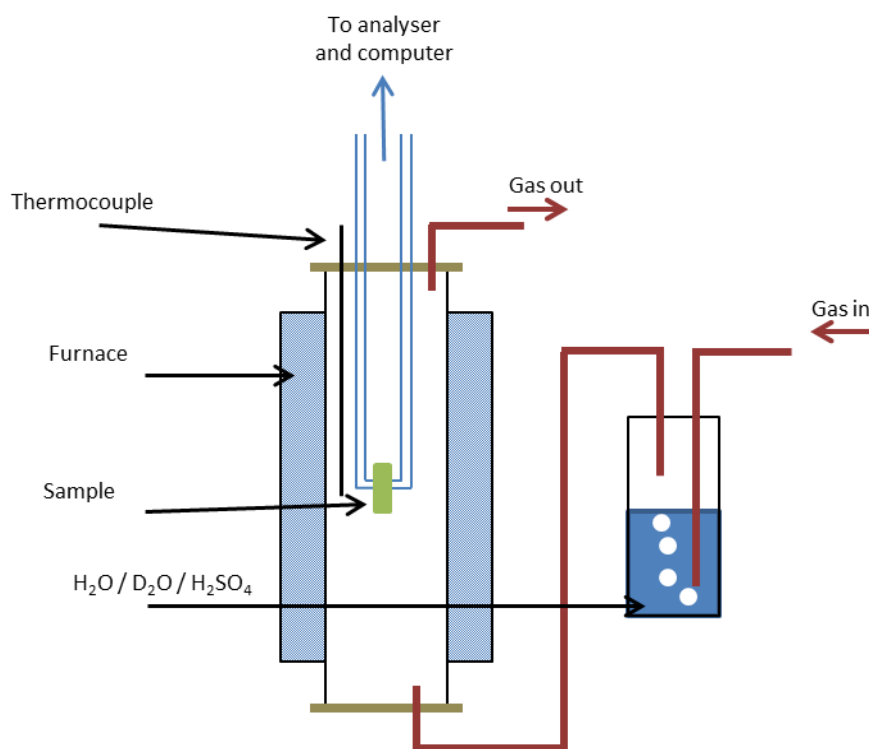


Figure 2.15 - Experimental set up for impedance analysis.

## 2.5 Raman Spectroscopy

Raman spectroscopy observes vibrations in molecules and crystals through Raman scattering. A single wavelength of radiation is used to irradiate the sample (a 532 nm green laser was used in this work). The detector then detects the radiation scattered by molecules which have shifted by one vibrational state either increasing or decreasing in energy. When the incident light hits the molecule it polarises the electron cloud forming an unstable excited or 'virtual' state. This quickly relaxes back to a vibrational state if the vibrational state has changed a photon of a different energy to the incident light is released. It is the energy difference that is of interest in Raman scattering. Most of the scattering involves only the distortion of the electron cloud which results in very small changes of energy this is usually seen as an elastic process and known as Rayleigh scattering. When scattering involves the nucleus of an atom much larger amounts of energy can be transferred resulting in inelastic or Raman scattering. If a molecule is in its lowest or ground state ( $v = 0$ ) it will absorb energy and increase in vibrational state. The resulting scattered photon will be reduced in energy by the difference between the states this is known as Stokes scattering. If a molecule is in a higher vibrational state (e.g.  $v = 1$ ) the molecule can be returned to its ground state and the energy can be transferred to the photon this is known as anti-Stokes scattering. At room temperature most molecules are in their ground state and therefore Stokes scattering is the main form of Raman scattering. As temperature increases the ratio of anti-Stokes to Stokes scattering also increases. (Figure 2.16)

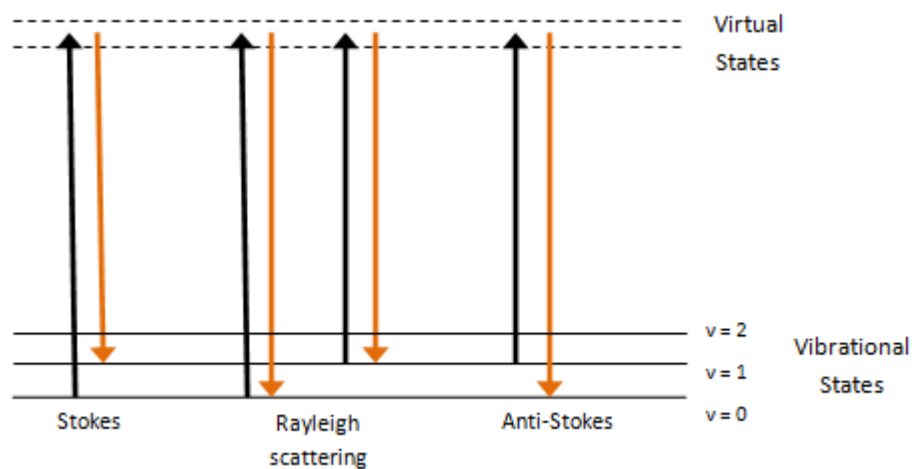


Figure 2.16 – Diagram of the Raman scattering process, incident and scattered energy are represented in black and orange respectively

Raman spectra were collected on a Renishaw InVia Raman microscope using an green laser with a wavelength of 532 nm on powdered samples.

## 2.6 References

1. A. R. West, *Solid State Chemistry and its Applications*, John Wiley and Sons, Chichester, 2<sup>nd</sup> edition, 2014
2. L. Smart, E. Moore, *Solid State Chemistry: An Introduction*, Nelson Thornes, UK, 2001
3. D. F. Shriver and P. Atkins, *Shriver and Atkins Inorganic Chemistry*, Oxford University Press, Oxford, 4<sup>th</sup> edition, 2006
4. M. Laue, *Annalen Der Physik*, 1913, **41**, 989
5. W.H. Bragg and W.L. Bragg, *X-rays and Crystal Structure*, G Bell and Sons, London, 5<sup>th</sup> edition, 1925
6. C. Hammond, *The basics of crystallography and diffraction*, Oxford University Press, Oxford, 1997
7. D.W. Bennett, *Understanding Single-Crystal X-ray Crystallography*, Wiley-VCH, Weinheim, 2010
8. LYNXEYE XE Datasheet, [http://www.bruker.com/fileadmin/user\\_upload/8-PDF-Docs/X-rayDiffraction\\_ElementalAnalysis/XRD/Flyers/LYNXEYE-XE\\_DOC-H88-EXS055\\_high\\_II.pdf](http://www.bruker.com/fileadmin/user_upload/8-PDF-Docs/X-rayDiffraction_ElementalAnalysis/XRD/Flyers/LYNXEYE-XE_DOC-H88-EXS055_high_II.pdf) (Accessed 15/08/14)
9. H.M. Rietveld, *Journal Applied Crystallography*, 1969, **2**, 65
10. R.A. Young, *The Rietveld Method*, Oxford University Press, Oxford, 1993
11. B.H. Toby, *Journal applied crystallography*, 2001, **34**, 210

12. A.C. Larson and R.B. von Dreele, *Los Alamos National Laboratory report*, LAUR, 1994, **86**
13. V.F. Sears, *Neutron News*, 1992, **3**
14. D.S. Silva, *Elementary Scattering Theory for X-ray and Neutron Users*, Oxford University Press, Oxford, 2011
15. J.R. Macdonald, *Impedance Spectroscopy: Emphasizing Solid Materials and Systems*, John Wiley and Sons, New York, 1987
16. J.R. Macdonald, *Annals of Biomedical Engineering*, 1992, **20**, 289
17. J.T.S. Irvine, D.C. Sinclair and A.R. West, *Advanced Materials*, 1990, **2**, 132
18. M. Pelletier, *Analytical Applications of Raman Spectroscopy*, Blackwell Publishing, Oxford, 1999.

# 3 Electrolyte materials with tetrahedral moieties

---

## 3.1 Introduction

The perovskite material  $\text{SrCeO}_3$  was found to display proton conductivity when doped with ions such as  $\text{Yb}^{3+}$  in 1981.<sup>1</sup> The acceptor dopant introduces oxygen vacancies into the structure, and in wet conditions water is incorporated into the vacancies allowing for proton conduction. Since then, there has been an interest in finding further ceramic materials which exhibit protonic conductivity with a principal focus on perovskites<sup>2</sup>

More recently protonic conductivity has also been found in systems containing tetrahedral moieties such as  $\text{LaPO}_4$ .<sup>3</sup> When doped with 1 mol % strontium,  $\text{LaPO}_4$  shows a sizeable increase in conductivity which, as with the perovskite systems, is due to the created oxygen vacancies incorporating water.

Other proton/oxide ion conducting systems with tetrahedral moieties include  $\text{LaBaGaO}_4$ ,<sup>4, 5</sup> and the apatites  $\text{La}_{9.33}\text{Si}_6\text{O}_{26}$  and  $\text{La}_{9.33}\text{Ge}_6\text{O}_{26}$ .<sup>7</sup> In the case of  $\text{LaBaGaO}_4$ , increasing the barium content at the expense of lanthanum creates the oxygen vacancies. In the apatite systems, significant water incorporation into interstitial sites can occur; in this case the enhancements in conductivity have been attributed to a resultant increase in oxide ion conductivity.

The work in this chapter examines structures with isolated tetrahedra based on the formula  $\text{A}_2\text{MO}_4$  (where A = alkaline earth or rare earth and M = Ge, Al, Ga).

## 3.2 Ba<sub>2</sub>GeO<sub>4</sub>/Sr<sub>2</sub>GeO<sub>4</sub>

### 3.2.1 Experimental

Stoichiometric mixtures of high purity barium/strontium carbonate, germanium (IV) oxide and M<sub>2</sub>O<sub>3</sub> (where M = Ga / Al) were ground together and heated to 1100°C for 12 h. Samples were then reground and heated for a second time to 1100°C for a further 12 h. Following this second heat treatment the samples were reground in a Fritsch pulverisette planetary ball mill at 350 rpm for 1 h and pressed into 13 mm pellets at a pressure of approximately 3,000 Kg cm<sup>-2</sup>. The pellets were sintered at 1300°C for 6 h in air.

Powder X-ray diffraction was used to check phase purity using a Bruker D8 diffractometer with Cu K<sub>α1</sub> radiation in transmission mode. Rietveld refinement was performed using the GSAS suite of programs.<sup>8</sup>

### 3.2.2 Ba<sub>2</sub>GeO<sub>4</sub>

X-ray diffraction indicated the successful synthesis of Ba<sub>2</sub>GeO<sub>4</sub>. The structure was refined using the orthorhombic K<sub>2</sub>SO<sub>4</sub> structure (space group Pmcn) by Rietveld refinement. The observed, calculated and difference profiles are shown Figure 3.1, with the refined structural parameters in Table 3.2.1.

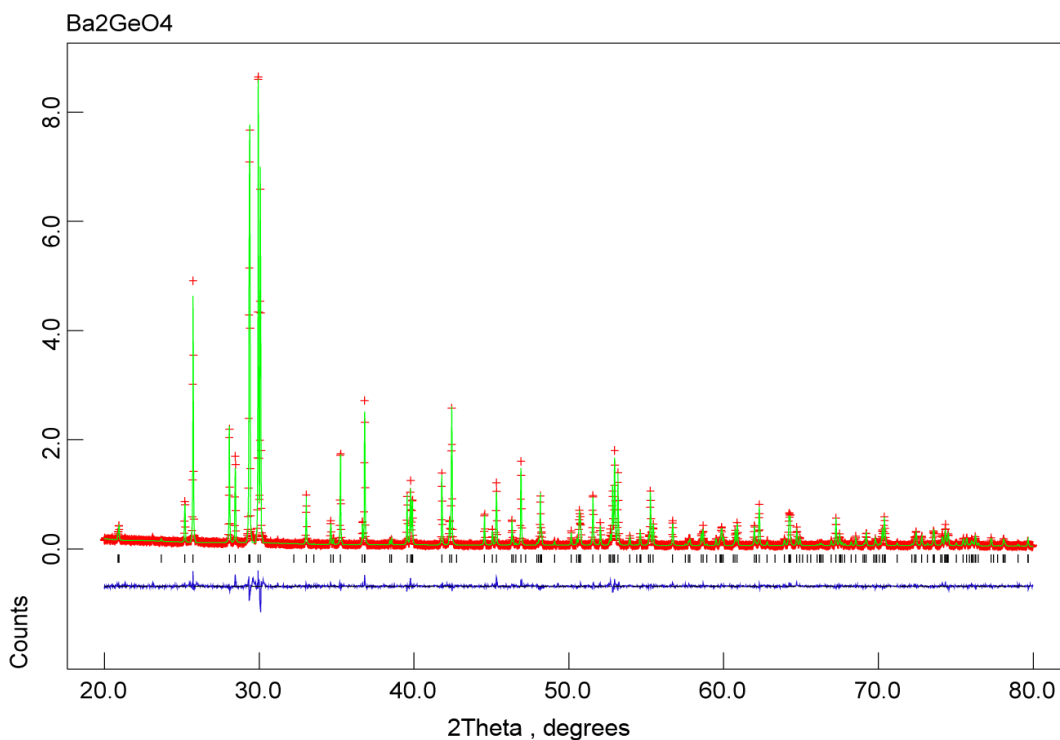


Figure 3.1 – Comparison plot showing observed (red cross), calculated (green line) and difference (blue line) profiles for Rietveld refinement of Ba<sub>2</sub>GeO<sub>4</sub>.

Table 3.1 – Rietveld refinement data for Ba<sub>2</sub>GeO<sub>4</sub>.

Formula	Space Group	$\chi^2$	wRp	Volume (Å <sup>3</sup> )	Theoretical density (g cm <sup>-3</sup> )	
Ba <sub>2</sub> GeO <sub>4</sub>	Pmcn	1.873	10.3%	470.16	5.79	
<b>a (Å)</b>	5.7916(6)	<b>b (Å)</b>	10.4062(1)	<b>c (Å)</b>	7.5658(3)	
Atomic Coordinates						
Atom	X	Y	Z	Ui/Ue*100	Multiplicity	Fraction
Ba1	0.25	0.0816(2)	0.1575(2)	1.789	4	1
Ba2	0.25	0.6968(1)	-0.0019(3)	1.479	4	1
Ge	0.25	0.4189(2)	0.2205(4)	1.089	4	1
O1	0.25	0.574(1)	0.322(2)	2.517	4	1
O2	0.0017(3)	0.3437(12)	0.2961(14)	3.327	8	1
O3	0.25	0.4228(16)	-0.0087(2)	3.177	4	0.920(2)

Once Ba<sub>2</sub>GeO<sub>4</sub> had been prepared as a pure single phase sample, attempts were made to introduce oxygen vacancies by doping with 2+ (M = Mg/Zn) and 3+ (M =

Mg/Zn) ions on the Ge site. Initially 10% doping was attempted to synthesise  $\text{Ba}_2\text{Ge}_{0.9}\text{M}_{0.1}\text{O}_{3.95}$  (for  $\text{M} = \text{Ga}/\text{Al}$ ) and  $\text{Ba}_2\text{Ge}_{0.9}\text{M}_{0.1}\text{O}_{3.9}$  (for  $\text{M} = \text{Mg}/\text{Zn}$ ). Samples were analysed for purity using x-ray diffraction and the gallium/aluminium samples were found to be single phase, but the samples for zinc and magnesium were found to contain ZnO and MgO respectively implying that it is not possible to incorporate either zinc or magnesium into the  $\text{Ba}_2\text{GeO}_4$  system.

AC impedance spectroscopy measurements were performed on the samples to see the effects of the doping on the conductivity. Impedance measurements were recorded in both dry and wet  $\text{N}_2$  atmospheres at various temperatures in the range 200 – 800°C; an example of the data obtained can be seen in Figure 3.2. It was not possible to resolve the bulk and grain boundary components, so total conductivity values are reported. Capacitance values in the region of  $10^{-12}$  F, however, suggest the observed semi-circle is mainly related to the bulk conductivity of the sample.<sup>9</sup>

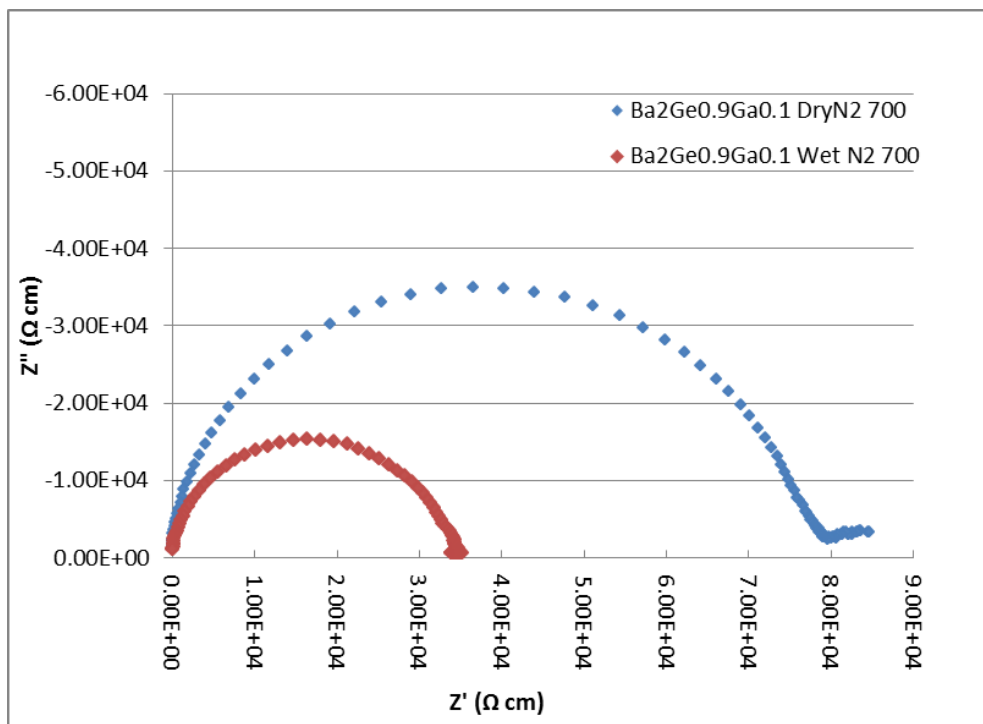
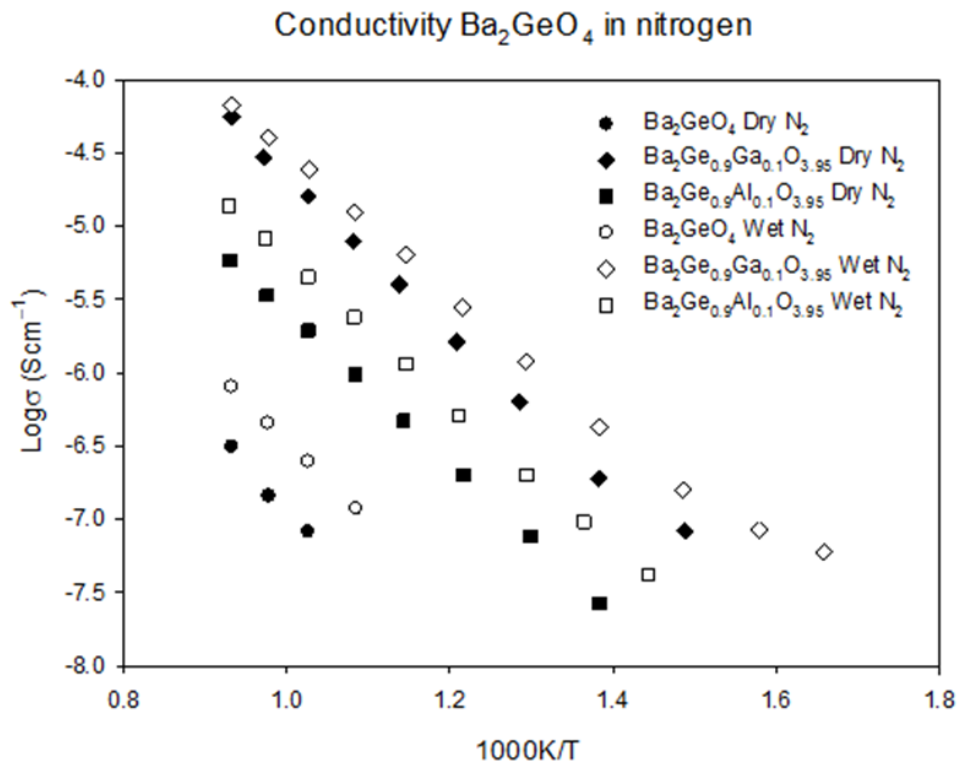


Figure 3.2 - Impedance plot for  $\text{Ba}_2\text{Ge}_{0.9}\text{Ga}_{0.1}\text{O}_{3.95}$  in Dry (blue) and Wet (red)  $\text{N}_2$  at 700°C

The parent  $\text{Ba}_2\text{GeO}_4$  sample had a low conductivity;  $3.1 \times 10^{-7} \text{ S cm}^{-1}$  at  $800^\circ\text{C}$  in dry  $\text{N}_2$ , and  $8.0 \times 10^{-7} \text{ S cm}^{-1}$  in wet  $\text{N}_2$ . The doped samples both showed an improvement in total conductivity; at  $800^\circ\text{C}$ , the sample doped with 10% aluminium had a conductivity of  $5.8 \times 10^{-6} \text{ S cm}^{-1}$  and  $1.4 \times 10^{-5} \text{ S cm}^{-1}$  in dry and wet  $\text{N}_2$  respectively. The 10% gallium doped sample exhibited a greater increase in conductivity with values of  $5.6 \times 10^{-5} \text{ S cm}^{-1}$  and  $6.7 \times 10^{-5} \text{ S cm}^{-1}$  at  $800^\circ\text{C}$  in dry and wet  $\text{N}_2$  respectively. There is an increase of almost 2 orders of magnitude in conductivity on Ga doping when compared with the undoped  $\text{Ba}_2\text{GeO}_4$  sample. (Figure 3.3)



**Figure 3.3 – Conductivity plots showing  $\text{Ba}_2\text{GeO}_4$  and samples doped 10% Ga/Al in both dry and wet  $\text{N}_2$  atmospheres.**

After successful doping at the 10% level, further work was performed to further vary the dopant level to investigate the effect on the conductivity. Therefore a series of

$\text{Ba}_2\text{Ge}_{1-x}\text{M}_x\text{O}_{4-x/2}$  (M = Al, Ga) samples were prepared for  $0.05 \leq x \leq 0.3$ . The Ga doped samples allowed for a greater amount of the dopant into the structure as was possible to increase the Ga content to 15% and still obtain a phase pure sample. With Al it was noticed that  $\text{Al}_2\text{O}_3$  was observed in the XRD pattern in samples containing more than 10% Al ( $\text{Al}_{0.1}$ ). Slight variations in reaction conditions including temperature increases up to 1450 °C and extending the number of heat treatments and treatment times also failed to produce pure samples for such high levels of Al. XRD results from the Ga samples showed that an impurity peak begins to appear in the  $2\theta = 30^\circ$  region for  $x > 0.15$  (Figure 3.4). It is believed that this peak is due to the formation of the Ga rich phase  $\text{Ba}_3\text{Ga}_2\text{O}_6$ . This impurity peak increases on further doping with Ga which implies that a limit for the amount of Ga which can be accepted into the structure has been reached in the 15% region.

Comparison between unit cell volumes in the doped and undoped  $\text{Ba}_2\text{GeO}_4$  samples shows that with both sets of samples an increase on Al/Ga content has led to a contraction in unit cell size despite the larger sizes of  $\text{Al}^{3+}$ ,  $\text{Ga}^{3+}$ . The decrease in cell size is possibly due to the creation of oxygen vacancies most likely accommodated by the formation of  $\text{M}_2\text{O}_7$  units which draw together two  $\text{MO}_4$  units. At the  $x = 0.1$  level Al reduces the cell size more than Ga, which is as expected given the smaller size of  $\text{Al}^{3+}$  compared to  $\text{Ga}^{3+}$ . Volume comparisons for  $\text{Ba}_2\text{GeO}_4$  and doped samples can be seen in Table 3.2. Samples doped with greater than 15% Ga start to show impurities and have not been included.

Table 3.2 – Unit cell volume change on doping in Ba<sub>2</sub>GeO<sub>4</sub>.

M	X Value	Unit Cell Volume (Å <sup>3</sup> )
Ga / Al	0	473.278
Ga	0.05	471.708
Ga	0.10	471.198
Ga	0.15	471.063
Al	0.10	470.089

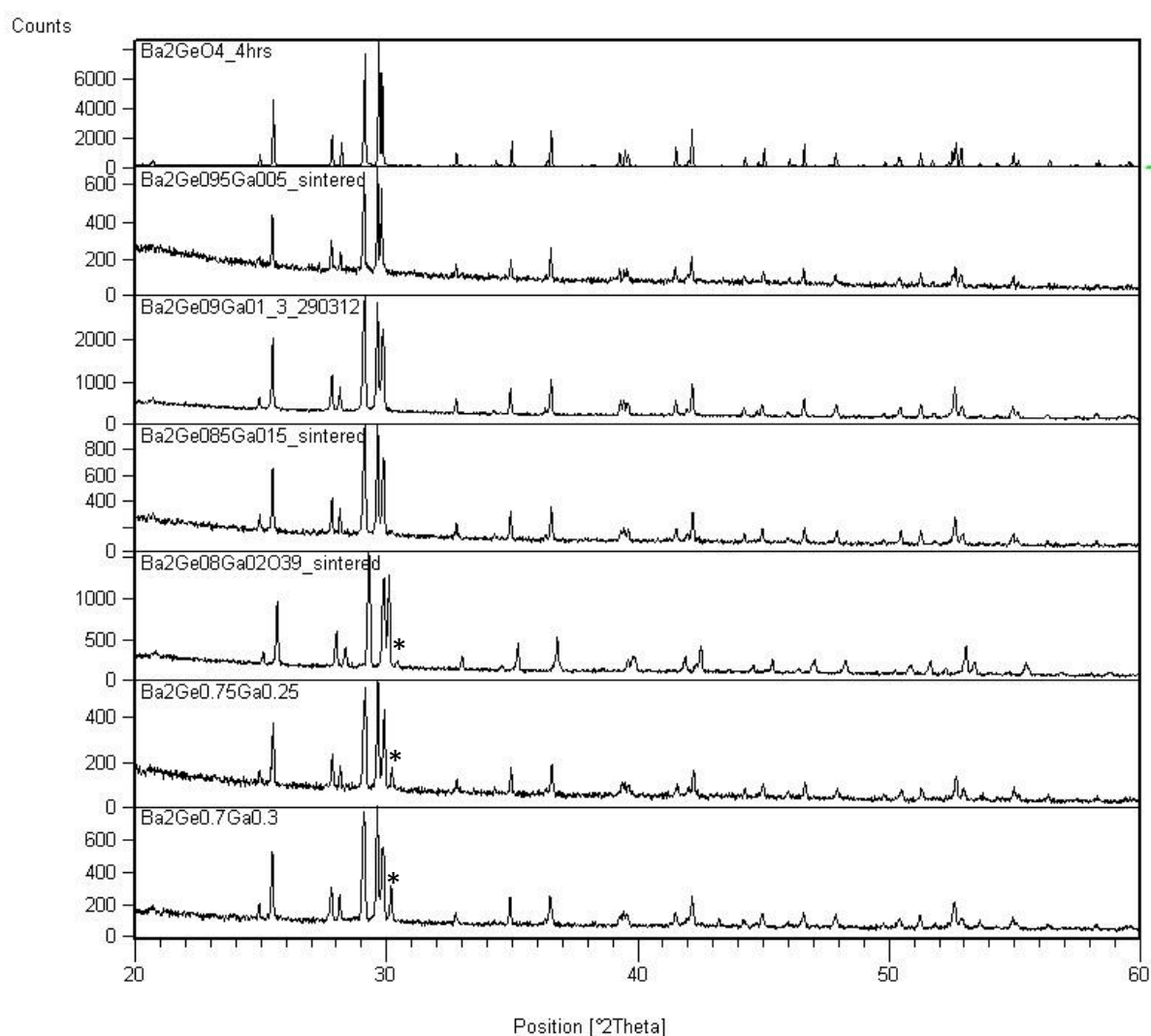


Figure 3.4 - XRD patterns for Ga doped Ba<sub>2</sub>GeO<sub>4</sub> samples containing 0 – 30% Ga (\* indicates Ba<sub>3</sub>Ga<sub>2</sub>O<sub>6</sub> impurity).

Now that a range of gallium doped samples had been prepared it was possible to examine the trend in conductivity related to gallium doping in  $\text{Ba}_2\text{GeO}_4$ . Figure 3.5 and Figure 3.6 show the conductivity values obtained for the gallium doped samples in dry and wet  $\text{N}_2$  atmospheres respectively. It can be seen that an increase in conductivity is observed with an increase in gallium content to a maximum of  $1.14 \times 10^{-4} \text{ S cm}^{-1}$  at  $800^\circ\text{C}$  in dry  $\text{N}_2$  and  $2.27 \times 10^{-4} \text{ S cm}^{-1}$  at  $800^\circ\text{C}$  in wet  $\text{N}_2$  for the 15% gallium doped sample. The 15% gallium sample shows a plateau in the decreasing conductivity values in wet  $\text{N}_2$  at  $400^\circ\text{C}$  this could possibly be attributed to an increase in the water incorporation at lower temperatures compared with higher temperatures which would result in a higher proton conductivity element. This was not noticed as a two-step dehydration using TGA in dry  $\text{N}_2$  but could be present during conductivity measurements due to the higher relative humidity observed using a wet  $\text{N}_2$  flow.

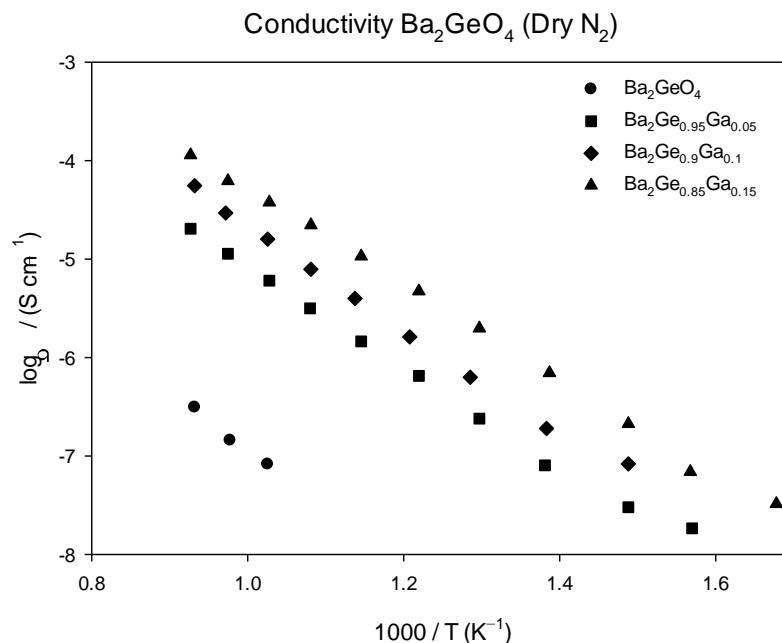


Figure 3.5 – Conductivity plot for  $\text{Ba}_2\text{GeO}_4$ ,  $\text{Ba}_2\text{Ge}_{0.95}\text{Ga}_{0.05}\text{O}_{3.975}$ ,  $\text{Ba}_2\text{Ge}_{0.9}\text{Ga}_{0.1}\text{O}_{3.95}$  and  $\text{Ba}_2\text{Ge}_{0.85}\text{Ga}_{0.15}\text{O}_{3.925}$  in a dry  $\text{N}_2$  atmosphere.

The trend in increasing conductivity with increasing gallium content can be seen in Table 3.3 and Table 3.4. A clear increase in conductivity is seen with an increase in gallium content. The samples in a wet N<sub>2</sub> gas flow show a further increase in conductivity when compared to their dry N<sub>2</sub> equivalents, this enhancement indicates a proton conducting element to the total conductivity in wet N<sub>2</sub>.

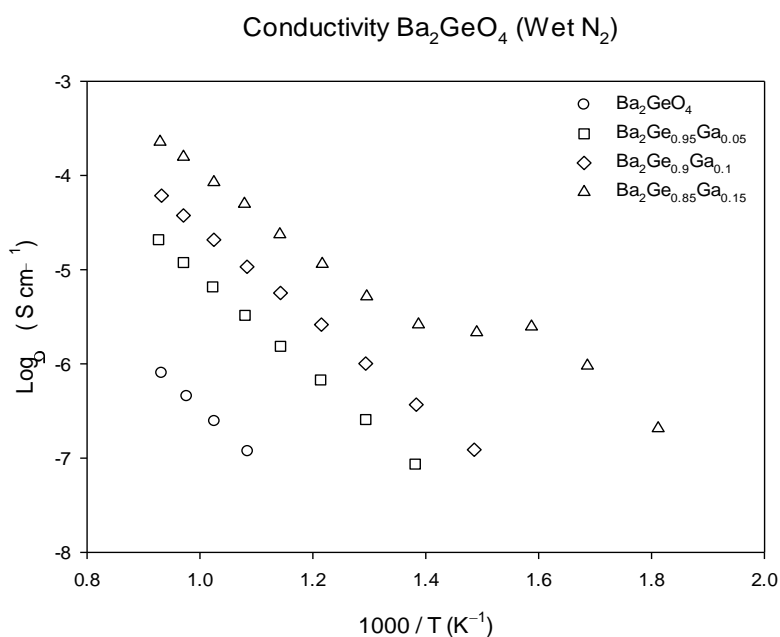


Figure 3.6 - Conductivity plot for Ba<sub>2</sub>GeO<sub>4</sub>, Ba<sub>2</sub>Ge<sub>0.95</sub>Ga<sub>0.05</sub>O<sub>3.975</sub>, Ba<sub>2</sub>Ge<sub>0.9</sub>Ga<sub>0.1</sub>O<sub>3.95</sub> and Ba<sub>2</sub>Ge<sub>0.85</sub>Ga<sub>0.15</sub>O<sub>3.925</sub> in a Wet N<sub>2</sub> atmosphere.

Table 3.3 - Comparison of conductivity at 700 °C and 500°C for increasing levels of Ga measured in a dry N<sub>2</sub> gas flow (\* indicates conductivity too low to measure)

Sample	Conductivity 700°C (S cm <sup>-1</sup> )	Conductivity 500°C (S cm <sup>-1</sup> )	Activation energy (eV)
Ba <sub>2</sub> GeO <sub>4</sub>	8.20x10 <sup>-8</sup>	*	1.31
Ba <sub>2</sub> Ge <sub>0.95</sub> Ga <sub>0.05</sub> O <sub>3.975</sub>	6.03x10 <sup>-6</sup>	2.39x10 <sup>-7</sup>	1.04
Ba <sub>2</sub> Ge <sub>0.9</sub> Ga <sub>0.1</sub> O <sub>3.95</sub>	1.59x10 <sup>-5</sup>	6.30x10 <sup>-7</sup>	1.09
Ba <sub>2</sub> Ge <sub>0.85</sub> Ga <sub>0.15</sub> O <sub>3.925</sub>	3.76x10 <sup>-5</sup>	1.97x10 <sup>-6</sup>	1.02

Table 3.4 - Comparison of conductivity data at 700 °C and 500 °C for increasing levels of Ga in a wet N<sub>2</sub> gas flow (\* indicates conductivity too low to measure)

Sample	Conductivity 700°C (S cm <sup>-1</sup> )	Conductivity 500°C (S cm <sup>-1</sup> )	Activation energy (eV)
Ba <sub>2</sub> GeO <sub>4</sub>	2.46x10 <sup>-7</sup>	*	1.16
Ba <sub>2</sub> Ge <sub>0.95</sub> Ga <sub>0.05</sub> O <sub>3.975</sub>	6.57 x10 <sup>-6</sup>	2.56 x10 <sup>-7</sup>	1.08
Ba <sub>2</sub> Ge <sub>0.9</sub> Ga <sub>0.1</sub> O <sub>3.95</sub>	2.43x10 <sup>-5</sup>	1.20x10 <sup>-6</sup>	0.94
Ba <sub>2</sub> Ge <sub>0.85</sub> Ga <sub>0.15</sub> O <sub>3.925</sub>	8.48 x10 <sup>-5</sup>	5.20 x10 <sup>-6</sup>	0.94

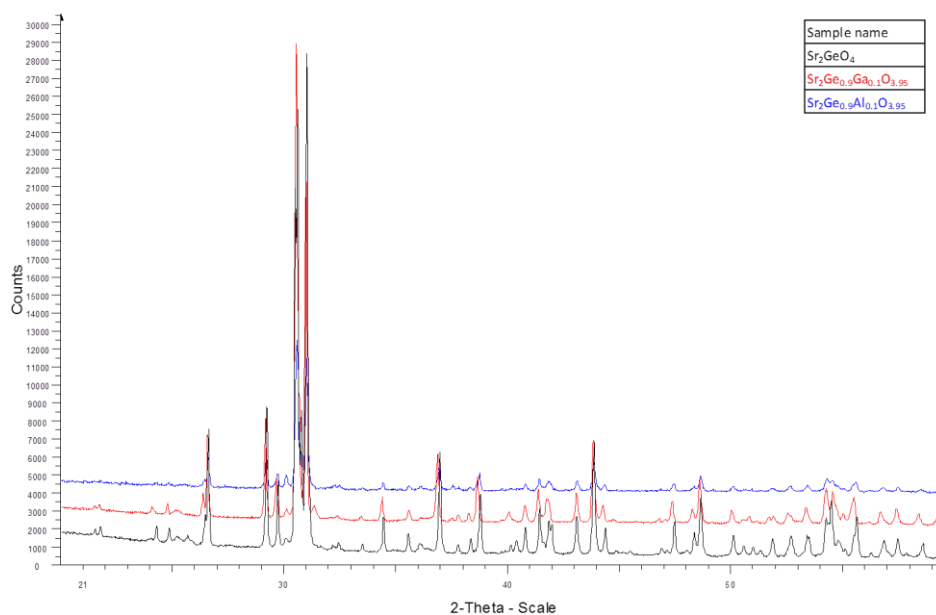
As density can be linked to total conductivity, the density of the tested samples was calculated to see if there was any correlation between the densities of the samples and increases in conductivity. Taking a look at the density of the doped samples, it can be seen that the gallium doped samples show higher densities than the undoped and aluminium doped samples, e.g. the 5% and 10% gallium doped samples achieve greater than 90% theoretical density. There was however no clear relationship between the higher densities and higher conductivities which means the increase in conductivity can be related to the changes due to doping (Table 3.5), i.e. the introduction of additional oxide ion vacancies.

Table 3.5 - Theoretical density comparison for Ba<sub>2</sub>GeO<sub>4</sub> series compared with conductivity in dry N<sub>2</sub>.

Sample	% theoretical density	Conductivity 700 °C (S cm <sup>-1</sup> )
Ba <sub>2</sub> GeO <sub>4</sub>	84.2	8.20x10 <sup>-8</sup>
Ba <sub>2</sub> Ge <sub>0.95</sub> Ga <sub>0.05</sub> O <sub>3.975</sub>	93.3	6.03x10 <sup>-6</sup>
Ba <sub>2</sub> Ge <sub>0.9</sub> Ga <sub>0.1</sub> O <sub>3.95</sub>	90.8	1.59x10 <sup>-5</sup>
Ba <sub>2</sub> Ge <sub>0.85</sub> Ga <sub>0.15</sub> O <sub>3.925</sub>	87.5	3.76x10 <sup>-5</sup>
Ba <sub>2</sub> Ge <sub>0.9</sub> Al <sub>0.1</sub> O <sub>3.95</sub>	83.9	5.80x10 <sup>-6</sup>

### 3.2.3 Sr<sub>2</sub>GeO<sub>4</sub>

In addition to work on the Ba<sub>2</sub>GeO<sub>4</sub> system, work on the related Sr<sub>2</sub>GeO<sub>4</sub> system has been investigated. Initially the synthesis of Sr<sub>2</sub>GeO<sub>4</sub> was attempted without doping and with 10% Ga, Al doping (Sr<sub>2</sub>Ge<sub>0.9</sub>Ga<sub>0.1</sub>O<sub>3.95</sub> and Sr<sub>2</sub>Ge<sub>0.9</sub>Al<sub>0.1</sub>O<sub>3.95</sub>) via conventional solid state synthesis methods. To check the purity of the resulting powder samples PXRD was performed. The resulting XRD patterns were compared to known reflections for the Sr<sub>2</sub>GeO<sub>4</sub> structure and this was found to be the only structure phase in all three samples indicating successful doping into the structure by aluminium and gallium. The pattern for the aluminium doped sample has a lower intensity as a different XRD was used with an older X-ray tube (Figure 3.7).<sup>10</sup>



**Figure 3.7 – X-ray diffraction patterns for Sr<sub>2</sub>GeO<sub>4</sub> (bottom), Sr<sub>2</sub>Ge<sub>0.9</sub>Ga<sub>0.1</sub>O<sub>3.95</sub> (middle and Sr<sub>2</sub>Ge<sub>0.9</sub>Al<sub>0.1</sub>O<sub>3.95</sub> (top).**

Rietveld refinement was performed on the undoped sample to extract unit cell and atomic position data, the initial model used for the refinement was an orthorhombic space group *PBN21* which was taken from F. Nishi *et al.* (1996).<sup>10</sup> The final

observed, calculated and difference profiles are shown in **Error! Reference source not found.** A comparison between the unit cell data extracted from the refinement and the literature data can be seen in Table 3.6

**Table 3.6 - Unit cell comparison between experimental and literature data for Sr<sub>2</sub>GeO<sub>4</sub>.**

	Experimental	Literature <sup>10</sup>
Formula	Sr <sub>2</sub> GeO <sub>4</sub>	Sr <sub>2</sub> GeO <sub>4</sub>
Space Group	PBN21	PBN21
a (Å)	5.8859(1)	5.852(4)
b (Å)	14.3110(2)	14.299(8)
c (Å)	9.9240(2)	9.916(6)
Volume (Å <sup>3</sup> )	831.68(4)	829.8
Theoretical Density (g cm <sup>-3</sup> )	4.981	
χ <sup>2</sup>	3.991	
wRp	5.9%	

As with the unit cell data the atomic positions are very similar to the literature data as both structures are very similar. (Table 3.7)

**Table 3.7 - Comparison of atomic positions in the experimental Sr<sub>2</sub>GeO<sub>4</sub> sample and literature values for Sr<sub>2</sub>GeO<sub>4</sub>.**

Atom	Experimental (x, y, z)			Literature (x, y, z) <sup>10</sup>		
Sr1	0.275(1)	0.5450(8)	0.569(1)	0.2716(4)	0.5441(1)	0.5719(2)
Sr2	0.284(1)	0.7950(9)	0.925(1)	0.2895(4)	0.7956(2)	0.9280(3)
Sr3	0.282(1)	0.6234(8)	0.196(1)	0.2957(3)	0.6210(2)	0.2032(3)
Sr4	0.231(1)	0.3691(8)	0.196(1)	0.2289(4)	0.3712(2)	0.2984(4)
Ge1	0.272(1)	0.764(1)	0.572(1)	0.2784(5)	0.7636(2)	0.5845(3)
Ge2	0.224(1)	0.521(1)	0.906(1)	0.2306(4)	0.5209(1)	0.9164(2)
O1	0.350(5)	0.715(2)	0.416(3)	0.3509(22)	0.7007(10)	0.4332(14)
O2	0.021(6)	0.704(2)	0.631(3)	0.0334(24)	0.7047(10)	0.6418(14)
O3	0.232(7)	0.884(2)	0.561(2)	0.1863(23)	0.8754(10)	0.5477(13)
O4	0.474(5)	0.737(2)	0.734(3)	0.4880(23)	0.7496(10)	0.7063(16)
O5	0.283(5)	0.441(1)	0.054(3)	0.2763(27)	0.4588(9)	0.0651(14)
O6	0.990(5)	0.490(2)	0.825(3)	0.9835(26)	0.4721(11)	0.8470(15)
O7	0.350(4)	0.129(2)	0.971(2)	0.3345(26)	0.1380(10)	0.9504(15)
O8	0.407(6)	0.512(2)	0.847(3)	0.4588(24)	0.5024(11)	0.8078(16)

Further doping with 10% Zn/Mg (Sr<sub>2</sub>Ge<sub>0.9</sub>M<sub>0.1</sub>O<sub>3.9</sub> (M = Mg, Zn) and up to 20% Ga/Al (Sr<sub>2</sub>Ge<sub>0.8</sub>M<sub>0.2</sub>O<sub>3.9</sub> (M =Al, Ga) was attempted but in all four samples powder X-ray

diffraction showed a presence of impurities, with larger impurities for the Mg, Zn doped samples.

**Table 3.8 - Density and cell volume comparison for Sr<sub>2</sub>GeO<sub>4</sub> samples**

Sample	% theoretical density	Unit cell volume (Å <sup>3</sup> )
Sr <sub>2</sub> GeO <sub>4</sub>	89.0%	828.40 (3)
Sr <sub>2</sub> Ge <sub>0.9</sub> Ga <sub>0.1</sub> O <sub>3.95</sub>	89.4%	830.06 (1)
Sr <sub>2</sub> Ge <sub>0.9</sub> Al <sub>0.1</sub> O <sub>3.95</sub>	83.9%	827.85 (3)

A look at the effects on the size of the unit cell with doping showed that on substitution with 10% gallium, an increase in the size of the unit cell was observed, however the 10% aluminium sample showed a reduction in cell volume (Table 3.8). Both Al<sup>3+</sup> and Ga<sup>3+</sup> are larger ions than Ge<sup>4+</sup> so an increase in cell volume might be expected however the Al<sup>3+</sup> ion is only fractionally larger than Ge<sup>4+</sup> and the decrease in unit cell volume can be attributed to the presence of oxygen vacancies as in the case of doping in Ba<sub>2</sub>GeO<sub>4</sub>.

Impedance spectroscopy measurements were carried out on as prepared, Ga and Al doped samples. An AC impedance plot for Sr<sub>2</sub>Ge<sub>0.9</sub>Ga<sub>0.1</sub>O<sub>3.95</sub> recorded at 700 °C is shown in Figure 3.8. As with the Ba<sub>2</sub>GeO<sub>4</sub> samples it was not possible to resolve the two bulk and grain boundary semi-circles, and total conductivity values are reported. Capacitance values in the region of 10<sup>-12</sup> F again suggest that the semi-circle is mainly due to the bulk component.<sup>9</sup>

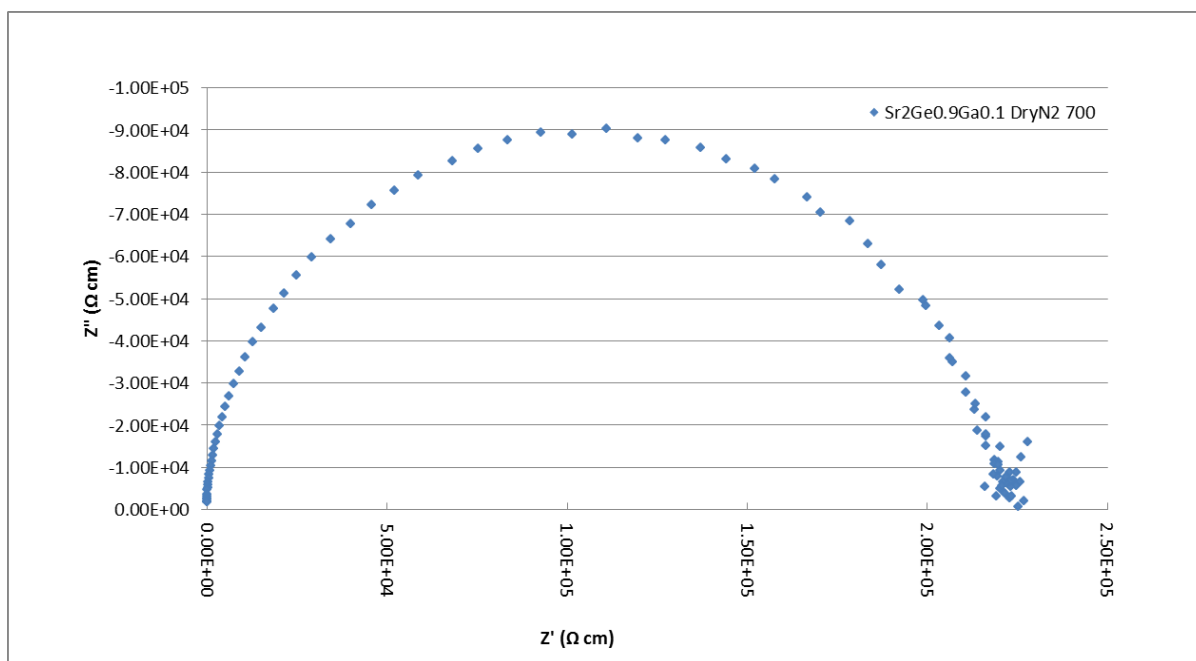
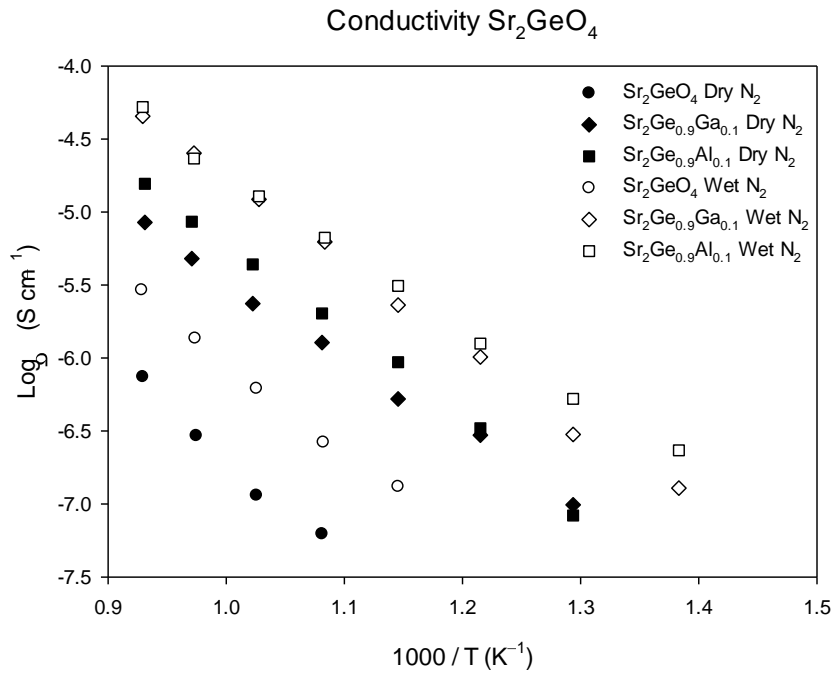


Figure 3.8 - Impedance plot for  $\text{Sr}_2\text{Ge}_{0.9}\text{Ga}_{0.1}\text{O}_{3.95}$  in Dry  $\text{N}_2$  at  $700^\circ\text{C}$

The two doped samples,  $\text{Sr}_2\text{Ge}_{0.9}\text{Ga}_{0.1}\text{O}_{3.95}$  and  $\text{Sr}_2\text{Ge}_{0.9}\text{Al}_{0.1}\text{O}_{3.95}$  had a conductivity an order of magnitude above  $\text{Sr}_2\text{GeO}_4$  in dry  $\text{N}_2$  (Figure 3.9) indicating that Ga / Al doping has been successful. All samples displayed an improvement in wet  $\text{N}_2$  due to proton conductivity, with this improvement being also one order of magnitude. Both of the doped samples showed very similar conductivities in dry atmospheres, with the 10% Al sample being slightly better at higher temperatures. In the wet atmospheres this trend was reversed, with both samples being very similar at high temperature and the 10% Al sample showing slight improvement on the 10% Ga sample as the temperature drops.



**Figure 3.9 - Conductivity plots showing  $\text{Sr}_2\text{GeO}_4$  and samples doped 10% Ga/Al in both dry and wet  $\text{N}_2$  atmospheres.**

Table 3.9 and Table 3.10 show a comparison of conductivity data at 700°C and 500°C illustrating a clear increase in conductivity when  $\text{Sr}_2\text{GeO}_4$  is doped with gallium or aluminium at the 10% level. The samples in a wet  $\text{N}_2$  gas flow show a further increase in conductivity when compared to their dry  $\text{N}_2$  equivalents due to a protonic contribution to the conductivity.

**Table 3.9 - Comparison of conductivity at 700 °C and 500°C in  $\text{Sr}_2\text{GeO}_4$  and doping with 10% Ga / Al measured in a dry  $\text{N}_2$  gas flow (\* indicates conductivity too low to measure)**

Sample	Conductivity 700°C ( $\text{S cm}^{-1}$ )	Conductivity 500°C ( $\text{S cm}^{-1}$ )	Activation energy (eV)
$\text{Sr}_2\text{GeO}_4$	$1.145 \times 10^{-7}$	*	1.54
$\text{Sr}_2\text{Ge}_{0.9}\text{Ga}_{0.1}\text{O}_{3.95}$	$2.356 \times 10^{-6}$	$9.884 \times 10^{-8}$	1.15
$\text{Sr}_2\text{Ge}_{0.9}\text{Al}_{0.1}\text{O}_{3.95}$	$4.380 \times 10^{-6}$	$8.335 \times 10^{-8}$	1.32

Table 3.10 - Comparison of conductivity at 700 °C and 500°C in Sr<sub>2</sub>GeO<sub>4</sub> and doping with 10% Ga / Al measured in a wet N<sub>2</sub> gas flow (\* indicates conductivity too low to measure)

Sample	Conductivity 700°C (S cm <sup>-1</sup> )	Conductivity 500°C (S cm <sup>-1</sup> )	Activation energy (eV)
Sr <sub>2</sub> GeO <sub>4</sub>	6.178x10 <sup>-7</sup>	*	1.36
Sr <sub>2</sub> Ge <sub>0.9</sub> Ga <sub>0.1</sub> O <sub>3.95</sub>	1.220x10 <sup>-5</sup>	2.996x10 <sup>-7</sup>	1.25
Sr <sub>2</sub> Ge <sub>0.9</sub> Al <sub>0.1</sub> O <sub>3.95</sub>	1.281x10 <sup>-5</sup>	5.260x10 <sup>-7</sup>	1.13

### 3.3 LaBaGaO<sub>4</sub> / LaSrGaO<sub>4</sub>

#### 3.3.1 Experimental

Stoichiometric mixtures of high purity barium/strontium carbonate (BaCO<sub>3</sub> / SrCO<sub>3</sub>), lanthanum (III) oxide (La<sub>2</sub>O<sub>3</sub>) and gallium (III) oxide Ga<sub>2</sub>O<sub>3</sub> were ground together and heated to 1100°C for 12 h. Samples were then reground and heated for a second time to 1100°C for a further 12 h. Following these two heat treatments the samples were reground in a planetary ball mill at 350 rpm for 1 h and pressed into 13 mm pellets at a pressure of approximately 3,000 kg cm<sup>-2</sup>. The pellets were sintered at 1300°C for 6h.

Powder X-ray diffraction was used to check phase purity using a Bruker D8 diffractometer with Cu K<sub>α1</sub> radiation in transmission mode. Rietveld refinement was performed using the GSAS suite of programs.<sup>8</sup>

### 3.3.2 LaBaGaO<sub>4</sub>

A pure sample of LaBaGaO<sub>4</sub> was synthesised and the structure was refined with an orthorhombic space group P2<sub>1</sub>2<sub>1</sub>2<sub>1</sub>, (the observed, calculated and difference profiles can be seen in Figure 3.10). From the refinement the unit cell and atomic position data were determined (Table 3.11).

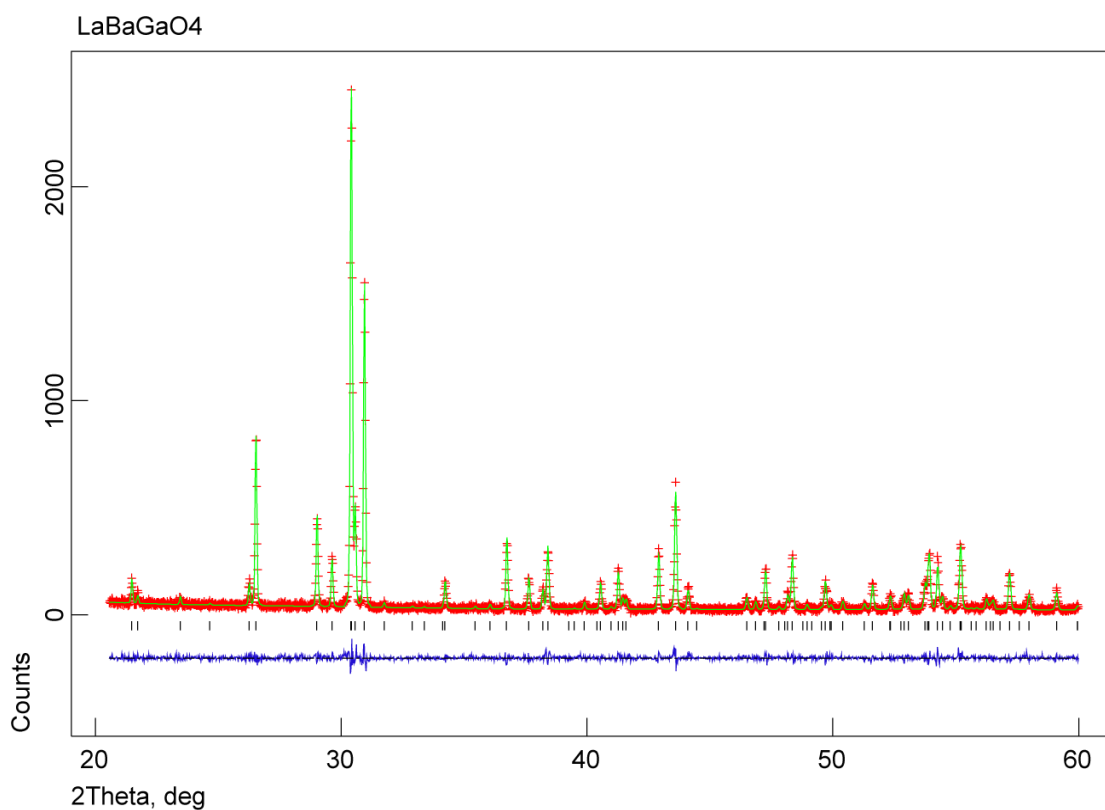


Figure 3.10 – Refinement profile for LaBaGaO<sub>4</sub> showing observed (red cross), calculated (green line) and difference (blue line) profiles

Table 3.11 – Refined atomic positions in LaBaGaO<sub>4</sub> with the space group P2<sub>1</sub>2<sub>1</sub>2<sub>1</sub>.

Sample		Space Group	wR <sub>p</sub>	χ <sup>2</sup>	Volume (Å <sup>3</sup> )	
LaBaGaO <sub>4</sub>		P2 <sub>1</sub> 2 <sub>1</sub> 2 <sub>1</sub>	13.9%	1.27	427.6(1)	
a (Å)	9.99(2)	b (Å)	7.25(1)	c (Å)	5.90(2)	
Atomic Coordinates						
Atom	x	y	z	U <sub>i</sub> /U <sub>e</sub> *100	Multiplicity	Site Occ
La1	0.0512(3)	0.4964(4)	0.2328(12)	0.55(23)	4	1
Ba1	0.6714(4)	0.3334(6)	0.2373(20)	1.09(28)	4	1
Ga1	0.3356(8)	0.2832(10)	0.256(4)	1.0(4)	4	1
O1	0.1775(34)	0.156(5)	0.255(11)	2.6(12)	4	1
O2	0.4254(65)	0.180(10)	0.490(10)	5.1(28)	4	1
O3	0.2899(34)	0.506(5)	0.402(7)	0.1	4	1
O4	0.4314(54)	0.237(7)	0.006(9)	0.6(28)	4	1

Strontium substitution for barium has been previously seen in many studies and LaSrGaO<sub>4</sub> has been previously reported and therefore strontium substitution was considered for this work. The structure of LaSrGaO<sub>4</sub> is slightly different to LaBaGaO<sub>4</sub> as it forms a tetragonal *I4/mmm* structure rather than the orthorhombic structure observed with LaBaGaO<sub>4</sub>. Strontium doping for barium was attempted for 0%, 25%, 50% and 100% to try and determine the crossover point between the LaBaGaO<sub>4</sub> and LaSrGaO<sub>4</sub> based structures. Pure samples were obtained for 25%, 50% and 100% however the 75% Sr sample contained both a LaBaGaO<sub>4</sub> and a LaSrGaO<sub>4</sub> phase along with traces of starting material. The the 25% and 50% doped samples maintain the P2<sub>1</sub>2<sub>1</sub>2<sub>1</sub> structure of LaBaGaO<sub>4</sub> with a slight decrease in cell size due to the smaller ion size of strontium (Table 3.13). The 100% sample (LaSrGaO<sub>4</sub>) is different to the LaBaGaO<sub>4</sub> sample and can be refined instead to a Tetragonal *I4/mmm* structure. The observed profile closely matches the calculated which indicates a

good fit with  $\chi^2 = 2.37$  and  $wRp = 15.0\%$ . Figure 3.11 shows the graphical fit and atomic positions can be viewed in Table 3.12.

The unit cell for  $\text{LaSrGaO}_4$  has a volume of  $187.38 \text{ \AA}^3$  and as with the  $\text{LaBaGaO}_4$  sample all sites are fully occupied. As the two structures are different and unrelated it was not expected that it would be possible to create a continual series where  $\text{LaBaGaO}_4$  becomes  $\text{LaSrGaO}_4$ , however a range of samples at 10% intervals was created to see the doping limits in both samples.

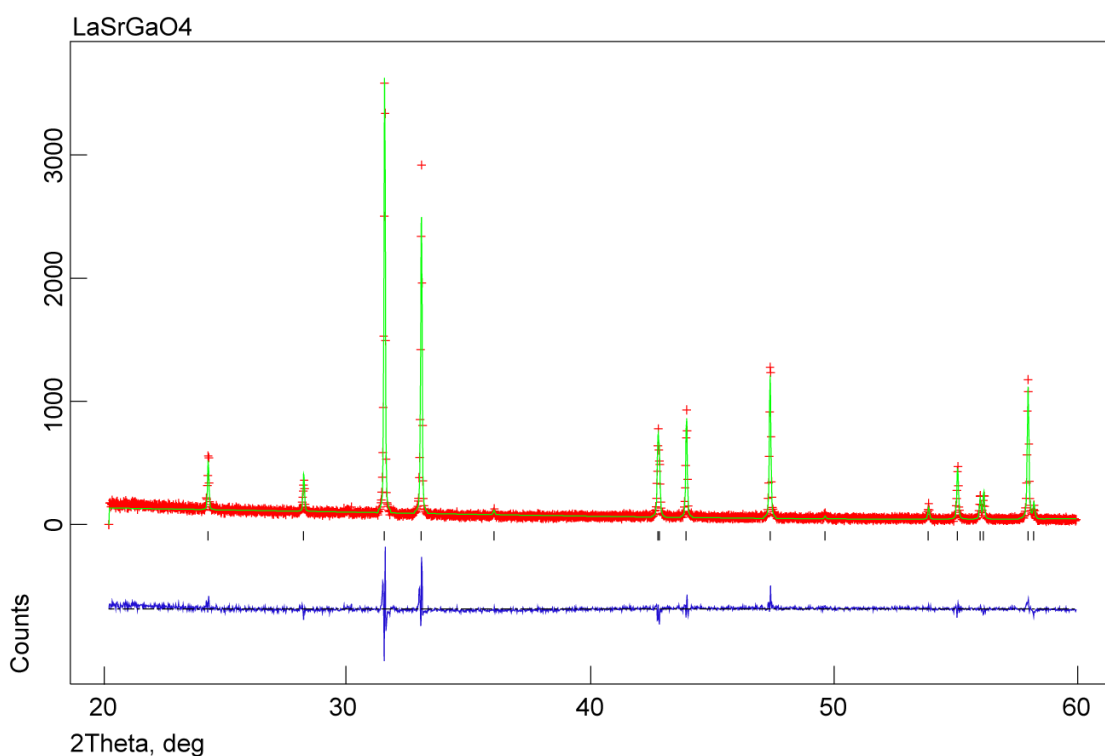


**Figure 3.11 - Refinement profile for  $\text{LaSrGaO}_4$  showing observed (red cross), calculated (green line) and difference (blue line) profiles**

Table 3.12 – Refined atomic positions in LaSrGaO<sub>4</sub> with the space group I4/mmm.

Sample	Space Group		wR <sub>p</sub>	χ <sup>2</sup>	Volume (Å <sup>3</sup> )	
LaSrGaO <sub>4</sub>	I4/mmm		15%	2.37	187.4	
<b>a (Å)</b>	3.843(1)	<b>b (Å)</b>	3.843(1)	<b>c (Å)</b>	12.689(4)	
Atomic Coordinates						
Atom	x	y	z	U <sub>i</sub> /U <sub>e</sub> *100	Multiplicity	Site Occ
Sr1	0	0	0.3592(3)	0.53(21)	4	0.5
La1	0	0	-0.3592(3)	0.53(21)	4	0.5
Ga1	0	0	0	1.19(32)	2	1
O1	½	0	0	2.4(9)	4	1
O2	0	0	0.1682(17)	2.3(8)	4	1

Table 3.13 - Cell volumes for LaBaGaO<sub>4</sub> - LaSrGaO<sub>4</sub> samples

Sample	Chi <sup>2</sup>	a (Å)	b (Å)	c (Å)	Volume (Å <sup>3</sup> )
LaBaGaO <sub>4</sub>	1.270	9.994(1)	7.255(3)	5.898(3)	427.6(2)
LaBa <sub>0.75</sub> Sr <sub>0.25</sub> GaO <sub>4</sub>	1.392	9.994(2)	7.232(2)	5.896(1)	426.1(2)
LaBa <sub>0.5</sub> Sr <sub>0.5</sub> GaO <sub>4</sub>	2.680	9.959(3)	7.226(3)	5.892(2)	424.0(2)
LaSrGaO <sub>4</sub>	2.371	3.843(1)	3.843(1)	12.689(4)	187.4(1)

Stacked XRD plots for the series of samples can be seen in Figure 3.12 and Figure 3.13; here we see that from the 10% Ba sample onwards, the doped LaSrGaO<sub>4</sub> samples display a mixed phase pattern containing both the LaSrGaO<sub>4</sub> and LaBaGaO<sub>4</sub> phases along with further unassigned peaks in the 2θ = 30° region. This shows that the I4/mmm structure of LaSrGaO<sub>4</sub> is less accommodating to substitution of barium for strontium when compared with the ability to substitute up to 50% of the barium for strontium in the LaBaGaO<sub>4</sub> samples.

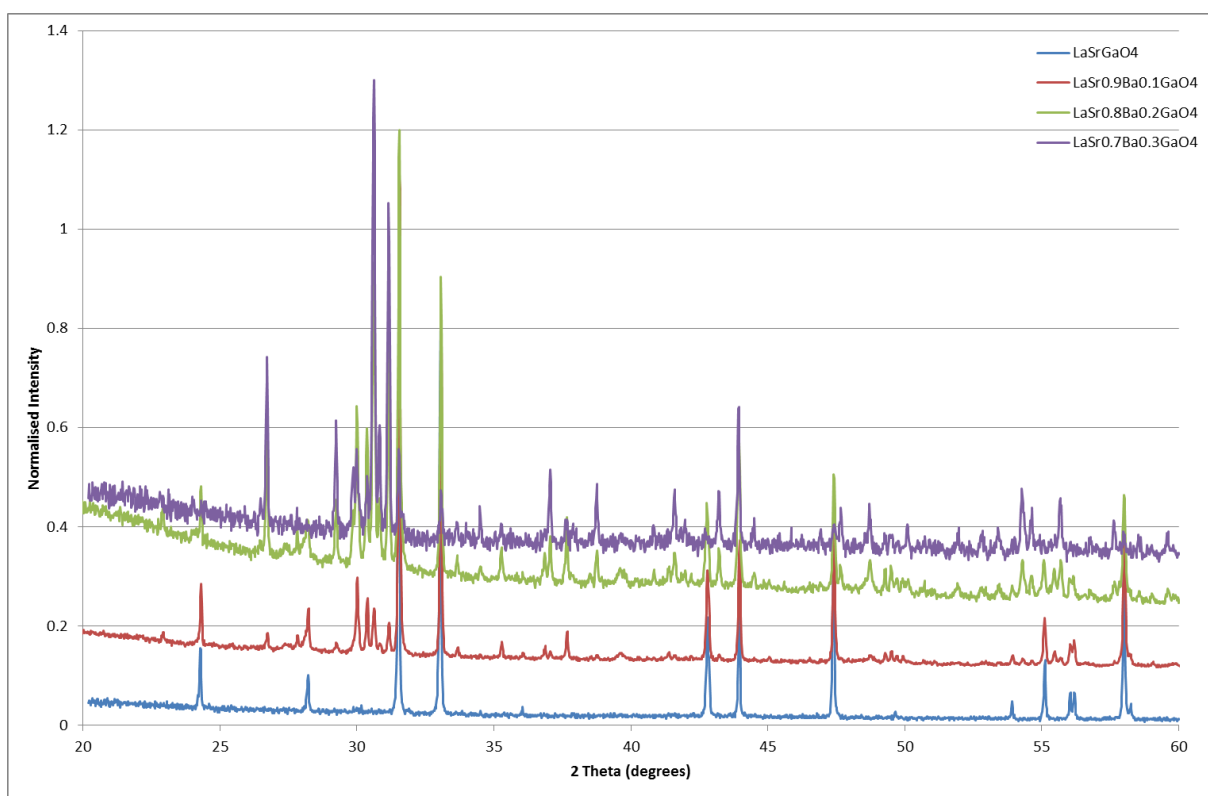


Figure 3.12 - XRD patterns for  $\text{LaSr}_{(1-x)}\text{Ba}_x\text{GaO}_4$  samples with an  $I4/mmm$  structure.

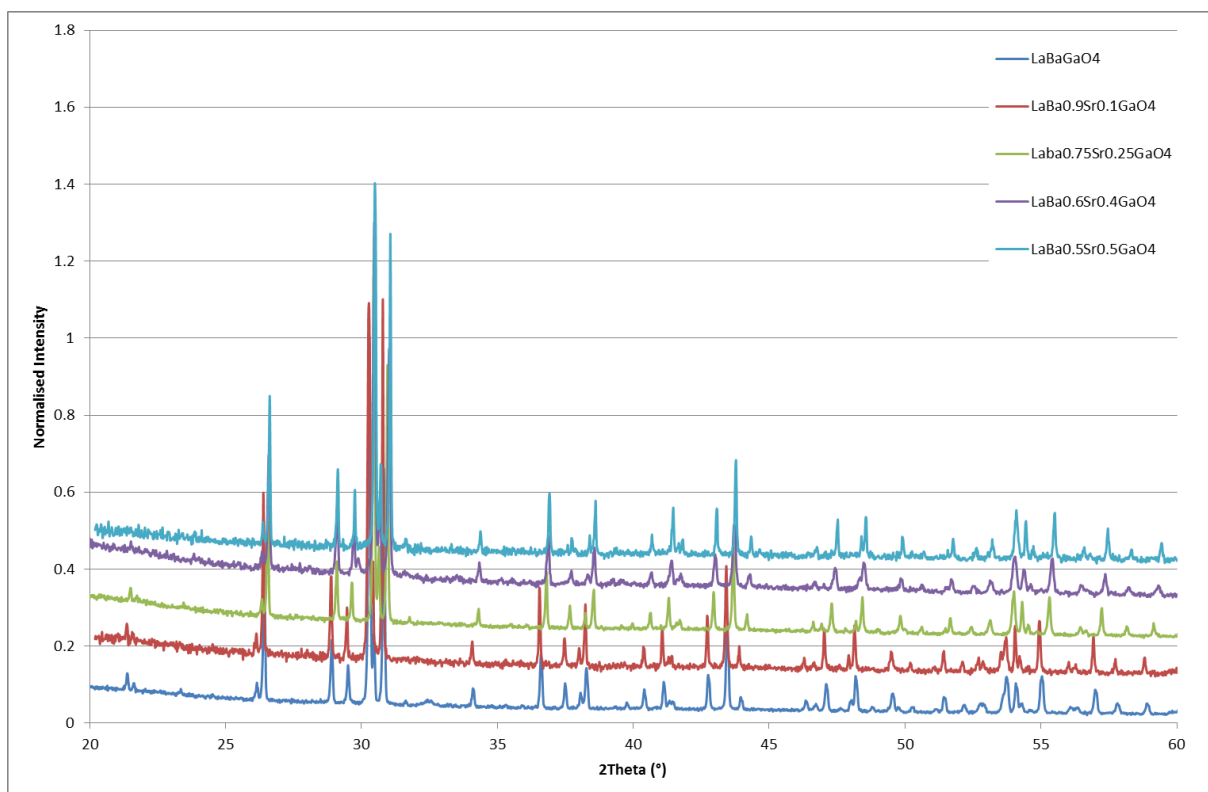


Figure 3.13 - XRD patterns for  $\text{LaBa}_{(1-x)}\text{Sr}_x\text{GaO}_4$  with a  $P2_12_12_1$  structure.

AC impedance spectroscopy measurements were performed on the  $\text{LaBaGaO}_4$ ,  $\text{LaBa}_{0.75}\text{Sr}_{0.25}\text{GaO}_4$ ,  $\text{LaBa}_{0.5}\text{Sr}_{0.5}\text{GaO}_4$  and  $\text{LaSrGaO}_4$  and conductivity values were determined. The 75% strontium sample was excluded as it is a mixed phase sample.

The  $\text{LaBaGaO}_4$  sample has the greatest conductivity across the whole temperature range studied with a conductivity of  $7.14 \times 10^{-5} \text{ S cm}^{-1}$  at  $700^\circ\text{C}$  in dry nitrogen. A decrease in conductivity was observed with an increase in strontium content with  $\text{LaSrGaO}_4$  displaying the lowest conductivity of the measured samples at  $4.57 \times 10^{-8} \text{ S cm}^{-1}$  at  $700^\circ\text{C}$  in dry nitrogen. (Figure 3.14)

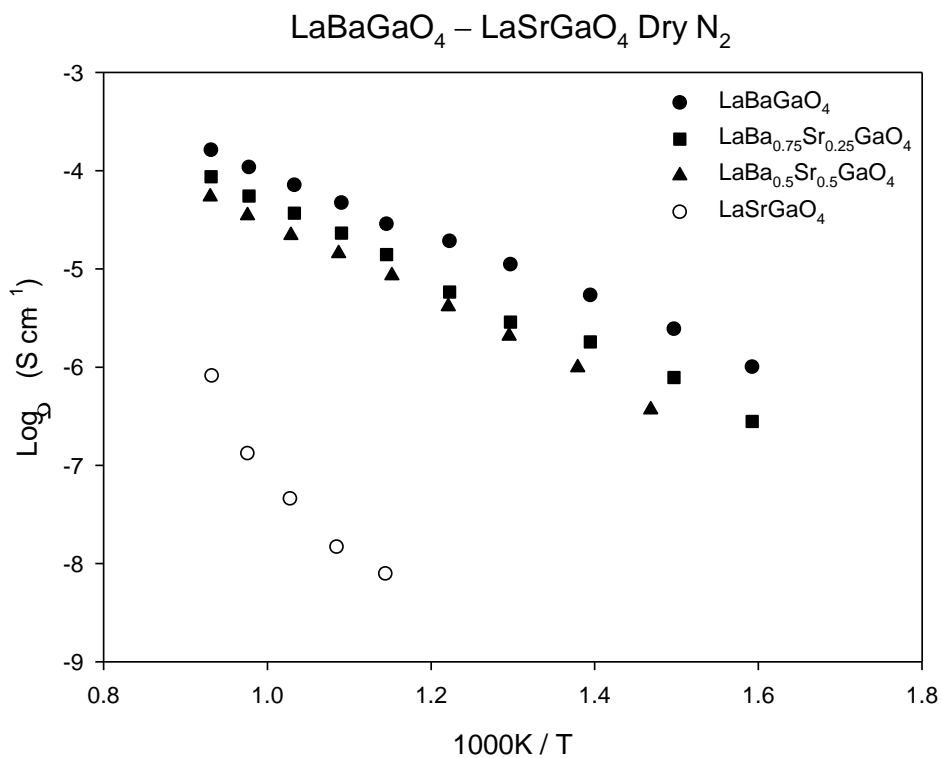


Figure 3.14 – Conductivity plots for  $\text{LaBaGaO}_4$ ,  $\text{LaBa}_{0.75}\text{Sr}_{0.25}\text{GaO}_4$ ,  $\text{LaBa}_{0.5}\text{Sr}_{0.5}\text{GaO}_4$  and  $\text{LaSrGaO}_4$ .

LaSrGaO<sub>4</sub> has a lower conductivity than would be expected if the trend in reduction with increasing strontium content was to continue which is no doubt due to the difference in structure type between LaBaGaO<sub>4</sub> (P2<sub>1</sub>2<sub>1</sub>2<sub>1</sub>) and LaSrGaO<sub>4</sub> (I4/mmm). No increase in conductivity was observed in wet nitrogen which was expected as there are negligible vacant oxygen sites to be filled by H<sub>2</sub>O molecules in the nominally fully stoichiometric samples. Conductivities and activation energies at 500°C and 700°C can be reported in Table 3.14.

**Table 3.14 - Comparison of conductivity at 700 °C and 500°C in LaBaGaO<sub>4</sub> and doping with Sr measured in a dry N<sub>2</sub> gas flow (\* indicates conductivity too low to measure)**

Sample	Conductivity 700°C (S cm <sup>-1</sup> )	Conductivity 500°C (S cm <sup>-1</sup> )	Activation energy (eV)
LaBaGaO <sub>4</sub>	7.14x10 <sup>-5</sup>	1.11x10 <sup>-5</sup>	0.712
LaBa <sub>0.75</sub> Sr <sub>0.25</sub> GaO <sub>4</sub>	3.70x10 <sup>-5</sup>	2.88x10 <sup>-6</sup>	0.806
LaBa <sub>0.5</sub> Sr <sub>0.5</sub> GaO <sub>4</sub>	2.20x10 <sup>-5</sup>	2.08x10 <sup>-6</sup>	0.859
LaSrGaO <sub>4</sub>	4.57x10 <sup>-8</sup>	*	1.913

### 3.4 LaBaAlO<sub>4</sub>

As with the LaBaGaO<sub>4</sub> structure, LaBaAlO<sub>4</sub> can be refined to an orthorhombic P2<sub>1</sub>2<sub>1</sub>2<sub>1</sub> space group the graphical fit can be seen in Figure 3.15 and the refined atomic positions are listed in Table 3.15. As expected it has a smaller unit cell than LaBaGaO<sub>4</sub> with a volume of 419.8(2) Å<sup>3</sup> due to the smaller size of aluminium compared to gallium.

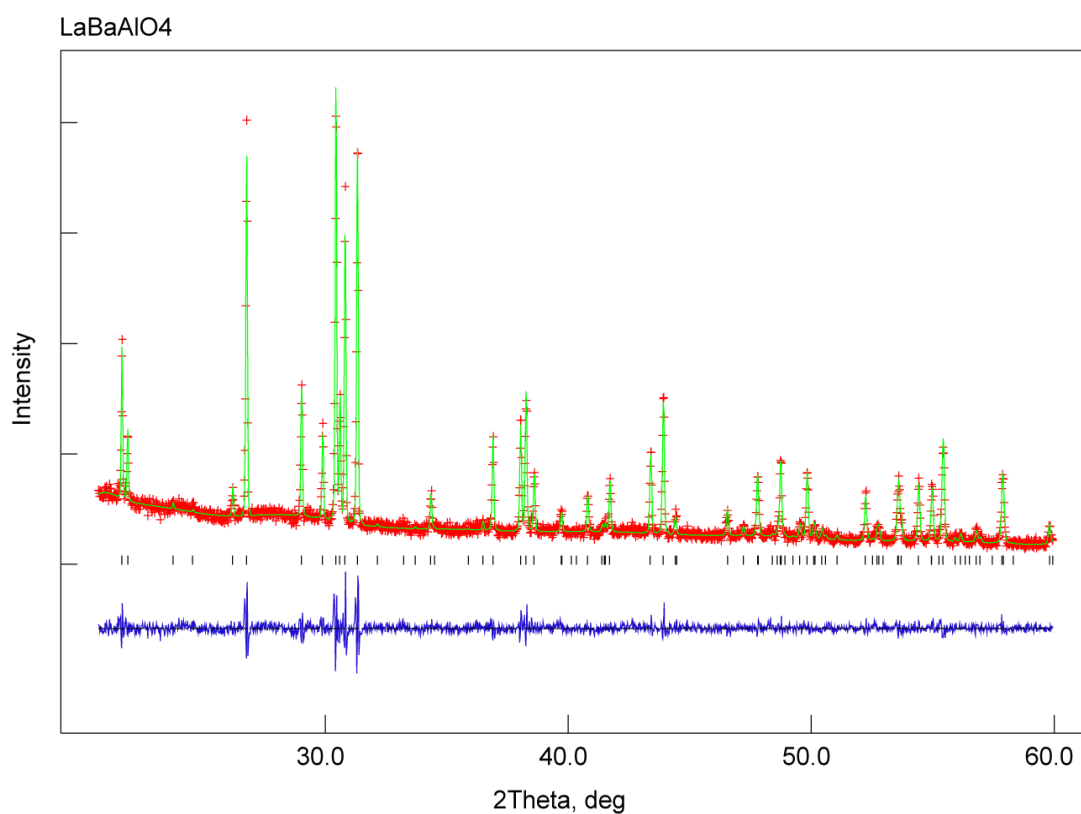


Figure 3.15 - Observed (red), Calculated (green) and difference profiles for the refinement of LaBaAlO<sub>4</sub>.

Table 3.15 - Atomic positions for LaBaAlO<sub>4</sub> refined to a P<sub>2</sub><sub>1</sub>2<sub>1</sub>2<sub>1</sub> space group.

Sample		Space Group	wRp	X <sup>2</sup>	Volume (Å <sup>3</sup> )	
LaBaAlO <sub>4</sub>		P <sub>2</sub> <sub>1</sub> 2 <sub>1</sub> 2 <sub>1</sub>	9.2%	1.78	419.8 (3)	
a (Å)	9.87(2)	b (Å)	7.28(2)	c (Å)	5.82(1)	
Atomic Coordinates						
Atom	x	y	z	U <sub>i</sub> /U <sub>e</sub> *100	Multiplicity	Site Occ
La1	0.0539(5)	0.4964(6)	0.2362(21)	1.12(14)	4	1
Ba1	2/3	1/3	0.2342(23)	0.723(18)	4	1
Al1	0.3379(30)	0.2816(29)	0.2211(34)	1.25	4	1
O1	0.1718(44)	0.1824(25)	0.2006(41)	1.41(21)	4	1
O2	0.4376(35)	0.2120(38)	0.4844(59)	1.17(12)	4	1
O3	0.3033(46)	0.4809(62)	0.3502(61)	2.45(15)	4	1
O4	0.4068(63)	0.2125(24)	0.0065(68)	1.25	4	1

Initially altering the La:Ba ratio was attempted to see if the conductivity could be improved by creating oxygen vacancies as for LaBaGaO<sub>4</sub>. A pure sample of La<sub>0.9</sub>Ba<sub>1.1</sub>AlO<sub>3.95</sub> was synthesised and found to have a unit cell volume of 418.67(3) Å<sup>3</sup> which is a slightly smaller volume than the 419.80(3) Å<sup>3</sup> recorded for the LaBaAlO<sub>4</sub> sample. Both samples were analysed using AC impedance spectroscopy measurements in both wet and dry nitrogen atmospheres. From the impedance data conductivity values were determined (Table 3.16); a very large increase of almost 3.5 orders of magnitude in conductivity can be seen for the barium enriched sample at 700°C, where LaBaAlO<sub>4</sub> has a conductivity of 1.83x10<sup>-9</sup> S cm<sup>-1</sup> compared with 3.59x10<sup>-5</sup> S cm<sup>-1</sup> for La<sub>0.9</sub>Ba<sub>1.1</sub>AlO<sub>3.95</sub>. As with the Ba<sub>2</sub>GeO<sub>4</sub> and Sr<sub>2</sub>GeO<sub>4</sub>, samples the resistance at 500°C for the LaBaAlO<sub>4</sub> sample was too high to be recorded and the conductivity therefore could not be determined (Table 3.16). A small increase in conductivity is observed when comparing the wet and dry atmospheres for the La<sub>0.9</sub>Ba<sub>1.1</sub>AlO<sub>3.95</sub> sample indicating a small contribution from protonic conductivity.

**Table 3.16 - Comparison of conductivity at 700 °C and 500°C in LaBaAlO<sub>4</sub> and La<sub>0.9</sub>Ba<sub>1.1</sub>AlO<sub>4</sub> measured in a dry N<sub>2</sub> gas flow (\* indicates conductivity too low to be measured)**

Sample	Conductivity 700°C (S cm <sup>-1</sup> )	Conductivity 500°C (S cm <sup>-1</sup> )	Activation energy (eV)
LaBaAlO <sub>4</sub>	1.827x10 <sup>-9</sup>	*	1.08
La <sub>0.9</sub> Ba <sub>1.1</sub> AlO <sub>3.95</sub>	3.586x10 <sup>-5</sup>	4.365x10 <sup>-6</sup>	0.90

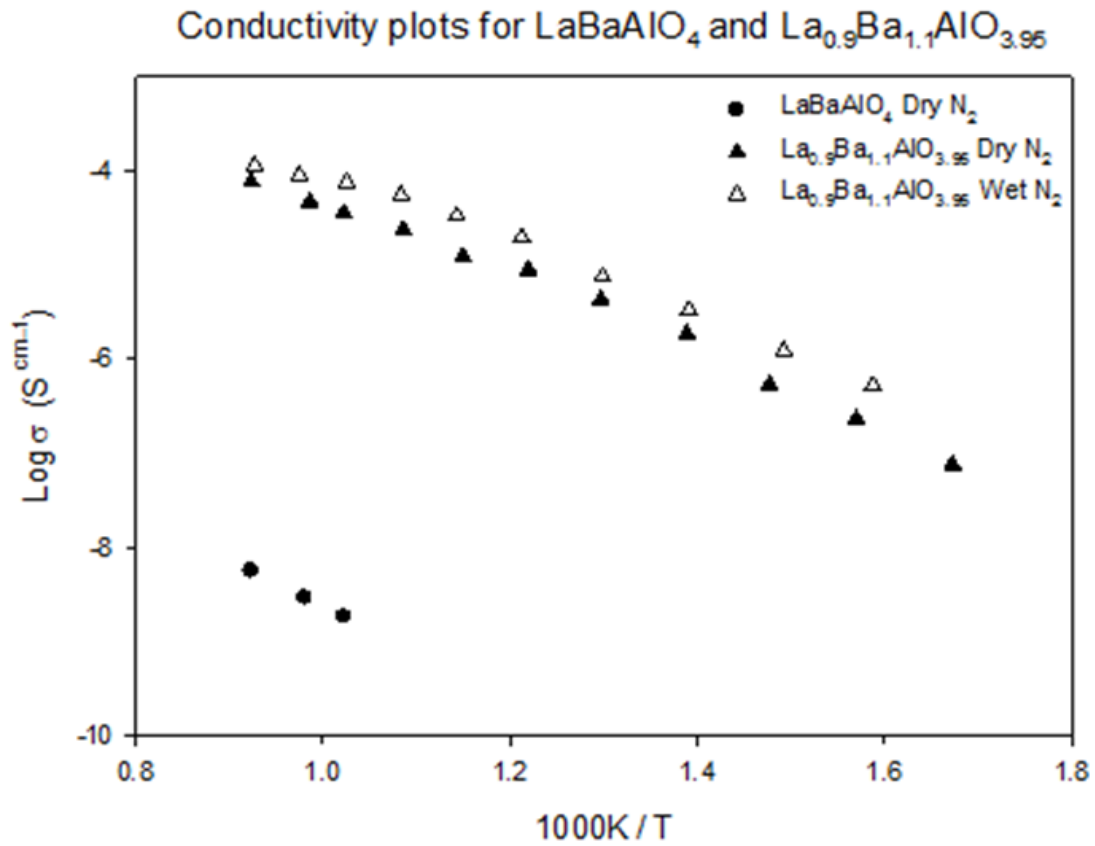


Figure 3.16 - Conductivity plots for  $\text{LaBaAlO}_4$ ,  $\text{La}_{0.9}\text{Ba}_{1.1}\text{GaO}_{3.95}$  in Dry  $\text{N}_2$

Both samples had very poor mechanical stability and were fragile when handled suggesting a poor density, which when calculated came to just 53.7% of the theoretical density for the  $\text{LaBaAlO}_4$  and 71.5% for the  $\text{La}_{0.9}\text{Ba}_{1.1}\text{AlO}_{3.95}$ . This could be one of the reasons behind the large difference in conductivity between the two samples as improved density generally results in lower resistance and therefore higher conductivity values. It was attempted to improve sintering / density via a range of different methods. Initially samples were ground in a ball mill for varying lengths of time (1 – 3 h) along with different sintering temperatures and times between 1300°C and 1550°C for between 3 and 12 h. Samples were also made with a 5% addition of cobalt or bismuth which have both been used as sintering aids previously<sup>11, 12</sup>.

However in the case of both the bismuth and cobalt containing samples it was not possible to create single phase samples eliminating the possibility of their use.

### 3.5 Conclusions

A variety of materials with tetrahedral moieties with the general formula  $A_2MO_4$  were successfully synthesised beginning initially with  $Ba/Sr_2Ge_{1-x}A_xO_{(4-x/2)}$  ( $A = Al, Ga, Zn, Mg$ ) to investigate the effect of oxygen vacancy creation on ionic conductivity. It was found that only the trivalent cation Ga and Al could be accommodated to low levels (15% Ga / 10% Al) in the Ba system and it was not possible to accommodate the divalent Zn or Mg. This suggests that the structure is possibly unable to accept larger localised changes affecting the  $MO_4$  tetrahedra but further experiments with a wider range of divalent cations would be required to confirm this. Incorporation of trivalent ions and therefore oxide ion vacancies into the structure was found to increase the oxide ion conductivity and dry conditions and protonic conductivity in humid conditions.

Conductivity increased with increasing Ga content (greater number of O vacancies) until single phase pure samples could no longer be synthesised (>15% Ga) suggesting that O vacancies play a large part in the conduction pathway.

Initial studies into  $LaBaGaO_4$  indicated that the smaller strontium ions could be incorporated in place of barium. This was increased to discover where the transition between the orthorhombic structure of  $LaBaGaO_4$  transforms into the tetragonal structure exhibited by  $LaSrGaO_4$ . A full series at 10% intervals was not possible and impurity phases could be observed in the XRD pattern beyond 50% Sr. Above 70%

Sr both the tetrahedral LaSrGaO<sub>4</sub> and orthorhombic LaBaGaO<sub>4</sub> phases along with other impurities are observed. The LaSrGaO<sub>4</sub> fails to accept 10% barium with a mixture of phases present in the resulting XRD pattern.

Accommodation of the smaller Sr<sup>2+</sup> ion in place of Ba<sup>2+</sup> had a negative effect on the ionic conductivity within the orthorhombic structure this was observed by a sharp decrease compared with the parent LaBaGaO<sub>4</sub>. Larger amounts of Sr incorporation decreased the unit cell size and conductivity further with LaSrGaO<sub>4</sub> exhibiting the lowest conductivity. This reduction in unit cell size could imply that more space within the cell could be beneficial to ionic conductivity.

As strontium has a negative effect on the parent LaBaGaO<sub>4</sub> material further experiments to introduce oxygen vacancies using substitution of Sr for La were not attempted as it was unlikely an improvement in conductivity would be seen when compared with the systems replacing La with Ba.

The final A<sub>2</sub>MO<sub>4</sub> system investigated was LaBaAlO<sub>4</sub> where oxygen vacancies were created by increasing Ba content and lowering La content. This showed an increase in ionic conductivity of four orders of magnitude although both samples had low density and mechanical strength. It is therefore possible that a portion of this increase could be due to the increase in density which would lower the grain boundary component of the resistance increasing conductivity. Sintering aids were used in an attempt to improve both density and mechanical strength but no significant increase was observed.

The conductivity of LaBaAlO<sub>4</sub> samples was lower than the related LaBaGaO<sub>4</sub> samples although if the densities of the samples could be improved this may

increase the conductivity of the LaBaAlO<sub>4</sub> samples to a similar value and further work is warranted to pass this hurdle.

### 3.6 References

1. H. Iwahara, T. Esaka, H. Uchida and N. Maeda, *Solid State Ion.*, 1981, **3-4**, 359.
2. H. Iwahara, *Solid State Ion.*, 1996, **86-8**, 9.
3. K. Amezawa, S. Kjelstrup, T. Norby and Y. Ito, *Journal of the Electrochemical Society*, 1998, **145**, 3313.
4. S. Li, F. Schonberger and P. Slater, *Chem. Commun.*, 2003, 2694.
5. F. Schonberger, E. Kendrick, M. S. Islam and P. R. Slater, *Solid State Ion.*, 2005, **176**, 2951.
6. M. Bieringer and J. E. Greedan, *J. Mater. Chem.*, 2002, **12**, 279.
7. E. Kendrick, M. S. Islam and P. R. Slater, *J. Mater. Chem.*, 2007, **17**, 3104.
8. B. H. Toby, *J. Appl. Cryst.*, 2001, **34**, 210.
9. J. Irvine, T., S., Sinclair, D., C., West A., R., *Advanced Materials*, 1990, **2**, 132.
10. F. Nishi and Y. Takeuchi, *Z. Kristall.*, 1996, **211**, 607.
11. D. P. Fagg, J. C. C. Abrantes, D. Perez-Coll, P. Nunez, V. V. Kharton and J. R. Frade, *Electrochim. Acta*, 2003, **48**, 1023.
12. P. Jaiban, A. Rachakom, S. Jiansirisomboon and A. Watcharapasorn, *Chiang Mai Journal of Science*, **38**, 527.

# 4 Water incorporation and Fluorination in Apatite Systems

---

## 4.1 Introduction

Materials with the apatite structure have the potential to be used as electrolyte materials in solid oxide fuel cells due to higher ionic conductivities at lower temperatures (600°C) than the leading YSZ and other proposed electrolytes.<sup>1</sup> The highest conductivities have been observed for silicate apatite systems with a large oxygen excess while an enhancement possibly due to proton conductivity has been observed in wet atmospheres in Ge analogues.<sup>3,2</sup> In terms of the latter, larger amounts of water can be incorporated in the germanate systems with a greater amount of water uptake observed when compared with the silicate systems.<sup>4</sup>

The incorporation of water leads both to the incorporation of protons and extra interstitial oxide ions. The latter is of interest since there have been discrepancies in the believed location of the interstitial oxygen atoms within the apatite structures. In particular for a number of silicate based systems, some groups believe that the interstitial sites are located in the centre of the channel where others believe they are located near to the  $\text{SiO}_4$  tetrahedra. This difficulty can be related to the generally low interstitial oxide ion content and the large local distortion around this interstitial oxygen.<sup>5,6,7,8</sup> The increase in interstitial oxide ion content through water incorporation may therefore aid in the determination of an accurate location. Another way of increasing the interstitial anion content would be through partial exchange of  $\text{O}^{2-}$  for  $\text{F}^-$  ( $2\text{F}^-$  replace 1  $\text{O}^{2-}$ )

In this chapter the aim is therefore to investigate the location of the interstitial atoms by hydrating and fluorinating fully stoichiometric systems ( $\text{La}_8\text{Sr}_2(\text{Ge/Si})_6\text{O}_{26}$ ) with no interstitial atoms, which will introduce interstitial atoms to be located using neutron diffraction.

## 4.2 Germanate apatites

### 4.2.1 Experimental

Stoichiometric mixtures of high purity lanthanum (III) oxide ( $\text{La}_2\text{O}_3$ ), germanium (IV) oxide ( $\text{GeO}_2$ ) and strontium carbonate ( $\text{SrCO}_3$ ) were ground together and heated to  $1100^\circ\text{C}$  for 12 h. Samples were then re ground and reheated for a second time at  $1100^\circ\text{C}$  for a further 12 h. Following this the samples were mechanically ground in a Fritsch Pulverisette planetary ball mill at 350 rpm for 1 h and pressed into 8 mm, 10 mm or 13 mm diameter pellets at pressures between 300 and  $4000\text{ kg cm}^{-2}$ . The pellets were then sintered at  $1300^\circ\text{C}$  for 6 h.

Powder X-ray diffraction was used to check phase purity of the samples using a Bruker D8 diffractometer with  $\text{Cu K}\alpha_1$  radiation. Rietveld refinement was used for structure determination using either the GSAS suite of programs or Topas v4.2.

### 4.3 $\text{La}_8\text{Sr}_2\text{Ge}_6\text{O}_{26}$

Fully stoichiometric  $\text{La}_8\text{Sr}_2\text{Ge}_6\text{O}_{26}$  was chosen first as it contains no interstitial atoms and previous work has shown Ge systems to have the largest water incorporation.<sup>2</sup> A starting point with no interstitial atoms meant that once interstitial oxygen/fluorine

atoms are added the location of the interstitial sites could be determined without interference from sites that were initially present in the undoped system.

### 4.3.1 Structure

Rietveld refinement was initially performed using powder X-ray diffraction data for  $\text{La}_8\text{Sr}_2\text{Ge}_6\text{O}_{26}$  and the structure was refined with a hexagonal P63/m space group. The resulting structural information extracted from the Rietveld refinement is shown in Table 4.1 and the observed, calculated and difference profiles are shown in Figure 4.1.

Table 4.1 - Structural data from Rietveld refinement of  $\text{La}_8\text{Sr}_2\text{Ge}_6\text{O}_{26}$

Sample name	Space Group	$\chi^2$	wRp	Volume ( $\text{\AA}^3$ )	Theoretical density ( $\text{g cm}^{-3}$ )	
$\text{La}_8\text{Sr}_2\text{Ge}_6\text{O}_{26}$	P63/m	1.77	5.9%	622.68	5.76	
<b>a</b> ( $\text{\AA}$ )	9.91	<b>b</b> ( $\text{\AA}$ )	9.91	<b>c</b> ( $\text{\AA}$ )	7.32	
Atomic Positions						
Atom	X	Y	Z	Ui/Ue*100	Multiplicity	Fraction
<b>La1</b>	1/3	2/3	0.0007(2)	1.133(8)	4	0.5
<b>Sr1</b>	1/3	2/3	0.0007(2)	1.133(8)	4	0.5
<b>La2</b>	0.2308(3)	0.9897(4)	1/4	1.961(7)	6	1
<b>Ge1</b>	0.4002(5)	0.3718(5)	1/4	1.582(11)	6	1
<b>O1</b>	0.3152(22)	0.4879(21)	1/4	1.681(12)	6	1
<b>O2</b>	0.5986(23)	0.4756(18)	1/4	1.738(12)	6	1
<b>O3</b>	0.3405(31)	0.2495(14)	0.0653(16)	2.735(15)	12	1
<b>O4</b>	0	0	0.2177(41)	1.610(11)	6	0.5

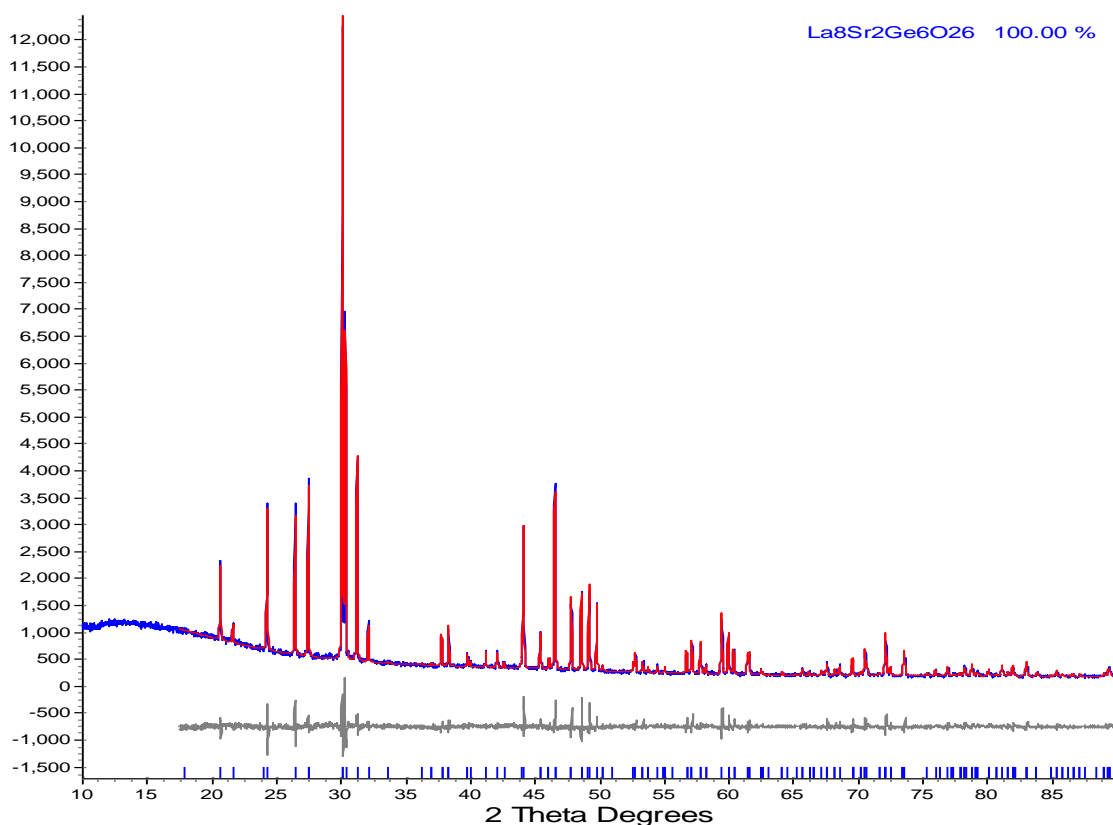


Figure 4.1 - Observed (blue), Calculated (red) and difference (grey) profiles for Rietveld refinement of  $\text{La}_8\text{Sr}_2\text{Ge}_6\text{O}_{26}$

### 4.3.2 Hydration

A sample of  $\text{La}_8\text{Sr}_2\text{Ge}_6\text{O}_{26}$  was placed in a furnace which was heated to  $600^\circ\text{C}$  and slow cooled in a wet  $\text{N}_2$  atmosphere. This slow cooling in a wet atmosphere allowed for water to be incorporated into the structure expanding the unit cell. Rietveld refinement suggests a cell expansion to a volume of  $626.62 \text{ \AA}^3$  which is  $3.94 \text{ \AA}^3$  larger than the dry sample although it was not possible to locate the interstitial water molecules with x-ray diffraction. Thermo gravimetric analysis suggests a total of 0.63% wt/wt water was incorporated into the sample which when the formula mass of the apatite is taken into consideration results in an incorporation of 0.84 mol of water

per stoichiometric formula of sample. These preliminary results allowed for a successful application to use the in-situ hydration cell on the high resolution powder diffractometer (HRPD) beam line at the ISIS neutron source.

#### **4.3.2.1 In-Situ Hydration / Neutron diffraction**

In situ neutron diffraction and hydration experiments were carried out on HRPD at ISIS using custom made apparatus. The sample sat on a glass frit within a silica tube which was within another silica tube which could be evacuated, whilst the inner tube could have a gas flowing through it. The silica tubes were lowered into a furnace that has vanadium windows. Vanadium was used as the material for the furnace windows and heating elements because vanadium has very little absorption or scattering of neutrons. Diffraction peaks from vanadium can easily be subtracted from the resulting diffraction pattern as it is also a simple structure. All aspects of the sample environment (excluding the inner silica tube) were kept under vacuum for the experiment as air has a large scattering effect of neutrons resulting in a lower number interacting with the sample or detectors. A diagram of the equipment used can be seen in Figure 4.2.<sup>10</sup>

The gas flow to the inner silica tube in this experiment was pure argon which was transferred using pipes heated to 100°C; this was to ensure that the carrier gas was exactly the same for both the wet and dry atmosphere experiments. For the “wet” atmosphere experiment, the argon gas was re directed and bubbled through a tank of D<sub>2</sub>O, which was heated to 70°C and resulted in some of the heavy water being carried by the argon gas. The heated pipes then ensured the water vapour didn’t

condense and was carried all the way to the sample. D<sub>2</sub>O was used in these experiments because H has large incoherent scattering cross section which results in a large background interference and a poorer signal to noise ratio for the other signals. D on the other hand has a very low incoherent scattering and a good level of coherent scattering which results in a much lower background interference.

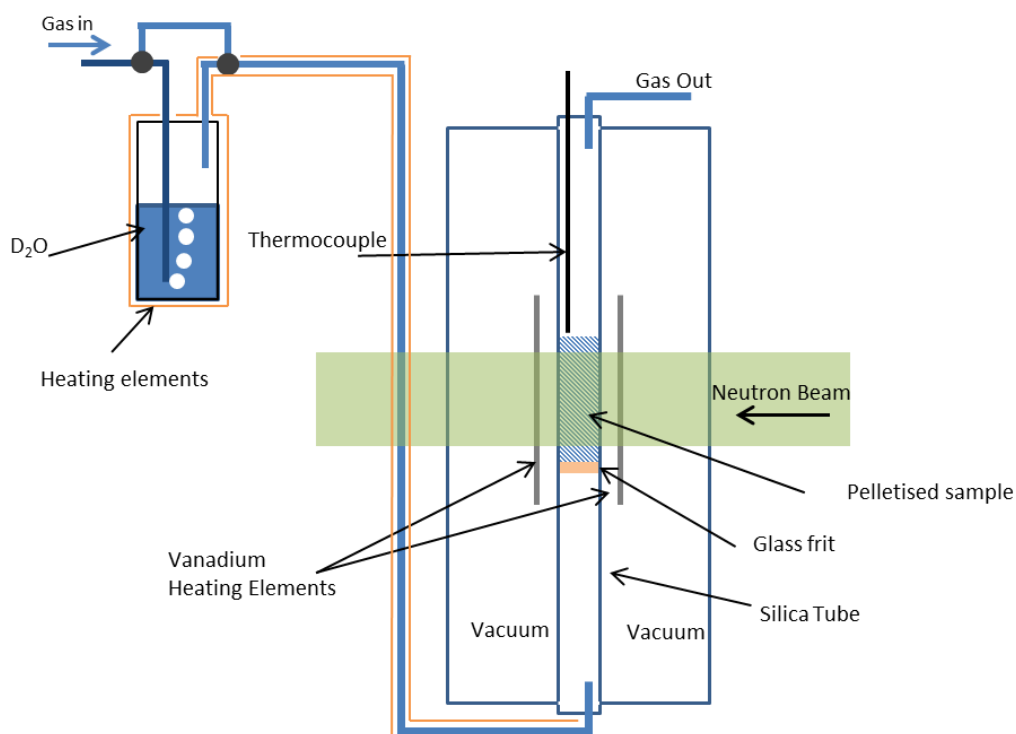


**Figure 4.2 - Diagram of ISIS Hydration cell**

In total, 18 g of,  $\text{La}_8\text{Sr}_2\text{Ge}_6\text{O}_{26}$  was prepared and this was pressed into a stack of 8mm pellets at a pressure of  $450 \text{ kg cm}^{-2}$  and sintered at  $1300^\circ\text{C}$  for 6 h. This resulted in a stack of pellets approximately 40 mm high. The beam at ISIS only has a height of 10 mm but as it was not possible to see the exact position of the sample once it was loaded into the furnace it was decided to use a large stack of pellets to ensure the entire beam was used for the best scattering results.

Rietveld analysis was initially performed on the data collected at room temperature with a dry atmosphere. The neutron diffraction pattern has a slightly unusual undulating background, which is due to scattering by the silica tubes which allow gas flow.

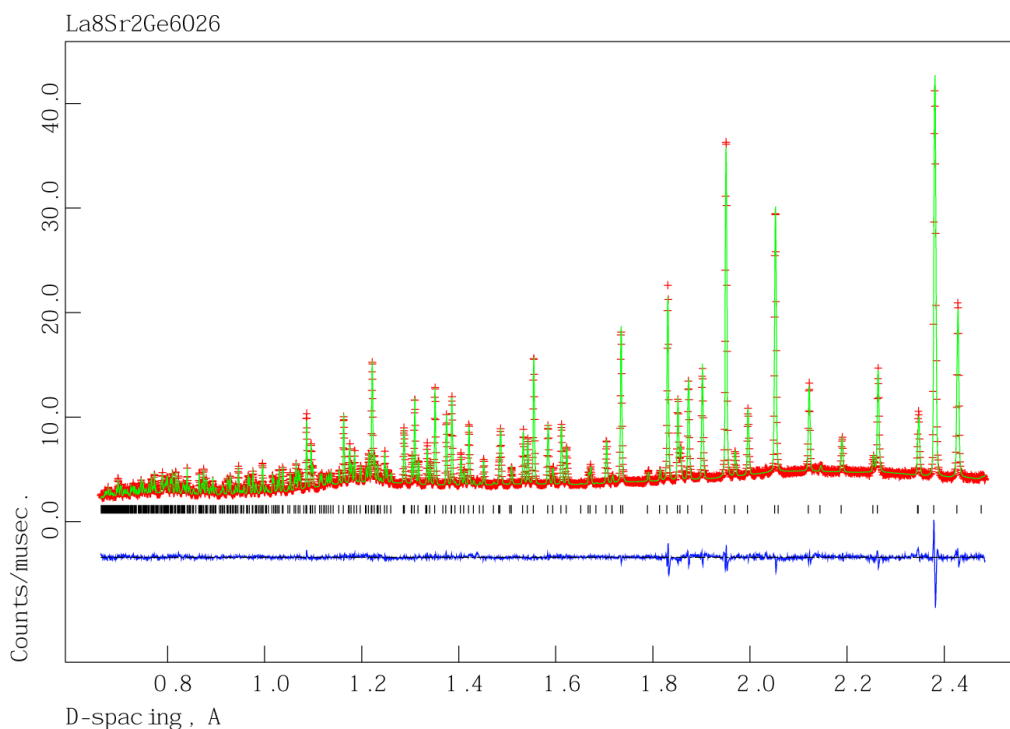


**Figure 4.3 - Observed (red), Calculated (green) and difference (blue) profiles for the room temperature neutron refinement of La<sub>8</sub>Sr<sub>2</sub>Ge<sub>6</sub>O<sub>26</sub>.**

The unit cell from the XRD refinement of La<sub>8</sub>Sr<sub>2</sub>Ge<sub>6</sub>O<sub>26</sub> was used as a starting point for the neutron refinement as the changes are very minor, the most notable change is that O3 and O4 thermal parameters have now been refined as anisotropic rather than isotropic. Minor changes to fractional coordinates and thermal parameters can also be seen in the atomic coordinates table (Table 4.2), and a graphical representation of the fit can be seen in Figure 4.3. The background contains two large broad humps

which are due to the silica from the glass tubes which contained the sample for the experiment.

**Table 4.2 - Structural data from Rietveld refinement of neutron diffraction of  $\text{La}_8\text{Sr}_2\text{Ge}_6\text{O}_{26}$**

Sample	Space Group	$\chi^2$	wRp	Volume ( $\text{\AA}^3$ )	Theoretical density ( $\text{g cm}^{-3}$ )	
$\text{La}_8\text{Sr}_2\text{Ge}_6\text{O}_{26}$ _RT	P63/m	4.67	2.1%	622.68	5.761	
<b>a</b> ( $\text{\AA}$ )	9.910(1)	<b>b</b> ( $\text{\AA}$ )	9.910(1)	<b>c</b> ( $\text{\AA}$ )	7.321(2)	
Atomic Positions						
Atom	X	Y	Z	Ui/Ue*100	Multiplicity	Fraction
<b>La1</b>	1/3	2/3	0.0012(2)	1.419(33)	4	0.5
<b>Sr1</b>	1/3	2/3	0.0012(2)	1.419(33)	4	0.5
<b>La2</b>	0.2312(1)	0.9897(2)	$\frac{1}{4}$	1.044(24)	6	1
<b>Ge1</b>	0.3994(1)	0.3719(1)	$\frac{1}{4}$	1.088(24)	6	1
<b>O1</b>	0.3116(2)	0.4862(2)	$\frac{1}{4}$	1.82(4)	6	1
<b>O2</b>	0.6014(2)	0.4743(2)	$\frac{1}{4}$	1.65(4)	6	1
<b>O3</b>	0.3394(1)	0.2465(1)	0.0622(1)	2.41*	12	1
<b>O4</b>	0	0	$\frac{1}{4}$	3.57*	2	1
Anisotropic Thermal Parameters						
Atom	U11	U22	U33	U12	U13	U23
<b>O1</b>	1.82(4)	1.82	1.82	0	0	0
<b>O2</b>	1.65(4)	1.65	1.65	0	0	0
<b>O3</b>	4.75(9)	1.92(7)	1.61(6)	1.80(6)	-0.70(6)	-0.78(5)
<b>O4</b>	1.26(10)	1.26(10)	8.17(27)	0.63(5)	0	0

The temperature was then increased to 800°C and diffraction patterns were recorded at 25°C intervals between 100°C and 800°C. Once a pattern for 800°C was obtained the atmosphere was changed from dry to wet and the sample was left for 1 h, although it was not expected any water would be incorporated at this temperature. The temperature was then lowered to 100°C in 50°C steps (fewer steps than the heating run due to instability in the beam and access time pressures). Samples were left for 45 min before data collection to allow for water to be incorporated. The experiment was completed with dry heating and wet cooling because it was expected

that there would be better kinetics of hydration and the sample would hydrate faster with cooling from a higher temperature than it would if we were to start at 100°C and increase the temperature.

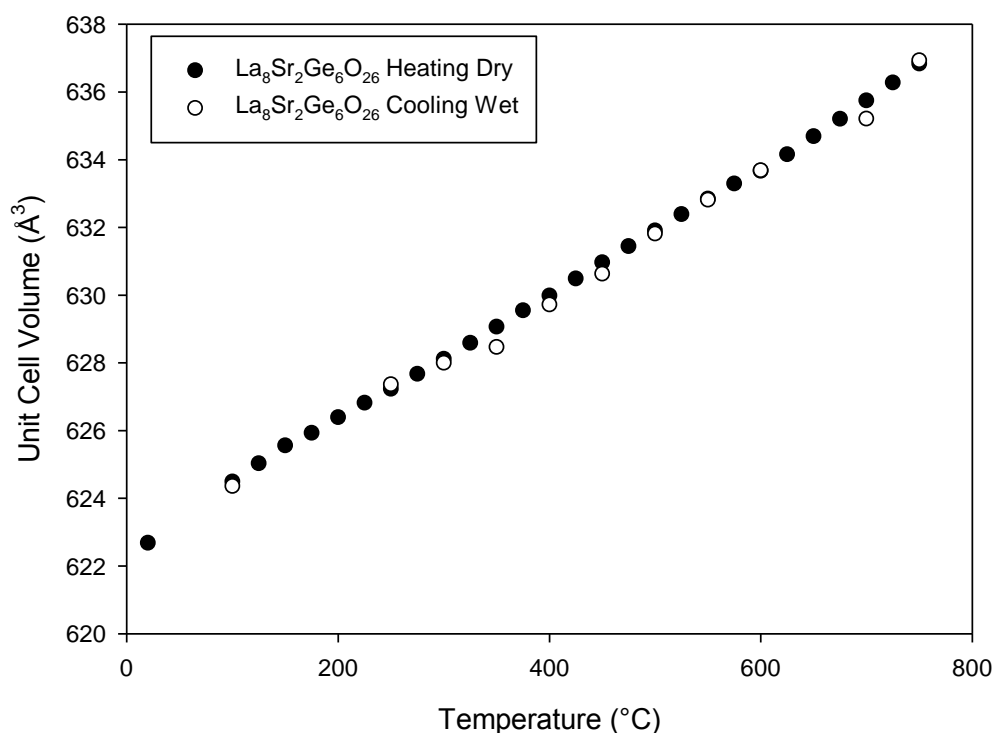


**Figure 4.4 - Unit cell volume of  $\text{La}_8\text{Sr}_2\text{Ge}_6\text{O}_{26}$  upon heating and cooling in dry and wet atmospheres.**

At each step the resulting diffraction pattern was analysed and the unit cell volumes were compared as an indication of water incorporation. On heating in a dry atmosphere a linear thermal expansion was observed as the temperature increased. Unfortunately, on cooling in a wet atmosphere the unit cell contracted in the reverse of the expansion seen on heating, (Figure 4.4). A comparison between the dry and wet heat treatments showed some unusual variations for the wet heat treatment. In this case it was expected that larger cell volumes would result due to water

incorporation, but in contrast some of the values were lower, the origin of which is not known.

Overall however, it appeared as if negligible water incorporation was achieved. The most likely conclusion as to why water incorporation was not observed in this neutron diffraction experiment is due to the difference in sample preparation, as in the lab samples were hydrated as loose powder form than pellets, and the latter might be expected to considerably slow down the rate of hydration. These slower reaction kinetics mean the sample would have had to be left in the wet gas flow for much longer and for time that was not available on the in situ hydration equipment.

#### **4.3.2.2 Hydrothermal treatment**

As the in-situ hydration experiment was unsuccessful pre-hydration of a powder sample was then performed before conducting neutron diffraction experiments. Hydrothermal treatment of the sample was chosen as it gives the highest level of hydration due to the higher partial pressure of water the sample is exposed to. Hydrothermal treatment also exposes the sample to much more extreme conditions than a wet flowing gas in a furnace, which results in much faster reaction times. XRD and TGA both show incorporation of water into the sample to higher levels than the flowing gas method. The sample was analysed on the POLARIS diffractometer. POLARIS differs from HRPD as it has a higher beam current, but lower resolution due to a much shorter wave guide. A diffraction pattern was taken at room temperature with the sample held within a vanadium can. In this case the sample

was hydrated with H<sub>2</sub>O rather than D<sub>2</sub>O which resulted in higher background with neutron diffraction although it was still possible to complete a structural refinement and locate interstitial oxide ions.

A graphical representation of the ND data fit can be seen in Figure 4.5 and the atomic positions and structural data extracted from the refinement can be seen in Table 4.3.

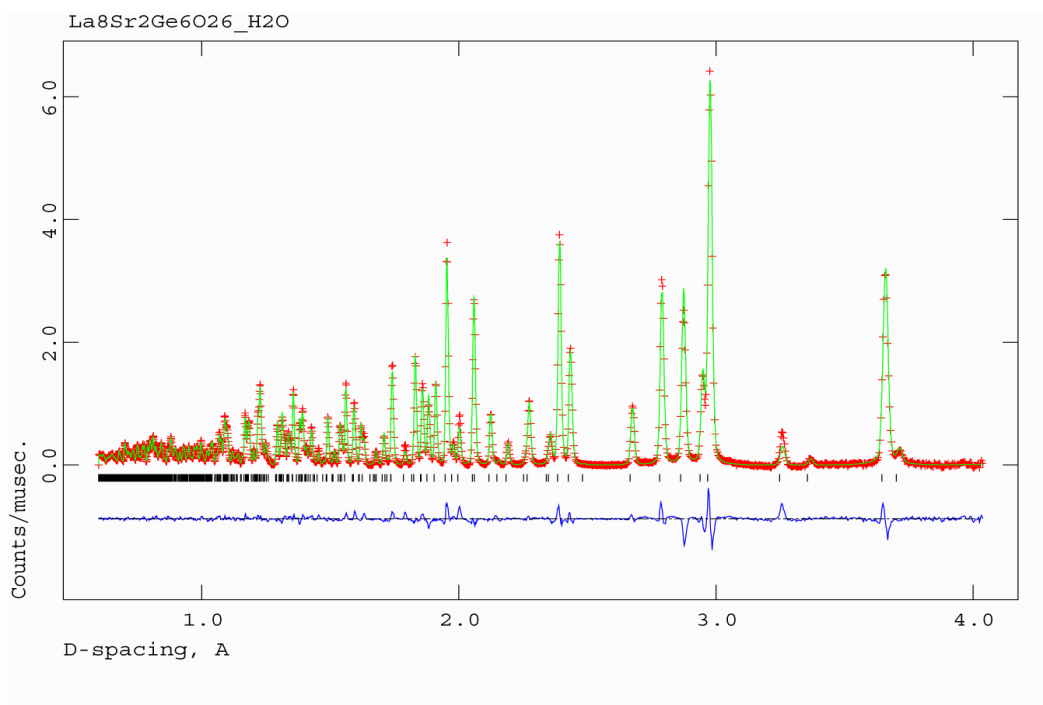


**Figure 4.5 - Rietveld refinement plot for Hydrated La<sub>8</sub>Sr<sub>2</sub>Ge<sub>6</sub>O<sub>26</sub>, the observed profile is indicated by red crosses, calculated green line and difference profile blue line**

The structural refinement data (Table 4.3) shows the interstitial oxide ions are located at two sites, O<sub>i</sub> which is part of a GeO<sub>5</sub> polyhedra and O<sub>ii</sub> which is in the channel, although site O<sub>i</sub> contains a larger level of oxide ions than the channel O<sub>ii</sub> site. The positions for the cations are approximately the same as they are in the dry

sample except for slight changes due to an expansion in the unit cell caused by water incorporation. The oxide ions show a greater displacement in particular O3 which has moved to incorporate the interstitial oxygen atom by expansion of the GeO<sub>4</sub> tetrahedra to GeO<sub>5</sub> polyhedra. There has also been movement in the channel oxygen (O4) as a small amount of the incorporated water (Oii) is located in the centre of the channel.

**Table 4.3 - Atomic position data for hydrated La<sub>8</sub>Sr<sub>2</sub>Ge<sub>6</sub>O<sub>26</sub> from neutron diffraction on POLARIS (\*indicates anisotropic thermal parameters were used)**

Sample	Space Group	$\chi^2$	wRp	Volume (Å <sup>3</sup> )	Theoretical density (g cm <sup>-3</sup> )	
La <sub>8</sub> Sr <sub>2</sub> Ge <sub>6</sub> O <sub>26</sub> 26_H <sub>2</sub> O	P63/m	6.99	2.4%	627.65	5.757	
<b>a (Å)</b>	9.953(7)	<b>b (Å)</b>	9.953(7)	<b>c (Å)</b>	7.317(6)	
Atomic Positions						
Name	X	Y	Z	U <sub>i</sub> /U <sub>e</sub> *100	Multiplicity	Fraction
<b>La1</b>	1/3	2/3	-0.0004(5)	1.03(7)	4	0.5
<b>Sr1</b>	1/3	2/3	-0.0004(5)	1.03(7)	4	0.5
<b>La2</b>	0.2352(2)	0.9904(3)	1/4	0.83(6)	6	1
<b>Ge1</b>	0.3997(2)	0.3738(2)	1/4	0.45(5)	6	1
<b>O1</b>	0.3117(4)	0.4854(4)	1/4	1.27(8)	6	1
<b>O2</b>	0.6030(4)	0.4767(4)	1/4	1.73(9)	6	1
<b>O3</b>	0.3434(4)	0.2502(4)	0.0623(3)	2.73*	12	1
<b>O4</b>	0	0	-0.325(4)	5.15(58)	4	0.576(37)
<b>Oi</b>	0.083(13)	0.434(13)	-0.018(15)	2.55*	12	0.056(7)
<b>Oii</b>	0	0	-0.690(76)	2.52*	4	0.01
Anisotropic Thermal Parameters						
Atom	U <sub>11</sub>	U <sub>22</sub>	U <sub>33</sub>	U <sub>12</sub>	U <sub>13</sub>	U <sub>23</sub>
<b>O1</b>	1.27(8)	1.27	1.27	0	0	0
<b>O2</b>	1.73(9)	1.73	1.73	0	0	0
<b>O3</b>	6.14(25)	2.64(17)	1.30(11)	2.82(18)	-2.41(12)	-1.33(12)
<b>O4</b>	5.15(58)	5.15	5.15	0	0	0
<b>Oi</b>	2.53	2.53	2.53	1.27	0	0
<b>Oii</b>	2.5	2.5	2.5	1.25	0	0

It was not possible to locate the  $H^+$  positions, most likely due to the large spread of potential sites, and the rapid interchange of  $H^+$  between oxide ions due to H bonding interactions. In this respect, lower temperature (e.g. 4K) measurements would be required to freeze out this motion.

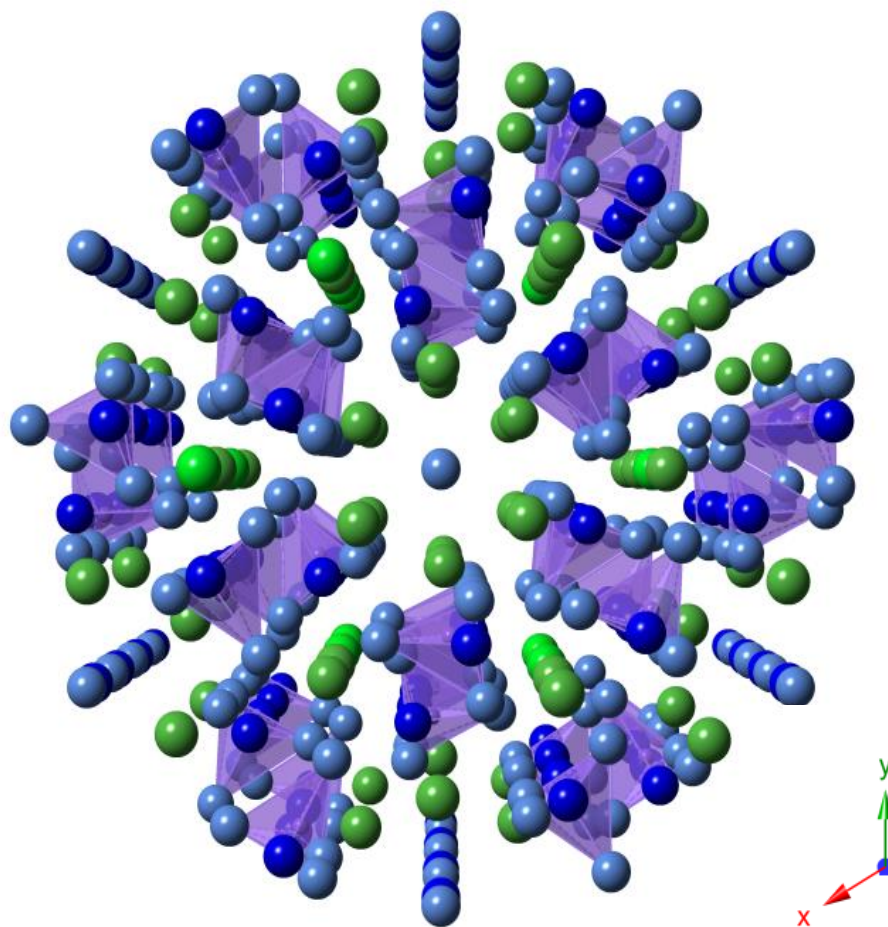
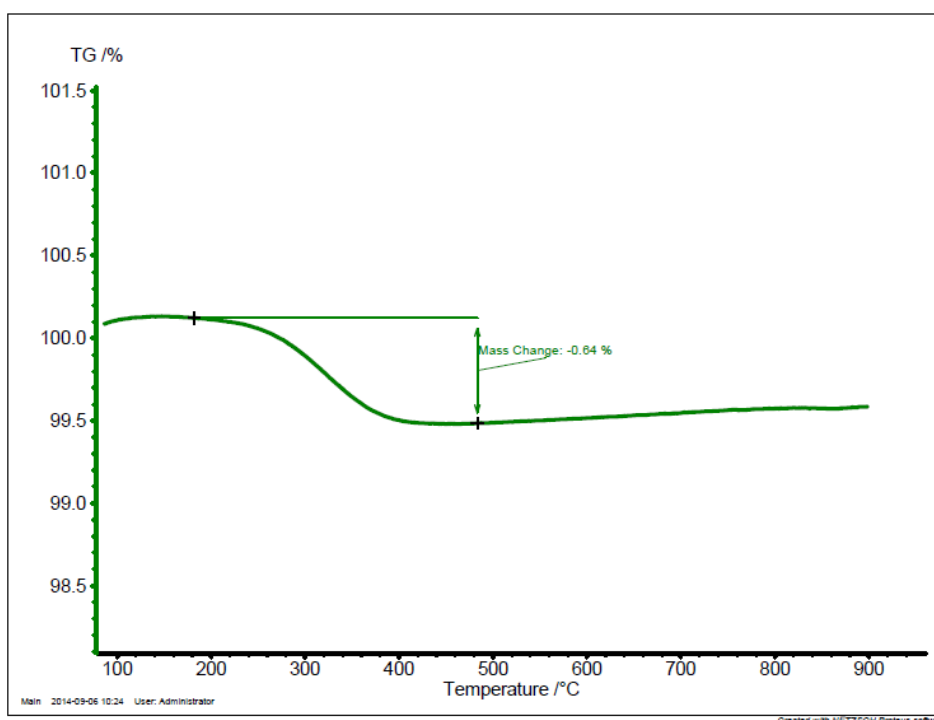


Figure 4.6 - Structure of Hydrated  $La_8Sr_2Ge_6O_{26}$ , La/Sr are green, Ge purple, O are shown in blue, darker blue are due to interstitial oxygen atoms

Figure 4.6 shows the structure of hydrated  $La_8Sr_2Ge_6O_{26}$  with interstitial oxygen atoms shown in a darker blue than the original oxygen atoms. These can be seen around the Ge atoms forming a  $GeO_5$  group. The second interstitial site is in the centre of the channel directly behind the channel oxide ion O4.

Quantification of the H<sub>2</sub>O present was carried out using TGA in nitrogen gas over a temperature range between 30°C and 900°C at a heating rate of 10°C min<sup>-1</sup>. The TGA plot (Figure 4.7) shows a mass loss of 0.64% at approximately 300°C which is due to the loss of water from the sample as verified by mass spectrometry( m/z = 18 peak observed). This mass loss relates to 0.84 moles of water per mole of La<sub>8</sub>Sr<sub>2</sub>Ge<sub>6</sub>O<sub>26</sub>.



**Figure 4.7 - TGA analysis of hydrated La<sub>8</sub>Sr<sub>2</sub>Ge<sub>6</sub>O<sub>26</sub> in a nitrogen atmosphere between 30°C and 900°C.**

### 4.3.3 Fluorination

Another potential strategy for increasing the interstitial anion content is through fluorination. In this case a substitution process involving 2xF<sup>-</sup> replacing 1xO<sup>2-</sup> occurs. La<sub>8</sub>Sr<sub>2</sub>Ge<sub>6</sub>O<sub>26</sub> was fluorinated by heating to either 360°C (PVDF) or 400°C (PTFE) for

72 h in a 1:1 molar ratio with PVDF ( $\text{CH}_2\text{CF}_2$ ) or PTFE ( $\text{CF}_2\text{CF}_2$ ). As PTFE contains more fluorine per polymer repeat unit it was expected that a higher level of fluorination would be obtained by the use of PTFE.

#### 4.3.3.1 PVDF

The sample heated with PVDF was analysed by XRD and shows no additional crystalline phases but a slight expansion in the unit cell was visible. This implies that a portion of the oxygen within the structure has been replaced with fluorine, and to test this TGA was performed. TGA shows a loss of 0.24% which relates to 0.23 moles  $\text{F}_2$  (0.46 moles  $\text{F}^-$ ) per mole of  $\text{La}_8\text{Sr}_2\text{Ge}_6\text{O}_{26}$ ; as each oxygen ion replaced requires an additional  $\text{F}^-$  ion for charge balancing this relates to an increase in interstitial ions by 0.23 per formula unit. Fluorine loss was confirmed by mass spectrometry.

As there is only a small difference in neutron scattering lengths between oxygen (5.80) and fluorine (5.65), it is not possible to accurately determine which site is occupied by  $\text{O}^{2-}$  and which by  $\text{F}^-$ , however the increased anion content would allow the identification of the interstitial sites. The sample was therefore examined on the POLARIS diffractometer at ISIS.

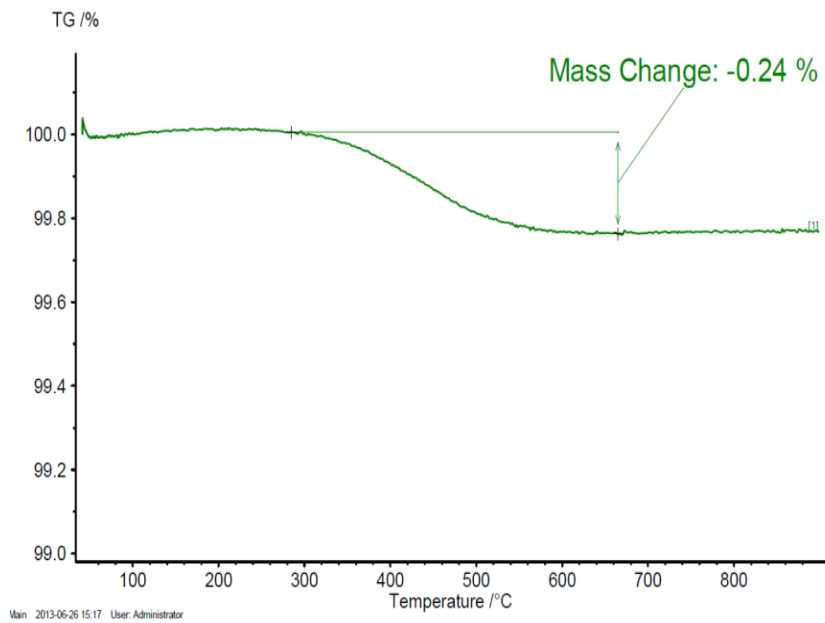


**Figure 4.8 - TGA mass trace for  $\text{La}_8\text{Sr}_2\text{Ge}_6\text{O}_{26}$  after treatment with PVDF.**

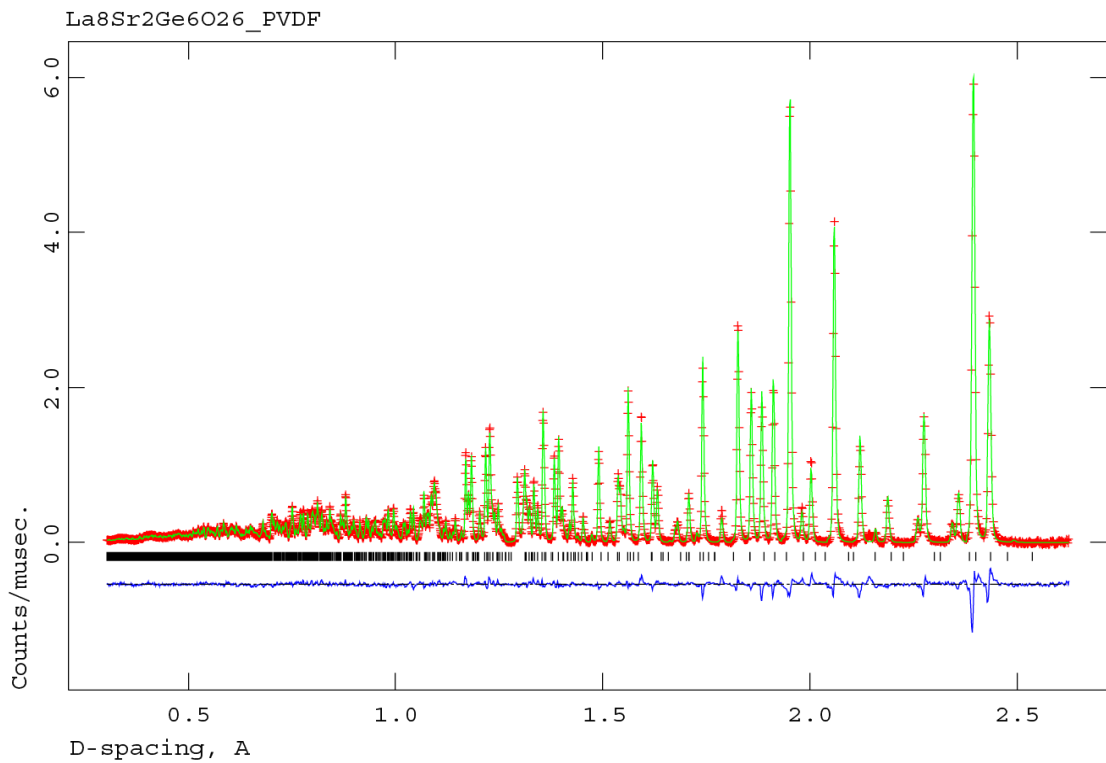


**Figure 4.9 - Observed (Red), Calculated (Green) and Difference (Blue) profiles for Neutron refinement of  $\text{La}_8\text{Sr}_2\text{Ge}_6\text{O}_{26}$  treated with PVDF**

A good fit between calculated and observed profiles can be seen for the Rietveld refinement of neutron diffraction data (Figure 4.9). The structure was refined to the same P63/m hexagonal space group as the as prepared sample. The refinement located the interstitial sites within the channels albeit displaced from the centre at the position, 0.1057(14), 0.0033(13), 0.5468(15); the other atomic positions have only moved slightly to accommodate the expansion in the cell and extra atoms in the channel atom O4 has moved from the special z position at 0.5 to 0.3167(8). Atomic positions and thermal parameters can be seen in Table 4.4. In addition the thermal parameter for the O4 oxygen is high, suggesting a range of local displacements for this site, most likely related to the presence of interstitial anions.

**Table 4.4 - Atomic positions and thermal parameters for  $\text{La}_8\text{Sr}_2\text{Ge}_6\text{O}_{26}$  reacted with PVDF (\* indicates anisotropic thermal parameters were used).**

Sample		Space Group		$\chi^2$	wRp	Volume ( $\text{\AA}^3$ )	
La8Sr2Ge6O26_PVDF		P63/m		8.91	1.9%	627.51(2)	
a ( $\text{\AA}$ )	9.962(1)	b ( $\text{\AA}$ )	9.962(1)	c ( $\text{\AA}$ )	7.300(1)		
Atomic Positions							
Atom	X	Y	Z	Ui/Ue*100	Multiplicity	Fraction	
La1	1/3	2/3	0.0017(2)	0.909(29)	4	0.5	
Sr1	1/3	2/3	0.0017(2)	0.909(29)	4	0.5	
La2	0.2330(1)	0.9890(2)	1/4	0.703(22)	6	1	
Ge1	0.4001(1)	0.3748(1)	1/4	0.406(19)	6	1	
O1	0.3096(2)	0.4850(1)	1/4	1.01*	6	1	
O2	0.6014(2)	0.4787(2)	1/4	2.25*	6	1	
O3	0.3421(2)	0.2497(2)	0.0636(2)	3.57*	12	1	
O4	0	0	0.3167(8)	5.44*	4	0.5080(4)	
Oi	0.1057(14)	-0.0033(13)	0.5468(5)	0.93*	12	0.0864(3)	
Anisotropic Thermal Parameters							
Atom	U11	U22	U33	U12	U13	U23	
O1	2.38(10)	0.85(9)	1.07(7)	1.44(8)	0	0	
O2	0.46(7)	0.67(7)	5.23(14)	0.04(6)	0	0	
O3	9.09(14)	3.49(8)	1.49(6)	4.41(9)	-3.77(7)	-2.19(6)	
O4	2.03(12)	2.03(12)	12.21(71)	1.02(6)	0	0	
Oi	1.50(53)	0.41(32)	2.33(46)	0.30(49)	2.93(38)	0.39(42)	

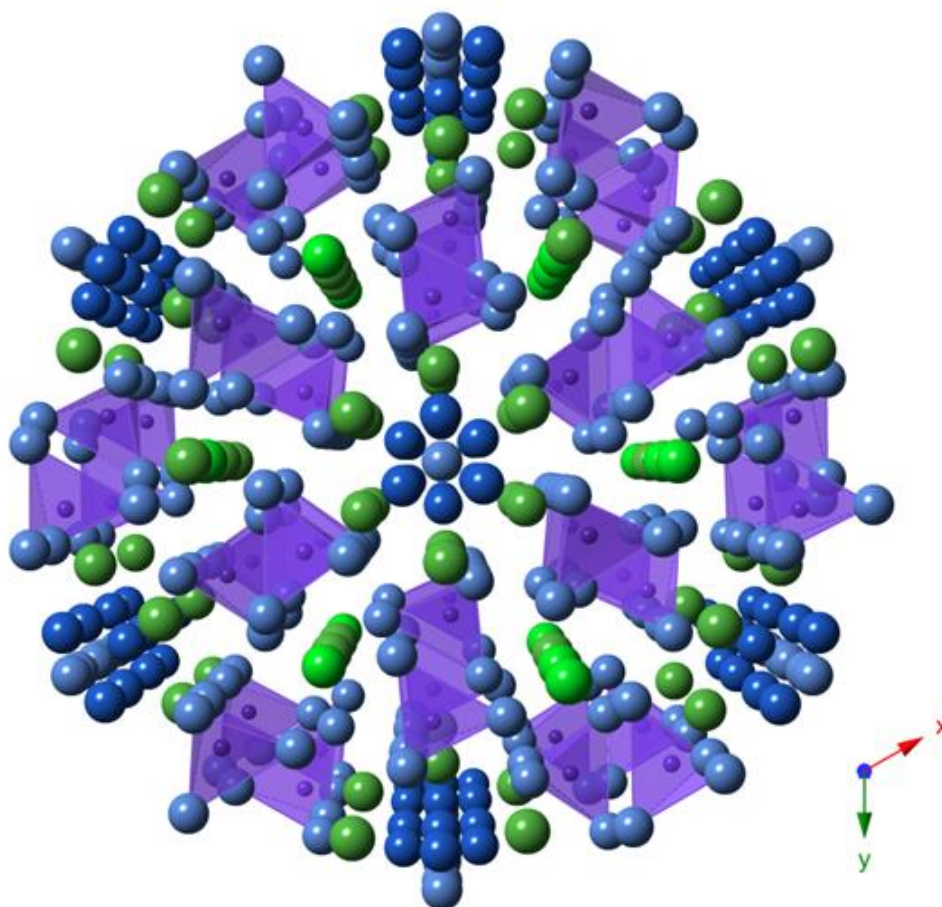


Figure 4.10- Crystal structure of  $\text{La}_8\text{Sr}_2\text{Ge}_6\text{O}_{26}$  reacted with PVDF, La/Sr - Green, Ge - Purple, O Blue. Dark blue atoms are interstitial atoms.

Figure 4.10 shows the structure of the  $\text{La}_8\text{Sr}_2\text{Ge}_6\text{O}_{26}$  sample reacted with PVDF; it can be seen that unlike the hydrated sample, the interstitial fluorine atoms have all been pushed into the channel and have not formed  $\text{GeX}_5$  ( $X = \text{O}, \text{F}$ ) polyhedra.

#### 4.3.3.2 PTFE

A sample of  $\text{La}_8\text{Sr}_2\text{Ge}_6\text{O}_{26}$  was also reacted with PTFE in a 1:1 molar ratio and showed a single phase sample by XRD with a peak shift to lower  $2\theta$  values suggesting an expansion in the unit cell due to incorporation of fluorine. The sample was then taken to the POLARIS diffractometer at ISIS for neutron diffraction to be

carried out to see if the interstitial fluorine atoms were located in the same place as in the PVDF doped sample. Rietveld refinement was performed on the resulting diffraction pattern and the extracted data and fit can be seen in Table 4.5.

**Table 4.5 - Atomic coordinates and unit cell data extracted from the Rietveld refinement of  $\text{La}_8\text{Sr}_2\text{Ge}_6\text{O}_{26}$  after reaction with PTFE.**

Sample		Space Group		$\chi^2$	wRp	Volume ( $\text{\AA}^3$ )
La8Sr2Ge6O26_PTFE		P63/m		8.88	7.7%	633.81(8)
a( $\text{\AA}$ )	10.038 (7)	b( $\text{\AA}$ )	10.038 (7)	c( $\text{\AA}$ )	7.263 (5)	
Atomic Coordinates						
Atom	X	Y	Z	Ui/Ui*100	Multiplicity	Site Occ
La1	0.33333	0.66667	-0.0017(12)	2.06(18)	4	0.5
Sr1	0.33333	0.66667	-0.0017(12)	2.06(18)	4	0.5
La2	0.2368(6)	0.9906(7)	0.25	1.59(12)	6	1
Ge1	0.4028(5)	0.3802(5)	0.25	1.16(12)	6	1
O1	0.3065(8)	0.4821(8)	0.25	2.25*	6	1
O2	0.6006(9)	0.4816(10)	0.25	3.53*	6	1
O3	0.3460(9)	0.2534(11)	0.0681(10)	6.87*	12	1
O4	0	0	0.2096(61)	9.41*	4	0.5
Oi	0.1738(43)	-0.0085(57)	0.6429(43)	6.72(38)	12	0.17(15)
Anisotropic Thermal Parameters						
Atom	U11	U22	U33	U12	U13	U23
O1	3.2(5)	1.4(5)	4.0(5)	2.17(38)	0	0
O2	0.9(4)	2.1(4)	5.7(7)	0.33(33)	0	0
O3	7.8(6)	6.6(5)	7.8(6)	4.73(50)	4.0(4)	2.5(4)
O4	8.2(9)	8.2(9)	11.6(38)	4.12(61)	0	0

As was the case for the sample reacted with PVDF the fluorine is inserted in the c axis channel. It is pushed towards the edge of the channel, with the displacement greater in this case due to the greater number of interstitial ions that have been inserted into the structure (TGA shown in Figure 4.12 and the structure is shown in Figure 4.11). The thermal displacement parameters for both the interstitial ions (Oi)

and the channel oxide ion (O4) are both large suggesting a range of positions with a range of displacements.

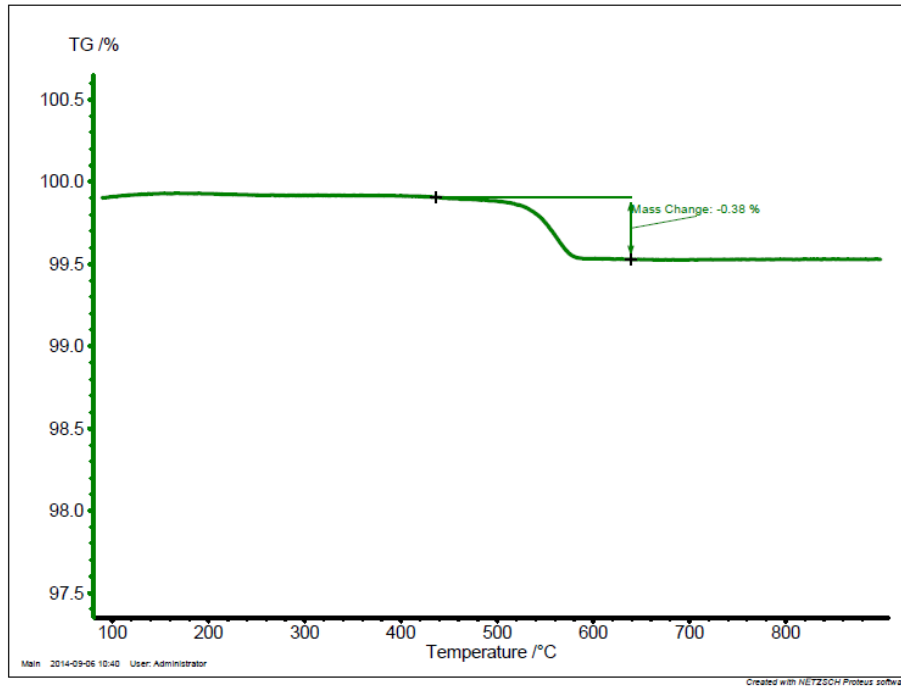


Figure 4.12 - TGA mass trace for  $\text{La}_8\text{Sr}_2\text{Ge}_6\text{O}_{26}$  after treatment with PTFE.

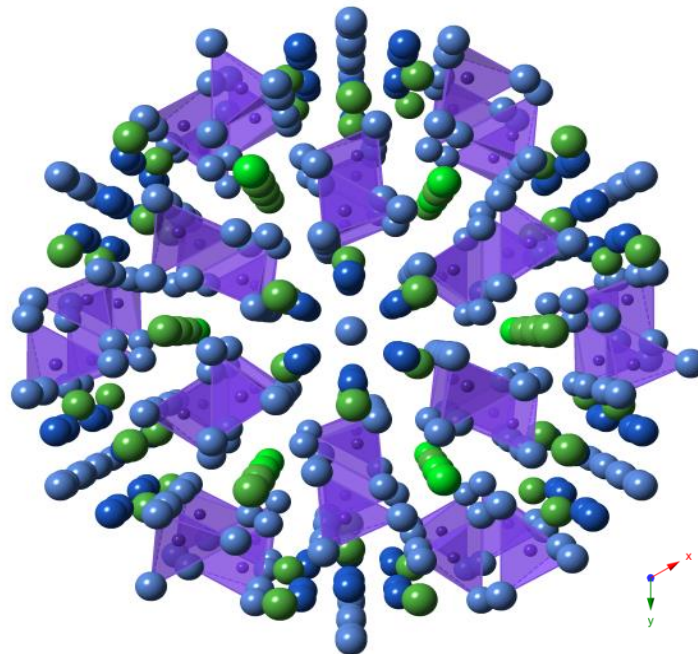


Figure 4.11 - Crystal structure of  $\text{La}_8\text{Sr}_2\text{Ge}_6\text{O}_{26}$  reacted with PTFE, La/Sr - Green, Ge - Purple, O Blue. Dark blue atoms

#### 4.3.4 In-Situ dehydration / defluorination examined by XRD

The fluorinated and hydrated samples showed expansion in the unit cell due to the incorporation of fluorine / water. These samples were then examined by XRD on heating in situ in air so changes in the unit cell size could be observed as water/fluorine is expelled.

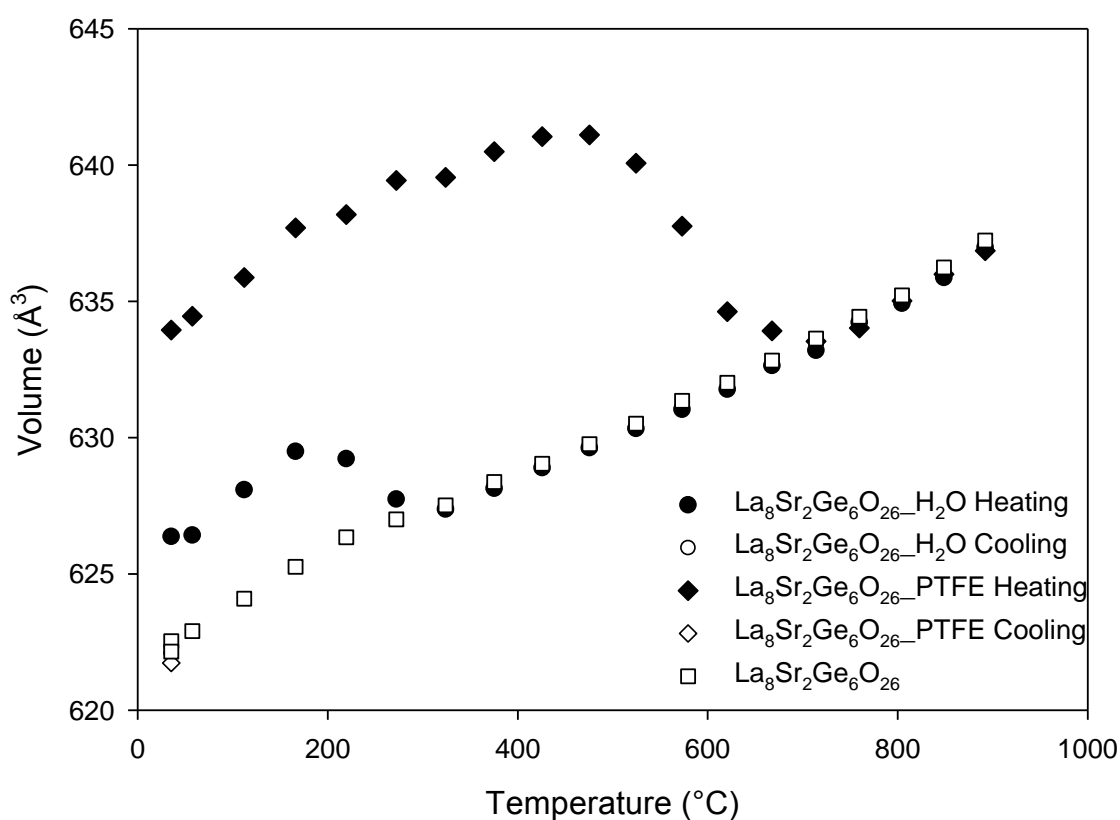


Figure 4.13 - Temperature vs Cell volume for as prepared, hydrated and fluorinated  $\text{La}_8\text{Sr}_2\text{Ge}_6\text{O}_{26}$  samples

XRD patterns were initially collected at room temperature and then the sample was heated at  $5^\circ\text{C min}^{-1}$  with XRD patterns collected every  $50^\circ\text{C}$  using a  $20\text{-}60^\circ 2\theta$  range with a  $0.018^\circ$  step size (70 min per scan). An equilibration time of 5 min was

included to ensure temperature had stabilised. The sample was then cooled to room temperature where another XRD pattern was collected for comparison between the fluorinated / hydrated sample and the sample after loss of F / H<sub>2</sub>O. (Figure 4.13)

The fluorinated samples had the greatest expansion in the unit cell and showed the largest increase in volume it was also seen that in the fluorinated samples, the fluorine is retained by the structure until a higher temperature than the water in the hydrated equivalents.

The main origin of the cell volume expansion is due to an expansion in the a, b parameters. The expansion in the a, b parameter due to the incorporation of interstitial ions closely matches the trend in the increase observed in cell volume, however the c parameter shows a small contraction on incorporation of interstitial ions. The main expansion along a, b is consistent with the accommodation in the channels with displacement from the channel centre.

#### 4.4 Hydration studies of La<sub>9.75</sub>Ge<sub>6</sub>O<sub>26.625</sub>

La<sub>9.75</sub>Ge<sub>6</sub>O<sub>26.625</sub> differs from La<sub>8</sub>Sr<sub>2</sub>Ge<sub>6</sub>O<sub>26</sub> because the as prepared sample already contains interstitial oxygen atoms. It has an oxygen content of 26.625 to be charge balanced whereas a fully stoichiometric sample with no interstitial atoms would have 26 oxygen atoms. This section uses neutron diffraction to locate these interstitial atoms before attempting to incorporate further interstitial water molecules, although no attempt will be made to locate the protons from the water molecules, due to issues outlined earlier with regard to a likely range of H<sup>+</sup> positions and rapid interchange between positions.

#### 4.4.1 Experimental

Stoichiometric mixtures of high purity lanthanum (III) oxide ( $\text{La}_2\text{O}_3$ ) and germanium (IV) oxide ( $\text{GeO}_2$ ) were ground together and heated to  $1100^\circ\text{C}$  for 12 h. Samples were then re ground and reheated for a second time at  $1100^\circ\text{C}$  for a further 12 h. Following this the samples were mechanically ground in a Fritsch Pulverisette planetary ball mill at 350 rpm for 1 h and pressed into 8 mm, 10 mm or 13 mm diameter pellets at pressures between 300 and  $4000\text{ kg cm}^{-2}$ . The pellets were then sintered at  $1300^\circ\text{C}$  for 6 h.

Powder X-ray diffraction was used to check phase purity of the samples using a Bruker D8 diffractometer with  $\text{Cu K}\alpha_1$  radiation. Rietveld refinement was completed using either the GSAS suite of programs or Topas v4.2.

#### 4.4.2 Structure

In situ neutron diffraction and hydration experiments were carried out on HRPD at ISIS using custom made apparatus (Figure 4.2). In total, 18g, of  $\text{La}_{9.75}\text{Ge}_6\text{O}_{26.625}$  was prepared and this was pressed into a stack of 8mm pellets at a pressure of  $450\text{ kg cm}^{-2}$  and sintered at  $1300^\circ\text{C}$  for 6hrs. This resulted in a stack of pellets approximately 40mm high. The beam at ISIS only has a height of 10mm but as it was not possible to see the exact position of the sample once it was loaded into the furnace it was decided to use a large stack of pellets to ensure the entire beam was used for the best scattering results. As experienced previously the diffraction patterns have a slightly unusual undulating background due to scattering from the silica tubes which allow gas flow.

The sample was heated between room temperature (25°C) and 800°C in a dry argon atmosphere before cooling in a wet argon atmosphere. It was noticed that at lower temperatures, the  $\text{La}_{9.75}\text{Ge}_6\text{O}_{26.65}$  sample exhibited a pattern which contained broad peaks with low intensity. As the sample was heated beyond approximately 550°C it displayed a structural phase transition to a pattern similar to the hexagonal patterns observed for the  $\text{La}_8\text{Sr}_2\text{Ge}_6\text{O}_{26}$  samples.

The room temperature data is consistent with a vastly lower symmetry unit cell and this room temperature structure of  $\text{La}_{9.75}\text{Ge}_6\text{O}_{26.625}$  could be refined to a triclinic P-1 space group using Topas v4.2 refinement software (Figure 4.14).

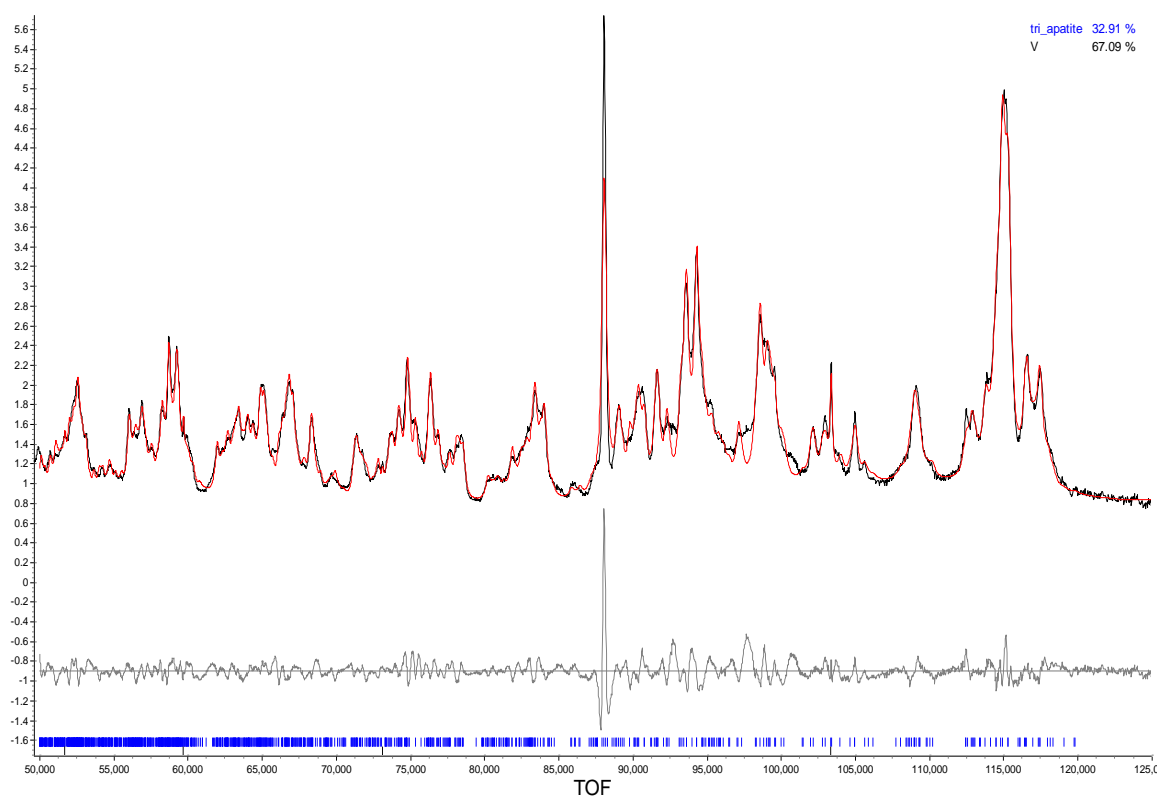


**Figure 4.14 – Refinement plot for  $\text{La}_{9.75}\text{Ge}_6\text{O}_{26.625}$  at room temperature. Showing traces for observed (black line), calculated (red line) and difference (grey line) profiles.**

The graphical fit to the P-1 space group shows a slight amount of intensity mismatch between some of the observed and calculated peaks. This is most noticeable for the peak at 88,000  $\mu\text{sec}$  (TOF) where the calculated pattern underestimates the intensity compared with what was expected. This peak relates to the (00l) reflection (004) and the other peaks which show the largest mismatch in intensity are also related to (00l) reflections (i.e.  $h = 0, k = 0$ ). The cause of these differences is possibly due to anisotropic peak broadening due to a substantial number of interstitial ions in the ab plane weakening and broadening reflections with either h or k components. Due to this complexity, the relative scattering of the triclinic phase is very low so the peaks that represent the vanadium from the sample container can also be seen in the diffraction pattern. These would not normally be seen as vanadium is also a poor scatterer of neutrons. The vanadium was refined as a second phase.

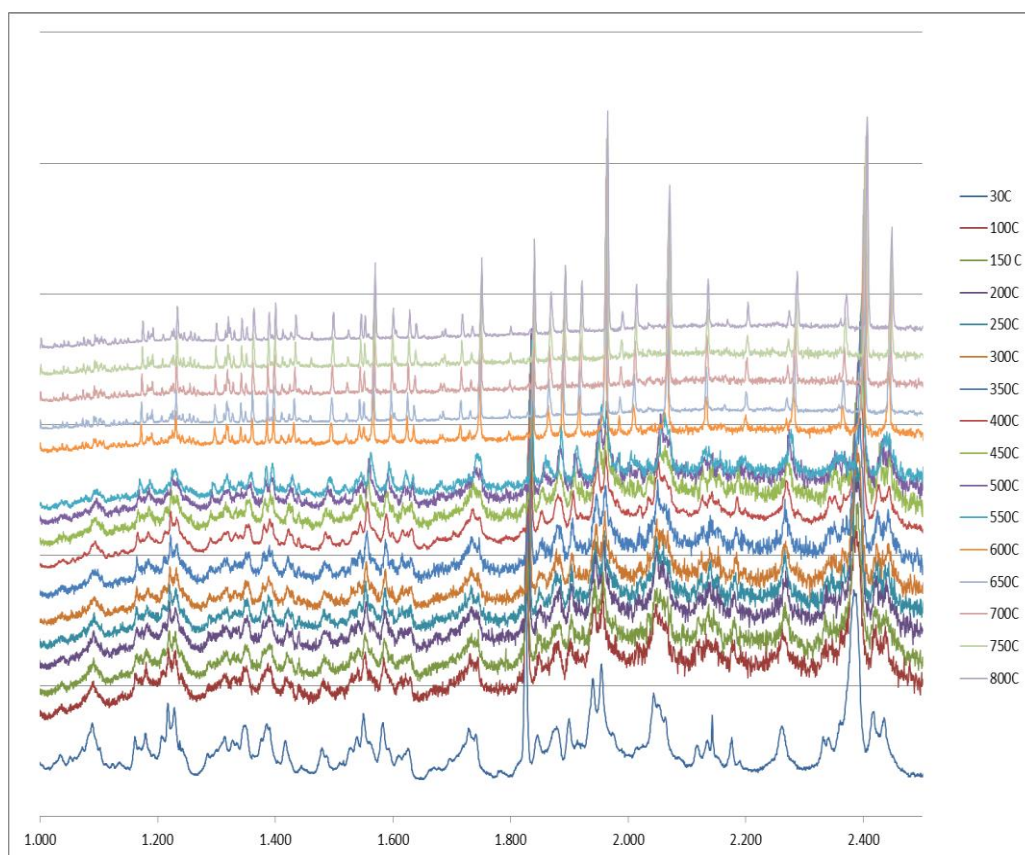


**Figure 4.15 - Stacked neutron diffraction patterns for  $\text{La}_{9.75}\text{Ge}_6\text{O}_{26.625}$  on heating.**

Atomic coordinates and unit cell parameters are given in Table 4.6. The interstitial oxygen ion positions have not been included as due to the complexity of the P-1 space group it was not possible to accurately locate the positions. Thermal parameters for cations and anions have also been constrained to equal each other.

**Table 4.6 - Unit cell and atomic coordinate data for room temperature  $\text{La}_{9.75}\text{Ge}_6\text{O}_{26.625}$**

Sample Name	Space Group		Rp		wRp		Volume ( $\text{\AA}^3$ )
$\text{La}_{9.75}\text{Ge}_6\text{O}_{26.625}$ RT	P-1		4.1%		5.8%		617.91(7)
a( $\text{\AA}$ )	9.921(1)	b( $\text{\AA}$ )	9.914(1)	c( $\text{\AA}$ )			7.286(2)
$\alpha$	89.37(2)	$\beta$	91.08(3)	$\gamma$			120.41(1)
Atomic Positions							
Atom	x	y	z	Ui/Ue*100	Multiplicity	Site Occ	
La1a	0.3472(20)	0.6409(16)	0.5105(17)	2.627(24)	2	1	
La1b	0.3512(18)	0.6924(16)	0.0093(19)	2.627(24)	2	1	
La2a	0.2222(18)	0.9814(18)	0.2537(17)	2.627(24)	2	1	
La2b	0.0048(20)	0.2441(17)	0.2387(20)	2.627(24)	2	1	
La2c	0.7644(23)	0.7653(16)	0.2567(19)	2.627(24)	2	1	
Ge1a	0.4056(19)	0.3734(17)	0.2316(20)	2.627(24)	2	1	
Ge1b	0.6191(20)	0.0209(14)	0.2505(19)	2.627(24)	2	1	
Ge1c	0.9721(18)	0.5991(17)	0.2406(21)	2.627(24)	2	1	
O1a	0.3170(25)	0.4759(21)	0.2216(25)	1.990(19)	2	1	
O1b	0.5170(25)	0.8219(19)	0.2523(28)	1.990(19)	2	1	
O1c	0.1816(26)	0.6753(23)	0.2430(28)	1.990(19)	2	1	
O2a	0.6061(31)	0.4607(25)	0.2327(32)	1.990(19)	2	1	
O2b	0.5227(28)	0.1322(21)	0.2692(25)	1.990(19)	2	1	
O2c	0.8637(26)	0.3879(24)	0.2762(28)	1.990(19)	2	1	
O3a	0.3279(30)	0.2274(24)	0.0713(28)	1.990(19)	2	1	
O3b	0.7257(27)	0.0962(24)	0.0418(25)	1.990(19)	2	1	
O3c	0.9160(27)	0.6991(22)	0.0927(24)	1.990(19)	2	1	
O3d	0.6771(28)	0.7387(22)	0.5711(27)	1.990(19)	2	1	
O3e	0.1953(27)	0.9166(20)	0.5502(25)	1.990(19)	2	1	
O3f	0.0984(27)	0.3516(20)	0.5585(24)	1.990(19)	2	1	
O4b	-0.0111(3)	-0.0136(3)	0.2415(8)	1.990(19)	2	1	

Other triclinic apatite systems have been seen to increase symmetry to a hexagonal system upon heating to higher temperatures.<sup>9</sup> This can be seen when the patterns are compared in contrast to the room temperature pattern (Figure 4.15), the pattern for the high temperature scans (above 650°C) contain fewer peaks. In these cases, the structure can be refined to the same hexagonal P63/m space group used for the  $\text{La}_8\text{Sr}_2\text{Ge}_6\text{O}_{26}$  structure although the unit cell is larger. (Figure 4.16 and Table 4.7) As for the  $\text{La}_8\text{Sr}_2\text{Ge}_6\text{O}_{26}$ , in situ hydration resulted in negligible changes, attributed to the slower kinetics of hydration for the sample pellets.

**Table 4.7 - Unit cell and atomic coordinate data for  $\text{La}_{9.75}\text{Ge}_6\text{O}_{26.625}$  at 800°C**

Sample	Space Group	$\chi^2$	wRp	Volume ( $\text{\AA}^3$ )	Theoretical Density ( $\text{g cm}^{-3}$ )	
$\text{La}_{9.75}\text{Ge}_6\text{O}_{26}$ 800C	P63/m	3.50	2.2%	637.67(5)	5.83	
a( $\text{\AA}$ )	10.01(2)	b( $\text{\AA}$ )	10.01(2)	c( $\text{\AA}$ )	7.35(4)	
Atomic Coordinates						
Name	X	Y	Z	Ui/Ue*100	Multiplicity	Site occ
La1	1/3	2/3	-0.0013(16)	4.84(3)	4	0.9738
La2	0.2284(2)	0.9886(2)	1/4	3.73(4)	6	1
Ge1	0.4005(2)	0.3742(2)	1/4	3.25(4)	6	1
O1	0.3163(3)	0.4887(2)	1/4	5.38*	6	1
O2	0.6028(2)	0.4710(3)	1/4	6.00*	6	1
O3	0.3393(2)	0.2498(2)	0.0633(2)	7.71*	12	1
O4	0	0	-0.2049(8)	4.64(16)	4	0.5
Anisotropic Thermal Parameters						
Name	U11	U22	U33	U12	U13	U23
O1	8.57(18)	5.15(17)	6.20(17)	5.59(15)	0	0
O2	3.64(13)	4.67(15)	8.78(22)	1.71(12)	0	0
O3	14.25(18)	6.82(13)	5.05(10)	6.60(15)	-4.44(12)	-2.61(9)

La<sub>9.75</sub>Ge<sub>6</sub>O<sub>26.625</sub>

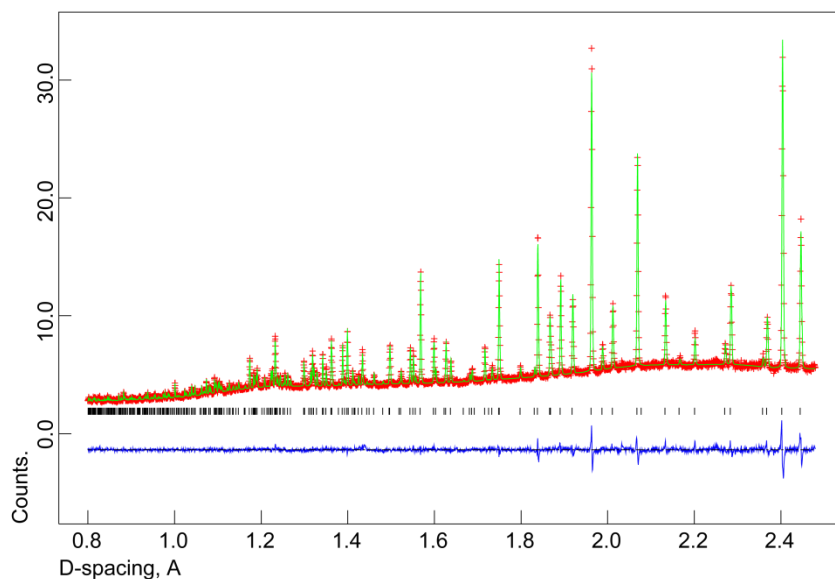


**Figure 4.16 - Observed (red), Calculated (green) and Difference (blue) profiles for Rietveld refinement of La<sub>9.75</sub>Ge<sub>6</sub>O<sub>26.625</sub> at 800°C**

### 2.1.1.1. Hydration

It was possible to hydrate the La<sub>9.75</sub>Ge<sub>6</sub>O<sub>26.625</sub> sample using a hydrothermal vessel under similar conditions as for La<sub>8</sub>Sr<sub>2</sub>Ge<sub>6</sub>O<sub>26</sub>. Water incorporation was verified with TGA-MS where a mass loss of 0.73% was observed, relating to a water content of 0.81 moles of water per mole of sample (Figure 4.17). This is a similar amount to the La<sub>8</sub>Sr<sub>2</sub>Ge<sub>6</sub>O<sub>26</sub> sample but will relate to a greater total number of interstitial atoms as the La<sub>9.75</sub>Ge<sub>6</sub>O<sub>26.625</sub> sample already contains interstitial atoms before hydration.

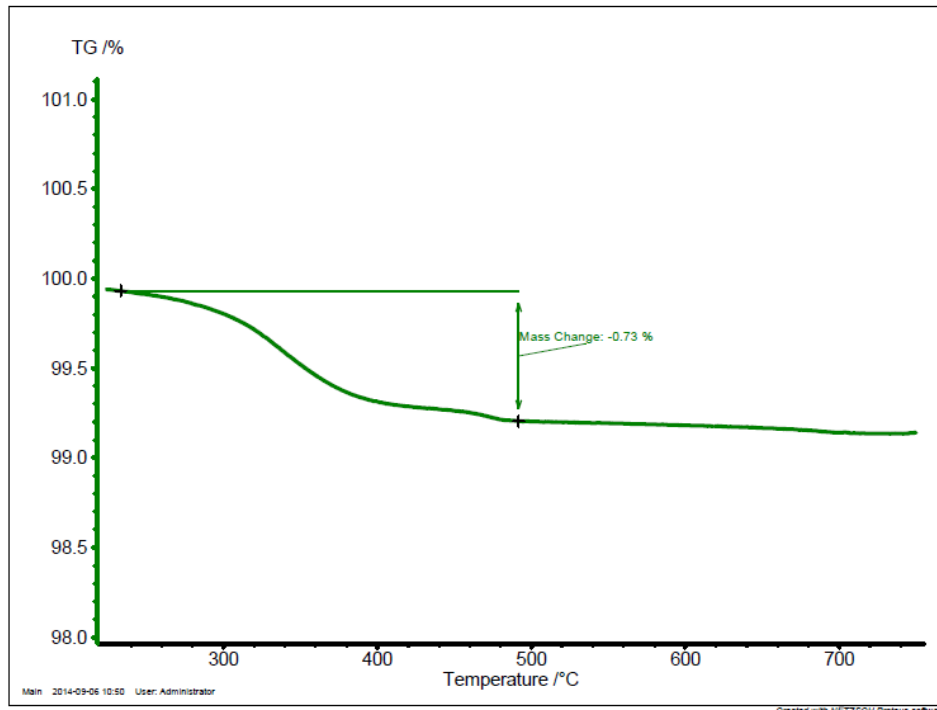


**Figure 4.17 - TGA mass trace for hydrated  $\text{La}_{9.75}\text{Ge}_6\text{O}_{26.625}$  in a  $\text{N}_2$  atmosphere.**

XRD analysis suggests a change in symmetry from triclinic to hexagonal. Rietveld refinement of the XRD data suggests interstitial water or oxide ions located in the channel, although not all interstitials have been found (as the total anion content is lower than TGA data suggests). (Figure 4.18 and Table 4.8) A hydrated sample of  $\text{La}_{9.75}\text{Ge}_6\text{O}_{26.625}$  was taken to the POLARIS diffractometer at ISIS for neutron diffraction patterns to be collected. Due to the disorder already present within the “as prepared” sample, it has not yet been possible to pin point a possible location for the interstitial water molecules within the structure, and further work is required in this area.

Table 4.8 - Unit cell and atomic coordinate data for hydrated  $\text{La}_{9.75}\text{Ge}_6\text{O}_{26.625}$  using XRD.

Sample		Space Group	$\chi^2$	$wR_p$	Volume ( $\text{\AA}^3$ )	
La9.75Ge6O26.625_H2O		P63/m	5.17	4.6%	627.87(4)	
<b>a</b> ( $\text{\AA}$ )	9.987 (3)	<b>b</b> ( $\text{\AA}$ )	9.987 (3)	<b>c</b> ( $\text{\AA}$ )	7.275 (2)	
Atomic Coordinates						
Atom	X	Y	Z	Ui/Ue*100	Multiplicity	Site Occ
<b>La1</b>	1/3	2/3	-0.0013(14)	4.18(9)	4	1
<b>La2</b>	0.2347(4)	0.9896(3)	0.25	1.35(11)	6	1
<b>Ge1</b>	0.3975(8)	0.3759(6)	0.25	2.38(7)	6	1
<b>O1</b>	0.3512(5)	0.4998(4)	0.25	10.53(48)	6	1
<b>O2</b>	0.5962(5)	0.4951(8)	0.25	10.53(48)	6	1
<b>O3</b>	0.3428(2)	0.2233(3)	0.0839(2)	10.53(48)	12	1
<b>O4</b>	0	0	1/4	10.53(48)	2	1
<b>Oi</b>	0	0	1/2	3.8	2	0.434(39)

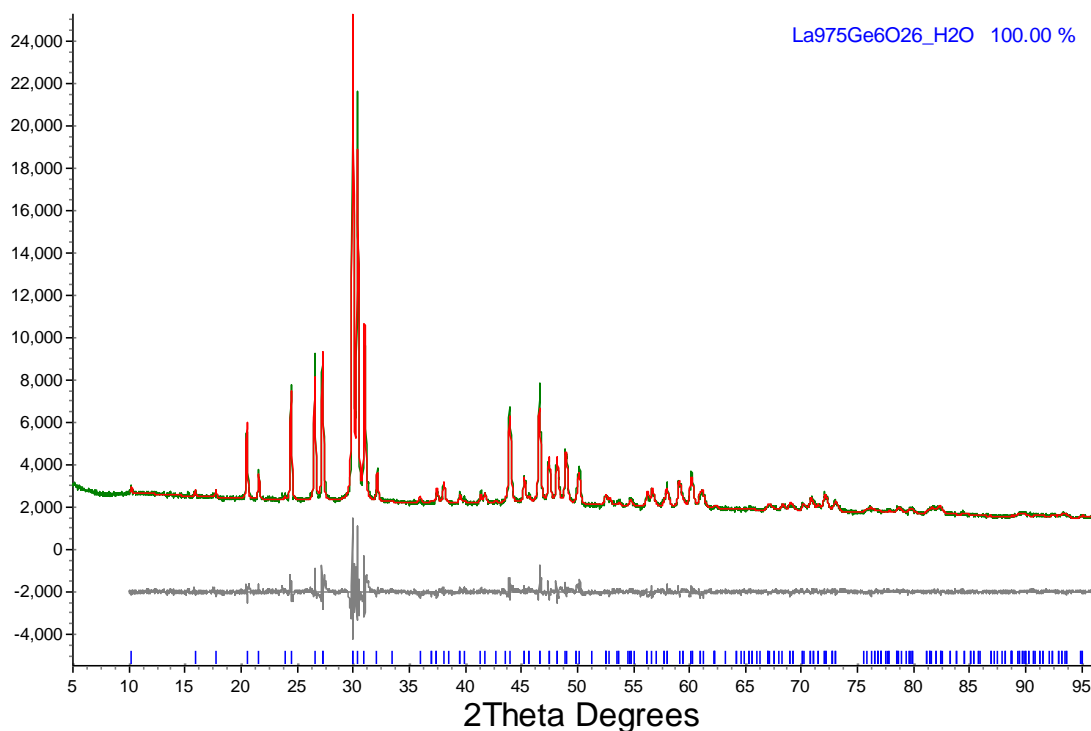


Figure 4.18 - Observed (Green), Calculated (Red), and difference (grey) profiles for the Rietveld refinement of XRD data of hydrated  $\text{La}_{9.75}\text{Ge}_6\text{O}_{26.625}$ .

## 4.5 Silicate apatites

In this work silicate apatites were also investigated as they show the highest levels of ionic conductivity of the reported apatite samples.<sup>3</sup>

### 4.5.1 Experimental

Stoichiometric mixtures of high purity lanthanum (III) oxide ( $\text{La}_2\text{O}_3$ ), silicon (IV) oxide ( $\text{SiO}_2$ ) and strontium carbonate ( $\text{SrCO}_3$ ) were ground together and heated to  $1100^\circ\text{C}$  for 12 h. Samples were then re ground and reheated for a second time at  $1100^\circ\text{C}$  for a further 12 h. Following this the samples were mechanically ground in a Fritsch Pulverisette planetary ball mill at 350 rpm for 1 h and pressed into 8 mm, 10 mm or 13 mm diameter pellets at pressures between 300 and  $4000 \text{ kg cm}^{-2}$ . The pellets were then sintered at  $1400^\circ\text{C}$  for 6 h.

Powder X-ray diffraction was used to check phase purity of the samples using a Bruker D8 diffractometer with  $\text{Cu K}\alpha_1$  radiation. Rietveld refinement was completed using the GSAS suite of programs.

### 4.5.2 $\text{La}_8\text{Sr}_2\text{Si}_6\text{O}_{26}$

As with the germanium systems a fully stoichiometric sample was initially chosen as there are no interstitial positions that are already occupied.

### 4.5.2.1 Structure

A sample of  $\text{La}_8\text{Sr}_2\text{Si}_6\text{O}_{26}$  was analysed by XRD and the structure refined to a hexagonal P63/m space group. The observed, calculated, and difference plots can be seen in Figure 4.19.

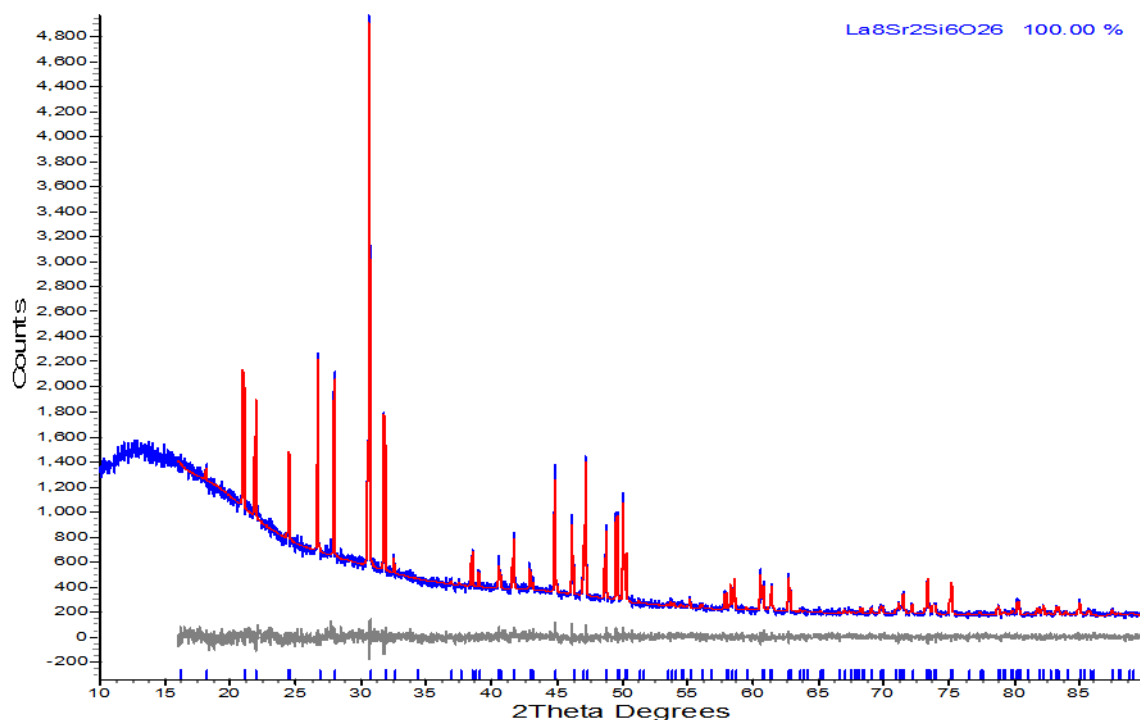


Figure 4.19 - Observed (blue), Calculated (red) and difference (grey) profiles for Rietveld refinement of  $\text{La}_8\text{Sr}_2\text{Si}_6\text{O}_{26}$

As expected  $\text{La}_8\text{Sr}_2\text{Si}_6\text{O}_{26}$  has a similar P63/m cell as the germanium equivalent but with a smaller unit cell due to the smaller size of silicon compared with germanium. (Table 4.9).

Table 4.9 - Atomic coordinates and unit cell data extracted from the Rietveld refinement of x-ray data for  $\text{La}_8\text{Sr}_2\text{Si}_6\text{O}_{26}$ .

Sample	Space Group	$\chi^2$	wRp	Volume ( $\text{\AA}^3$ )	Theoretical Density ( $\text{g cm}^{-3}$ )	
$\text{La}_8\text{Sr}_2\text{Si}_6\text{O}_{26}$	P63/m	1.124	5.1%	590.61	5.260	
<b>a(<math>\text{\AA}</math>)</b>	9.706(1)	<b>b(<math>\text{\AA}</math>)</b>	9.706(1)	<b>c(<math>\text{\AA}</math>)</b>	7.238(1)	
Atomic Coordinates						
Atom	X	Y	Z	Ui/Ue*100	Multiplicity	Site Occ
<b>La1</b>	1/3	2/3	-0.00103(9)	1.091(11)	4	0.5
<b>Sr1</b>	1/3	2/3	-0.00103(9)	1.091(11)	4	0.5
<b>La2</b>	0.0119(7)	0.2443(43)	1/4	1.879(21)	6	1
<b>Si1</b>	0.4001(18)	0.3690(21)	1/4	1.077(18)	6	1
<b>O1</b>	0.3253(35)	0.4843(35)	1/4	1.929(31)	6	1
<b>O2</b>	0.5850(32)	0.4671(32)	1/4	0.284(27)	6	1
<b>O3</b>	0.3396(18)	0.2553(20)	0.0765(12)	0.125(21)	12	1
<b>O4</b>	0	0	1/4	0.137(33)	2	1

#### 4.5.2.2 Fluorination

$\text{La}_8\text{Sr}_2\text{Si}_6\text{O}_{26}$  was fluorinated by heating in a 1:1 molar ratio with PVDF ( $\text{CH}_2\text{CF}_2$ ), or PTFE ( $\text{CF}_2\text{CF}_2$ ). As PTFE contains double the fluorine content per polymer repeat unit it was expected that a higher level of fluorination would be obtained by the use of PTFE.

##### 4.5.2.2.1 PVDF

The sample heated with PVDF was checked by XRD and shows no additional crystalline peaks or phases but a slight expansion in the unit cell was visible. This implies that a portion of the oxygen within the structure has been replaced with fluorine. In order to test this, TGA was performed. Thermo gravimetric analysis shows a loss of 0.16% which relates to 0.14 moles  $\text{F}_2$  (0.27 moles  $\text{F}^-$ ) per mole of  $\text{La}_8\text{Sr}_2\text{Si}_6\text{O}_{26}$  (fluorine loss was confirmed by mass spectrometry).

In order to provide further evidence for the successful incorporation of fluorine, Raman spectroscopy studies were performed. The Raman spectroscopy data revealed an additional peak at approximately  $770\text{ cm}^{-1}$  (Figure 4.20). It is believed that this peak is due to Si-F bonds which are formed when an oxygen atom is replaced by  $\text{F}_2$  leaving one  $\text{F}^-$  in the position of the oxygen and one  $\text{F}^-$  atom at an interstitial site within the channel.

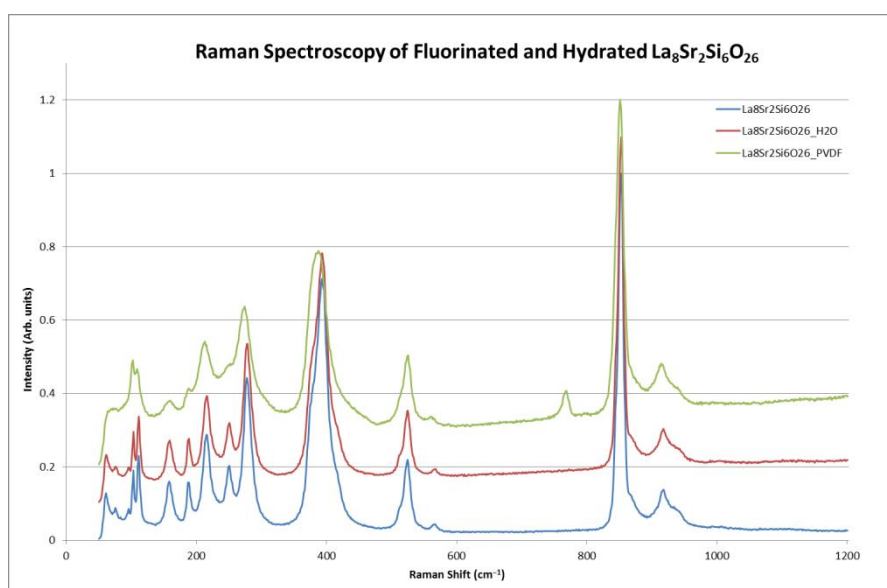


**Figure 4.20 - Raman spectroscopy of  $\text{La}_8\text{Sr}_2\text{Si}_6\text{O}_{26}$  as prepared (blue), hydrated (red) and fluorinated (with PVDF).**

These preliminary XRD and TGA results allowed for a successful application for neutron diffraction at the Paul Scherrer Institut (PSI) in Switzerland. The aim of the neutron experiment was to locate interstitial anion positions. For this the high resolution powder diffractometer for thermal neutrons was selected as it offers the greatest resolution.

For a direct comparison, data for both the as prepared  $\text{La}_8\text{Sr}_2\text{Si}_6\text{O}_{26}$  sample and a sample of  $\text{La}_8\text{Sr}_2\text{Si}_6\text{O}_{26}$  which had been reacted with PVDF in a 1:1 molar ratio were collected.

The neutron source at PSI differs from ISIS even though they are both spallation sources as PSI offers a constant wavelength neutron beam compared with the time of flight pulse ISIS offers, allowing for data to be collected over a  $2\theta$  range. Rietveld refinement was carried out firstly on the as prepared sample (Figure 4.21)

**Table 4.10 - Atomic coordinates and unit cell data from the Rietveld refinement of neutron data for  $\text{La}_8\text{Sr}_2\text{Si}_6\text{O}_{26}$ .**

Sample	Space Group	$\chi^2$	wRp	Volume ( $\text{\AA}^3$ )	Theoretical Density ( $\text{g cm}^{-3}$ )	
$\text{La}_8\text{Sr}_2\text{Si}_6\text{O}_{26}$	P63/m	5.88	2.5%	590.60	5.230	
<b>a(<math>\text{\AA}</math>)</b>	9.707(1)	<b>b(<math>\text{\AA}</math>)</b>	9.707(1)	<b>c(<math>\text{\AA}</math>)</b>	7.238(1)	
Atomic Coordinates						
Atom	X	Y	Z	Ui/Ue*100	Multiplicity	Site Occ
La1	1/3	2/3	-0.0007(2)	0.597(20)	4	0.5
Sr1	1/3	2/3	-0.0007(2)	0.597(20)	4	0.5
La2	0.0129(1)	0.2450(9)	1/4	0.436(15)	6	1
Si1	0.4009(8)	0.3705(7)	1/4	0.160(30)	6	1
O1	0.3217(1)	0.4833(4)	1/4	0.88*	6	1
O2	0.5940(3)	0.4712(5)	1/4	0.74*	6	1
O3	0.3426(1)	0.2536(1)	0.0702(1)	0.97*	12	1
O4	0	0	1/4	1.26*	2	1
Anisotropic Thermal Parameters						
Atom	U11	U22	U33	U12	U13	U23
O1	1.40(6)	1.04(6)	0.867(67)	1.049(56)	0	0
O2	0.43(6)	0.42(5)	1.229(58)	0.116(50)	0	0
O3	2.02(5)	0.77(4)	0.552(34)	0.739(38)	-0.573(33)	-0.287(30)
O4	0.67(5)	0.67(5)	2.427(17)	0.335(26)	0	0

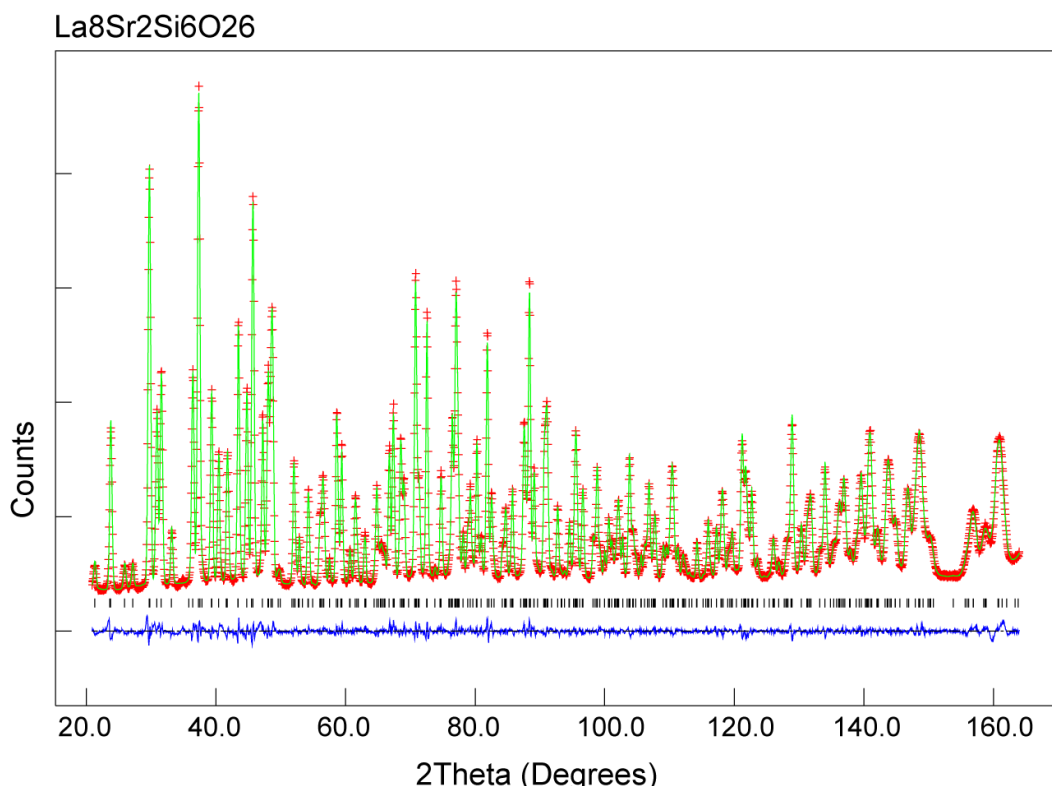


**Figure 4.21 - Observed (red), calculated (green) and difference (blue) profiles for the refinement of the neutron diffraction pattern for La<sub>8</sub>Sr<sub>2</sub>Si<sub>6</sub>O<sub>26</sub>.**

The unit cell from the XRD refinement of La<sub>8</sub>Sr<sub>2</sub>Si<sub>6</sub>O<sub>26</sub> was used as a starting point for the Rietveld analysis of the neutron refinement for both as prepared and fluorinated samples. The observed, calculated and difference profiles for the refinement of the fluorinated sample can be seen in Figure 4.22. The most notable change from the X-ray refinement is that O3 and O4 thermal parameters have now been refined as anisotropic rather than isotropic. Minor changes to fractional coordinates and thermal parameters can also be seen in the atomic coordinates table with a reduction in error, as neutron diffraction has a higher level of accuracy (Table 4.10).

Table 4.11 - Atomic coordinates and unit cell data extracted from the Rietveld refinement of neutron data for  $\text{La}_8\text{Sr}_2\text{Si}_6\text{O}_{26}$  reacted with PVDF.

Sample	Space Group	$\chi^2$	wRp	Volume ( $\text{\AA}^3$ )	Theoretical Density ( $\text{g cm}^{-3}$ )	
$\text{La}_8\text{Sr}_2\text{Si}_6\text{O}_{26}$ _PVDF	P63/m	3.43	2.5%	591.58	5.273	
<b>a(<math>\text{\AA}</math>)</b>	9.721(1)	<b>b(<math>\text{\AA}</math>)</b>	9.721(1)	<b>c(<math>\text{\AA}</math>)</b>	7.228(1)	
Atomic Coordinates						
Name	X	Y	Z	Ui/Ue*100	Multiplicity	Site Occ
La1	0.3333	0.6667	-0.0002(2)	0.549(24)	4	0.49
Sr1	0.3333	0.6667	-0.0002(2)	0.549(24)	4	0.51
La2	0.0126(1)	0.2447(1)	0.25	0.639(18)	6	0.99
Si1	0.4012(2)	0.3724(2)	0.25	0.36(4)	6	1
O1	0.3210(2)	0.4831(2)	0.25	1.04*	6	1
O2	0.5942(2)	0.4730(2)	0.25	1.10*	6	1
O3	0.3438(1)	0.2548(1)	0.0702(1)	1.60*	12	1
O4	0	0	0.25	6.55*	2	1
Oi	-0.0063(4)	0.0580(5)	0.5762(3)	0.25	12	0.021(8)
Anisotropic Thermal Parameters						
Name	U11	U22	U33	U12	U13	U23
O1	1.34(9)	0.97(9)	1.38(8)	0.94(8)	0	0
O2	0.56(8)	0.77(8)	1.95(8)	0.39(7)	0	0
O3	3.36(9)	1.22(6)	1.34(5)	1.50(6)	-1.36(5)	-0.80(4)
O4	0.94(16)	0.94(16)	11.76(16)	0.47(8)	0	0

The structure refinement using neutron diffraction data for the sample reacted with PVDF shows an expansion in the unit cell volume from  $590.6 \text{ \AA}^3$  to  $591.6 \text{ \AA}^3$  on fluorination with an increase in a/b and a small decrease in the length of c observed. The interstitial anions (Oi) were located (Table 4.11) in the centre of the channel in the spaces between O4 atoms, albeit somewhat displaced off-centre. The very high thermal displacement parameter for this site implies a range of closely spaced positions. Although Si-F bonds can be seen by Raman spectroscopy it was not possible to differentiate between the oxygen and fluorine atoms within the  $\text{SiO}_4$  tetrahedra using neutron diffraction.

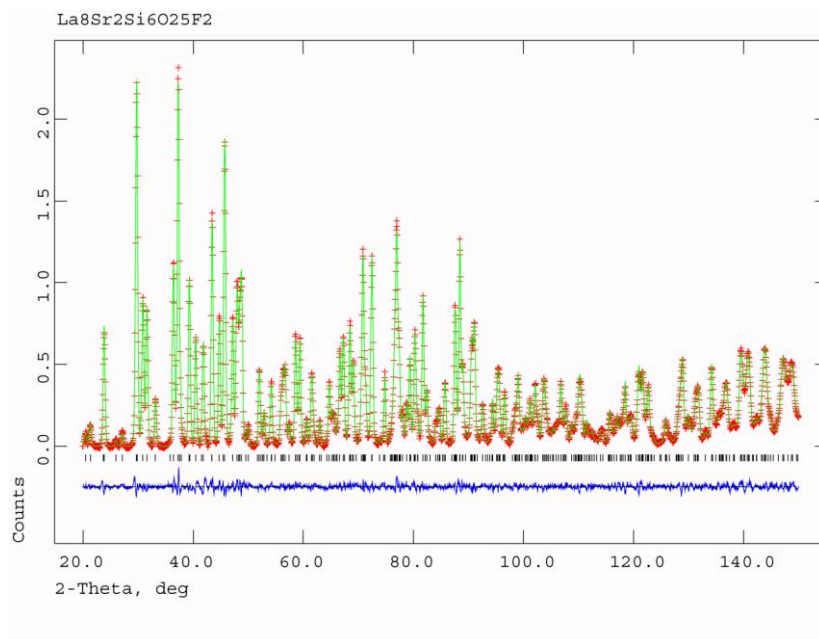


Figure 4.22 - Observed (red), Calculated (green) and difference (blue) profiles for the Rietveld refinement of  $\text{La}_8\text{Sr}_2\text{Si}_6\text{O}_{26}$  reacted with PVDF.

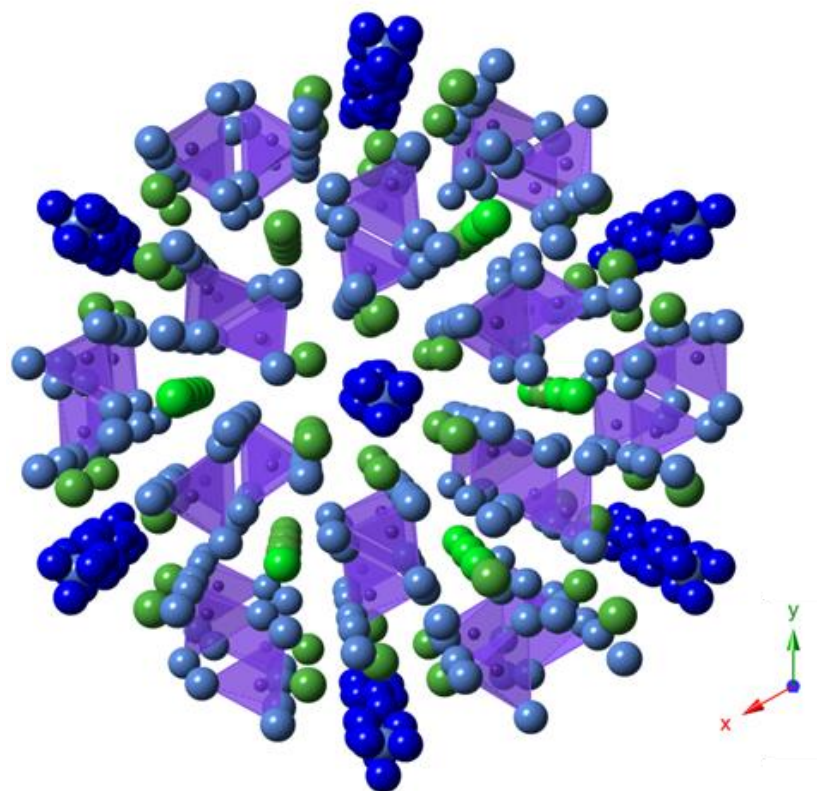
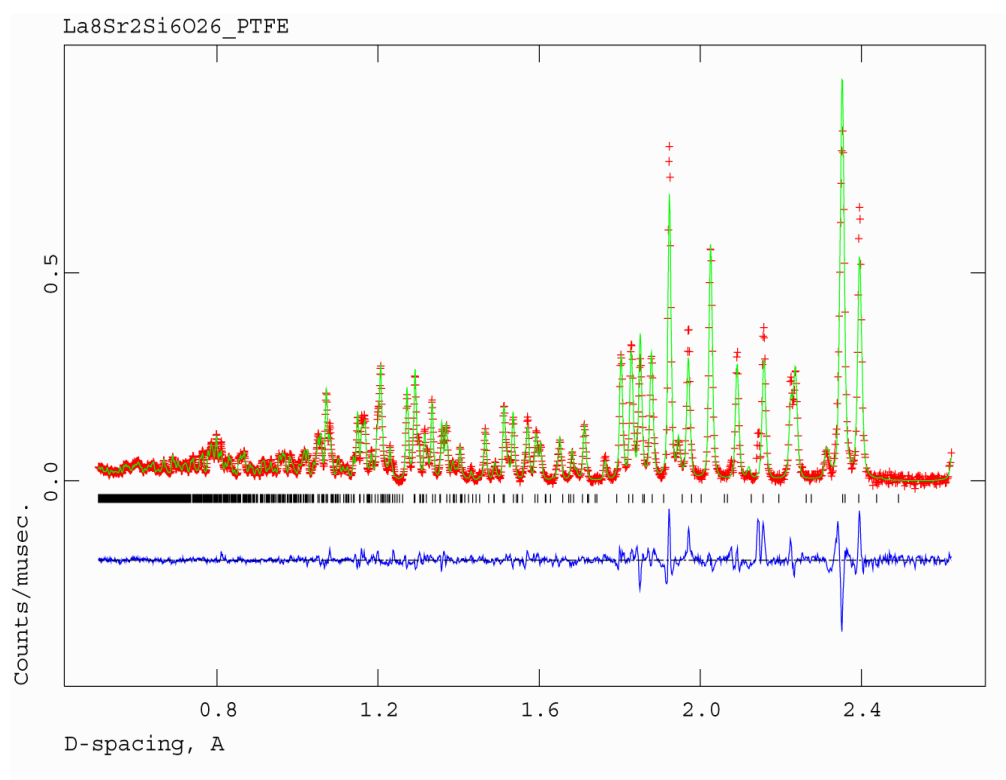


Figure 4.23 - Structure of  $\text{La}_8\text{Sr}_2\text{Ge}_6\text{O}_{26}$  fluorinated with PVDF, La/Sr are green, Ge are purple and O are shown in blue, darker blue represents interstitial ions.

#### 4.5.2.2.2 PTFE

A sample of  $\text{La}_8\text{Sr}_2\text{Si}_6\text{O}_{26}$  was reacted with PTFE in an attempt to achieve a higher level of fluorination than was possible with the use of PVDF. XRD analysis of the sample reacted with PTFE shows an expansion in the unit cell suggesting incorporation of fluorine has been successful. The sample was then taken to the POLARIS diffractometer at ISIS where neutron diffraction experiments were carried out. Rietveld refinement of the data shows a large expansion in the unit cell from  $590.6\text{\AA}^3$  to  $597.8\text{\AA}^3$  when compared with the unreacted sample. (Figure 4.24 and Table 4.12)



**Figure 4.24 - Observed (red), Calculated (green) and Difference (blue) profiles (back scattering bank) for the Rietveld refinement of  $\text{La}_8\text{Sr}_2\text{Si}_6\text{O}_{26}$  reacted with PTFE.**

Table 4.12 - Unit cell and atomic position data extracted from Rietveld refinement of  $\text{La}_8\text{Sr}_2\text{Si}_6\text{O}_{26}$  after reaction with PTFE.

Sample	Space Group	$\chi^2$	wRp	Volume ( $\text{\AA}^3$ )	Theoretical Density ( $\text{gcm}^{-3}$ )	
$\text{La}_8\text{Sr}_2\text{Si}_6\text{O}_{26}$ _PTFE	P63/m	3.506	2.2%	597.8	5.175	
<b>a(<math>\text{\AA}</math>)</b>	9.787	<b>b(<math>\text{\AA}</math>)</b>	9.787	<b>c(<math>\text{\AA}</math>)</b>	7.207	
Atomic Coordinates						
Atom	X	Y	Z	Ui/Ue*100	Multiplicity	Site Occ
La1	0.3333	0.6667	0.0005(5)	0.58(5)	4	0.49
Sr1	0.3333	0.6667	0.0005(5)	0.58(5)	4	0.51
La2	0.0112(3)	0.2462(3)	0.25	0.57(5)	6	0.99
Si1	0.4013(6)	0.3750(5)	0.25	0.49(8)	6	1
O1	0.3156(4)	0.4778(4)	0.25	0.79*	6	1
O2	0.5953(5)	0.4724(5)	0.25	2.03*	6	1
O3	0.3442(4)	0.2551(4)	0.07933(4)	2.54*	12	1
O4	0	0	0.25	12.71(18)	2	0.999
Oi	0.0396(24)	0.1403(26)	0.3097(25)	2.5	12	0.017(6)
Anisotropic thermal parameters						
Atom	U11	U22	U33	U12	U13	U23
O1	2.88(21)	1.01(18)	-0.25(11)	1.50(18)	0	0
O2	2.20(23)	1.42(20)	2.56(25)	0.80(19)	0	0
O3	6.71(25)	2.01(15)	0.68(10)	2.42(16)	-2.65(13)	0.92(10)

As with the PVDF sample, the interstitial fluorine atoms are located in the c axis channel but pushed slightly further away from the central O4 atom due to the greater occupancy of fluorine in the PTFE sample. (Figure 4.25) The thermal displacement parameter for the O4 channel site is also very high especially along the c direction, suggesting a range of local displacements due to the presence of interstitial ions.

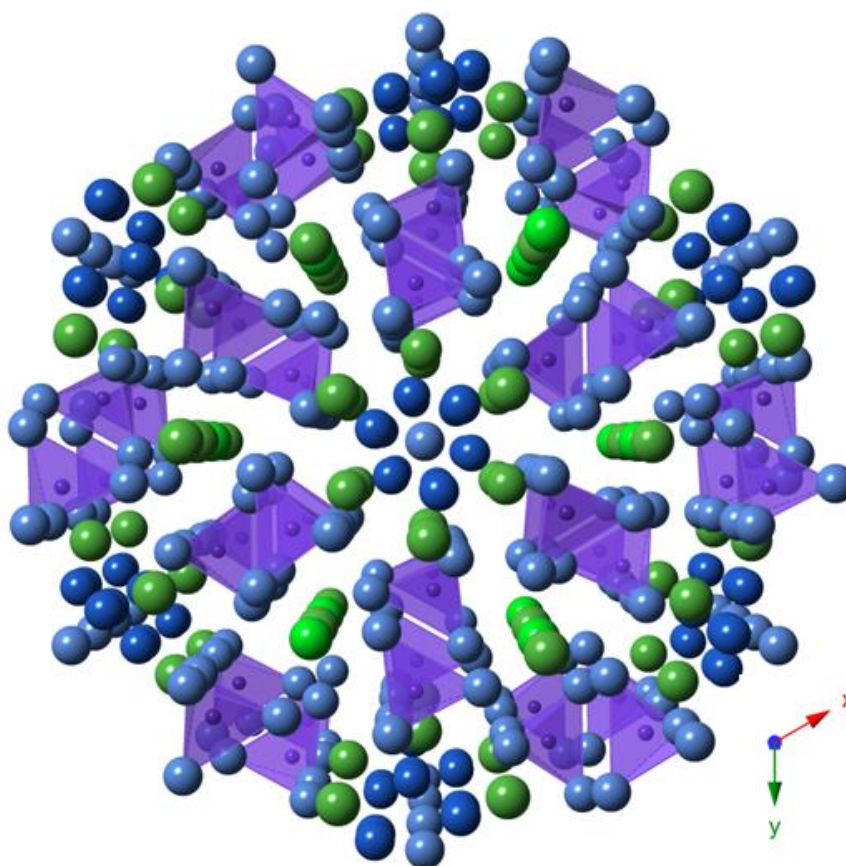


Figure 4.25 – Refined structure of  $\text{La}_8\text{Sr}_2\text{Si}_6\text{O}_{26}$  reacted with PTFE with Sr/La (green), Si (purple), oxygen (blue) and interstitial sites (dark blue).

#### 4.5.2.3 Hydration

A sample of  $\text{La}_8\text{Sr}_2\text{Si}_6\text{O}_{26}$  was placed in a furnace which was heated to 600 °C and then slow cooled in a wet  $\text{N}_2$  atmosphere. This slow cooling in a wet atmosphere allowed for water to be incorporated into the structure expanding the unit cell. Rietveld refinement suggests a cell expansion to a volume of  $594.33 \text{ \AA}^3$  which is  $3.72 \text{ \AA}^3$  larger than the dry sample; it was not possible to locate the interstitial water molecules from the X-ray diffraction data. Thermo gravimetric analysis suggests a total of 0.18 wt% water was incorporated into the sample, which, when the formula mass of the apatite is taken into consideration, corresponds to an incorporation of 0.2

moles of water per mole of sample. These preliminary results allowed for a successful application to use the POLARIS beam line at the ISIS neutron source.

A neutron diffraction pattern for the hydrated sample was collected at room temperature in a vanadium can. Rietveld refinement was performed on the resulting pattern and a graphical fit to the backscattering detector bank (bank 5) is shown in Figure 4.26. Rietveld refinement allowed for the extraction of unit cell and structural data, as shown in Table 4.13.

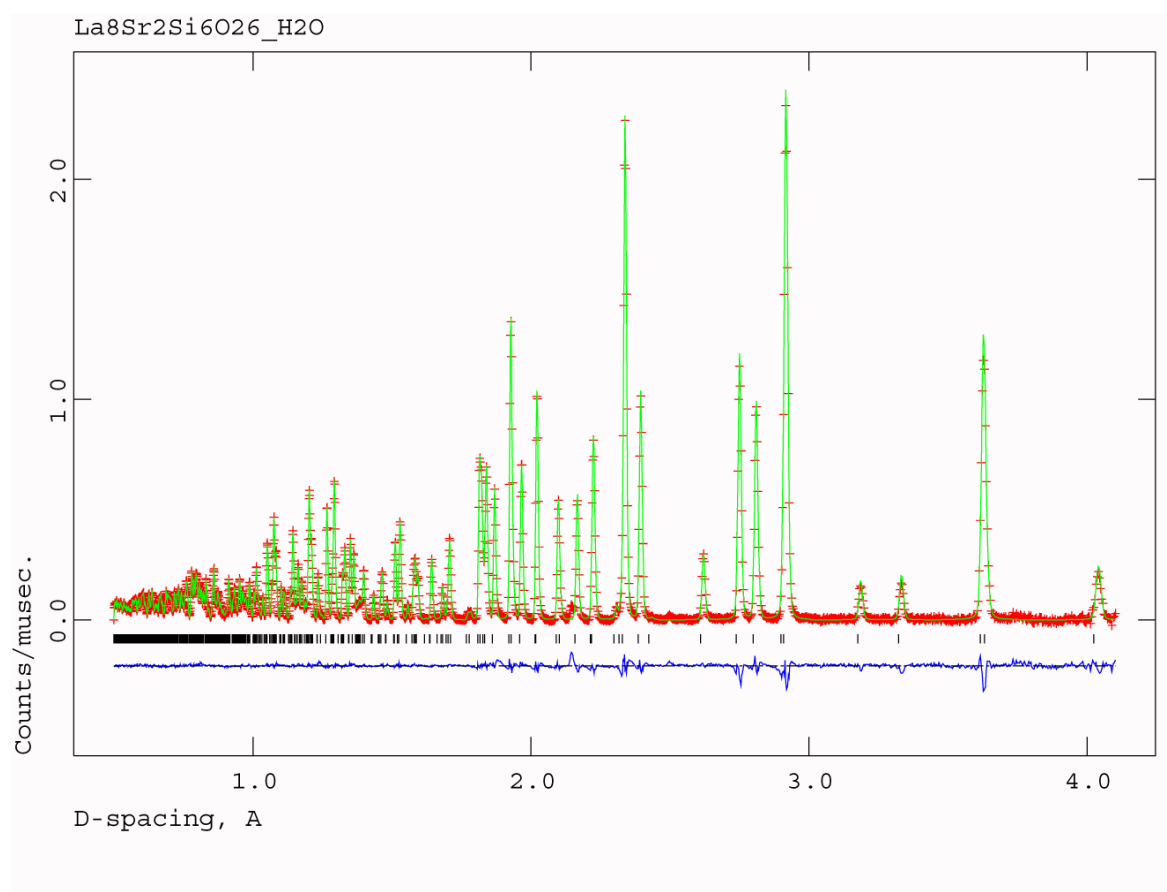


**Figure 4.26 - Observed (red), Calculated (green) and Difference (blue) profiles for the Rietveld refinement of hydrated  $\text{La}_8\text{Sr}_2\text{Si}_6\text{O}_{26}$  from the back scattering bank.**

Table 4.13 - Atomic coordinates and unit cell data extracted from the Rietveld refinement of neutron data for hydrated  $\text{La}_8\text{Sr}_2\text{Si}_6\text{O}_{26}\cdot\text{H}_2\text{O}$ .

Sample	Space Group	$\chi^2$	wRp	Volume ( $\text{\AA}^3$ )	Theoretical Density ( $\text{g cm}^{-3}$ )	
$\text{La}_8\text{Sr}_2\text{Si}_6\text{O}_{26}\cdot\text{H}_2\text{O}$	P63/m	7.745	1.4%	594.44	5.23	
<b>a(<math>\text{\AA}</math>)</b>	9.728(1)	<b>b(<math>\text{\AA}</math>)</b>	9.728(1)	<b>c(<math>\text{\AA}</math>)</b>	7.253(2)	
Atomic Coordinates						
Atom	X	Y	Z	Ui/Ue*100	Multiplicity	Site Occ
La1	1/3	2/3	-0.0009(1)	0.531(16)	4	0.5
Sr1	1/3	2/3	-0.0009(1)	0.531(16)	4	0.5
La2	0.0132 (7)	0.2449(8)	1/4	0.454(12)	6	1
Si1	0.4009(6)	0.3710(3)	1/4	0.301(22)	6	1
O1	0.3214(2)	0.4831 (1)	1/4	0.81*	6	1
O2	0.5939(1)	0.4712(1)	1/4	0.71*	6	1
O3	0.3432 (4)	0.2541 (2)	0.0705(2)	0.98*	12	1
O4	0	0	1/4	1.43*	2	0.981(6)
Oi	-0.0410(56)	0.1503 (48)	0.6768 (35)	2.5	12	0.020(2)
Anisotropic Thermal Parameters						
	U11	U22	U33	U12	U13	U23
O1	1.49(5)	1.11(6)	0.496(47)	1.084(49)	0	0
O2	0.24(5)	0.37(4)	1.260(57)	-0.001(41)	0	0
O3	2.39(5)	0.68(4)	0.404(26)	0.774(34)	-0.798(31)	-0.234(27)
O4	0.84(6)	0.84(6)	2.598(120)	0.418(29)	0	0

The atomic positions extracted from the refinement show that unlike with the germanate apatite samples the interstitial oxygen positions from the water molecules are located exclusively in the central channel. Whereas in hydrated  $\text{La}_8\text{Sr}_2\text{Ge}_6\text{O}_{26}\cdot\text{H}_2\text{O}$  a large portion of the interstitial anions were located within the  $\text{GeO}_4$  tetrahedra leading to the formation of  $\text{GeO}_5$  units. This is likely to be due to the reduced ability of silicon to form a  $\text{SiO}_5$  unit and could possibly explain the reason why germanium apatite materials can achieve a greater level of hydration / interstitial anion content, there are more places within the structure that can accommodate interstitial water molecules.

Figure 4.27 shows the structure of hydrated  $\text{La}_8\text{Sr}_2\text{Si}_6\text{O}_{26}$  with the interstitial water molecules shown in dark blue.

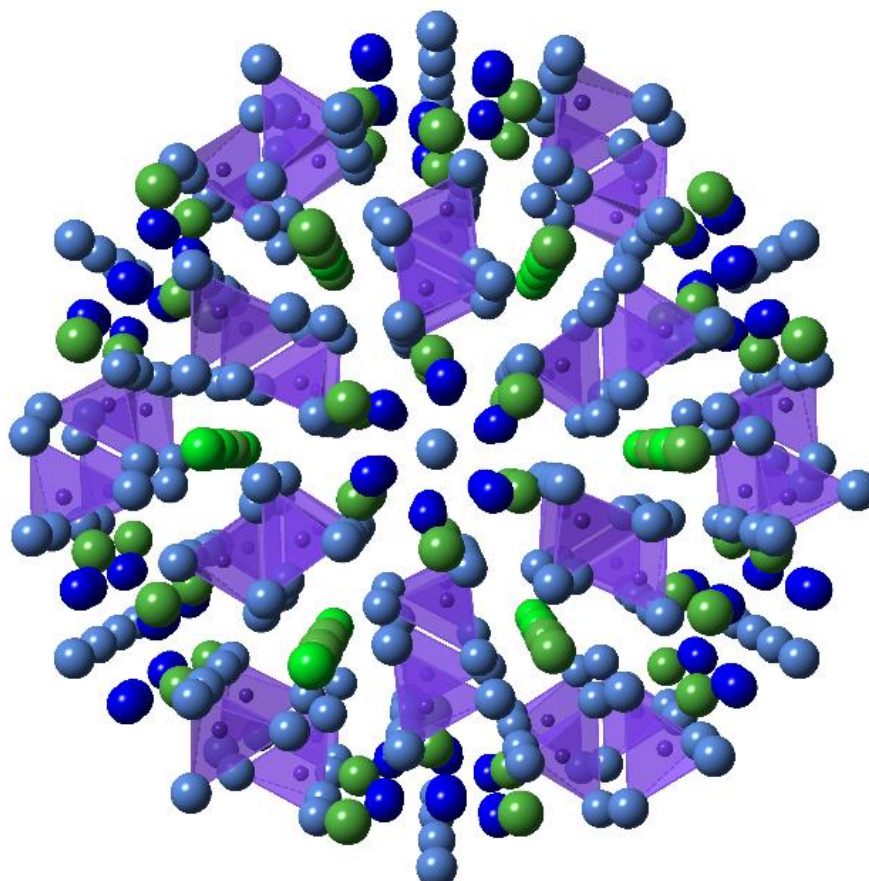


Figure 4.27 - Structure of hydrated  $\text{La}_8\text{Sr}_2\text{Si}_6\text{O}_{26}$  looking down the c axis, green atoms are La/Sr, purple represents Si, pale blue are O, interstitial water molecules are shown in dark blue.

## 4.6 Conclusions

Both silicate and germanate apatite systems were synthesised and investigated for their ability to incorporate water and fluorine. Initially  $\text{La}_8\text{Sr}_2(\text{Ge}/\text{Si})_6\text{O}_{26}$  was selected as this was a fully stoichiometric sample with no interstitial oxide ions leaving a larger amount of space internally. The larger  $\text{La}_8\text{Sr}_2\text{Ge}_6\text{O}_{26}$  incorporated a larger amount of

water, 0.84 mol compared with just 0.2 mol for the silicate sample. A large portion of this increase can be attributed to the ability of the  $\text{GeO}_4$  tetrahedra to accommodate an extra oxide ion to form  $\text{GeO}_5$  polyhedra. The inability of silica to increase from  $\text{SiO}_4$  to  $\text{SiO}_5$  removes this additional space from the structure leaving the channel as the only space to accommodate the water molecules.

As the c-axis channel in the germanate samples is also larger than the silicate equivalent due to the larger radii of Ge it was also possible to accommodate a greater amount of water in the channel.

Fluorination in these samples was successful using both PVDF and PTFE as a fluorine source. Incorporation of fluorine had a larger increase in the volume of the unit cell when compared with the hydrated sample. In both the germanate and silicate samples fewer moles of fluorine were incorporated than the number of moles of water incorporated with hydration. In the case of the germanate samples it was expected that  $\text{GeX}_5$  ( $X = \text{O}, \text{F}$ ) units would be formed however all of the interstitials from the fluorine accommodation were located within the c-axis channel. It was not possible to differentiate between fluorine and oxygen using the neutron diffraction patterns and therefore whether the fluorine chooses a favoured oxygen site. Although due to charge balancing  $2\text{xF}^-$  will replace  $1\text{xO}^{2-}$  and therefore fluorine must be present in addition to the interstitial fluorine observed in the channel.

In the fluorinated  $\text{La}_8\text{Sr}_2\text{Si}_6\text{O}_{26}$  the fluorine was also incorporated in the channel centre for lower quantities although when PTFE was used and a larger amount was accommodated the fluorine was pushed further towards the channel edges. There have been reports of both these interstitial site positions previously for different

samples suggesting that there is not one interstitial site for silicate apatites but the positions are related to the composition of the sample and the characteristics of the incorporated ions. Raman spectroscopy indicated a Si-F bond suggesting that there is fluorine present within the SiO<sub>4</sub> groups.

The oxygen excess germanate apatite material, La<sub>9.75</sub>Ge<sub>6</sub>O<sub>26.625</sub>, which shows a triclinic structure at room temperature in dry conditions was also hydrated in an attempt to further increase the quantity of interstitial ions. This was successful and 0.81 mol of water could be accommodated. Accommodation of water transformed the triclinic P-1 structure to the hexagonal P63/m space group observed for both La<sub>8</sub>Sr<sub>2</sub>Ge<sub>6</sub>O<sub>26</sub> and La<sub>8</sub>Sr<sub>2</sub>Si<sub>6</sub>O<sub>26</sub>. Refinement of XRD data suggested a portion of the interstitial are located within the channel although the total anion content was lower than suggested by TGA implying that not all anions have been located. A transition to a hexagonal structure was also observed on heating (>650°C), although it was also not possible to locate all of the interstitial sites.

## 4.7 References

1. H. Yoshioka, Y. Nojiri, S. Tanase, *Solid State Ionics* 2008, **179**, 2165
2. L. León-Reina, J. M. Porras-Vázquez, E. R. Losilla and M. A. G. Aranda, *J. Solid State Chem.*, 2007, **180**, 1250
3. E. Kendrick, M. S. Islam and P.R. Slater, *J. Mater Chem.*, 2007, **17**, 3104
4. Orera and P.R. Slater, *Solid State Ionics*, 2010, **181**, 110
5. J.E.H. Sansom, J. R. Tolchard, M. S. Islam, D. Apperley and P. R. Slater, *J. Mater Chem.*, 2006, **16**, 1410
6. L. Leon-Reina, M.C. Martin-Sedeno, E. R. Losilla, A. Cabeza, M. Martinez-Lara, S. Bruque, F. M. B. Marques, D. V. Sheptyakov and M. A. G. Aranda, *Chem Mater.*, 2003, **15**, 2099.
7. E. Belchade, O. Masson, T. Iwata, I. Julien, K. Fukuda, P. Thomas and E. Champion, *Chem Mater.*, 2009, **21**, 2508

8. S. Guillot, S. B-Savignat, S. Lambert, R. N. Vannier, P. Roussel and F. Porcher, *J. Solid State Chem.*, 2009, **182**, 3358
9. L. León-Reina, E. R. Losilla, M. Martínez-Lara, M. C. Martín-Sedeño, S. Bruque, P. Núñez, D. V. Sheptyakov, M. A. G. Aranda, *Chem. Mater.* 2005, **17**, 596.
10. R. Haynes, S.T. Norberg, S.G. Eriksson, M.A.H. Chowdhury, C.M. Goodway, G.D. Howells, O. Kirichek and S. Hull, *J. Phys. Chem. Solids*, 2009, **251**, 4
11. . R. Tolchard and P. R. Slater, *J. of Phys. Chem. Solids*, 2008, **69**, 2433.

# 5 Yttrium and ytterbium doping in titanium doped barium scandate systems

---

## 5.1 Introduction

Barium containing perovskite systems have attracted considerable attention as proton conducting electrolytes for potential use in fuel cells.<sup>1</sup> Such systems contain oxide ion vacancies, which allow the incorporation of water and hence proton conduction.  $\text{Ba}_2\text{In}_2\text{O}_5$  is an archetypal system in this respect, allowing the incorporation of up to 1 mole of water per formula unit. This system has attracted considerable interest and through a range of studies, titanium doping has been shown to be an extremely positive strategy to optimize the performance of this material, leading to compositions with high oxide ion/proton conductivity, along with good high temperature stability towards  $\text{CO}_2$ .<sup>2-5</sup> We have been extending such studies to examine the related system,  $\text{Ba}_2\text{Sc}_2\text{O}_5$ . This  $\text{Ba}_2\text{Sc}_2\text{O}_5$  system has been previously reported to be thermally unstable above  $1000^\circ\text{C}$  with heating to higher temperatures giving  $\text{Ba}_3\text{Sc}_4\text{O}_9$  as the main phase which is a problem for sintering.<sup>5</sup> Work in our group has shown that this is due to the fact “ $\text{Ba}_2\text{Sc}_2\text{O}_5$ ” contains carbonate, such that the actual formula should be written  $\text{Ba}_2\text{Sc}_{2-x}\text{C}_x\text{O}_{5+x/2}$ . Thus on heating above  $1000^\circ\text{C}$   $\text{CO}_2$  is lost and the perovskite phase decomposes. The thermal stability has shown to be improved by phosphate doping, to give  $\text{Ba}_2\text{Sc}_{2-x}\text{P}_x\text{O}_{5+x}$ , with samples showing high conductivity as well as good  $\text{CO}_2$

stability<sup>6</sup>. In this work we extend these studies to investigate the stabilization of  $\text{Ba}_2\text{Sc}_2\text{O}_5$  with other dopants. A particular aim has been to reduce the Scandium content as a result of the high cost of Scandium.

## 5.2 Experimental

Stoichiometric mixtures of high purity barium carbonate, scandium (III) oxide, titanium (IV) oxide,  $\text{M}_2\text{O}_3$  (where  $\text{M} = \text{Y} / \text{Yb}$ ) were ground together and heated to  $1100^\circ\text{C}$  for 12 h. Samples were then reground and heated for a second time to  $1100^\circ\text{C}$  for a further 12 h. Following this second heat treatment the samples were re ground in a Fritsch pulverisette planetary ball mill (zirconia vessels and balls) at 350 rpm for 1 h and pressed into 13 mm pellets at a pressure of approximately  $3,000 \text{ kg cm}^{-2}$ . The pellets were sintered at  $1400^\circ\text{C}$  for 6 h in air.

Powder X-ray diffraction was used to check phase purity using a Bruker D8 diffractometer with  $\text{Cu K}\alpha_1$  radiation in transmission mode. Rietveld refinement was performed for structure determination using the GSAS suite of programs and Topas v4.2.<sup>7,8</sup>

## 5.3 Ti doping in $\text{BaScO}_{2.5}$

Perovskite type " $\text{Ba}_2\text{Sc}_2\text{O}_5$ " is an unstable material above  $1000^\circ\text{C}$  which contains a lot of bond strain and contains carbonate to relieve this.<sup>6</sup> This can be transformed into a cubic perovskite structure by doping on the scandium site. A titanium doped sample was initially prepared to stabilise the cubic perovskite form of the structure

with anion vacancies. Samples containing 30% and 50% titanium substitution for scandium were prepared and analysed using XRD. The structure of the  $\text{BaSc}_{0.7}\text{Ti}_{0.3}\text{O}_{2.65}$  sample can be fitted to a cubic perovskite ( $\text{ABX}_3$ ) structure. This was refined to a Pm-3m cubic structure with just three sites (Ti and Sc share the same site)(Table 5.1 and Figure 5.1).

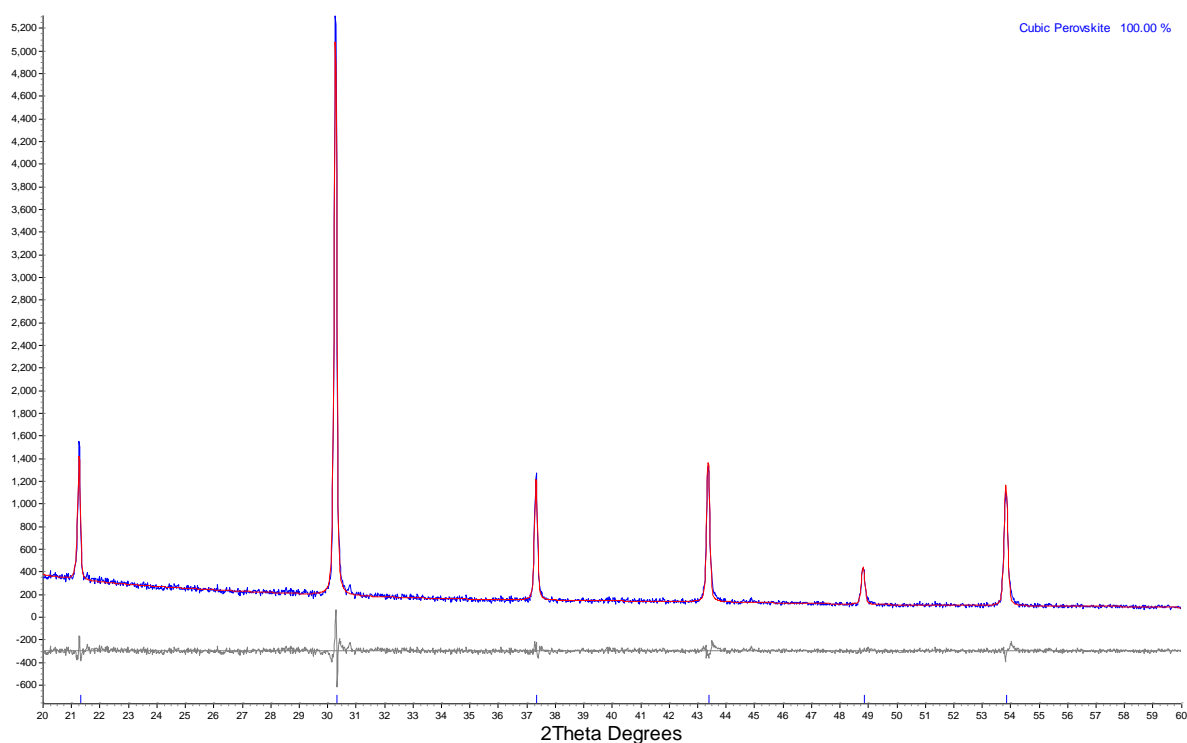


Figure 5.1- Observed (blue), Calculated (red) and difference (grey) profiles for  $\text{BaSc}_{0.7}\text{Ti}_{0.3}\text{O}_{2.65}$ .

As all of the atomic positions in the Pm-3m space group are considered special positions these cannot be refined which reduces the number of parameters which can be refined to just the background, unit cell size, thermal parameters, crystallite size and strain.

Table 5.1 - Refined structural data for BaSc<sub>0.7</sub>Ti<sub>0.3</sub>O<sub>2.65</sub>

Sample Name	Space Group	$\chi^2$	wRp	a(Å)		
BaSc <sub>0.7</sub> Ti <sub>0.3</sub> O <sub>2.65</sub>	Pm-3m	1.4	8.2%	4.164(2)		
Atomic Positions						
Atom	x	y	z	Ui/Ue*100	Multiplicity	Site Occ
Ba	0	0	0	3.97(3)	1	1
Sc	½	½	½	3.38(5)	1	0.7
Ti	½	½	½	3.38(5)	1	0.3
O	½	½	0	6.32(6)	3	1

The second sample, BaSc<sub>0.5</sub>Ti<sub>0.5</sub>O<sub>2.75</sub>, could also be refined to the same Pm-3m space group although a cell contraction is observed with a equalling 4.132(1) Å. The cell contraction can be correlated with the smaller size of Ti<sup>4+</sup> versus Sc<sup>3+</sup>

AC impedance measurements were performed on the samples to see the effects on the titanium doping on the conductivity of the samples. The BaSc<sub>0.7</sub>Ti<sub>0.3</sub>O<sub>2.65</sub> sample had poor mechanical stability and it was not possible to measure the conductivity of the sample. The mechanical strength of the sample was improved by the incorporation of boron on the scandium site as boron has been reported in the past to act as a sintering aid to lower sintering temperature and improve sintering.<sup>9, 10</sup> The sample was re made adding 5 mol% boron (H<sub>3</sub>BO<sub>3</sub>) in place of scandium to make the sample BaSc<sub>0.65</sub>Ti<sub>0.3</sub>B<sub>0.05</sub>O<sub>2.65</sub>.

AC impedance measurements were collected as described in section 2.5 using the HP 4192A impedance analyser. Measurements were taken in a N<sub>2</sub> atmosphere in both wet and dry conditions an example of the spectra obtained is shown in Figure 5.2. It was possible to resolve bulk and grain boundary components at low temperatures but at higher temperatures overlapping of the semi circles was

observed. As a result of the difficulty resolving bulk and grain boundary components at higher temperature, total (bulk + gb) conductivities are reported in this work.

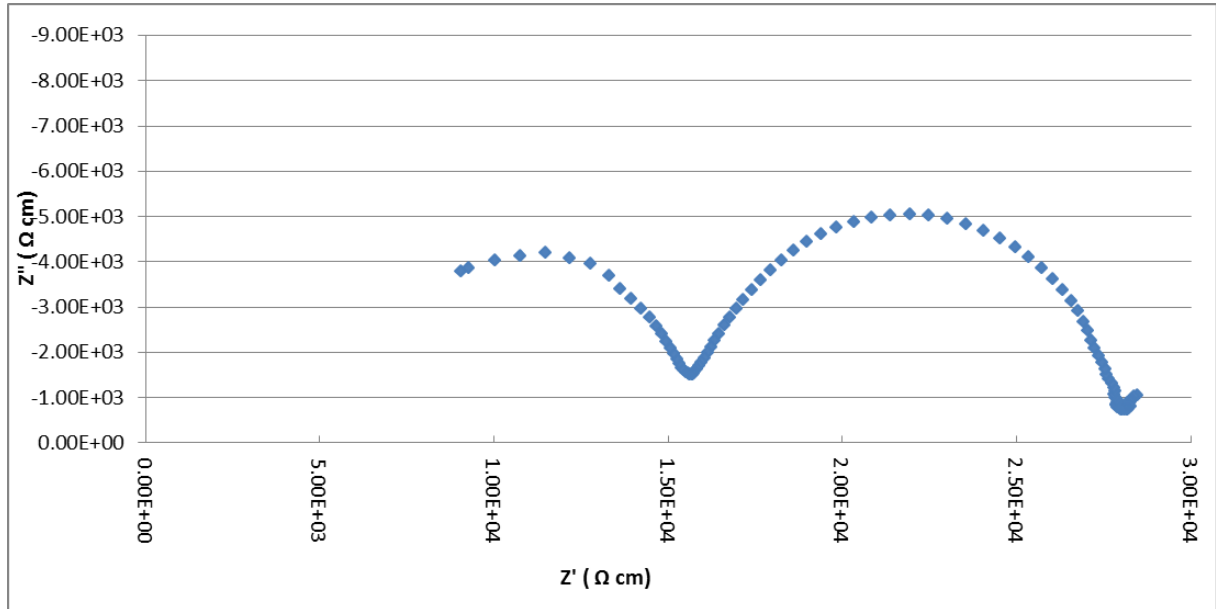


Figure 5.2 - Impedance spectra for BaSc<sub>0.65</sub>Ti<sub>0.3</sub>B<sub>0.05</sub>O<sub>2.65</sub> in dry N<sub>2</sub> at 400 °C.

The sample BaSc<sub>0.65</sub>Ti<sub>0.3</sub>B<sub>0.05</sub>O<sub>2.65</sub> has a greater conductivity,  $1.3 \times 10^{-3} \text{ S cm}^{-1}$  at 500°C in dry conditions compared with  $4.3 \times 10^{-5} \text{ S cm}^{-1}$  for the lower scandium content sample BaSc<sub>0.5</sub>Ti<sub>0.5</sub>O<sub>2.75</sub>. In wet conditions the former sample had a small increase in conductivity to  $1.5 \times 10^{-3} \text{ S cm}^{-1}$  at 500°C whereas for the latter sample the conductivity increased to  $1.3 \times 10^{-4} \text{ S cm}^{-1}$  (Table 5.2). Further values can be seen in Figure 5.3. It can be seen at the conditions tested that the “Sc<sub>0.65</sub>” sample has a higher conductivity than the “Sc<sub>0.5</sub>” sample and therefore this was the sample used for further co-doping studies.

Table 5.2 - Conductivity values and activation energies for titanium doped BaScO<sub>2.5</sub>

Sample	Conductivity 500°C (S cm <sup>-1</sup> )	Activation energy (eV)
BaSc <sub>0.65</sub> Ti <sub>0.3</sub> B <sub>0.05</sub> O <sub>2.65</sub> (Dry)	1.3x10 <sup>-3</sup>	0.57
BaSc <sub>0.65</sub> Ti <sub>0.3</sub> B <sub>0.05</sub> O <sub>2.65</sub> (Wet)	1.5x10 <sup>-3</sup>	0.58
BaSc <sub>0.5</sub> Ti <sub>0.5</sub> O <sub>2.75</sub> (Dry)	4.3x10 <sup>-5</sup>	0.61
BaSc <sub>0.5</sub> Ti <sub>0.5</sub> O <sub>2.75</sub> (Wet)	1.3x10 <sup>-4</sup>	0.45

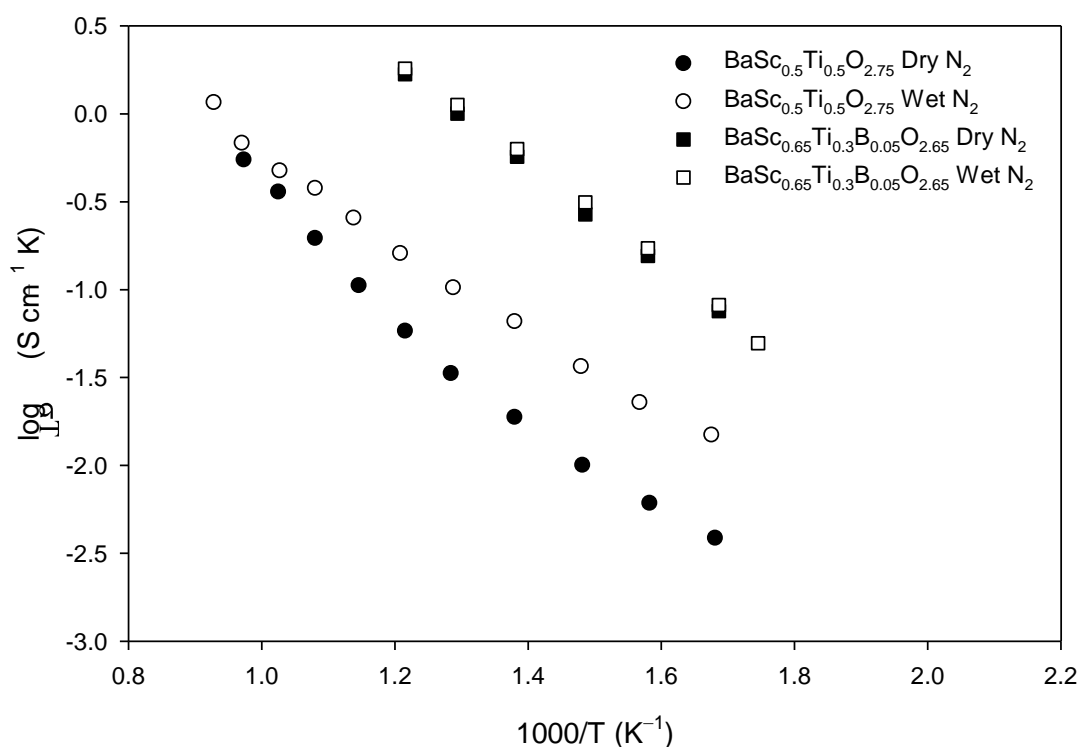


Figure 5.3 - Plot of  $\log \sigma T$  vs  $1000/T$  in dry and wet N<sub>2</sub> for BaSc<sub>0.5</sub>Ti<sub>0.5</sub>O<sub>2.75</sub> and BaSc<sub>0.65</sub>Ti<sub>0.3</sub>B<sub>0.05</sub>O<sub>2.65</sub>.

#### 5.4 Yttrium doping in BaSc<sub>0.65</sub>Ti<sub>0.3</sub>B<sub>0.05</sub>O<sub>2.65</sub>.

Yttrium was doped into BaSc<sub>0.65</sub>Ti<sub>0.3</sub>B<sub>0.05</sub>O<sub>2.65</sub> in place of scandium, in an attempt to lower the scandium content without a negative effect on the observed ionic conductivity. These samples were prepared in the same way as the initial sample.

The samples were analysed using XRD, and this showed that doping was successful with a peak shift to lower angles due to an expansion in the unit cell on increased

yttrium content. The structure was refined using Rietveld refinement to extract information on the changes to the unit cell lengths (Table 5.3).

**Table 5.3 - Unit cell parameters for  $\text{BaSc}_{0.65}\text{Ti}_{0.3}\text{B}_{0.05}\text{O}_{2.65}$  samples doped with Yttrium**

Sample	Unit Cell a (Å)
$\text{BaSc}_{0.65}\text{Ti}_{0.3}\text{B}_{0.05}\text{O}_{2.65}$	4.164(2)
$\text{BaSc}_{0.6}\text{Y}_{0.05}\text{Ti}_{0.3}\text{B}_{0.05}\text{O}_{2.65}$	4.165(2)
$\text{BaSc}_{0.5}\text{Y}_{0.15}\text{Ti}_{0.3}\text{B}_{0.05}\text{O}_{2.65}$	4.194(3)
$\text{BaSc}_{0.45}\text{Y}_{0.2}\text{Ti}_{0.3}\text{B}_{0.05}\text{O}_{2.65}$	4.211(2)
$\text{BaSc}_{0.4}\text{Y}_{0.25}\text{Ti}_{0.3}\text{B}_{0.05}\text{O}_{2.65}$	4.209(1)
$\text{BaSc}_{0.35}\text{Y}_{0.3}\text{Ti}_{0.3}\text{B}_{0.05}\text{O}_{2.65}$	4.224(2)
$\text{BaSc}_{0.3}\text{Y}_{0.35}\text{Ti}_{0.3}\text{B}_{0.05}\text{O}_{2.65}$	4.234(2)
$\text{BaSc}_{0.25}\text{Y}_{0.4}\text{Ti}_{0.3}\text{B}_{0.05}\text{O}_{2.65}$	4.250(2)
$\text{BaSc}_{0.2}\text{Y}_{0.45}\text{Ti}_{0.3}\text{B}_{0.05}\text{O}_{2.65}$	4.265(3)

It can be seen that as predicted an expansion is seen in the unit cell on substitution of scandium for yttrium due to the larger size of the  $\text{Y}^{3+}$  ion (Figure 5.4).

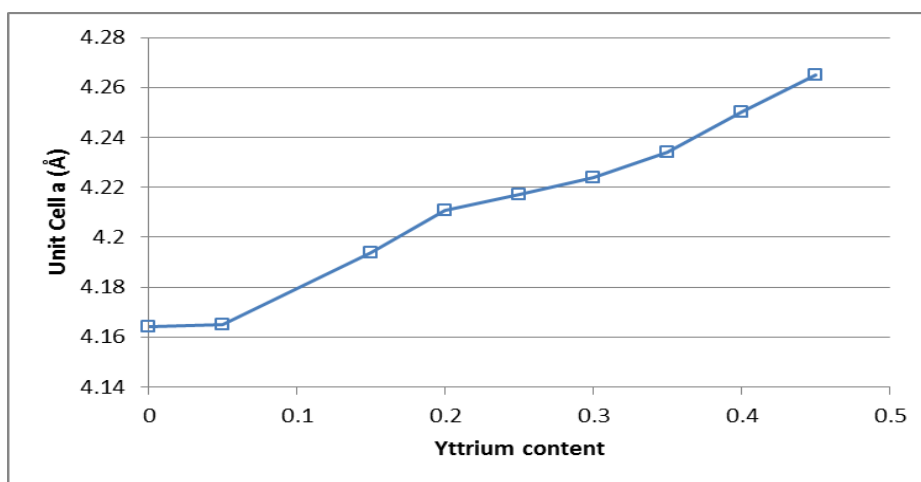


**Figure 5.4 - Unit cell length changes on increasing yttrium content**

### 5.4.1 Conductivity

AC impedance spectroscopy was performed on the samples to determine the effects of yttrium substitution on the ionic conductivity of the samples. Measurements were recorded in both dry and wet N<sub>2</sub> atmospheres at various temperatures between 200 – 800°C. It was not possible to fully resolve the bulk and grain boundary components for all of the samples, and total conductivity values are given for comparison between samples. The parent material BaSc<sub>0.65</sub>Ti<sub>0.3</sub>B<sub>0.05</sub>O<sub>2.65</sub> had a conductivity of 1.3 x 10<sup>-3</sup> S cm<sup>-1</sup> at 500°C in dry conditions, which is higher than the conductivities observed for all of the yttrium doped samples excluding BaSc<sub>0.25</sub>Y<sub>0.4</sub>Ti<sub>0.3</sub>B<sub>0.05</sub>O<sub>2.65</sub> which matched the parent material at higher temperatures but at lower temperatures exhibited a small increase over the parent (Figure 5.5). The activation energies and conductivity values for the remaining samples are shown in Table 5.4.

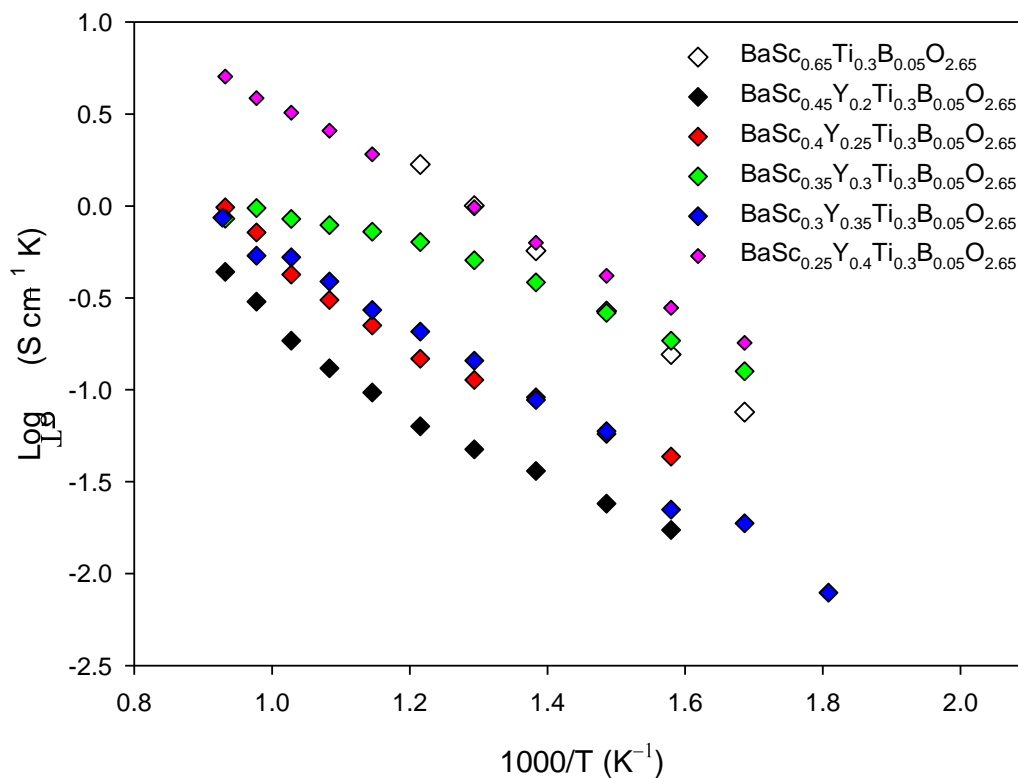


Figure 5.5 - Conductivity plot for BaSc<sub>(1-x)</sub>Y<sub>x</sub>Ti<sub>0.3</sub>B<sub>0.05</sub>O<sub>2.65</sub> samples in Dry N<sub>2</sub>.

**Table 5.4 - Conductivity and activation energy values for  $\text{BaSc}_{(0.65-x)}\text{Y}_x\text{Ti}_{0.3}\text{B}_{0.05}\text{O}_{2.65}$  samples in a dry  $\text{N}_2$  atmosphere.**

Sample	Conductivity 500°C ( $\text{S cm}^{-1}$ )	Activation energy (eV)
<b><math>\text{BaSc}_{0.65}\text{Ti}_{0.3}\text{B}_{0.05}\text{O}_{2.65}</math> (Dry)</b>	$1.3 \times 10^{-3}$	0.568
$\text{BaSc}_{0.45}\text{Y}_{0.2}\text{Ti}_{0.3}\text{B}_{0.05}\text{O}_{2.65}$	$6.1 \times 10^{-5}$	0.414
$\text{BaSc}_{0.4}\text{Y}_{0.25}\text{Ti}_{0.3}\text{B}_{0.05}\text{O}_{2.65}$	$1.5 \times 10^{-5}$	0.402
$\text{BaSc}_{0.35}\text{Y}_{0.3}\text{Ti}_{0.3}\text{B}_{0.05}\text{O}_{2.65}$	$3.1 \times 10^{-4}$	0.391
$\text{BaSc}_{0.3}\text{Y}_{0.35}\text{Ti}_{0.3}\text{B}_{0.05}\text{O}_{2.65}$	$1.9 \times 10^{-4}$	0.446
$\text{BaSc}_{0.25}\text{Y}_{0.4}\text{Ti}_{0.3}\text{B}_{0.05}\text{O}_{2.65}$	$1.3 \times 10^{-3}$	0.380

In wet  $\text{N}_2$  conditions, the samples doped with yttrium exhibited a significant increase in conductivity which indicates a proton conducting element to the total conductivity in wet atmospheres. In contrast, the parent sample showed only a slight increase in conductivity in the wet  $\text{N}_2$  atmosphere (Table 5.5 and Figure 5.6).

**Table 5.5 - Conductivity and activation energy values for  $\text{BaSc}_{(0.65-x)}\text{Y}_x\text{Ti}_{0.3}\text{B}_{0.05}\text{O}_{2.65}$  samples in a wet  $\text{N}_2$  atmosphere.**

Sample	Conductivity 500°C ( $\text{S cm}^{-1}$ )	Activation energy (eV)
<b><math>\text{BaSc}_{0.65}\text{Ti}_{0.3}\text{B}_{0.05}\text{O}_{2.65}</math> (Wet)</b>	$1.5 \times 10^{-3}$	0.580
$\text{BaSc}_{0.45}\text{Y}_{0.2}\text{Ti}_{0.3}\text{B}_{0.05}\text{O}_{2.65}$	$2.8 \times 10^{-5}$	0.196
$\text{BaSc}_{0.4}\text{Y}_{0.25}\text{Ti}_{0.3}\text{B}_{0.05}\text{O}_{2.65}$	$6.5 \times 10^{-4}$	0.274
$\text{BaSc}_{0.35}\text{Y}_{0.3}\text{Ti}_{0.3}\text{B}_{0.05}\text{O}_{2.65}$	$6.6 \times 10^{-4}$	0.230
$\text{BaSc}_{0.3}\text{Y}_{0.35}\text{Ti}_{0.3}\text{B}_{0.05}\text{O}_{2.65}$	$1.0 \times 10^{-3}$	0.313
$\text{BaSc}_{0.25}\text{Y}_{0.4}\text{Ti}_{0.3}\text{B}_{0.05}\text{O}_{2.65}$	$2.2 \times 10^{-3}$	0.232

It is possible that a portion of the decrease in conductivity observed for the yttrium doped samples when compared with the parent material could be related to the sample density. (Table 5.6) The parent material achieved a density that was 87% of the theoretical density for the material whereas the yttrium doped samples had a density over 10% lower between 73-76%. Density can be related to conductivity as a

lower density would increase the grain boundary component of the total resistance which is usually higher than the bulk decreasing the total conductivity. Density changes would also affect the kinetics of hydration which would result in slower hydration for the samples with higher density. This could explain the lack of increase on hydration for the parent material during the AC impedance measurements.

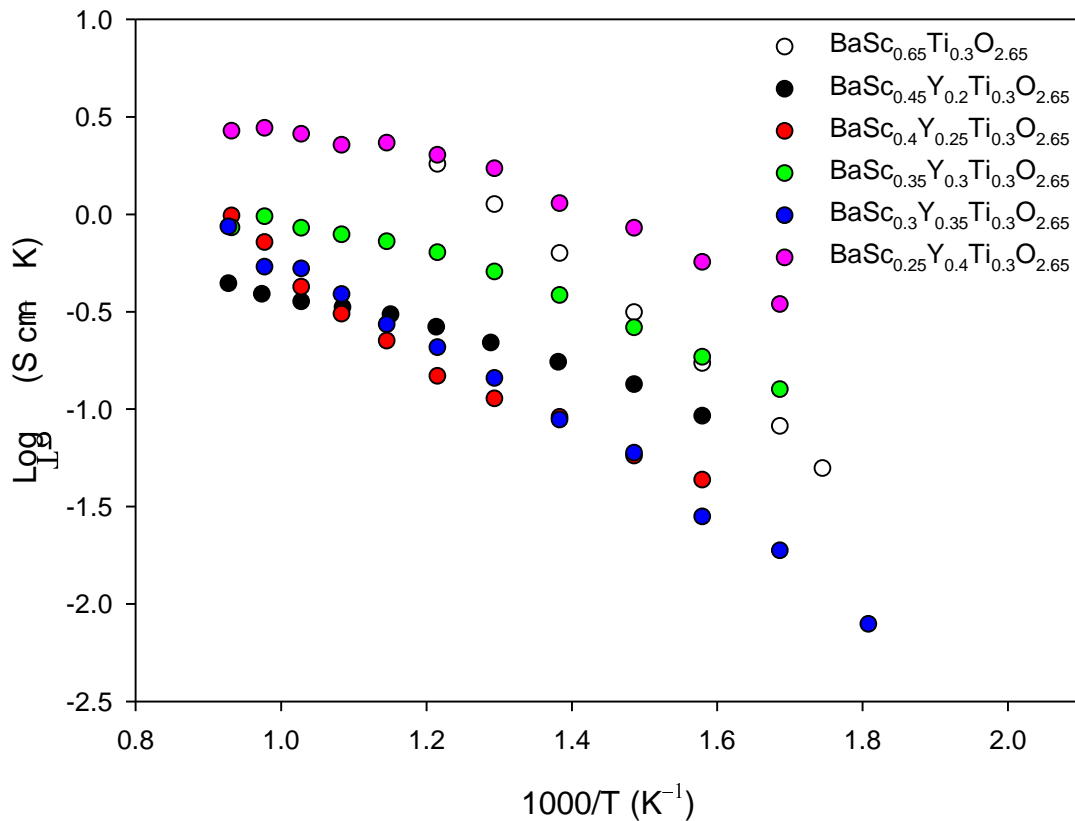


Figure 5.6 - Conductivity plot for  $\text{BaSc}_{(1-x)}\text{Y}_x\text{Ti}_{0.3}\text{B}_{0.05}\text{O}_{2.65}$  samples in Wet  $\text{N}_2$ .

Table 5.6 - Theoretical densities for  $\text{BaSc}_{0.65-x}\text{Y}_x\text{Ti}_{0.3}\text{B}_{0.05}\text{O}_{2.65}$  samples.

Sample	% Theoretical
$\text{BaSc}_{0.65}\text{Ti}_{0.3}\text{B}_{0.05}\text{O}_{2.65}$	87
$\text{BaSc}_{0.45}\text{Y}_{0.2}\text{Ti}_{0.3}\text{B}_{0.05}\text{O}_{2.65}$	73
$\text{BaSc}_{0.4}\text{Y}_{0.25}\text{Ti}_{0.3}\text{B}_{0.05}\text{O}_{2.65}$	74
$\text{BaSc}_{0.35}\text{Y}_{0.3}\text{Ti}_{0.3}\text{B}_{0.05}\text{O}_{2.65}$	75
$\text{BaSc}_{0.3}\text{Y}_{0.35}\text{Ti}_{0.3}\text{B}_{0.05}\text{O}_{2.65}$	76
$\text{BaSc}_{0.25}\text{Y}_{0.4}\text{Ti}_{0.3}\text{B}_{0.05}\text{O}_{2.65}$	76

## 5.4.2 Hydration of yttrium doped samples

In order to investigate further the effect of water incorporation, the water contents of the hydrated phases were analysed. Samples were hydrated in powdered form using a wet flow of N<sub>2</sub> gas in a furnace. The furnace was heated to 600°C for 12 h and cooled slowly at 1°C min<sup>-1</sup> under the wet N<sub>2</sub> atmosphere. This slow cooling in a wet atmosphere allowed for water to be incorporated into the structure expanding the unit cell. A peak shift in the XRD patterns to lower 2θ values confirmed the expansion in the unit cell for the hydrated samples. Rietveld refinement of the XRD data was used to measure the expansion in the unit cell caused by the incorporation of water. (Table 5.7)

**Table 5.7 - Unit cell volumes for hydrated barium scandate samples.**

Sample	Hydrated Volume (Å <sup>3</sup> )
BaSc <sub>0.65</sub> Ti <sub>0.3</sub> B <sub>0.05</sub> O <sub>2.65</sub>	72.60
BaSc <sub>0.45</sub> Y <sub>0.2</sub> Ti <sub>0.3</sub> B <sub>0.05</sub> O <sub>2.65</sub>	74.71
BaSc <sub>0.4</sub> Y <sub>0.25</sub> Ti <sub>0.3</sub> B <sub>0.05</sub> O <sub>2.65</sub>	75.28
BaSc <sub>0.35</sub> Y <sub>0.3</sub> Ti <sub>0.3</sub> B <sub>0.05</sub> O <sub>2.65</sub>	75.99
BaSc <sub>0.25</sub> Y <sub>0.4</sub> Ti <sub>0.3</sub> B <sub>0.05</sub> O <sub>2.65</sub>	76.82

TGA was used to determine the amount of water incorporated within the hydrated samples. (Figure 5.7) Samples were heated to 900°C in a N<sub>2</sub> atmosphere with a heating rate of 10°C min<sup>-1</sup>. The TGA data shows that more than 1% water was incorporated for all of the samples (Table 5.8). This water content relates to 0.19-0.23 moles of water per mole of sample. As there are 0.35 oxygen vacancies in the structure per mole of sample, the vacancies have not been completely filled by hydration.

Table 5.8 - Water incorporation % in barium scandate samples.

Sample	Water content (%)	Moles water per mole sample
$\text{BaSc}_{0.65}\text{Ti}_{0.3}\text{B}_{0.05}\text{O}_{2.65}$	1.79	0.23
$\text{BaSc}_{0.45}\text{Y}_{0.2}\text{Ti}_{0.3}\text{B}_{0.05}\text{O}_{2.65}$	1.76	0.23
$\text{BaSc}_{0.4}\text{Y}_{0.25}\text{Ti}_{0.3}\text{B}_{0.05}\text{O}_{2.65}$	1.53	0.20
$\text{BaSc}_{0.35}\text{Y}_{0.3}\text{Ti}_{0.3}\text{B}_{0.05}\text{O}_{2.65}$	1.43	0.19
$\text{BaSc}_{0.25}\text{Y}_{0.4}\text{Ti}_{0.3}\text{B}_{0.05}\text{O}_{2.65}$	1.37	0.19

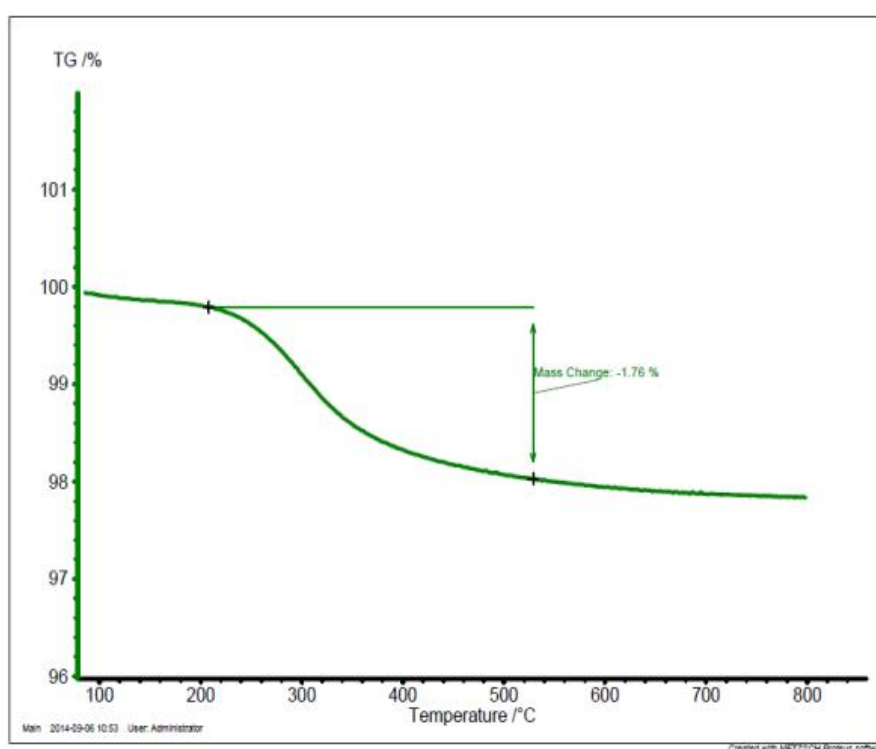


Figure 5.7 - TGA mass trace for  $\text{BaSc}_{0.45}\text{Y}_{0.2}\text{Ti}_{0.3}\text{B}_{0.05}\text{O}_{2.65}$

### 5.1.1 Neutron diffraction studies

As the  $\text{BaSc}_{0.25}\text{Y}_{0.4}\text{Ti}_{0.3}\text{B}_{0.05}\text{O}_{2.65}$  sample exhibited the highest conductivity values it was selected for neutron diffraction experiment to locate proton positions. In order to remove the effect of proton motion, data were collected with the sample in a cryostat

held at 4.2K. Due to the large absorption of neutrons by boron a sample of  $\text{BaSc}_{0.25}\text{Y}_{0.45}\text{Ti}_{0.3}\text{O}_{2.65}$  was prepared, without the addition of boron. The sample was hydrated using a wet flow of  $\text{N}_2$  gas, and for the deuterated sample the  $\text{H}_2\text{O}$  in the bubbler was replaced with  $\text{D}_2\text{O}$ . TGA indicated a water incorporation of 0.272 moles of water per mole of sample. The sample was measured on the diffractometer HRPD at ISIS in as prepared, hydrated and deuterated forms and diffraction patterns were recorded at room temperature and 4.2K. A small unknown impurity is visible in the neutron diffraction pattern which was not visible by XRD (Figure 5.8 and Figure 5.9).

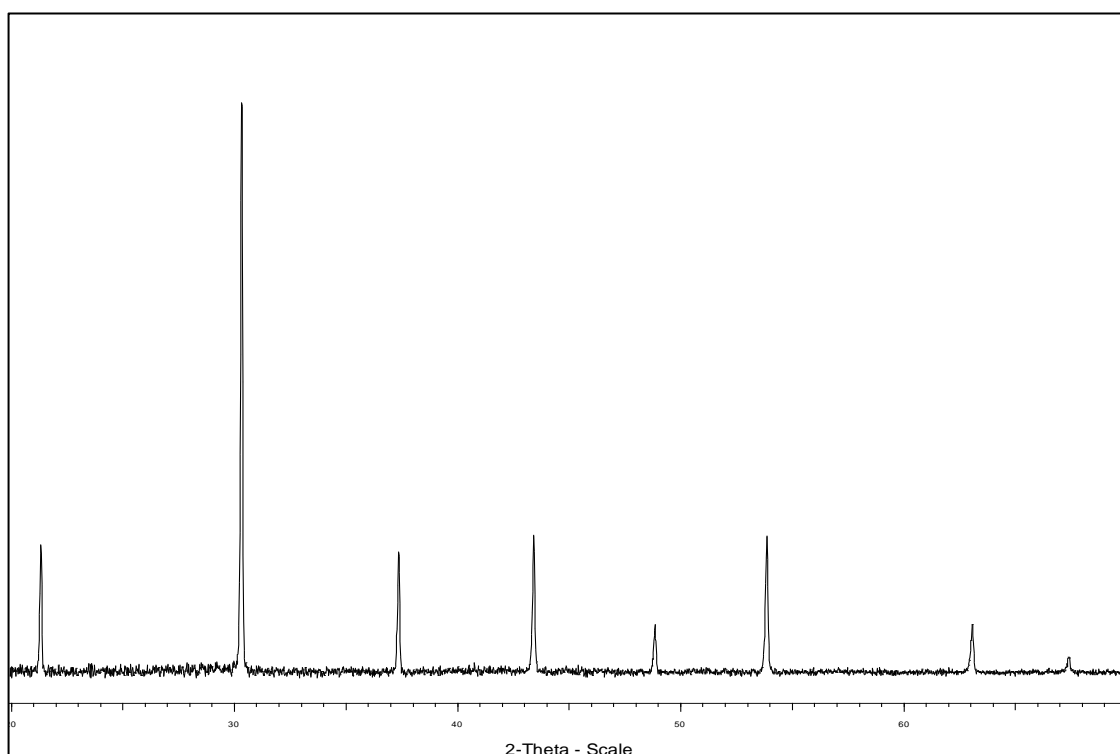
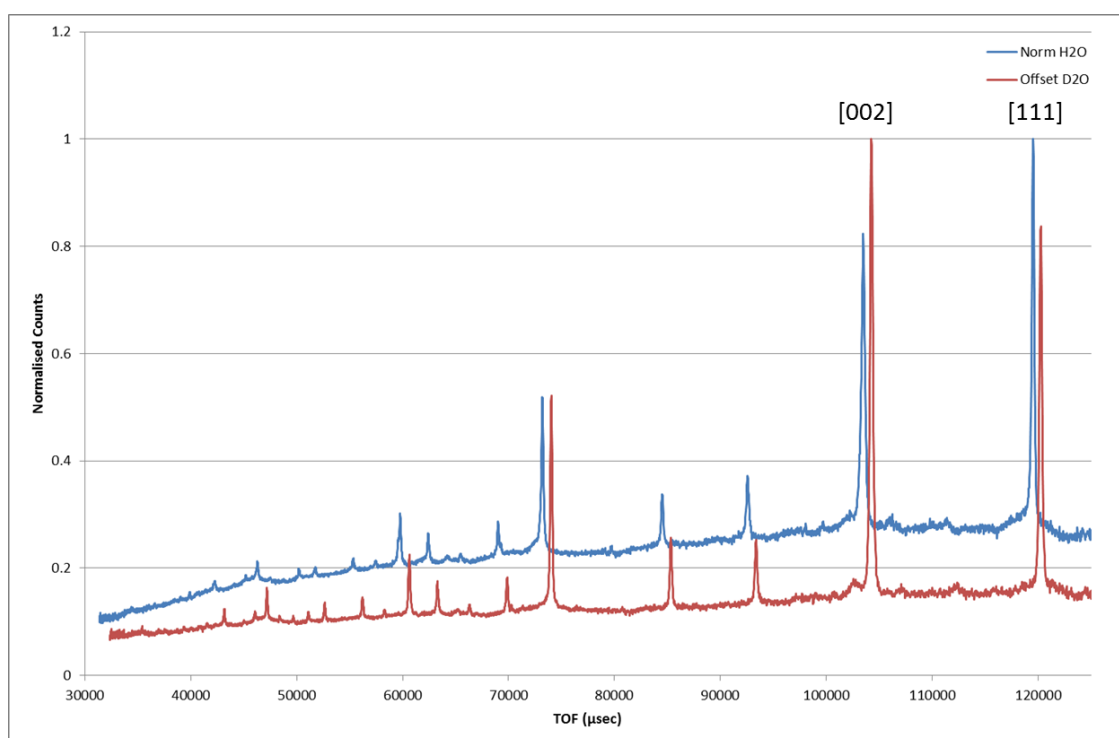


Figure 5.8 - XRD pattern for  $\text{BaSc}_{0.25}\text{Y}_{0.45}\text{Ti}_{0.3}\text{O}_{2.65}$  ISIS sample in dry conditions.

The neutron diffraction patterns for the hydrated and deuterated samples show a difference in intensity ratio between the [111] and [002] peaks due to the differences

in scattering factors of H and D; for the deuterated sample the [002] peak is the most intense and for the hydrated sample the [111] peak has the largest intensity. This can be seen in Figure 5.9 where the data has been normalised and the D<sub>2</sub>O data has been offset by 1000 μsec.



**Figure 5.9 - Neutron diffraction patterns at 4.2K for deuterated (red) and hydrated (blue) BaSc<sub>0.25</sub>Y<sub>0.45</sub>Ti<sub>0.3</sub>O<sub>2.65</sub>, D<sub>2</sub>O pattern has been offset by 1000 μsec for presentational purposes.**

Prior studies on deuterium positions in BaIn<sub>0.5</sub>Zr<sub>0.5</sub>O<sub>2.75</sub> which has a similar cubic perovskite structure to BaSc<sub>0.25</sub>Y<sub>0.45</sub>Ti<sub>0.3</sub>O<sub>2</sub> suggested 2 possible H/D sites, a 12h (0.5, y, 0) and a 24k (x, y, 0) position. Ahmed et al.<sup>11</sup> preferred the 24k site and Nagasaki et al.<sup>12</sup> preferred the 12h site. Given the similarities between the barium scandate and barium indate samples, these positions were investigated as possible

starting points for the location of H/D in  $\text{BaSc}_{0.25}\text{Y}_{0.45}\text{Ti}_{0.3}\text{O}_{2.65}$ . Rietveld refinement was performed on both the deuterated and hydrated patterns simultaneously using linked structures to locate the H/D positions. The structure was fixed to be the same for both patterns allowing only the atom type to change between H and D. It was possible to fit the structure using either the 12h or 24k positions for H/D with an improvement in fit noticed for both when compared to a structure without H/D positions ( $wR_p$  values of 3.49% and 3.54% respectively compared with 3.68% without the inclusion of a H/D position). Fourier mapping can be used to view differences between the calculated and observed structures in 3D indicating possible areas where atoms are being placed in incorrect positions or interstitial atoms may exist. Using Fourier mapping it can be seen that the areas of positive scattering difference in the  $\text{D}_2\text{O}$  sample overlap with areas of negative energy difference in the map for the  $\text{H}_2\text{O}$  sample, (Figure 5.10 a and Figure 5.10 b). This consistency gives confidence that these areas are the location of the H/D in the structure.

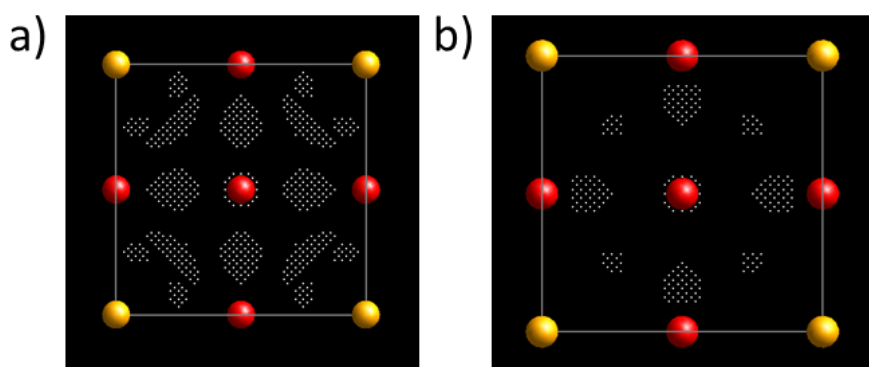


Figure 5.10 - Fourier difference map for [100] in the hydrated sample.  
b) Fourier difference map for [100] in the deuterated sample.

When sites using the 12h and 24k positions were used for refinement it was noticed that they were not in the same position as the mismatches in the Fourier map and therefore a different position was needed. From the Fourier map, a position at (0.1, 0.55, 0.8) was selected. This position has a multiplicity of 48 and therefore a lower site occupancy fraction was also selected as the starting point in the refinement, (as TGA estimates 0.272 moles of water per mole of sample). The final position of the protons was (0.1030(31), 0.5599(48), 0.7749(25)) this is a 48n position. In this case not all 48 of the equal positions would be filled as there is only a partial site occupancy of 0.0116(8) which represents 0.277 moles of water per mole sample, in very good agreement with the TGA data. Refined structural parameters are shown in Table 5.9 and a graphical representation of the fit to both hydrated and deuterated samples is shown in Figure 5.11. The oxygen atomic displacement parameter ( $U_i$ ) is high which is probably due to the presence of three different elements on the Ti / Sc / B site. These would all prefer different bond lengths to O and would therefore lead to variations in oxygen position, which show as an increased atomic displacement parameter. This could also explain the slightly long O–H (D) bond length which is 1.28(4) Å as it is possible that the protons prefer to attach to the oxygen of one of the dopants (e.g. Ti or Y) rather than a random distribution. This would make the bond length appear longer than the actual bond length as the oxygen would be moved from the (0, 0, 0.5) position used in the refinement.

Table 5.9 - Structural parameters extracted from refinement of  $\text{BaSc}_{0.25}\text{Y}_{0.45}\text{Ti}_{0.3}\text{O}_{2.65}$  neutron patterns.

Sample		Space Group	$wR_p$	$R_p$	$a$ (Å)	Volume (Å <sup>3</sup> )
$\text{BaSc}_{0.25}\text{Y}_{0.45}\text{Ti}_{0.3}\text{O}_{2.65}$		Pm-3m	3.5%	2.6%	4.278(4)	78.31(6)
Atom	X	Y	Z	Ui/Ue*100	Multiplicity	Site Occ
Ba	0	0	0	4.12(9)	1	1
Sc	0.5	0.5	0.5	2.33(11)	1	0.25
Y	0.5	0.5	0.5	2.33(11)	1	0.45
Ti	0.5	0.5	0.5	2.33(11)	1	0.3
O	0.5	0.5	0	5.93(18)	3	0.9830(61)
H/D	0.1030(31)	0.5599(48)	0.7749(25)	5.00(19)	48	0.01156(76)

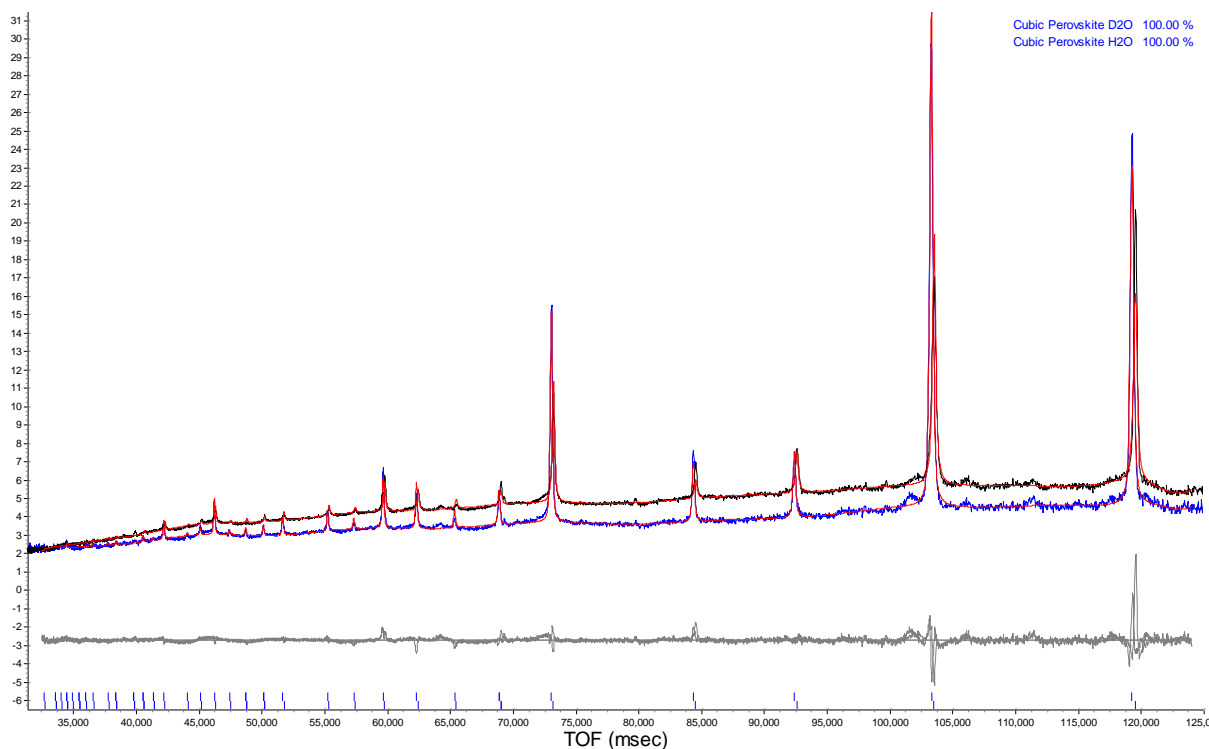


Figure 5.11 - Observed ( $\text{H}_2\text{O}$  black,  $\text{D}_2\text{O}$  blue), calculated (red) and difference (grey) profiles for the combined Rietveld refinement of HRPD data for hydrated and deuterated  $\text{BaSc}_{0.25}\text{Y}_{0.45}\text{Ti}_{0.3}\text{O}_{2.65}$ .

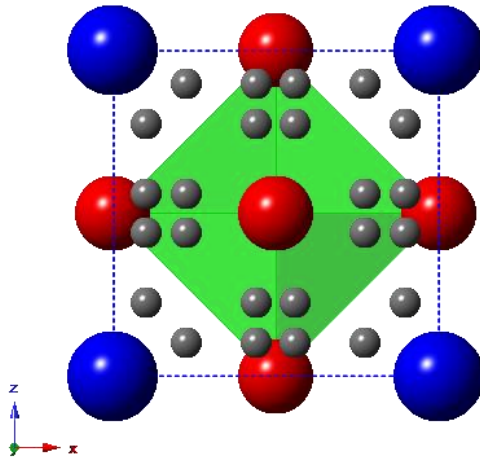


Figure 5.12 - Structure of hydrated  $\text{BaSc}_{0.25}\text{Y}_{0.45}\text{Ti}_{0.3}\text{O}_{2.65}$  seen from [100] with Ba (blue), Sc (green), O (red) and H (grey).

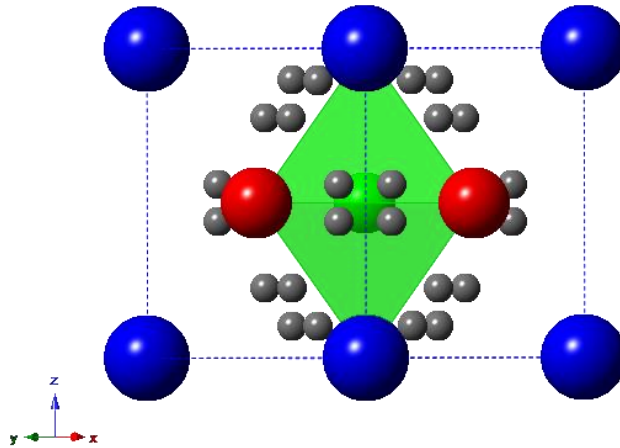


Figure 5.13 - Structure of hydrated  $\text{BaSc}_{0.25}\text{Y}_{0.45}\text{Ti}_{0.3}\text{O}_{2.65}$  seen from [110] with Ba (blue), Sc (green), O (red) and H (grey).

When the final structure is compared with the Fourier maps it can be seen that the proton positions lie in the same place as the intensity mismatch in the Fourier maps (the structure can be seen looking at the [100] plane in Figure 5.12 and the [110] in Figure 5.13.).

### 5.1.1 CO<sub>2</sub> Stability

One of the issues with some proton conducting perovskites, eg. Yttrium doped BaCeO<sub>3</sub>, is the instability towards CO<sub>2</sub> at fuel cell operating temperatures. therefore the stability of these mixed Sc/Y/Ti systems were analysed. The stability to CO<sub>2</sub> was tested using both TGA and by XRD of samples which had been heated in a CO<sub>2</sub> atmosphere. The samples tested by TGA had no change between room temperature and 900°C in a CO<sub>2</sub> atmosphere. Samples were then tested using a flow of CO<sub>2</sub> gas in a furnace which was heated to 800°C for 12 h and then cooled at 1°C min<sup>-1</sup>. The samples were initially tested using a dry CO<sub>2</sub> gas flow and exhibited no change in XRD pattern after a 24 h heat treatment (Figure 5.14).

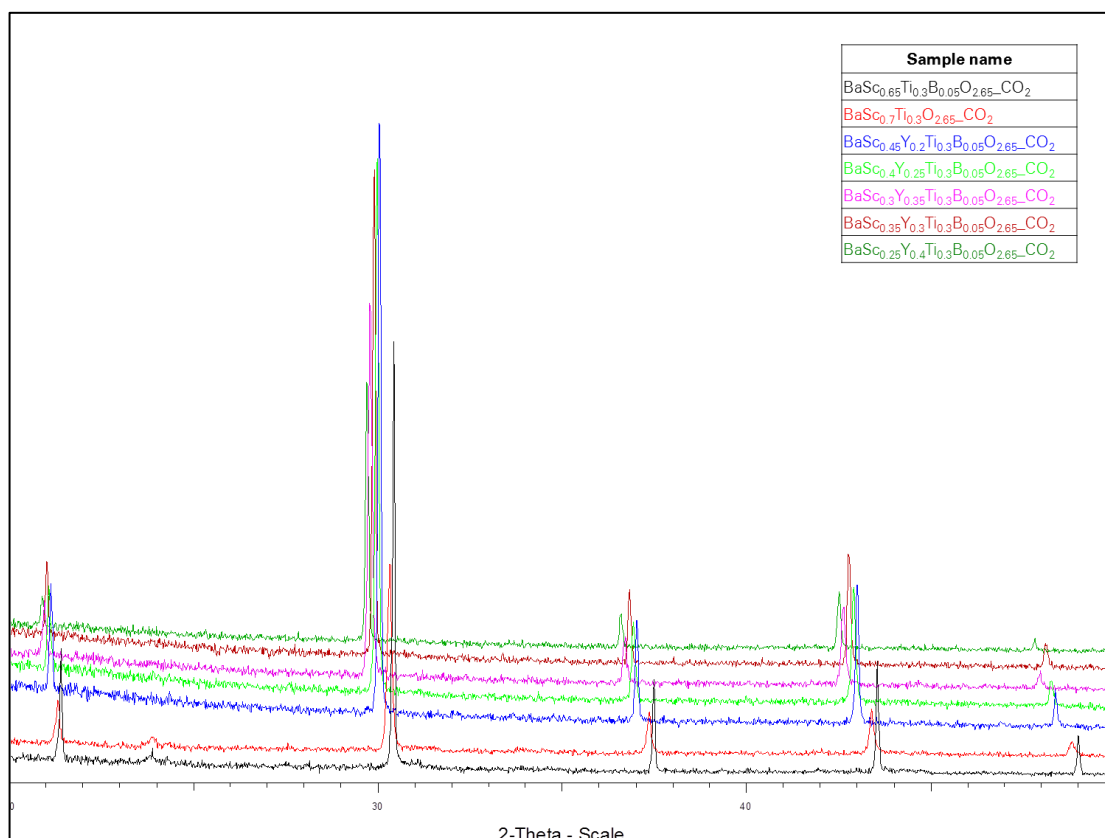


Figure 5.14 - XRD patterns of yttrium and titanium doped barium scandate samples after heating in a dry CO<sub>2</sub> atmosphere

The samples were then heated in a wet CO<sub>2</sub> gas flow using a water filled bubbler to mimic more extreme conditions. They were heated to 800°C for 12 h before cooling at 1°C min<sup>-1</sup> in the wet CO<sub>2</sub> atmosphere. After 24 h in this wet CO<sub>2</sub> atmosphere, it was possible to see impurities forming in the XRD pattern caused by the formation of a barium carbonate phase as peaks are emerging at 24° 2θ. Nevertheless the level is quite low, even under these extreme conditions, which are far more extreme than would be observed in an operating fuel cell.

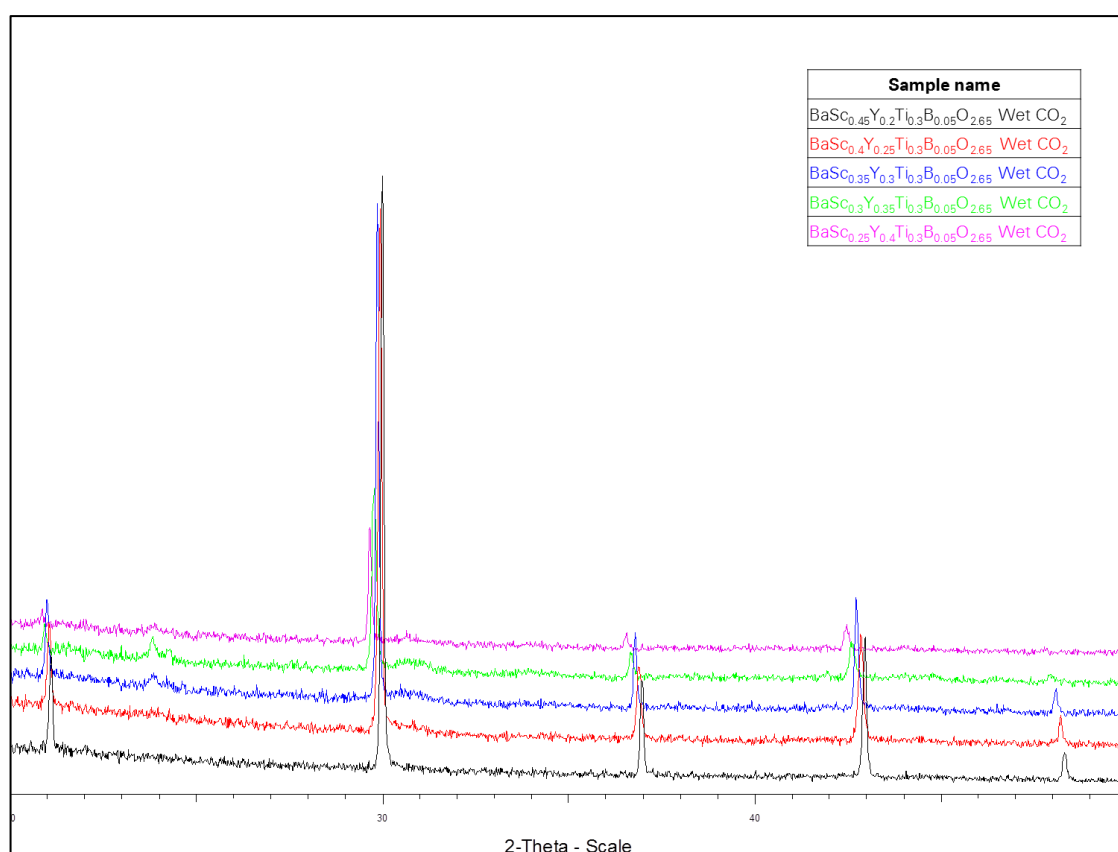


Figure 5.15 - XRD patterns of yttrium and titanium doped barium scandate samples after heating in a wet CO<sub>2</sub> atmosphere

## 5.5 Ytterbium doping in $\text{BaSc}_{0.65}\text{Ti}_{0.3}\text{B}_{0.05}\text{O}_{2.65}$

Ytterbium was also doped into  $\text{BaSc}_{0.65}\text{Ti}_{0.3}\text{B}_{0.05}\text{O}_{2.65}$  in an attempt to lower the scandium content without a negative effect on the observed ionic conductivity. These samples were prepared in the same way as the initial sample.

The samples were analysed using XRD, with doping shown to be successful with a peak shift to lower angle due to the unit cell changes observed. The structure was refined using Rietveld refinement to extract information on the changes to the unit cell lengths (Table 5.10).

**Table 5.10 - Unit cell parameters for  $\text{BaSc}_{0.65}\text{Ti}_{0.3}\text{B}_{0.05}\text{O}_{2.65}$  samples doped with Yttrium**

Sample	Unit Cell a (Å)
$\text{BaSc}_{0.65}\text{Ti}_{0.3}\text{B}_{0.05}\text{O}_{2.65}$	4.164(2)
$\text{BaSc}_{0.5}\text{Yb}_{0.15}\text{Ti}_{0.3}\text{B}_{0.05}\text{O}_{2.65}$	4.177(1)
$\text{BaSc}_{0.4}\text{Yb}_{0.25}\text{Ti}_{0.3}\text{B}_{0.05}\text{O}_{2.65}$	4.194(3)
$\text{BaSc}_{0.35}\text{Yb}_{0.3}\text{Ti}_{0.3}\text{B}_{0.05}\text{O}_{2.65}$	4.209(2)
$\text{BaSc}_{0.3}\text{Yb}_{0.35}\text{Ti}_{0.3}\text{B}_{0.05}\text{O}_{2.65}$	4.215(3)
$\text{BaSc}_{0.2}\text{Yb}_{0.45}\text{Ti}_{0.3}\text{B}_{0.05}\text{O}_{2.65}$	4.225(2)
$\text{BaSc}_{0.15}\text{Yb}_{0.5}\text{Ti}_{0.3}\text{B}_{0.05}\text{O}_{2.65}$	4.245(2)

It can be seen that as predicted, an expansion is seen in the unit cell on substitution of scandium for ytterbium due to the larger size of the  $\text{Yb}^{3+}$  ion compared with  $\text{Sc}^{3+}$ . The observed increase is smaller than the increase observed with yttrium doping as  $\text{Y}^{3+}$  is a larger ion than  $\text{Yb}^{3+}$  (Figure 5.16). The cell parameter change is non-linear, which may be related to some water incorporation from the atmosphere in selected samples.

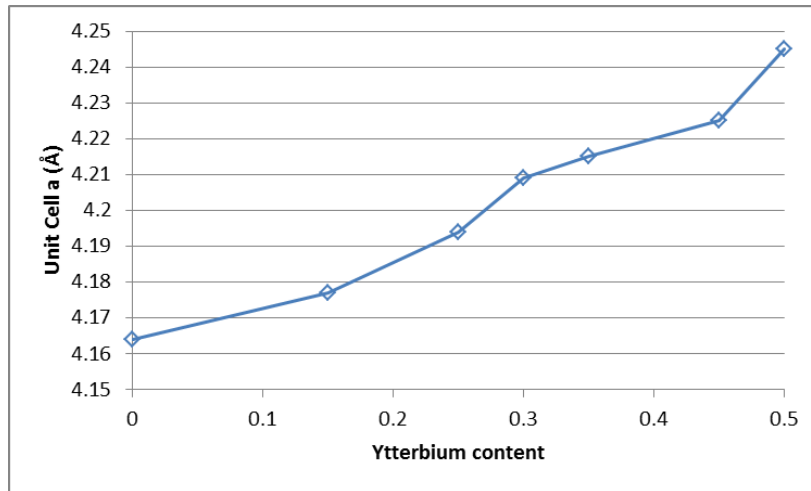


Figure 5.16 - Unit cell changes on changing ytterbium content

### 5.5.1 Conductivity data

AC impedance measurements were performed on the samples to determine the effects of ytterbium substitution on the ionic conductivity. Impedance measurements were recorded in both dry and wet N<sub>2</sub> atmospheres at various temperatures between 200 – 800°C. It was not possible to fully resolve the bulk and grain boundary components for all of the samples, so total conductivity values are given. The parent material BaSc<sub>0.65</sub>Ti<sub>0.3</sub>B<sub>0.05</sub>O<sub>2.65</sub> had a conductivity of 1.3 x 10<sup>-3</sup> S cm<sup>-1</sup> at 500°C in dry conditions, which is higher than the conductivities observed for the ytterbium doped samples (Figure 5.17). In wet N<sub>2</sub> conditions at lower temperatures (below 500°C), the samples doped with ytterbium exhibited an increase in conductivity, which indicates a proton conducting contribution to the total conductivity. In comparison, the parent sample showed only a slight increase in conductivity in the wet N<sub>2</sub> atmosphere (Figure 5.18). The activation energies and conductivity values for the remaining samples are shown in Table 5.11.

Table 5.11 - Conductivity and activation energy values for  $\text{BaSc}_{(0.65-x)}\text{Yb}_x\text{Ti}_{0.3}\text{B}_{0.05}\text{O}_{2.65}$  samples in a  $\text{N}_2$  atmosphere.

Sample	Conductivity 500°C ( $\text{S cm}^{-1}$ )	Activation energy (eV)
$\text{BaSc}_{0.65}\text{Ti}_{0.3}\text{B}_{0.05}\text{O}_{2.65}$ (Dry)	$1.3 \times 10^{-3}$	0.57
$\text{BaSc}_{0.65}\text{Ti}_{0.3}\text{B}_{0.05}\text{O}_{2.65}$ (Wet)	$1.5 \times 10^{-3}$	0.58
$\text{BaSc}_{0.35}\text{Yb}_{0.3}\text{Ti}_{0.3}\text{B}_{0.05}\text{O}_{2.65}$ (Dry)	$7.5 \times 10^{-6}$	0.83
$\text{BaSc}_{0.35}\text{Yb}_{0.3}\text{Ti}_{0.3}\text{B}_{0.05}\text{O}_{2.65}$ (Wet)	$1.8 \times 10^{-3}$	0.26
$\text{BaSc}_{0.3}\text{Yb}_{0.35}\text{Ti}_{0.3}\text{B}_{0.05}\text{O}_{2.65}$ (Dry)	$1.1 \times 10^{-4}$	0.63
$\text{BaSc}_{0.3}\text{Yb}_{0.35}\text{Ti}_{0.3}\text{B}_{0.05}\text{O}_{2.65}$ (Wet)	$1.4 \times 10^{-3}$	0.70

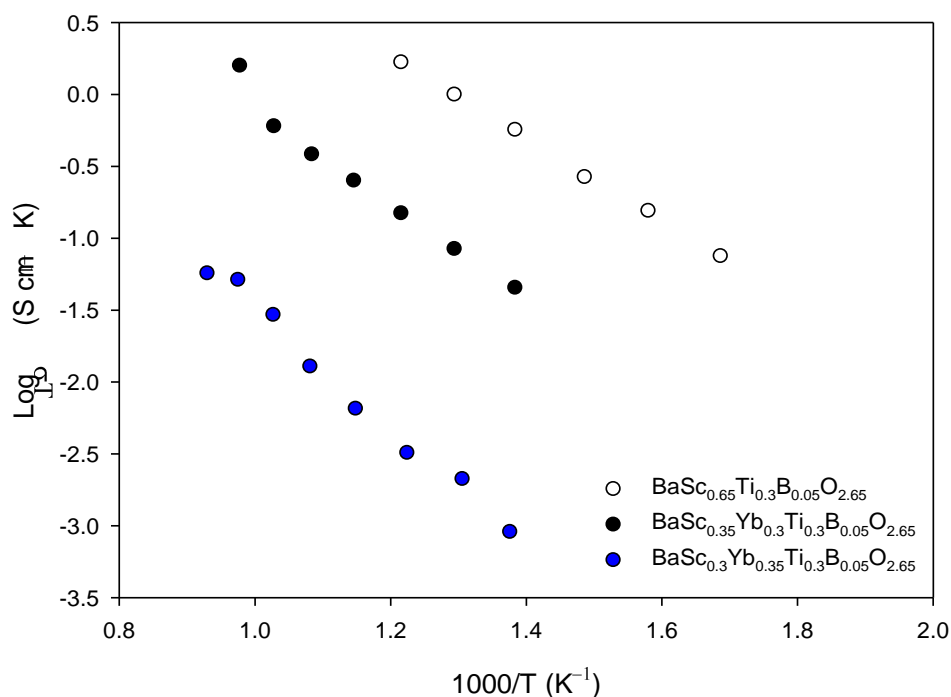


Figure 5.17 - Plot of  $\log\sigma T$  vs  $1000/T$  for  $\text{BaSc}_{(0.65-x)}\text{Yb}_x\text{Ti}_{0.3}\text{O}_{2.65}$  samples in Dry  $\text{N}_2$ .

As with the yttrium doped samples, the density of the Yb doped samples was lower than the parent material,  $\text{BaSc}_{0.65}\text{Ti}_{0.3}\text{B}_{0.05}\text{O}_{2.65}$  (Table 5.12). This could lower the conductivity as it would increase the resistance of the grain boundary component.

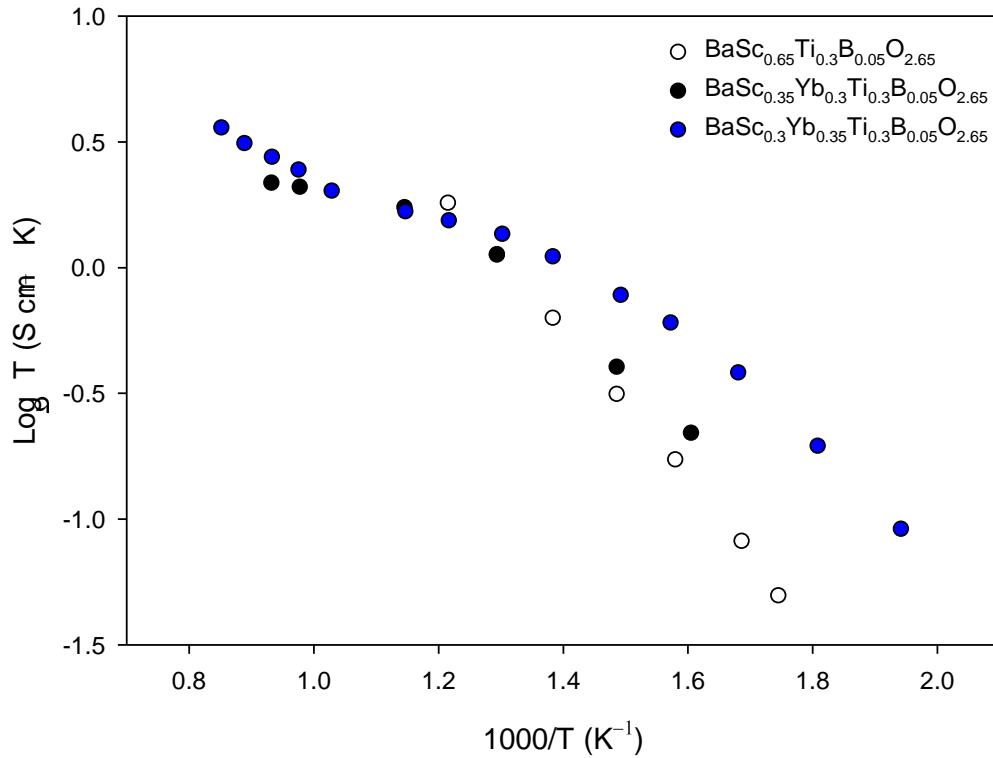


Figure 5.18 - Plot of  $\log \sigma T$  vs  $1000/T$  for  $\text{BaSc}_{(0.65-x)}\text{Yb}_x\text{Ti}_{0.3}\text{B}_{0.05}\text{O}_{2.65}$  samples in wet  $\text{N}_2$ .

Table 5.12 - Theoretical densities for  $\text{BaSc}_{0.65-x}\text{Yb}_x\text{Ti}_{0.3}\text{B}_{0.05}\text{O}_{2.65}$  samples.

Sample	% Theoretical density
$\text{BaSc}_{0.65}\text{Ti}_{0.3}\text{B}_{0.05}\text{O}_{2.65}$	87
$\text{BaSc}_{0.35}\text{Yb}_{0.3}\text{Ti}_{0.3}\text{B}_{0.05}\text{O}_{2.65}$	71
$\text{BaSc}_{0.3}\text{Yb}_{0.35}\text{Ti}_{0.3}\text{B}_{0.05}\text{O}_{2.65}$	75

## 5.6 Conclusions

Titanium doping in  $\text{Ba}_2\text{Sc}_2\text{O}_5$  successfully stabilised the oxygen deficient cubic perovskite structure at room temperature. Replacing scandium with titanium altered the number of oxygen vacancies and the ionic conductivity which was found to reach a peak at 30% titanium as  $\text{BaSc}_{0.7}\text{Ti}_{0.3}\text{O}_{2.65}$  exhibited the highest conductivity values. As this material requires a large amount of scandium the cost could be prohibitive to the potential uses as an electrolyte material in a SOFC, with this in mind further

doping on the scandium site was attempted. It was decided to initially dope with trivalent ions as these would not alter the number of oxide ion vacancies which appear to be beneficial to the conductivity. Yttrium and ytterbium were chosen as they are of lower cost than scandium and have ionic radii in between that of scandium and barium. Initially doping with yttrium and ytterbium reduced the strength and density of the samples to a level where conductivity measurements could not be completed and could not be used as electrolytes, this was improved when boron was added as a sintering aid replacing  $\text{Sc}_{0.05}$  with  $\text{B}_{0.05}$  increased the density. For the yttrium samples low amounts of yttrium ( $\text{Y}_{0.2} - \text{Y}_{0.3}$ ) significantly lowered the ionic conductivity. As the yttrium content increases to  $\text{Y}_{0.35}-\text{Y}_{0.4}$  the conductivity is very similar to that of  $\text{BaSc}_{0.7}\text{Ti}_{0.3}\text{O}_{2.65}$ . The  $\text{Y}_{0.4}$  ( $\text{BaSc}_{0.25}\text{Y}_{0.4}\text{Ti}_{0.3}\text{B}_{0.05}\text{O}_{2.65}$ ) sample exhibits an improvement on the conductivity of  $\text{BaSc}_{0.7}\text{Ti}_{0.3}\text{O}_{2.65}$  at low temperatures, below  $500^\circ\text{C}$ .

In wet atmospheres the conductivity of the  $\text{Y}_{0.4}$  sample is double the parent material at  $500^\circ\text{C}$  although  $\text{BaSc}_{0.7}\text{Ti}_{0.3}\text{O}_{2.65}$  showed almost no increase due to protonic conductivity in humid atmospheres. This is likely to be due to the kinetics of hydration and a greater proton conducting element may be observed with longer equilibration times.

Substitution of Yb for Sc was also successful although all amounts of ytterbium incorporation resulted in a drop in ionic conductivity across the temperature range studied.

Yttrium doped samples were tested in both dry and humid  $\text{CO}_2$  atmospheres to observe their stability and resistance to the formation of  $\text{BaCO}_3$ . Samples doped with

yttrium showed no change by XRD after 12 h in a pure dry CO<sub>2</sub> environment however in a wet environment very small amounts of BaCO<sub>3</sub> were observed after 12 h. these conditions are more severe than would be seen in a fuel cell and the yttrium doped material showed enhanced stability when compared with the undoped sample.

TGA and neutron diffraction studies on hydrated / deuterated BaSc<sub>0.25</sub>Y<sub>0.45</sub>Ti<sub>0.3</sub>O<sub>2.65</sub> indicated that not all of the vacant oxygen sites in the perovskite structure can be filled. Neutron diffraction at 4 K was used to locate the H sites within the hydrated structure. These were found to be located in a 48n position at (0.1030(31), 0.5599(48), 0.7749(25)) which is slightly displaced from the 24h site reported in the literature for the related Ba<sub>2</sub>In<sub>2</sub>O<sub>5</sub> based materials. Overall the results suggest that given good ionic conductivities and CO<sub>2</sub> stability further work on the Ba-Sc-Y-Ti-B-O system is warranted.

## 5.7 References

1. A. Orera and P. R. Slater, *Chem. Mater.* 2010, **22**, 675.
2. S. M. H. Rahman, C. S. Knee, I. Ahmed, S. G. Eriksson and R. Haugrud, *Int. J. Hydrogen Energ.* 2012, **37**, 7975.
3. A. Jarry, E. Quarez, K. Kravchyk and O. Joubert, *Solid State Ionics* 2012, **216**, 11.
4. N. Hideshima and K. Hashizume, *Solid State Ionics* 2010, **181**, 1659-1664.
5. T. Omata, T. Fuke and S. Otsuka-Yao-Matsuo, *Solid State Ionics* 2006, **177**, 2447.
6. J.F. Shin, K. Joubel, D.C. Apperley, P.R. Slater; *Dalton Trans.* 2012, **41**, 261.
7. B.H. Toby, *J. Appl. Crystallogr.*, 2001, **34**, 210
8. A.C. Larson and R.B. von Dreele, *Los Alamos National Laboratory report*, LAUR, 1994, **86**
9. C. L. Huang, J.J. Wang, B.J. Li and W.L. Lee, *J. Alloy. Compd.*, 2008, **461**, 440.
10. S. Guo-Ce, S. Hua, Z. Huang-Luo, J. Yu-Lan and T. Xiao-Li, *Chin. Phys. B*, 2013, **22**
11. I. Ahmed, C.S. Knee, M. Karlsson, S.G. Eriksson, P.F. Henry, A. Matic, , D. Engberg and L Borjesson, *J. Alloy. Compd.*, 2008, **450**, 103

12. T. Nagasaki, T. Ito, M. Yoshino, K. Iwasaki, H. Fukazawa, N. Igawa and Y. Ishii, *J. Nucl. Sci. Technol.*, 2008, **122**

# 6 Conclusions and Further Work

---

A range of materials with tetrahedral moieties have been prepared and characterised using a variety of techniques. The work was carried out to gain a greater understanding of solid oxide electrolyte materials with tetrahedral moieties for use as solid oxide fuel cell electrolytes.

The phases presented in this thesis were synthesised using standard solid state synthesis techniques and pressed into pellets for to aid sintering. Characterisation of these materials included X-ray diffraction, neutron diffraction, AC impedance spectroscopy TGA and Raman spectroscopy.

As the work presented in this thesis was completed the results observed were sometimes expected and others unexpected, some of the results answered questions and others added more questions to the list. The materials examined during this project, the results obtained and potential further work to extend the project are summarised here.

## 6.1 $A_2MO_4$ electrolyte materials

A variety of materials with tetrahedral moieties with the general formula  $A_2MO_4$  were successfully synthesised beginning initially with  $Ba/Sr_2Ge_{1-x}A_xO_{(4-x/2)}$  ( $A = Al, Ga, Zn, Mg$ ) to investigate the effect of oxygen vacancy creation on ionic conductivity. It was found that only the trivalent cation Ga and Al could be accommodated to low levels (15% Ga / 10% Al) in the Ba system and it was not possible to accommodate the

divalent Zn or Mg. This suggests that the structure is possibly unable to accept larger localised changes affecting the  $\text{MO}_4$  tetrahedra but further experiments with a wider range of divalent cations would be required to confirm this. Incorporation of trivalent ions and therefore oxide ion vacancies into the structure was found to increase the oxide ion conductivity and dry conditions and protonic conductivity in humid conditions.

Conductivity increased with increasing Ga content (greater number of O vacancies) until single phase pure samples could no longer be synthesised (>15% Ga) suggesting that O vacancies play a large part in the conduction pathway.

Initial studies into  $\text{LaBaGaO}_4$  indicated that the smaller strontium ions could be incorporated in place of barium. This was increased to discover where the transition between the orthorhombic structure of  $\text{LaBaGaO}_4$  transforms into the tetragonal structure exhibited by  $\text{LaSrGaO}_4$ . A full series at 10% intervals was not possible and impurity phases could be observed in the XRD pattern beyond 50% Sr. Above 70% Sr both the tetrahedral  $\text{LaSrGaO}_4$  and orthorhombic  $\text{LaBaGaO}_4$  phases along with other impurities are observed. The  $\text{LaSrGaO}_4$  fails to accept 10% barium with a mixture of phases present in the resulting XRD pattern.

Accommodation of the smaller  $\text{Sr}^{2+}$  ion in place of  $\text{Ba}^{2+}$  had a negative effect on the ionic conductivity within the orthorhombic structure this was observed by a sharp decrease compared with the parent  $\text{LaBaGaO}_4$ . Larger amounts of Sr incorporation decreased the unit cell size and conductivity further with  $\text{LaSrGaO}_4$  exhibiting the lowest conductivity. This reduction in unit cell size could imply that more space within the cell could be beneficial to ionic conductivity.

As strontium has a negative effect on the parent  $\text{LaBaGaO}_4$  material further experiments to introduce oxygen vacancies using substitution of Sr for La were not attempted as it was unlikely an improvement in conductivity would be seen when compared with the systems replacing La with Ba.

The final  $\text{A}_2\text{MO}_4$  system investigated was  $\text{LaBaAlO}_4$  where oxygen vacancies were created by increasing Ba content and lowering La content. This showed an increase in ionic conductivity of four orders of magnitude although both samples had low density and mechanical strength. It is therefore possible that a portion of this increase could be due to the increase in density which would lower the grain boundary component of the resistance increasing conductivity. Sintering aids were used in an attempt to improve both density and mechanical strength but no significant increase was observed.

The conductivity of  $\text{LaBaAlO}_4$  samples was lower than the related  $\text{LaBaGaO}_4$  samples although if the densities of the samples could be improved this may increase the conductivity of the  $\text{LaBaAlO}_4$  samples to a similar value and further work is warranted to pass this hurdle.

## **6.2 Water and fluorine incorporation in apatite systems.**

Both silicate and germanate apatite systems were synthesised and investigated for their ability to incorporate water and fluorine. Initially  $\text{La}_8\text{Sr}_2(\text{Ge/Si})_6\text{O}_{26}$  was selected as this was a fully stoichiometric sample with no interstitial oxide ions leaving a larger amount of space internally. The larger  $\text{La}_8\text{Sr}_2\text{Ge}_6\text{O}_{26}$  incorporated a larger amount of water, 0.84 mol compared with just 0.2 mol for the silicate sample. A large portion of

this increase can be attributed to the ability of the  $\text{GeO}_4$  tetrahedra to accommodate an extra oxide ion to form  $\text{GeO}_5$  polyhedra. The inability of silica to increase from  $\text{SiO}_4$  to  $\text{SiO}_5$  removes this additional space from the structure leaving the channel as the only space to accommodate the water molecules.

As the c-axis channel in the germanate samples is also larger than the silicate equivalent due to the larger radii of Ge it was also possible to accommodate a greater amount of water in the channel.

Fluorination in these samples was successful using both PVDF and PTFE as a fluorine source. Incorporation of fluorine had a larger increase in the volume of the unit cell when compared with the hydrated sample. In both the germanate and silicate samples fewer moles of fluorine were incorporated than the number of moles of water incorporated with hydration. In the case of the germanate samples it was expected that  $\text{GeX}_5$  ( $X = \text{O}, \text{F}$ ) units would be formed however all of the interstitials from the fluorine accommodation were located within the c-axis channel. It was not possible to differentiate between fluorine and oxygen using the neutron diffraction patterns and therefore whether the fluorine chooses a favoured oxygen site. Although due to charge balancing  $2\text{xF}^-$  will replace  $1\text{xO}^{2-}$  and therefore fluorine must be present in addition to the interstitial fluorine observed in the channel.

In the fluorinated  $\text{La}_8\text{Sr}_2\text{Si}_6\text{O}_{26}$  the fluorine was also incorporated in the channel centre for lower quantities although when PTFE was used and a larger amount was accommodated the fluorine was pushed further towards the channel edges. There have been reports of both these interstitial site positions previously for different samples suggesting that there is not one interstitial site for silicate apatites but the

positions are related to the composition of the sample and the characteristics of the incorporated ions. Raman spectroscopy indicated a Si-F bond suggesting that there is fluorine present within the  $\text{SiO}_4$  groups.

The oxygen excess germanate apatite material,  $\text{La}_{9.75}\text{Ge}_6\text{O}_{26.625}$ , which shows a triclinic structure at room temperature in dry conditions was also hydrated in an attempt to further increase the quantity of interstitial ions. This was successful and 0.81 mol of water could be accommodated. Accommodation of water transformed the triclinic P-1 structure to the hexagonal P63/m space group observed for both  $\text{La}_8\text{Sr}_2\text{Ge}_6\text{O}_{26}$  and  $\text{La}_8\text{Sr}_2\text{Si}_6\text{O}_{26}$ . Refinement of XRD data suggested a portion of the interstitial are located within the channel although the total anion content was lower than suggested by TGA implying that not all anions have been located. A transition to a hexagonal structure was also observed on heating ( $>650^\circ\text{C}$ ), although it was also not possible to locate all of the interstitial sites.

### **6.3 Yttrium and ytterbium doping in barium scandate systems.**

Titanium doping in  $\text{Ba}_2\text{Sc}_2\text{O}_5$  successfully stabilised the oxygen deficient cubic perovskite structure at room temperature. Replacing scandium with titanium altered the number of oxygen vacancies and the ionic conductivity which was found to reach a peak at 30% titanium as  $\text{BaSc}_{0.7}\text{Ti}_{0.3}\text{O}_{2.65}$  exhibited the highest conductivity values. As this material requires a large amount of scandium the cost could be prohibitive to the potential uses as an electrolyte material in a SOFC, with this in mind further doping on the scandium site was attempted. It was decided to initially dope with

trivalent ions as these would not alter the number of oxide ion vacancies which appear to be beneficial to the conductivity. Yttrium and ytterbium were chosen as they are of lower cost than scandium and have ionic radii in between that of scandium and barium. Initially doping with yttrium and ytterbium reduced the strength and density of the samples to a level where conductivity measurements could not be completed and could not be used as electrolytes, this was improved when boron was added as a sintering aid replacing  $\text{Sc}_{0.05}$  with  $\text{B}_{0.05}$  increased the density. For the yttrium samples low amounts of yttrium ( $\text{Y}_{0.2} - \text{Y}_{0.3}$ ) significantly lowered the ionic conductivity. As the yttrium content increases to  $\text{Y}_{0.35} - \text{Y}_{0.4}$  the conductivity is very similar to that of  $\text{BaSc}_{0.7}\text{Ti}_{0.3}\text{O}_{2.65}$ . The  $\text{Y}_{0.4}$  ( $\text{BaSc}_{0.25}\text{Y}_{0.4}\text{Ti}_{0.3}\text{B}_{0.05}\text{O}_{2.65}$ ) sample exhibits an improvement on the conductivity of  $\text{BaSc}_{0.7}\text{Ti}_{0.3}\text{O}_{2.65}$  at low temperatures, below  $500^\circ\text{C}$ .

In wet atmospheres the conductivity of the  $\text{Y}_{0.4}$  sample is double the parent material at  $500^\circ\text{C}$  although  $\text{BaSc}_{0.7}\text{Ti}_{0.3}\text{O}_{2.65}$  showed almost no increase due to protonic conductivity in humid atmospheres. This is likely to be due to the kinetics of hydration and a greater proton conducting element may be observed with longer equilibration times.

Substitution of Yb for Sc was also successful although all amounts of ytterbium incorporation resulted in a drop in ionic conductivity across the temperature range studied.

Yttrium doped samples were tested in both dry and humid  $\text{CO}_2$  atmospheres to observe their stability and resistance to the formation of  $\text{BaCO}_3$ . Samples doped with yttrium showed no change by XRD after 12 h in a pure dry  $\text{CO}_2$  environment however

in a wet environment very small amounts of  $\text{BaCO}_3$  were observed after 12 h. these conditions are more severe than would be seen in a fuel cell and the yttrium doped material showed enhanced stability when compared with the undoped sample.

TGA and neutron diffraction studies on hydrated / deuterated  $\text{BaSc}_{0.25}\text{Y}_{0.45}\text{Ti}_{0.3}\text{O}_{2.65}$  indicated that not all of the vacant oxygen sites in the perovskite structure can be filled. Neutron diffraction at 4 K was used to locate the H sites within the hydrated structure. These were found to be located in a 48n position at (0.1030(31), 0.5599(48), 0.7749(25)) which is slightly displaced from the 24h site reported in the literature for the related  $\text{Ba}_2\text{In}_2\text{O}_5$  based materials. Overall the results suggest that given good ionic conductivities and  $\text{CO}_2$  stability further work on the Ba-Sc-Y-Ti-B-O system is warranted.

## 6.4 Further work

There is a great deal of further work which could be investigated based on the systems studied within this thesis.

Further work in the area of the  $\text{A}_2\text{MO}_4$  systems could include extending the range of dopants to further alkaline earth metals and rare earth metals for the La/Ba site in the  $\text{LaBaAlO}_4$  systems to look for further improvements in ionic conductivity and possible proton conductivity. Doping with transition metals on the aluminium site may lead to greater density and mechanical stability which in turn would likely increase the conductivity.

For the germanate systems conductivity may be improved with doping with trivalent lanthanides on the Ba/Sr site. Using La and Ba on the A site has shown improvements in conductivity for other systems such as LaBaGaO<sub>4</sub> which exhibits a conductivity far in excess of the BaGeO<sub>4</sub> systems. Another possibility could involve creating a mixed Ba-Sr system to see the effects on proton conductivity and water incorporation although it is likely that the oxide ion conductivity would be reduced compared with the Ba<sub>2</sub>GeO<sub>4</sub> samples.

With the apatite samples there is a wide range of potential further work which could be of interest and expand this work. Currently the work uses a humidity system which is rather uncontrolled with only the options for on or off and further work could involve using a controlled humidity system. This could control the relative humidity of the atmosphere between 0 – 300% this would allow more specific information on the hydration of the samples and the level of humidity required to incorporate water within the sample. The possibility of controlling the humidity could provide the answers to several questions including noting the effects on dehydration temperatures the conductivity would also be altered as there may be different levels of hydration which in turn would change the proton conductivity.

Neutron diffraction on the hydrated / deuterated apatite samples at 4 K could be used to freeze out thermal motion in the protons / deuterons allowing for the positions to be confirmed. In the case of the silicate samples this could be used to see if any of the water is located within the structure or just within the c-axis channels.

Ion exchange in the apatite samples reacted with either PVDF or PTFE would be useful to see if the increased fluorine content can be exchanged for an increased

hydration level, this could be confirmed using TGA-MS. The conductivity of these samples could then be compared with conductivity of fluorinated samples which have been isostatic pressed which would give strength and density without heating and losing the fluorine content.

Apatite samples with an oxygen excess such as  $\text{La}_{9.75}\text{Ge}_6\text{O}_{26.625}$  could be treated with ammonia in an attempt to replace some of the excess oxygen with nitrogen lowering the total anion content and potentially stabilising the hexagonal structure. The locations of nitrogen atoms could be confirmed using neutron diffraction.

Further work on the yttrium doped  $\text{BaSc}_{0.65-x}\text{Ti}_{0.3}\text{B}_{0.05}\text{O}_{2.65}$  systems could investigate the incorporation of fluorine ions to potentially fill all of the vacancies in the perovskite structure, as this was not possible with water incorporation. As high levels of Y doping for the high cost Sc was successful with no reduction in conductivity and an increase in stability to  $\text{CO}_2$ , further doping studies to investigate other materials which could replace Sc are warranted. Fuel cell testing to obtain power density curves using both air and oxygen as oxidant could be completed to investigate practical uses and stability with electrode materials.

For the ytterbium doped  $\text{BaSc}_{0.65-x}\text{Ti}_{0.3}\text{B}_{0.05}\text{O}_{2.65}$ , further samples are required to see the overall effects on Yb doping on the conductivity of these samples. Proton conductivity in the Yb doped samples exhibited an increase compared with the parent  $\text{BaSc}_{0.65}\text{Ti}_{0.3}\text{B}_{0.05}\text{O}_{2.65}$  sample suggesting further work on water incorporation or fluorine incorporation is justified. Stability to  $\text{CO}_2$  in wet and dry atmospheres could well be improved compared with the  $\text{BaSc}_{0.65}\text{Ti}_{0.3}\text{B}_{0.05}\text{O}_{2.65}$ , as was seen with Y doping and tests to investigate this should be performed.